# Numerical Studies on Melting and Solidification Using Lattice Boltzmann Method

**Thesis Submitted by**

**RUNA SAMANTA**

## Doctor of Philosophy (Engineering)

Department of Mechanical Engineering
Faculty Council of Engineering & Technology
Jadavpur University
Kolkata, India

**2024**

**INDEX NO. 218/18/E**

**1. Title of the Thesis:** Numerical Studies on Melting and Solidification Using Lattice Boltzmann Method

**2. Name, Designation & Institution of the Supervisor/s:**

Dr. Himadri Chattopadhyay

Professor

Department of Mechanical Engineering,

Jadavpur University,

Kolkata – 700 032, India

**3. List of Publications:**

***International Journal***

- **Samanta, R.,** Chattopadhyay, H. and Guha, C. "Transport phenomena in a differentially heated lid-driven cavity: A study using multi-relaxation-time thermal lattice Boltzmann modelling," ***Physics of Fluids*** 32, 093610 (2020). https://doi.org/10.1063/5.0021105
- **Samanta, R.,** Chattopadhyay, H. and Guha, C. "A review on the application of lattice Boltzmann method for melting and solidification problems", ***Computational Materials Science*** 206, 111288 (2022). https://doi.org/10.1016/j.commatsci.2022.
- **Samanta, R**., Chattopadhyay, H. and Guha, C. "Study of thermal convection in corner melting problems using lattice Boltzmann method", ***Numerical Heat Transfer Part A Applications***, (under review).
- **Samanta, R**., Chattopadhyay, H. and Guha, C. "Effect of Low Prandtl number on natural convection dominated melt zone by modified lattice Boltzmann method", ***Physics of Fluids***, (under review).
- **Samanta, R**., Chattopadhyay, H. and Guha, C. "Study of Convective Flow Instability in Melt Zone for Solid-liquid Phase Change Problem", ***Chaos, Solitons & Fractals*** (Submitted).

**4. List of Patents:** Nil

## 5. List of Presentations in National / International / Conferences/Workshops/Symposiums:

- **Samanta, R.**, Chattopadhyay, H. and Guha, C. “Effect of Prandtl Number on Differentially Heated Lid Driven Cavity: Analysis using Lattice Boltzmann Method”, 7th International and 45th National Conference on Fluid Mechanics and Fluid Power (FMFP 2018) ,December 10-12, IIT Bombay, Mumbai, India.
- **Samanta, R.**, Chattopadhyay, H. and Guha, C. “Study of Solid-Liquid Phase Change using Lattice Boltzmann Simulation”, Proceeding of International Conference on Advancements in Mechanical Engineering (ICAME 2020), January 16-18, Aliah University, Kolkata, India. ISBN 978-81-943641-6-0.
- **Samanta, R.**, Chattopadhyay, H. and Guha, C. “Study of Solidification in a Partially Filled Square Cavity Using Lattice Boltzmann Method”, Proceeding of International Conference on Energy and Sustainable Development (ICESD 2020), February 14-15, Jadavpur University, Kolkata, India. ISBN 978-93-83660-56-8.
- **Samanta, R.**, Chattopadhyay, H. and Guha, C. “Study of Corner Solidification of pure metal using Lattice Boltzmann Method” , Proceedings of the 48th National Conference on Fluid Mechanics and Fluid Power (FMFP 2022), December 27-29, 2021, BITS Pilani, Pilani Campus, RJ, India. ISSN 2195-4356.
- **Samanta, R.**, Chattopadhyay, H. and Guha, C. “Study of Natural Convection in Corner Melting Problem using Lattice Boltzmann Method”, Proceedings of International Conference on Chemical Engineering Innovation and Sustainability (ICEIS 2023), February 26-27, 2023, Jadavpur University, India.
- **Samanta, R.** and Chattopadhyay, H. “Study of Natural Convection in Corner Melting of Low Prandtl Number Materials using Modified Lattice Boltzmann Method”, Proceedings of the 27th National and 5th International ISHMT-ASTFE Heat and Mass Transfer Conference December 14-17, 2023, IIT Patna, Patna-801106, Bihar, India.

## “Statement of Originality”

I Runa Samanta registered on 28th March, 2018 do hereby declare that this thesis entitled ”**Numerical Studies on Melting and Solidification Using Lattice Boltzmann Method**” contains literature survey and original research work done by the undersigned candidate as part of Doctoral studies.

All information in this thesis have been obtained and presented in accordance with existing academic rules and ethical conduct. I declare that, as required by these rules and conduct, I have fully cited and referred all materials and results that are not original to this work.

I also declare that I have checked this thesis as per the “Policy on Anti Plagiarism, Jadavpur University, 2019”, and the level of similarity as checked by iThenticate software is ____03___%.

Runa Samanta

Signature of Candidate:

Date:

H. Chattopadhyay
8.2.2024

Professor
Dept. of Mechanical Engineering
Jadavpur University, Kolkata-32

Certified by Supervisor:

(Signature with date, seal)

# CERTIFICATE FROM THE SUPERVISOR

This is to certify that the thesis entitled **"Numerical Studies on Melting and Solidification Using Lattice Boltzmann Method"** submitted by Smt. **Runa Samanta**, who got her name registered on 28th March, 2018 for the award of Ph. D (Engg.) degree of Jadavpur University is absolutely based upon her own work under the supervision of Dr. Himadri Chattopadhyay and that neither her thesis nor any part of the thesis has been submitted for any degree or any other academic award anywhere before.

H. Chattopadhyay
8.2.2024

Professor
Dept. of Mechanical Engineering
Jadavpur University, Kolkata-32

---

(Dr. Himadri Chattopadhyay)
Professor
Department of Mechanical Engineering
Jadavpur University
Kolkata 700032, India
**Signature of the Supervisor**
**and date with Office Seal**

उर्ध्वमूलमधःशाखमश्वत्थं प्राहुरव्ययम् |

छन्दांसि यस्य पर्णानि यस्तं वेद स वेदवित् ||

(verse 15.1, Bhagavad-Gita)

The eternal banyan tree has its roots in the sky and the branches are downward to the earth. To the savants the leaves are the rhythms of life.

Dedicated to

My Family

# ACKNOWLEDGEMENTS

Research has been defined as the systematized effort to gain new knowledge. This journey to new insights becomes easier when one receives proper direction and encouragement. During my journey of Ph.D. work, there were many ups and downs. I would like to express my sincere gratitude to those people who helped me to overcome all the hurdles throughout my PhD period.

First and foremost, I would like to gratefully acknowledge my PhD supervisor, Prof. Himadri Chattopadhyay for his invaluable guidance, thorough encouragement and total involvement in my endeavour through every step to complete my research work. It is not an exaggeration to say that my curiosity and eagerness in research was evoked by Prof. Himadri Chattopadhyay. The importance of supervision is well-known to anyone who conducts research. In this context, I would thank my supervisor for his unconditional support to take new challenges in achieving the target at the right time.

It is my pleasure to express my heartiest gratitude to Prof. Chandan Guha for his enthusiastic support and guidance. He helped me to broaden my view and knowledge. I would like to thank him for inspiring me to pursue excellence. The fruitful discussions with him stimulated new ideas.  His research ideas and motivations helped me to shape my research.

Next, I want to express gratitude to my parents (Late. Chandi charan Samanta and Smt. Rupa Samanta) for standing by me always and keeping faith in me. I want to thank my beloved brother Mr. Rintu Samanta for his continuous support and motivation.

Next, I would like to specially thank my husband Mr. Abinash Sil for his love, patience, understanding and inspiration in spite of all the ups and downs of my life.

Finally, I would like to thank my friend Mr. Sukanta Mitra who continuously motivates and inspires throughout my research period. .

Signature:

Runa Samanta

(Runa Samanta)

# ABSTRACT

Melting and solidification of pure metals and alloys are important research areas due to its practical applications, where the study of dynamic evolution of the interface offers a challenging task to the researchers. For the last two decades, lattice Boltzmann method (LBM) has been extensively used to model transport phenomena for melting and solidification problems involving complex boundary at the phase interface because of high computational efficiency and cost effectiveness of LBM.

In the present work double distribution function (DDF) with single relaxation time based lattice Boltzmann method (LBM) is used to perform the solid-liquid phase change simulation. D2Q9 lattice stencil is used for the prediction of flow and thermal field. However, in order to overcome numerical instabilities for simulation of low *Pr* fluids, modification of lattice Boltzmann Bhatnagar-Gross-Krook (LBGK) models for incompressible Navier-Stokes equation and the energy equation are proposed in this study. The present work reports development of a lattice Boltzmann model to overcome the numerical instability associated in handling convection in low *Pr* fluids. This modification has been employed to analyze very low *Pr* liquid metals $Pr \in [0.001, 0.1]$. In a systematic analysis, the thermo-fluidic behavior of liquid metals in the melt zone is examined in a square cavity at a wide range of Rayleigh number $Ra \in [10^4, 10^6]$. Transport phenomena in a side heated cavity undergoing melting has been reported where wall and interface heat flux, melting rate and length of interface was studied up to a Rayleigh number of $10^6$.

In next part of the work, the melting dynamics has been studied for investigating the flow instability in the melt zone. The parameters are taken as Prandtl number in the range of 0.005-0.05 and Rayleigh number between $10^5$-$10^6$. The presence of different flow circulation in the melt zone is investigated as the flow transition is observed from steady to transition regime. The time series plots of velocity components in the entire melt zone are investigated and peak frequency mapping is performed using Fast Fourier Transform (FFT) analysis to characterize the non-linear flow dynamics in an evolving melt one.

In corner melting/solidification, heating or cooling is performed on two adjacent sides of the cavity. Studies on corner melting for bottom side heated and top side heated melting were undertaken where the related physics was explored and improved melting phenomena was noted. The improved melting performance was explored for corner melting and at the same time the complex physics of natural convection under corner melting could be unveiled. The natural convection effect in corner melting problem is investigated based on enthalpy based lattice Boltzmann model (ELBM). The investigation is performed for two distinct cases. In the first one the left wall and the bottom wall form the corner (case 1). The counterpart is where the right wall and the top wall form the corner (case 2). The main focus of the work includes capturing the effect of natural convection in melt zone and predicts the evolution of the melt zone dynamics. The effect of Rayleigh number in the range of $Ra=10^2$ - $10^7$ on the convective flow field is evaluated for a typical parametric values of Stefan number of 0.01 and Prandtl number of 0.025. Results show distinct convection rolls which also include Rayleigh-Benard cells at the melt zone for the cases under investigations. Evolution of flow fields in the melt zone has been described by presenting sets of isotherms and streamlines. The modified lattice Boltzmann model to simulate melting in low *Pr* materials was also applied in the case of corner melting problems for very low *Pr* number liquid metals $Pr \in [0.001, 0.01]$. The main focus of the work includes the tracing of transient interface movement, calculation of average heat flux at the interface; determine the effect of natural convection in melt zone, distribution of isotherms in the cavity and variation of average melt fraction with time.

As solidification process has numerous applications in metallurgy, geology and other disciplines where environment may not be always predictable and the boundary conditions may vary with time and space, investigation of mushy region dynamics and segregation within an alloy is of special interest where the progress of LBM is still very limited. A hybrid LBM is developed to study the solidification phenomena of *Ni*-*Cu* alloy in which the flow field is simulated using LBM combined with finite different method (FDM) to solve for thermal and species continuity equation. In the present work, 2-D simulation of *Ni*-*Cu* (50-50%) alloy has been taken up to understand the effect of boundary conditions on the morphology of mushy region dynamics. Capability of the code is demonstrated to a limited extent due to huge demand on computation time.

To summarize, the thesis demonstrated the capability of LBM for solution of solid to liquid phase change problems. A modified LB model is developed to handle low Pr materials. Studies were performed for melting in side heated cavities as well as for corner melting. Corner solidification and segregation of binary alloy are the other highlights of the work.

# Numerical Studies on Melting and Solidification Using

# Lattice Boltzmann Method

# CONTENTS

**Subject** **Page No.**

# LIST OF FIGURES

# LIST OF TABLES

# NOMENCLATURE

| | | |
|---|---|---|
| $Bo$ | Boussinesq number | $Bo=Ra.Pr$ |
| $c$ | Lattice speed | [m/s] |
| $c_p$ | Specific heat capacity | [KJ/kg-K] |
| $c_s$ | Sound speed | [m/s] |
| $e$ | Discrete velocity | [m/s] |
| $F$ | Body force | Kg-m/s$^2$ |
| $Fo$ | Fourier number | $Fo=\alpha t/W^2$ |
| $f$ | Density distribution function of velocity | |
| $f^{eq}$ | Equilibrium density distribution function of velocity | |
| $f_l$ | Liquid fraction | |
| $g$ | Density distribution function of energy | |
| $\mathbf{g}$ | Acceleration due to gravity | m/s$^2$ |
| $g^{eq}$ | Equilibrium density distribution function of energy | |
| $Gr$ | Grashof number | $Ra=g\beta\Delta TW^3/(\nu^2)$ |
| $H$ | Total enthalpy | KJ/kg |
| $k_T$ | Thermal conductivity | KJ/kg-K |
| $L$ | Length of the cavity | m |
| $P$ | pressure | Pa |
| $Pr$ | Prandtl number | $Pr=\nu/\alpha$ |
| $Ra$ | Rayleigh number | $Ra=g\beta\Delta TW^3/(\nu\alpha)$ |
| $Re$ | Reynolds number | $\frac{Lu_L}{\nu}$ |

|  |  |  |
|---|---|---|
| $Ri$ | Richardson number | $\frac{Gr}{\mathrm{Re}^2}$ |
| $Ste$ | Stefan number | $Ste=c(T_h-T_m)/\lambda$ |
| $S'_{Total}$ | Total rate of volumetric entropy generation | $\mathrm{W/m^3K}$ |
| $S_{th}$ | Rate of entropy generation due to heat transfer | $\mathrm{W/m^3K}$ |
| $S_f$ | Rate of entropy generation due to fluid flow | $\mathrm{W/m^3K}$ |
| $S_{Total}$ | Total rate of entropy generation | W/K |
| $t$ | Time | s |
| $T$ | Temperature | K |
| $T_h$ | Hot wall temperature | K |
| $T_l$ | Liquidus temperature |  |
| $T_m$ | Phase change temperature | K |
| $T_s$ | Solidus temperature | K |
| $\boldsymbol{u}$ | Velocity vector | m/s |
| $U_{RMS}$ | RMS velocity | m/s |
| $u_L$ | Lid velocity | m/s |
| $W$ | Width of the square cavity | m |
| $x$ | Coordinate position |  |
| $y$ | Coordinate position |  |
| $\alpha$ | Thermal diffusivity | $(\mathrm{m^2/s})$ |
| $\beta_T$ | Coefficient of thermal expansion | 1/K |
| $\beta_c$ | Volume expansion for concentration change | $\mathrm{m^3/kg}$ |
| $\rho_m$ | Density | $[\mathrm{kg/m^3}]$ |
| $\lambda$ | Latent heat | kJ/kg |

| | | |
|---|---|---|
| $\tau_f$ | Relaxation time of velocity evolution equation | |
| $\tau_g$ | Relaxation time for energy evolution equation | |
| $w$ | Weight factor | |
| $\omega$ | Reciprocal of relaxation time | [rad/s] |
| $v$ | Kinematic viscosity | $m^2/s$ |

*Subscript*

| | |
|---|---|
| *k* | Direction of discrete velocity |
| *avg.* | Average |
| *n* | Last node in x axis |
| *r* | Right wall |
| *h* | Hot wall |
| *c* | Cold wall |
| *RMS* | Root-mean-square |
| *max* | Maximum |

# CHAPTER 1

# INTRODUCTION

## 1.1 General Overview

Problems involving melting and solidification have attracted considerable attention due to its large number of industrial applications such as casting of metals, thermal heat storage, processing of materials, wire and metal coating, food conservation, additive manufacturing, growth of crystals, matrix composites and cryosurgery as well as natural processes such as formation of crust and magma, evolution of iceberg and many others (Danaila et al., 2014; López et al., 2013; Pielichowska and Pielichowski, 2014; Wang et al., 2010). Mathematical modeling of melting and solidification is a challenging task to the research community as it involves prediction of moving boundary at the solid-liquid interface and tackling the associated physical and computational complexities near the phase interface. For alloys, additional difficulties are encountered during solidification of alloy, a mushy zone is formed in which fractional amount of solid and liquid both coexist. Accurate investigation of mushy zone where solid-liquid phases coexist is very difficult as the controlling parameters drastically change during solidification. Considering the high cost of experiments, numerical simulation has become indispensable to accurately focus on the underlying physics during both melting and solidification problems. In last decades, the significant progress of particle based simulation methods over conventional continuum based methods has become noteworthy (Miller et al., 2001; Rao et al., 2013; Shibuta et al., 2017; Song et al., 2016; Liwei Zhang et al., 2021) in investigating melting and solidification. Lattice Boltzmann method (LBM), a novel technique arising out of kinetics based approach, has evolved as a versatile and powerful computational methodology for both fundamental research and engineering applications. The use of LBM for melting and solidification problems provide an alternative approach to assumption of no-slip boundary condition in conventional methods at the complex interface geometry through simple ‘streaming-collision’ assumptions (Chopard and Droz, 1998). The straightforward parallelization of the main lattice Boltzmann (LB) algorithm due to successive repletion of the ‘collision-streaming’ steps (Nourgaliev et al., 2003; Yang et al., 2000) offers significant advantage in computation.

## 1.2 Melting of Low Prandtl Number Substances

For a variety of applications, including cooling systems (cooling of high-density power electronic devices, nuclear reactors), heat exchangers, metallurgical processes and solidification and melting of metals (such as development of crystals from melts, metal treatment, casting and welding), it is crucial to comprehend the dynamics of low Prandtl number (*Pr*) liquid metals under the influence of natural convection. Prandtl numbers of fluids describe the relative strength of momentum diffusivity (kinematic viscosity) to thermal diffusivity. For liquid metals, thermal diffusivity is relatively high and kinematic viscosity is low leading to low values of *Pr*. A low Prandtl number value indicates that heat diffusion is occurring in liquid metals significantly faster than momentum diffusion. The value of Prandtl number has significant impact on the flow field including boundary layer formation and heat transfer.

Due to the instability of the solution, the numerical modelling of the impact of natural convection at liquid metals with very low Prandtl numbers (*Pr*=0.001 to 0.01) causes concern to the researchers. Researchers have noted the difficulty in achieving stable solution for low *Pr* materials in closed cavities (Arcidiacono and Ciofalo, 2001; Bhattacharya and Basak, 2021; Kosec and Šarler, 2013; Mohamad and Viskanta, 1991; Sammouda et al., 1999; Sheriff and Davies, 1979) as lower *Pr* introduces higher non-linear effect. These studies also forecasted the oscillatory behavior of the results in terms of dependent variables like velocity and average Nusselt number (Mohamad and Viskanta, 1993; Sammouda et al., 1999). However, several metals have quite low values of *Pr* e.g., *Pr* of Gallium (*Ga*), Mercury (*Hg*), Sodium (*Na*), Potassium (*K*) and Lithium (*Li*) are 0.022, 0.021, 0.013, 0.01 and 0.005 respectively in decreasing order (Bejan, 2013; Lyon and Poppendiek, 1951). Many of them are of special importance in semiconductor industries and find use in automobiles, energy, telecommunication and aerospace sectors.

In cavity melting problem while melting occurs from side heated wall or bottom walls the density difference induces natural convection in the melt zone. Thermal gradient in differentially heated cavity provokes the formation of Rayleigh-Benard cells which appears in melt zone. The moving melting boundary moves towards normal to the direction of heat flux and the melt zone grows with time. The fluid flow transition from conduction to convection is governed by Rayleigh number (*Ra*) while *Pr* plays an important role in development of instability of the flow field. The convective instability arises in melt zone due to the combination of *Ra-Pr* relationship for liquid metals (Bejan, 2013). The convection cell sizes and oscillating nature of the fluid flow components owing to effect on the dynamics of melting boundary. Quantification of the flow instability in the melt zone explains the oscillation nature of velocity components. The transient evolution of the melt zone promotes the internal kinetic energy which is related to the effective melted area.

## 1.3 Corner Melting

The term ‘corner melting’ involves melting which occurs due to heating of two adjacent walls of the cavity. Corner melting owing to natural convection in an enclosure leads to more complicated situation as a consequence of interaction of buoyancy forces, conduction and gravity field in the melt zone. In case of corner melting, the direction of gravity is oblique to the overall gradient in the cavity as the heated walls form an L-shaped zone facing other two sides at lower temperature. While melting phenomena are studied for decades, investigations on corner melting are reported only in this millennium (Lee and Tzong, 1991; Lin and Chen, 1997; Rathjen and Jui, 1971). The effect of natural convection in melt zone is the main concern of corner melting problem. The corner melting could be in two different ways: the top-bottom walls temperature gradient and the gravity force direction are parallel but opposite to each other for case 1 while the temperature gradient and the gravity force direction are parallel with same direction for case 2. Thus case 1 and case 2 refer to ‘corner melting heated from bottom’ and ‘corner melting heated from top’ respectively. Distinct convection rolls at the melt zone for the cases under investigations is the main concern of the study. Evolution of flow fields in the melt zone has been described by a set of isotherms and streamlines for both the cases.

## 1.4 Solidification of Alloy

Solidification of binary alloy causes phase separation into three distinct zones, namely solid, two phases or mushy region, and liquid phase or melt zone. As the melting point of components forming alloy are different, solidification takes place over a range of temperature causing a non-uniform distribution of components in the mushy region. This phenomenon is called macro segregation. Solidification of pure metal and alloy follows different physics as shown the following Fig. 1.1.

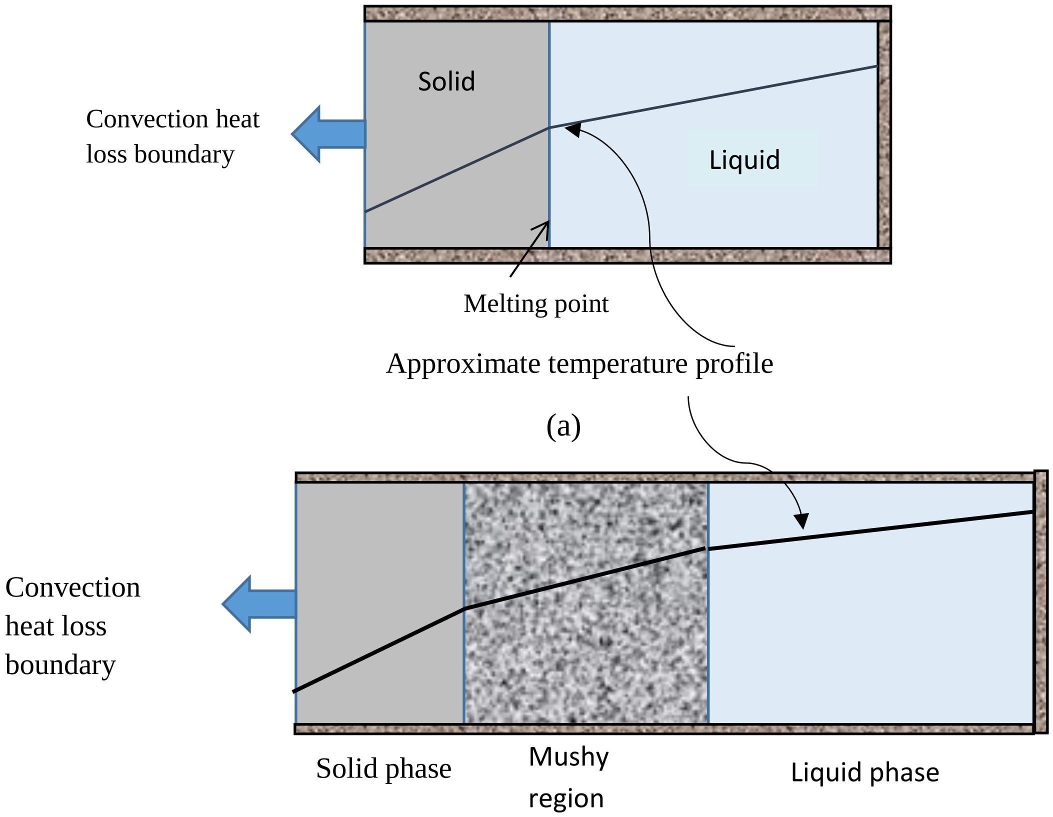

(a)

(b)

Figure 1.1: (a) Schematic of pure metal solidification and (b) Schematic of an alloy solidification process.

Figure 1.1 shows that a mass of molten alloy kept in a rectangular cavity losing heat from left wall. Other boundaries are insulated. Solidification starts from the left wall through which heat is lost. The boundary of the solid phase grows towards right. Adjacent to the right boundary of solid phase a zone develops where solid crystals and liquid coexist together. Near the solid boundary amount of solid formation is dense which gradually tails off on the right and smeared with the liquid zone.

### 1.4.1 Description of Mushy Layer

In the mushy layer non uniform crystal structure of solidified materials coexists with the liquid phase. For alloy solidification, momentum, heat and mass transfer in mushy layer are a coupled complicated process. Investigation of mushy layer is important because distribution of components in solidified phase controls the mechanical and metallurgical property of alloy casting. As the flow is hindered by the porous zone formed by crystal structure present having different geometrical shapes, the path of fluid is tortuous rivulet like and surpassing the tiny islands of crystal matrix. Depending on the extent of assumed formation of crystal growth in mushy region dendritic structure is formed.

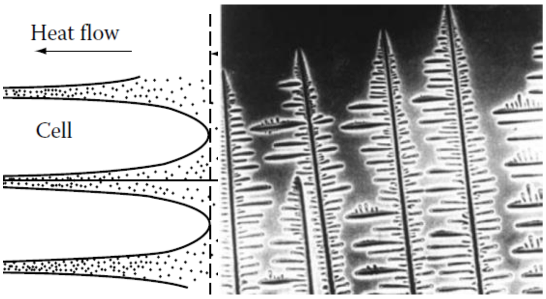

(a) (b)

Figure 1.2: Microstructure in mushy region (Porter et al., 2009).

A detailed view of mushy region is shown in Fig. 1.2. At the interface of solid zone columnar growth of crystal (Fig. 1.2a) and branching off morphology (Fig. 1.2b) occurs which hinder the flow of liquid and two-phase flow with heat and mass transfer occurs. Due to the limited solubility of secondary phase which is also temperature dependent the solute is segregated in this zone as a result of diffusion and convection.

## 1.5 Computation Schemes for Melting-Solidification Problems

Figure 1.3 shows several available computational schemes which are deployed for modeling of melting and solidification of metals and alloys with melt flow. The flow field of the solid-liquid phase change problems can be numerically simulated using either macroscopic or mesoscopic approach.

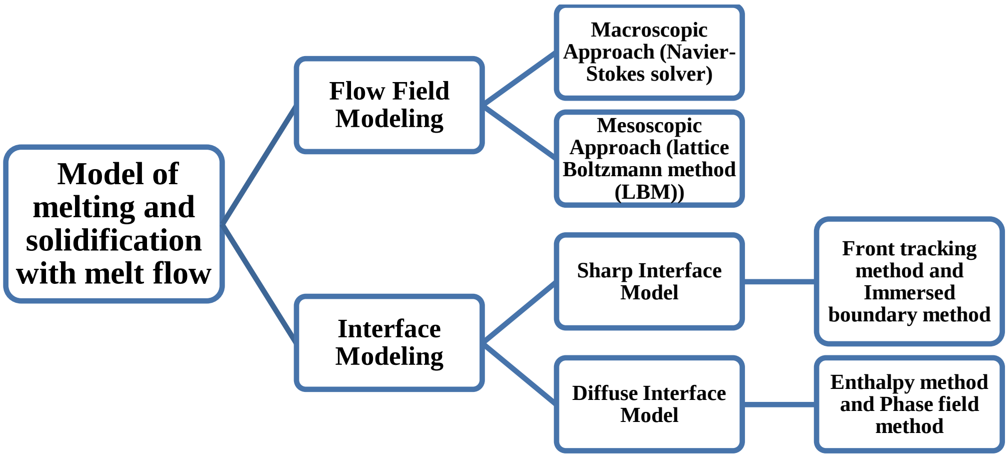

Figure 1.3: Different computation schemes of melting and solidification.

The flow induced melting-solidification problems can be numerically modeled using macroscopic Navier-Stokes (NS) equation solver (Anderson et al., 2000; Chattopadhyay, 2011; Dhar et al., 2014; Wintruff et al., 2001), which demands a large computational cost to the melting-solidification problems. In order to improve the computational efficiency (Chatterjee and Chakraborty, 2006; Jelinek et al., 2014; Sun et al., 2009; Zhang et al., 2018), LBM was introduced as an alternative of conventional methods to calculate the fluid flow in melt. The lattice Boltzmann method has a potential to solve the species transport problems ensuring robustness to describe the fluid flow and is capable of simulating complex fluid systems. In melting-solidification problems, the prediction of interface can be performed assuming ‘sharp’ or ‘diffuse’ interface. Several interface tracking methods are available to investigate melting-solidification phenomena. The research field is still evolving towards better understanding of the dynamics of interface between solid and liquid phases with an aim to accurately predict the structure of ‘diffuse’ or ‘sharp’ interface considering the local physics during melting and solidification (Chen et al., 2013; Hu et al., 2019a; Knutson and Noble, 2009; Liu et al., 2022).

## 1.6 Lattice Boltzmann Modelling for Melting and Solidification Problems

Melting and solidification studies are non-isothermal flow problems involving phase change in which energy transfer plays an important role. There are several LB coupled methods which are developed based on different interface tracking techniques to study interface dynamics in melting and solidification problems. A birds-eye view of different LB coupled models pertinent to melting and solidification problems is shown in Fig. 1.4. Generally, the LB modelling of solid-liquid phase change problems consists of two parts: a thermal lattice Boltzmann model for flow and thermal field and a second model for interface tracking. Enthalpy based LBM (ELBM), phase field based LBM (PFLBM) and immersed boundary based LBM (IBLBM) are the three main LB coupled interface tracking methods, which are used to investigate the melting and solidification phenomena.

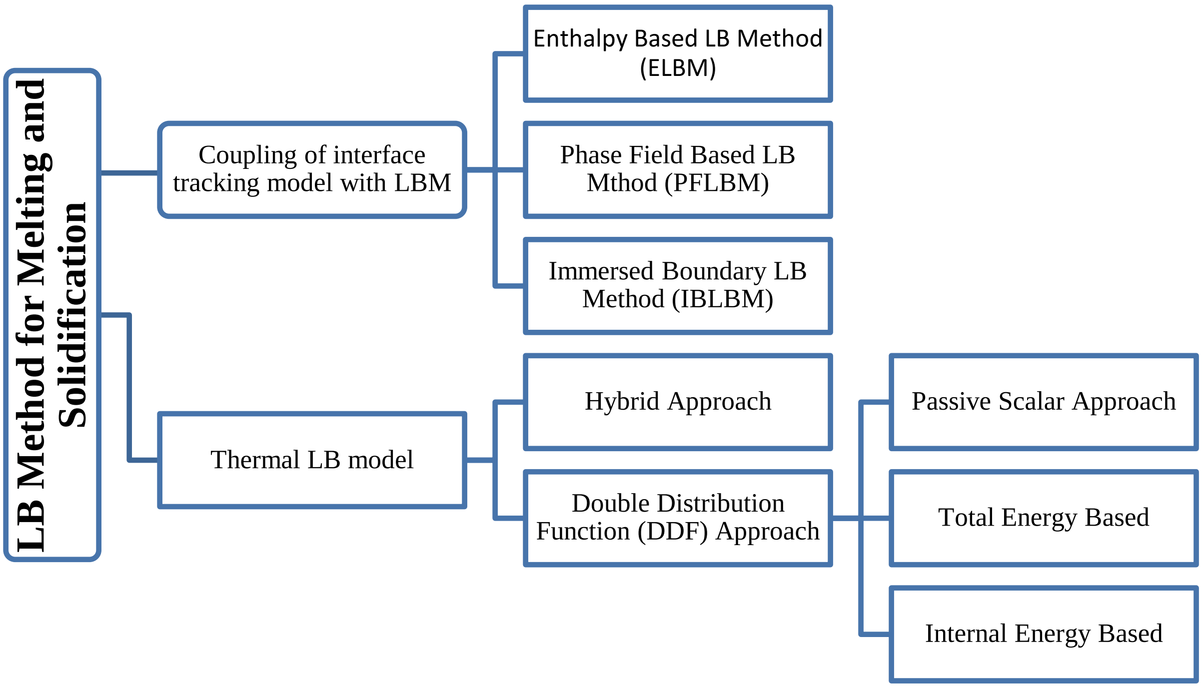

Figure 1.4: Different LB methods for melting and solidification.

In ELBM, the temperature field is solved using LB algorithm with either enthalpy or temperature as dependent variable and the interface is captured by calculating as well as updating enthalpy at each lattice node near interface vicinity in which the liquid fraction is implicitly obtained at the corresponding lattice node. In PFLBM, an auxiliary phase field variable across the diffuse interface is used to track the phase interface. Both ELBM and PFLBM involving finite thickness of interface, track the solid-liquid interface implicitly. In IBLBM, a sharp infinite thin interface is traced assuming Eulerian grids for flow field and Lagrangian grids for immersed boundary in the fluid. In thermal lattice Boltzmann model, two possible approaches have been used to study the flow and thermal part of the melting and solidification problems; one is the hybrid method in which LBM is combined with conventional methods like finite difference (FD), finite volume (FV) or finite element (FE) method (Chiappini et al., 2018; Fakhari and Lee, 2015; Ganaoui and Semma, 2009; Li et al., 2020). The other approach involves using two separate distribution functions for flow and thermal field and is known as double distribution function (DDF) approach (He et al., 2019; Huang et al., 2013a; Samanta et al., 2022).

In hybrid method, isothermal LB method is used to solve the flow field, along with finite difference method, finite volume method or any other numerical methods to simulate energy field (Chatterjee and Chakraborty, 2005; Li et al., 2014). Over past few decades, double distribution function (DDF) based LB method has been extensively used to study phase transition involving melting and solidification. In DDF based approach, two distribution functions are used; the first one as the density distribution function for velocity in the flow field and another is the density distribution function for energy in the thermal field. The energy field for melting and solidification problems can be expressed in terms of temperature, internal energy or total enthalpy. A survey of literature clearly establishes the superiority of DDF approach, which is now the prevailing one for modeling solid-liquid phase change problems (Karlin et al., 2013; Li et al., 2018; Wang et al., 2020).

While there exist different melting and solidification models for predicting solid-liquid interface with their capacities and limitations, in this work, we focus on enthalpy based lattice Boltzmann method for prediction of interface which is possibly the easiest for implementation, useful and popular numerical tool in generating solid-liquid interface.

The application of LBM in binary alloy solidification problem has been taken widely because of its computational efficacy compared to the other traditional methods such Finite Difference Method (FDM), Finite Volume Method (FVM) etc. Literature shows there are lots of study has been performed to investigate alloy solidification using hybrid LBM to investigate the morphology of the microstructure in which LBM is coupled with conventional FDM, FVM etc (Medvedev and Kassner, 2005) (Selzer et al., 2009) (Chatterjee and Chakraborty, 2005; Li et al., 2014). while the dynamics of mushy region with macro-segregation has been studied a few (Kosec and Šarler, 2013; Ohno and Sato, 2018a). The solidification study of *Ni-Cu* alloy has been performed using hybrid LBM in which the flow field is modelled using LBM and FDM is used to solve thermal and solute balance equations.

## 1.7 Motivation of Work

The focus of the current work is to develop simulation methodology for melting and solidification and extend the ability of lattice Boltzmann model (LBM) for application in low *Pr* solid to liquid phase change problem. While existing thermal LBM is used for the studies for the case of $Pr = 0.025$, the lattice Bhatnagar-Gross-Krook (LBGK) model has been modified in the current research by adding correction terms to the density and energy distribution functions. This modification has been employed to analyze melting of very low *Pr* number liquid metals $Pr \in [0.001, 0.1]$.

While going through the open literature in the area of concern, it is evident that the problem of ‘corner melting’ demands further attention as relatively fewer studies has dealt with this problem. The scope of improved melting performance could be explored for corner melting and at the same time the complex physics of natural convection under corner melting could be unveiled.

After performing the melting and solidification study globally, the dynamics of melting boundary has been investigated for low Prandtl number liquid metals. Dynamic transition of melting boundary and topography amplitudes appears as a result of the ongoing melting of the solid. The interface dynamics and the thermo-fluidic behaviour in a planer cavity are performed using modified lattice Boltzmann simulation.

The application of LBM on alloy solidification problem is yet to be matured as only a couple of works had been done using hybrid LB model to study the mushy zone in binary alloy solidification problem. The dynamics of mushy zone with macro-segregation study using hybrid LBM was reported in a few methods (Contrino et al., 2014; Lallemand and Luo, 2003). A hybrid LBM is developed to study the solidification phenomena of *Ni-Cu* alloy in which the flow field is simulated using LBM and finite different method is used to solve for thermal and species continuity equation. The extension of the LB model coupled with FDM is used to perform the simulation which reduces the computational cost of the simulation.

## 1.8 Thesis Organization

The present thesis contains seven chapters. The content of the chapters are discussed below:

- In the first chapter, a brief introduction has been given on the solid-liquid phase change of metals and alloys in general. Application of LBM to study the melting behaviour of low Prandtl number liquid metals in closed cavity, flow instability of low *Pr* liquid metals, melting from two adjacent walls (corner meting) and solidification of binary alloy are discussed eventually. Different numerical modelling techniques for melting-solidification problems and a brief about importance of lattice Boltzmann modelling for solid-liquid phase change problems are introduced.
- Chapter two which includes an extensive literature review on application of LBM on melting and solidification is subcategorised into two sub-sections. The first part of this chapter presents a state of art survey for research activities on melting and solidification problems focusing on melting of low *Pr* liquid metals, convective instability of low *Pr* liquid metals in the melt zone, corner melting and solidification

for a wide range of *Pr* number and binary alloy solidification. The second part of the chapter covers literatures on the application of lattice Boltzmann models for melting and solidification problems.

- Chapter three deals with the development of basic lattice Boltzmann modelling (LBM) of heat transfer and fluid flow related to solid-liquid phase change problems. Initially, the basic lattice Boltzmann structure for flow and heat transfer problem has been discussed with implementation of boundary conditions and in the next section the LB modelling is extended for solid-liquid phase change problems. Modification of the LB methodology for simulation of low Pr is presented finally.
- In chapter four melting of low Prandtl number liquid metals is discussed using modified lattice Boltzmann modelling. The effect of natural convection in the melt zone has been investigated for low Prandtl number liquid metals with a range of $Pr \in [0.001, 0.1]$. After the global study of low *Pr* liquid metals melting, the dynamics of melting boundary has been investigated in terms of flow instability arisen in the melt zone. A flow instability mapping has been performed in the melt zone and the oscillating velocity field is quantified using Fast Fourier Transform (FFT) analysis.
- Chapter five deals with the flow physics involving corner melting and solidification problem of pure substances. The effect of natural convection in the melt zone is performed for two distinct cases. In the first one the left wall and the bottom wall form the corner (case 1). The counterpart is where the right wall and the top wall form the corner (case 2). The effect of natural convection in melt zone and predicts the evolution of the melt zone dynamics has been discussed in this section. The application of corner melting problem with low *Pr* liquid metals has been studied in the next part of the section.
- In chapter six solidification of *Ni-Cu* binary alloy has been investigated using hybrid lattice Boltzmann method. Three different types of temperature boundary conditions at the cold wall are considered. The flow field in the liquid zone, the solute distribution and the distribution of solid fraction in the mushy zone has been predicted. Macro segregation in the mushy region has been analysed and discussed in this section.
- Chapter seven briefly describes the conclusions drawn from the analysis that is done in preceding chapters. Then the future scope of studies is also presented in this chapter.

# CHAPTER 2

# STATE OF ART

The study of melting and solidification phenomena in solid liquid phase change problems has become a popular research interest to the researchers due to its wide applications in thermal energy storage systems, freezing of foods, metallurgical solidification processes (Du et al., 2021; Tong, et al., 2017; Năstase et al., 2016; Ren et al., 2017; Zorrilla and Rubiolo, 2005). Melting and solidification problems involves two phase heat transfer, evolution of phase change boundary, fluid flow dynamics in uneven geometry, transient evolution of melt zone and associated energy kinetics. The energy needed to transform a solid into a liquid during melting is provided by heat propagation from a heated boundary wall. When heat is removed during solidification, with the removal of latent heat the phases switch from liquid to solid. Melting and solidification of pure metals shows a distinct interface between solid-and liquid phases while a mushy region is formed during alloy solidification. As the position of the moving interface in solid-liquid phases is unknown a priori, the solution procedure for prediction of the interface is inherently difficult. The major concerns to simulate the melting and solidification problems are the prediction of transient phase change boundary which is an outcome of thermodynamics of phase transformation.

## 2.1 Literature Survey on Melting and Solidification

A brief state-of-art on solid-liquid phase change is first placed. Many conventional macroscopic based methods had been applied to investigate the melting and solidification problems, such as Finite Difference Method (FDM), Finite Volume Method (FVM), and Finite Element Method (FEM) (Chessa et al., 2002; Lacroix and Voller, 1990; Voller et al., 1990). The phenomena of melting in the natural convection regime in cavity were studied over the years. Several experimental and numerical investigation of melting and solidification in closed cavity had been done by many researchers for pure metals and alloys (Chakraborty et al., 2003; Dhar et al., 2014; Gau and Viskanta, 1986; Voller et al., 1989; S. Wang et al., 2010; Wolff and Viskanta, 1988). Lattice Boltzmann method (LBM), a mesoscopic model based on kinetic theory is economically efficient for flow modelling as compared to conventional Navier-Stokes solver. Naturally LBM has become a popular tool due to its simple mathematical formulation consisting of streaming and collision steps, scope of parallelization and lower CPU time (Samanta et al., 2022). Different mathematical modellings and numerical techniques for conduction melting (Chatterjee and Chakraborty, 2005; Jiaung et al., 2001) and natural convection melting (Huang et al., 2013a; Huo and Rao, 2017; Jourabian et al., 2013; Rui et al., 2020a) were reported using different system configurations (Azad et al., 2021; Daniele Chiappini, 2021; D. Gao and Chen, 2011; Q. Li et al., 2021; Sharma et al., 2017) subjected to various heat flux and temperature boundary conditions (Dai et al., 2018; Gu et al., 2019; Hasan and Saha, 2021b; Huang et al., 2013a; Huo and Rao, 2015). Melting studies in square or rectangular cavity using LBM, focusing on the flow and thermal characteristics in the melt zone subjected to temperature gradient at different walls such as melting from bottom (Dai et al., 2018; Hasan and Saha, 2021b; Rui et al., 2020b), and melting from side walls of the cavity (Huang et al., 2013b; Huber et al., 2008; Huo and Rao, 2015; Rui et al., 2020b) were reported in literature. These two categories of problems were well attended so far experimentally and computationally by number of workers. Recently, an extensive review article on solid-liquid phase change using lattice Boltzmann method has been reported by (Samanta et al., 2022) in which melting-solidification involving physics of pure metal and alloys has been systematically presented covering vast literature on different pure lattice Boltzmann models and hybrid models.

In this section literatures pertaining to the problems undertaken in this thesis are reviewed. The topics are i) Melting of phase change in low Prandtl number liquid metals, ii) Corner melting and solidification and iii) Solidification of binary alloy.

### 2.1.1 Melting of Phase Change in Low Prandtl Number Liquid Metals

Several researchers were conducted extensive research on natural convection phenomena in the melt zone experimentally and numerically (Azad et al., 2022; Mrinmoy Dhar et al., 2014; Gau and Viskanta, 1986; Jones et al., 2006; Mallya and Haussener, 2021; S. Wang et al., 2010; Wolff and Viskanta, 1987). In this context, phase change in low Prandtl number materials deserve special attention in which the flow and thermal behavior in melt zone has been investigated in a wide range $Pr \in [0.001, 0.1]$. Due to the instability of the solution, the numerical modelling of the impact of natural convection at liquid metals with very low Prandtl numbers ($Pr$=0.001 to 0.01) causes concern to the researchers. Researchers had noted the difficulty in achieving stable solution for low $Pr$ materials in closed cavities (Arcidiacono and Ciofalo, 2001; Bhattacharya and Basak, 2021; Kosec and Šarler, 2013; Mohamad and Viskanta, 1991; Sammouda et al., 1999; Sheriff and Davies, 1979) as lower Pr introduces higher non-linear effect. These studies also forecasted the oscillatory behavior of the results in terms of dependent variables like velocity and average Nusselt number (Mohamad and Viskanta, 1993; Sammouda et al., 1999). Lattice Boltzmann method (LBM) is increasingly being popular in simulation of fluid flow and heat transfer problems over time. A number of studies had been documented the use of the LBM for low *Pr* fluid flow issues (Bawazeer et al., 2019; Hussein et al., 2016; Li et al., 2016; Nabavizadeh et al., 2020; Sahraoui et al., 2020; Samanta et al., 2020). Some of them addressed the issue of numerical instability by modifying the lattice Boltzmann approach for low Prandtl numbers fluids (Bawazeer et al., 2019; Li et al., 2016). Li et al. (Li et al., 2016) investigated the oscillatory behavior at low *Pr* fluids in a differentially heated cavity for $Pr \in [0.005, 0.01]$ and $Ra \in [10^4, 10^5]$. The simulation was performed using double multi-relaxation time (MRT) based thermal LBM and focused on the oscillatory behavior of heat flux. Bawazeer et al. (Bawazeer et al., 2019) applied a modified lattice Boltzmann model incorporating a constant term to the relaxation parameter to enhance the stability of the numerical scheme. Using modified LBM they investigated the thermo-fluidic instability at low *Pr*. All of the aforementioned investigations look towards low *Pr* fluids without phase transition. Comparatively, only a few studies were done on the melt zone natural convection effect for liquid metals with very low *Pr* numbers (Dai et al., 2018; Hasan and Saha, 2021b; Hu et al., 2017; Huang et al., 2013b; Huber et al., 2008; Huo and Rao, 2015; Lu et al., 2019; K. Luo et al., 2015; Rui et al., 2020a; Samanta et al., 2023; Xu et al., 2019). It is shown from the earlier studies that the investigation was limited to a specific Prandtl number range, which is primarily employed for a certain liquid metals. Table 2.1 summarizes the range of Rayleigh number and Prandtl number in which phase change studies are reported. It can be noted from the table that the phase change behavior for metals are mostly studied for $Pr \geq 0.02$ and only one work reports studies at $Pr = 0.01$.

Table 2.1: Range of *Pr* and *Ra* in literature.

| **References** | **Prandtl Number** | **Rayleigh Number** |
|---|---|---|
| (Hasan and Saha, 2021a) | 0.025 | 6708,11708,21708 |
| (Dai et al., 2018) | 0.02 | $2.5\text{x}10^4$-$5\text{x}10^4$ |
| (Huang et al., 2013b) | 0.02 | $2.5\text{x}10^4$-$2.5\text{x}10^5$ |
| .(Rui et al., 2020a) | 0.02 | $2.5\text{x}10^4$ |
| (Lu et al., 2019) | 0.02 | $2.5\text{x}10^4$ |
| .(P. Xu et al., 2019) | 0.02 | $2.5\text{x}10^4$ |

|  |  |  |
|---|---|---|
| (Huber et al., 2008) | 0.02 | $5x10^4$-$6.8x10^6$ |
| (Hu et al., 2017) | 0.01 | $5x10^4$ |

However, several metals have quite low values of *Pr* e.g., *Pr* of Gallium (*Ga*), Mercury (*Hg*), Sodium (*Na*), Potassium (*K*) and Lithium (*Li*) are 0.022, 0.021, 0.013, 0.01 and 0.005 respectively in decreasing order (Bejan, 2013; Lyon and Poppendiek, 1951). Many of them are of special importance in semiconductor industries and find use in automobiles, energy, telecommunication and aerospace sectors.

### 2.1.2 Corner Melting and Solidification

Corner melting and solidification refers to the cases where two adjacent sides forming a corner is heated or cooled for heat removal. While melting phenomena are studied for decades, investigations on corner melting are reported only in this millennium (Lee and Tzong, 1991; Lin and Chen, 1997; Rathjen and Jui, 1971). (Rathjen and Jui, 1971) presented an analytical solution of heat conduction with melting in a semi-infinite corner. An enthalpy based formulation for phase change materials with a large thermal diffusivity jump across the interface was investigated by (Lee and Tzong, 1991). In their work they validated their results with the exact solution developed by (Rathjen and Jui, 1971) for a solidification phenomenon in a two dimensional corner. Two-dimensional nonlinear phase-change problem with the irregular geometry was investigated by (Lin and Chen, 1997) in which the position of phase change interface was validated with the above results. (Jiji et al., 1970) conducted a two dimensional solidification study using internal and external corners analytically as well as numerically to evaluate influence of Stefan number (*Ste*) on melt zone aspect ratio and predicted an asymptotic relationship between them. The above mentioned corner melting problems are conduction driven. Recently, a comparison of convection melting in a square cavity had been studied with double adjacent heating walls, and double opposite heating walls with other walls were adiabatic by (Rui et al., 2020b). They compared the melt fraction for these two different situations and reported the transient temperature profiles in the cavity.

### 2.1.3 Solidification of Binary Alloy

During solidification of alloy, a mushy zone is formed in which fractional amount of solid and liquid both coexist. The morphology during solidification results in different microstructures in the form of dendrites, equi-axed or columnar growth. The hybrid LBM model for binary alloy solidification can be categorised as enthalpy based lattice Boltzmann model (ELBM) and phase field based lattice Boltzmann method (PFLBM). The morphology structures in the two phase zone, the growth kinetics of dendrites were simulated widely using PFLBM (Chen et al., 2021; Sakane et al., 2020; A. Zhang et al., 2019). However a few study of mushy zone dynamics, macro-segregation in the mushy region had been investigated using hybrid LBM (Ohno and Sato, 2018a). Due to this physical non-uniformity mathematical description of mushy layer was complicated and had been analysed by many researchers and nicely covered by (Prescott and Incropera, 1996) and mathematical description and numerical technique was broadly covered by (Zhu et al., 2008). While macro-segregation is a critical issue in material processing, the progress here is still limited with mesoscopic methods such as LBM.

## 2.2 Literature Survey on Application of LBM on Melting and Solidification

The mesoscopic, kinetic approach based lattice Boltzmann method (LBM) has been successfully applied as a numerical tool to study the phase transition phenomena from the last two decades. The applications of LBM for solid-liquid phase change of pure metals can be categorized based on the prediction of ‘sharp’ or ‘diffuse’ interface between the solid-liquid phases. Interface tracking methods for solid-liquid phase change problems can be categorized as immersed boundary (IB) based LBM has been used for prediction of sharp interface while enthalpy based lattice Boltzmann method (ELBM) for diffuse interface. Several works were reported assuming zero velocity at the solid-liquid interface in the solid-liquid phases using IBLBM (Huang and Wu, 2014; Zhao et al., 2019). In ELBM total enthalpy is updated in each lattice node with time which combines the sensible heat and latent heat. ELBM as an interface tracking technique covers a vast applications of solid-liquid phase change problems due to its computational efficiency which does not requires finer grid spacing near interface. (Wolf-Gladrow, 2004) first derived heat conduction equation using Lattice Boltzmann method. (De Fabritiis et al., 1998) developed a generalized meso-scopic LB model of solid/liquid phase transition in which two types of quasi-particles were used for different phases. In the LB model, was developed by (Miller et al., 2001), the interface boundary was traced using phase-field methodology. They showed a more elegant computational capability in treating the solid-liquid phase transition using only one type of quasi particle. The above works to track the interface were based on phase-field method. But extremely finer grid spacing is required to resolve the interface dynamics using phase–field method. However, in the enthalpy based methods, such finer grid spacing is not a requirement.

(Jiaung et al., 2001) first introduced ELBM stating solid-liquid phase change dominated by conduction. In their work, temperature based energy equation with non-linear source term was used which needed massive iterations. Subsequently, (Chatterjee and Chakraborty, 2008) revised the model of (Jiaung et al., 2001) and extended their work through publishing a series of research works to investigate convection melting and crystal growth (Chatterjee and Chakraborty, 2005, 2006). (Huber et al., 2008) coupled convection and change of phase using double distribution functions to track interface movement using the total enthalpy. They performed modifications on (Jiaung et al., 2001) and applied to study melting in a cavity in presence of natural convection which reduce the iteration steps by choosing a proper relaxation time. (Huang et al., 2013a) introduced a new ELBM technique in which temperature in the energy equation was replaced by enthalpy so that the non-linear source term could be avoided. (Luo et al., 2016) reported that, choice between either temperature or enthalpy based energy equation did not impact on the solution accuracy very much. Recently, using the model developed by (Huber et al., 2008) melting efficiency in cavity was calculated under the influence of free convection by (Dai et al., 2018). A LB model describing the solid-liquid phase change phenomena under constant heat flux was established by (Huo and Rao, 2017). Lattice Boltzmann modelling of melting and solidification problems shows variety of numerical schemes while using collision operator based on single relaxation time, two relaxation time and multi relaxation time techniques. However, the application of single relaxation time is the most popular LB model for solving melting with natural convection used by number of investigators (Dai et al., 2018; Hasan and Saha, 2021b; Huang et al., 2013a; Huang and Wu, 2014; Liu et al., 2022; Rui et al., 2020a). The advantage of total enthalpy based models for the numerical simulation of interface dynamics reduces the iterations in the presence of nonlinear source term in the energy equation (Huang et al., 2013a; Luo et al., 2015).

### 2.2.1 LB Coupled Interface Modelling

Though there are several interface tracking methods available in literature for the prediction of moving interface dynamics in melting and solidification problems, LB coupled interface tracking methods find an extensive use for the prediction of solid-liquid interface because of its capability and wide use. Literature suggest that the application of lattice Boltzmann method on solid-liquid phase change of pure substances and alloys can be categorized into three major subsections according to the interface modeling: enthalpy based method, immersed moving boundary based method, and phase field based method (Huang and Wu, 2015). The application of different interface tracking methods coupling with LB model such as ELBM and IBLBM have been used in melting and solidification problems on pure substances and alloy. In enthalpy based method, the total enthalpy at each lattice node is calculated in the phase change computational domain and the location of interface is predicted from the consideration of the liquid fraction. In phase field method, the interface is tracked using a phase field variable. Immersed boundary lattice Boltzmann method is a relatively new technique to predict sharp interface between solid-liquid phases (Huang and Wu, 2014; Zhao et al., 2019).

The LB coupled interface tracking methods for pure substances and alloy materials cover enthalpy based method while immersed boundary based method investigate pure substance which are briefly discussed in the following subsections.

## 2.2.2 Enthalpy Based Lattice Boltzmann Model (ELBM)

Due to its simplicity and robustness, enthalpy method coupled with LBM had been used by many researchers to simulate melting and solidification problems (Dai et al., 2018; Hu et al., 2017; Huang et al., 2013b; Huang and Wu, 2015; Lu et al., 2019; Rui et al., 2020b; Xu et al., 2019). In enthalpy based lattice Boltzmann method, total enthalpy is used to track the solid-liquid interface in terms of liquid fraction. Figure 2.1 illustrates a schematic of solid-liquid phase change of pure metals during melting or solidification. $H_l$ and $H_s$ are the liquidus and solidus enthalpy, respectively.

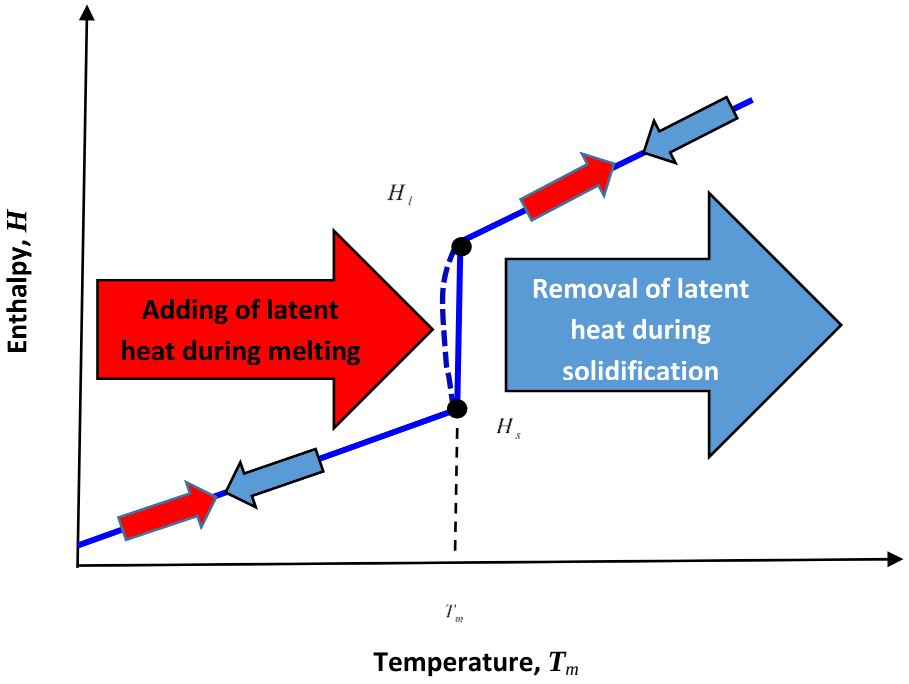

Fig. 2.1: Enthalpy-temperature relationship in melting or solidification phenomena

In enthalpy method, the enthalpy is calculated in the lattice nodes of the computational domain during melting and solidification. The isotherm at the two-phase interface indicates the interface temperature $(T_m)$ which may be a straight line for pure metal melting or dotted line during undercooling.

The energy equation in terms of temperature with a source term can be expressed as

$$\frac{\partial(\rho_m c_p \mathrm{T})}{\partial t} + \nabla.(\rho_m c_p \mathrm{T}\mathbf{u}_m) = \nabla.(k_T \nabla \mathrm{T}) + \mathrm{q}_e \tag{2.1}$$

where, $T$ is temperature, $c_p$ is specific heat, $k_T$ is thermal conductivity and $\mathrm{q}_e$ is the energy equation source term.

The energy equation source term $\mathrm{q}_e$ in Eq. (2.1) which is a function of latent heat enthalpy can be expressed as (Filippova and Hänel, 2000):

$$\mathrm{q}_e = -\left[\frac{\partial\left(\rho_m \Delta H\right)}{\partial t} + \nabla.\left(\rho_m \mathbf{u}_m \Delta H\right)\right] \tag{2.2}$$

where $\Delta H$ is the latent enthalpy of the nodes in the computational domain. Assuming no latent enthalpy change in liquid for pure metal, the second term of the Eq. (2.2) can be neglected, so $\mathrm{q}_e$ becomes

$$\mathrm{q}_e = -\frac{\partial\left(\rho_m \Delta H\right)}{\partial t} = -\frac{\partial\left(\rho_m \lambda f_l\right)}{\partial t} \tag{2.3}$$

where, $\lambda$ is the latent heat of the phase change and $f_l$ is fraction of liquid, given as

$$f_l = \Delta H / \lambda \tag{2.4}$$

Combining energy equation, Eq. (2.1) and source term, Eq. (2.3), the advection-diffusion equation (2.5) with a source term for solid-liquid phase change of pure substance is obtained as follows.

$$\frac{\partial(\rho_m c_p T)}{\partial t} + \nabla(\rho_m c_p T\mathbf{u}_m) = \nabla(k_T \nabla T) - \frac{\partial\left(\rho_m \lambda f_l\right)}{\partial t} \tag{2.5}$$

Among the earlier studies on solid-liquid phase change, (Jiaung et al., 2001) treated Eq. (2.3) as a heat conduction problem with phase change omitting the convection term, leading to the form

$$\frac{\partial(\rho_m c_p T)}{\partial t} = \nabla(k_T \nabla T) - \frac{\partial\left(\rho_m \lambda f_l\right)}{\partial t} \tag{2.6}$$

The non-linear source term in the Eq. (2.6) can be solved explicitly requiring massive iterations.

The total enthalpy $(H)$ is expressed by sensible enthalpy and latent heat,

$$H = c_p T + f_l \lambda \tag{2.7}$$

Calculating enthalpy using Eq. (2.7), the liquid fraction can be obtained as:

$$f_l = \frac{H - H_s}{H_l - H_s} \tag{2.8}$$

$H_l$ and $H_s$ are the liquidus enthalpy and solidus enthalpy respectively.

(Chatterjee and Chakraborty, 2006) revised the enthalpy model adopting a modified enthalpy updating scheme which was thermodynamically consistent. (Huber et al., 2008) developed a LB model modifying the collision step assuming $H(\mathbf{x}) < c_p T_i$ where, $T_i$ is initial temperature for better numerical accuracy and proposed a range of relaxation time to reduce computational cost by reducing the number of iterations. (Eshraghi and Felicelli, 2012) proposed an implicit formulation to deal with latent heat source term in the energy equation as in Eq. (2.2). They expressed liquid fraction in terms of macroscopic and mesoscopic parameters of energy model. (Huang et al., 2013b) was first to propose a total enthalpy based LB method combining the source term Eq. (2.3) with Eq. (2.1). The energy equation Eq. (2.1) can be modified in terms of total enthalpy as Eq. (2.9).

$$\frac{\partial\left(\rho_m \mathrm{H}\right)}{\partial t} + \nabla.\left(\rho_m c_p \mathrm{T} \mathbf{u}_m\right) = \nabla.\left(k_T \nabla \mathrm{T}\right) \tag{2.9}$$

The non-linear energy source term in this way leads to convergence. The macroscopic total enthalpy can be obtained summing the distribution functions. The temperature can be calculated from the total enthalpy as follows

$$\mathrm{T}=\begin{cases}\dfrac{H}{c_p} & \mathrm{T}<T_s\\ T_s+\dfrac{H-H_s}{H_l-H_s}\left(T_l-T_s\right) & T_s\le \mathrm{T}\le T_l\\ T_l+\left(H-H_l\right)/c_p & \mathrm{T}>T_l\end{cases} \tag{2.10}$$

A modified form of specific heat was introduced by (Huang and Wu, 2015) where the total enthalpy based LB method was improved so that the equation could be solved without iterations. The modified forms of thermal conductivity $(k_T)$ and specific heat $(c_p)$ were calculated in terms of liquid fraction by

$$k_T=(1-f_l)k_s+f_lk_l \tag{2.11}$$

$$c_p=(1-f_l)c_{p,s}+f_lc_{p,l} \tag{2.12}$$

where, subscripts $'s'$ and $'l'$ indicate the solid phase and liquid phase, respectively. A 'magic' parameter ($\Lambda$) of magnitude 'one fourth' was proposed by (Huang and Wu, 2015) by setting relaxation parameters as $0<r_e<2$ and $r_j=\dfrac{1}{\tau_g}$ and has to satisfy the relationship:

$$\Lambda=\left(\frac{1}{r_e}-\frac{1}{2}\right)\left(\frac{1}{r_j}-\frac{1}{2}\right)\equiv\frac{1}{4} \tag{2.13}$$

To accurately realize the no-slip velocity condition at the diffusive interface, adaptive mesh refinement (AMR) technique based LB scheme was proposed by (Huang and Wu, 2016) considering finer grids near interface vicinity and coarser grids at the bulk. Recently (P. Xu et al., 2019) extended two dimensional enthalpy based LB method to solve axisymmetric solidification process in the heat exchange method (HEM) based crystal growth system with convective boundaries. (Huo and Rao, 2017) proposed quasi-enthalpy method in which temperature is divided into two steps: 'prediction' (for melting) and 'consumption' (for solidification) which was able to capture the interface location at the solid-liquid interface accurately. (W. Zhu et al., 2017) extended the LB model developed by (Huber et al., 2008) to study solid-liquid phase change in three dimensional cavities and observed a significant difference between the results of three dimensional and two-dimensional during the initial stage of phase change. A MRT based LB model was proposed by (D. Li, Tong, et al., 2017) to study the influence of Rayleigh number and Prandtl number on three dimensional melting.

A total enthalpy based LB model combining with smoothed profile method was developed by (Hu et al., 2017) to simulate 3D convection melting. Naturally the researchers are focusing on the aspect of improving accuracy and striving for better CPU performance. A notable recent work of (Noyola-García and Rodriguez-Romo, 2021) was the development of a Python based new solver for use in  NVIDIA GPU device with CUDA technology to solve MRT-LB based phase change problem.

### 2.2.3 Immersed Boundary Lattice Boltzmann Model

Immersed boundary based lattice Boltzmann method (IBLBM) focuses on the moving boundary as sharp interface and the location of the thin interface is tracked explicitly assuming Lagrangian grids. (Feng and Michaelides, 2004) introduced IBLBM to simulate particulate flow. Subsequently, IBLBM were developed and used for isothermal and non-isothermal fluid flow problems (Zhiqiang Chen and Wang, 2020; Delouei et al., 2015; Dong et al., 2018; Kang and Hassan, 2011). (Huang and Wu, 2014) applied immersed boundary thermal lattice Boltzmann method (IBTLBM) to investigate the effect of surface forces at the immersed boundary of the solid-liquid phase interface including 'momentum force' due to velocity and the 'energy force' due to temperature. (Huang et al., 2013b) studied melting in square cavity in the presence of natural convection in which the phase interface was traced updating total enthalpy on the moving interface based on immersed moving boundary method proposed by (Noble and Torczynski, 1998). The effects of heat source location (left half, middle half and right half on the upper wall) for solid-liquid phase change was investigated by (P. Xu et al., 2019). The melting phenomena in presence of internal cylindrical heat source in a cubic cavity have been studied by (Zhang et al., 2021). In their work, a convection dominated melting has been simulated using two-relaxation time (TRT) based LB method. The effects of the inner cylinder location and the direction of inner cylinder placement are investigated.

In recent years, lot of works have been published in multiphase multi-physics problems where ELBM and IBLBM have been used. (Gao et al., 2017) developed an improved method to simulate solid-liquid phase change with natural convection in porous media under local thermal non-equilibrium (LTNE) conditions. (Yang and Liu, 2018) studied the Rayleigh-Benard melting process for a low melting point metals (LMPM). IBLBM has been extensively applied in diverse areas e.g.: effect of protruding heater in phase change process (Pepona and Favier, 2016), PCM melting process in a heat pipe assisted latent heat thermal energy storage system (LHTES) enhance with nano-particles and metal foams (Ren et al., 2018), electro thermos convection in complex geometries (Hu et al., 2019b), transport of rags in waste water pumps (Specklin et al., 2019), solid-liquid interaction in slurry fluid (Suzuki et al., 2020), nano-particles deposition patterns in evaporating nano fluid droplets on smooth heated hydrophilic substance (Wang and Cheng, 2021) - just to mention a few.

From the above literature survey it is seen that enthalpy based lattice Boltzmann method has a wide application to simulate the solid liquid phase change problems comparatively, immersed moving boundary based lattice Boltzmann method newer to predict the sharp interface

## 2.3 Objective of the Thesis

The present survey of literature shows that while LBM is increasingly being applied to study solid-liquid phase change problems very limited research have been conducted to look into the fluid flow and thermal behaviour for liquid metals with low Prandtl numbers. The difficulties associated in modelling of low Prandtl number liquid metal necessitates the development of modified lattice Boltzmann models. It is also noted that only a few works discuss the non-linear dynamics and flow evolution during melting. There is ample scope to study non-linear flow dynamics using tools such as Fast Fourier Transform (FFT). The lack of a numerical stability of LB models for low *Pr* the researchers despite robust character of LBM and greater computing value to analyse alloy solidification. The objectives of the thesis have been given as follows:

- Development of lattice Boltzmann method (LBM) for Solid-Liquid Phase Change Problems.
- Extension of the LBM to study convection and phase change process in low Prandtl materials in side heated cavity.
- Investigation of non-linear flow dynamics and instability in the growing melt zone.
- Study of thermal and flow behaviour in a closed cavity for corner melting and solidification using LBM.
- Development of LB coupled model to investigate the phase change in solidification of binary alloy and study of macro-segregation.

## CHAPTER 3

# DEVELOPMENT OF LATTICE BOLTZMANN CODE

There are several computational techniques available to study heat transfer and fluid flow problems. Such numerical simulations can be performed in different scales such as macroscopic scale, mesoscopic scale and microscopic scale. The macroscopic scale is based on continuum approach which follows traditional computational fluid dynamics (CFD) approach such as Finite Difference Method (FDM), Finite Volume Method (FVM) and Finite Element Method (FEM). The basic Navier –Stokes set of equations are solved using any conventional methods for fluid flow and heat transfer problems. In mesoscopic scale, lattice Boltzmann equations are solved assuming the movement of a cluster of particles from one space to another space with time.

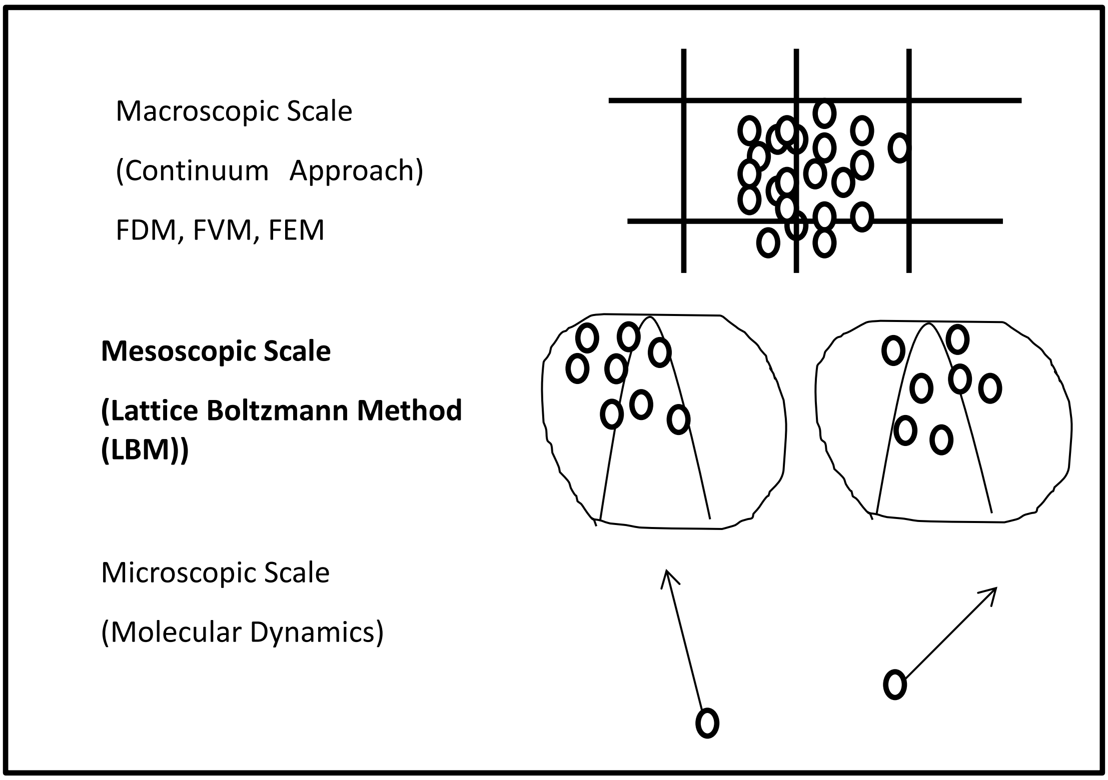

Figure 3.1: Schematic of macroscopic, mesoscopic and microscopic scale.

Figure 3.1 shows schematic of different computational scale for numerical formulation. Microscopic modelling is computationally difficult, since it involves molecular level studies which consume a lot of memory and processing time. Hence microscopic modelling is only used where the study demands high level of accuracy and good computational resources are available to the researchers (Tiwari et al., 2023). So calculation on each particle is performed in microscopic scale which shows huge computational cost.

As the mesoscopic model combines the advantages of macroscopic and microscopic models, the lattice Boltzmann method (LBM) has emerged as a popular numerical tool with high computational efficiency. Lattice Boltzmann method (LBM) has been promisingly used to investigate heat transfer and fluid flow problems for several years which is reviewed by (He et al., 2019).

## 3.1 Lattice Boltzmann Method for Heat Transfer and Fluid Flow

In lattice Boltzmann method (LBM), the computational domain is divided in lattice nodes in which a central lattice node is connected with neighbouring lattice nodes through lattice linkages. Depending on the dimensions of the problem, different lattice models are introduced varying number of lattice speed which is represented as $D_nQ_m$, in which ‘D’ indicates dimension of the problem and ‘Q’ represents number of lattice linkages. Figure 3.2 shows a D2Q5 lattice model, D2Q9 lattice model and D3Q19 model. Figure 3.2 (a) and (b) represents the two-dimensional square lattice with a central node is connected with four neighbouring nodes and eight neighbouring nodes respectively. A three dimensional lattice model with a central node is connected with eighteen neighbouring nodes which are shown in Fig. 3.2 (c). Transport of momentum and energy takes place among central node and neighbouring nodes through streaming-collision mechanism quantised by distribution functions. The LB simulation for heat and fluid flow problems can be categorised in two ways, isothermal LB method and non-isothermal LB method.

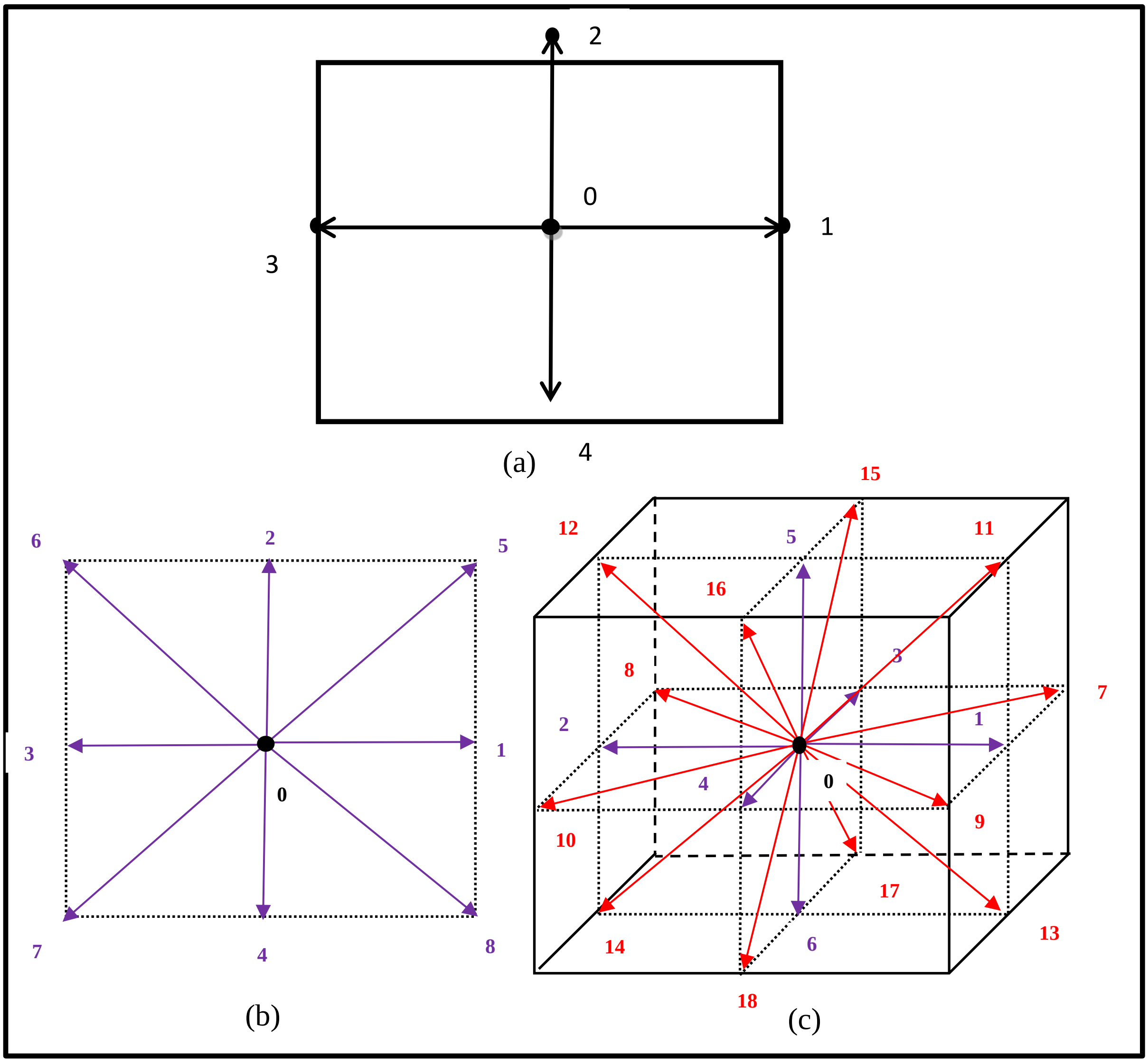

Figure 3.2: LB model stencils for a) D2Q5 model and b) D2Q9 model and c) D3Q19 model.

### 3.1.1 Isothermal Lattice Boltzmann Model

The isothermal LB model can be expressed using a density distribution function for velocity and the corresponding equilibrium distribution function depends on local macroscopic variables velocity $(\mathbf{u}_m)$ and density $(\rho_m)$. The LB modelling for velocity field can be expressed using 'Bhatnagar-Gross-Krook (BGK) collision operator'. Based on collision operator, LB model can be termed as the BGK-LB scheme. The density distribution function of velocity $(f_k)$ with a source term $(F_k)$ of lattice Bhatnagar-Gross-Krook (LBGK) model can be expressed as (Huang et al., 2013a),

$$f_k(\mathbf{x}+\mathbf{e}_k\Delta t, t+\Delta t) = f_k(\mathbf{x},t) - \frac{1}{\tau_f}\left[ f_k(\mathbf{x},t) - f_k^{eq}(\mathbf{x},t)\right] + \Delta t F_k \tag{3.1}$$

where **x** is coordinate of lattice nodes, t is time and Δt is time step, $\mathbf{e}_k$ is the discrete velocity, $k$ is direction in a lattice, and $\tau_f$ represents the dimensionless relaxation time and $F_k$ is the source term. The equilibrium density distribution function $f_k^{eq}$ is given as (Huang et al., 2013a),

$$f_k^{eq} = w_k \rho_m \left[ 1 + \frac{\mathbf{e}_k . \mathbf{u}_m}{c_s^2} + \frac{\mathbf{u}_m \mathbf{u}_m : (\mathbf{e}_k \mathbf{e}_k - c_s^2 \mathbf{I})}{2 c_s^4} \right] \tag{3.2}$$

where $w_k$ is the weight co-efficient, $\mathbf{u}_m$ is velocity, $c_s$ is the lattice speed of sound, $\mathbf{I}$ is unit tensor. The macroscopic variables density $(\rho_m)$ and momentum $(\rho \mathbf{u}_m)$ can be obtained as,

$$\rho_m = \sum_0^n f_k \tag{3.3}$$

$$\rho_m \mathbf{u}_m = \sum_0^n \boldsymbol{e}_k f_k + \frac{\Delta t}{2} \rho_m \mathbf{F} \tag{3.4}$$

Here $\mathbf{F}$ is body force per unit mass.

For, D2Q9 lattice, the discrete velocities ( $\mathbf{e}_k$ ) are given by,

$$\mathbf{e}_k = c \begin{bmatrix} 0 & 1 & 0 & -1 & 0 & 1 & -1 & -1 & 1 \\ 0 & 0 & 1 & 0 & -1 & 1 & 1 & -1 & -1 \end{bmatrix} \tag{3.5}$$

Similarly, for D3Q19 model the discrete velocities ( $\mathbf{e}_k$ ) are given by,

$$\mathbf{e}_k = c \begin{bmatrix} 0 & 1 & -1 & 0 & 0 & 0 & 0 & 1 & -1 & 1 & -1 & 1 & -1 & 1 & -1 & 0 & 0 & 0 & 0 \\ 0 & 0 & 0 & 1 & -1 & 0 & 0 & 1 & 1 & -1 & -1 & 0 & 0 & 0 & 0 & 1 & -1 & 1 & -1 \\ 0 & 0 & 0 & 0 & 0 & 1 & -1 & 0 & 0 & 0 & 0 & 1 & 1 & -1 & -1 & 1 & 1 & -1 & -1 \end{bmatrix} \tag{3.6}$$

where, $c$ indicates the lattice speed.

The above LBGK model is also called single relaxation time (SRT) based LB method. The detailing of the multi relaxation based isothermal LB model has been described in many books (Guo and Shu, 2013; Succi, 2001; Wolf-Gladrow, 2004) and in review papers (Chen and Doolen, 1998; Perumal and Dass, 2015). Different force scheme as well as hydrodynamic boundary conditions for isothermal LB scheme is discussed in (Krüger et al., 2017). For non-isothermal fluid flow problems, the thermal field has to be modeled using a separate distribution function for energy. As already mentioned, the solid liquid phase change is a non-isothermal flow problem with interface dynamics. Accordingly, in the next section of the article, thermal LB method is presented.

### 3.1.2 Thermal lattice Boltzmann Model

In general, the application of LB models for non-isothermal fluid flow problems can be classified into three categories, the multispeed approach (Lamarti et al., 2019; Semma et al., 2008), the double distribution function approach (Gao et al., 2021; Li et al., 2007; Nabavizadeh et al., 2021) and the hybrid approach (Nee, 2021; Satjaritanun et al., 2021). Multispeed approach has been used to solve different thermal flow problems (Klass et al., 2021; Sharma et al., 2017) despite its numerical instability and narrow range temperature variations which severely restrict its applications (Liao and Jen, 2011). DDF approach is widely acceptable to simulate thermo-fluidic problems as it uses different relaxation time for fluid flow and thermal field (Karlin et al., 2013; Li et al., 2018; Wang et al., 2020). In hybrid approach, the flow part is simulated using isothermal LB model and the energy field is solved using one of the continuum based methods (Contrino et al., 2014; Lallemand and Luo, 2003). In the present paper, DDF approaches as well as hybrid modelling of LBM are discussed in the next section. According to the review work done by (He et al., 2019) the framework of the DDF approach can be subdivided into passive scalar approach, internal energy based method and total energy based method. In passive scalar approach, the energy field can be modelled using temperature as a scalar quantity. For the other two methods, the internal energy field or total energy is considered for solving the thermal part. The above DDF approaches can be expressed with a single relaxation time (SRT). The MRT based DDF approach is also used for the thermal fluid flow problems. Several works on melting-solidification using hybrid LB model and DDF based LB scheme have been reported in literature (Chen et al., 2018; Chen et al., 2021; Hasan and Saha, 2021b; Huo and Rao, 2018; D. Li, Ren, et al., 2017; Li et al., 2018; Liu et al., 2017; Wu et al., 2017). Hybrid LB scheme as well as DDF based LB model for solid-liquid phase change problems have been described in the following section.

### 3.1.3 Double Distribution Function (DDF) Based LB Scheme with Single Relaxation Time (SRT)

A lot of work on melting-solidification of metals and alloys have been reported using single relaxation time based DDF approach (Chen et al., 2018; Z Chen et al., 2021; Hasan and Saha, 2021b; Li, Ren, et al., 2017; Wu et al., 2017; Zhu et al., 2017). The source term in density distribution function in Eq. 3.1 can be written as:

$$F_k = w_k \left(1 - \frac{1}{2\tau_f}\right)\left(\frac{\mathbf{e}_k - \mathbf{u}_m}{c_s^2} + \frac{\mathbf{e}_k.\mathbf{u}_m}{c_s^4}\mathbf{e}_k\right)\left(\rho_m.\mathbf{S}_m\right) \tag{3.7}$$

For the case of natural convection, the source term $(\mathbf{S}_m)$ can be defined as

$$\mathbf{S}_m = \mathbf{g}\beta_T (\mathrm{T} - \mathrm{T}_{ref}) \tag{3.8}$$

where $\mathbf{g}$ is acceleration due to gravity, $\beta_T$ is thermal expansion co-efficient and $\mathrm{T}_{ref}$ is reference temperature.

The energy equation in terms of temperature with a source term can be expressed as Eq. 2.1.

The general energy distribution function $(g_k)$ in LB simulation without a source term can be expressed as

$$g_k\left(\mathbf{x} + \boldsymbol{e}_k \Delta t, t + \Delta t\right) = g_k\left(\mathbf{x}, t\right) - \frac{1}{\tau_g}\left(g_k\left(\mathbf{x}, t\right) - g_k^{eq}\left(\mathbf{x}, t\right)\right) \tag{3.9}$$

where, $\tau_g$ is relaxation time and the corresponding equilibrium energy distribution functions $(g_k^{eq})$ can be described for temperature, internal energy or total energy separately.

In passive scalar approach, the energy distribution function is expressed in terms of temperature.

The macroscopic temperature can be calculated as

$$\sum_0^n g_k = T \tag{3.10}$$

The total energy based model is used widely in which the total enthalpy is calculated as a summation of density distribution function of energy combining the source term with temperature.

### *Total energy based model*

The energy equation in terms of temperature is expressed in terms of temperature in Eq. (2.10 and conversion of the energy equation in terms of total enthalpy is illustrated in Eq. (2.1) to Eq. (2.9).

The evolution equation for equilibrium distribution function $(g_k^{eq})$ can be expressed as

$$g_k^{eq} = \begin{cases} H - c_p T + \omega_k c_p T \left(1 - \dfrac{u_m^2}{2c_s^2}\right) & k = 0 \\ \omega_k c_p T \left[1 + \dfrac{\mathbf{e}_k . \mathbf{u}_m}{c_s^2} + \xi \dfrac{\mathbf{u}_m \mathbf{u}_m : (\mathbf{e}_k \mathbf{e}_k - c_s^2 \mathbf{I})}{2c_s^4}\right] & k \neq 0 \end{cases} \tag{3.11}$$

The macroscopic enthalpy can be calculated as

$$\sum_{0}^{n} g_k = \mathrm{H} \tag{3.12}$$

### 3.1.4 Hybrid Lattice Boltzmann (LB) Scheme

As earlier mentioned that, in hybrid approach, the flow field is solved using isothermal LB model and the thermal part of the problem can be approximated using conventional macroscopic methods. The hybrid approach was developed by combining isothermal LB model for flow field with finite difference method for energy equation and incorporated on to study melting-solidification problems (Filippova and Hänel, 2000; Hu et al., 2019a; Noyola-García and Rodriguez-Romo, 2021). In recent years, hybrid LBM has been used to solve segregation problems, and complex micro structural solid-liquid phase change problem of metal and metal alloy (Nee, 2021; Ohno and Sato, 2018a; Satjaritanun et al., 2021).

### 3.1.5 Treatment of Source Term

The LBGK energy distribution function of Eq. (3.9) adding a source term can be written as (Hasan and Saha, 2021b)

$$g_k(x+\mathbf{e}_k\Delta t, t+\Delta t) = g_k(x,t) - \frac{1}{\tau_e}\left[g_k(x,t) - g_k^{eq}(x,t)\right] + \Delta t S_k \tag{3.13}$$

where, $S_k$ is the source term in the equation of energy distribution function. Through Chapmann-Enskog analysis from the BGK-LB equation it was found that, an additional term appears in the recovered macroscopic equation which is caused by the discrete lattice effect (Li et al., 2017; Shi and Guo, 2009). When the effect of this additional term is considered, the source term in Eq. (3.13) takes the following form:

$$S_k = w_k\left(1-\frac{2}{\tau_e}\right)S \tag{3.14}$$

$S$ is a source term in Eq. (3.14) (He et al., 2019). The corresponding temperature can be calculated as (He et al., 2019)

$$\mathrm{T} = \sum_{0}^{n} g_k + \frac{\Delta t}{2} S \tag{3.15}$$

### 3.1.6 Treatment of Boundary Conditions

The boundary conditions of LBM were discussed in many published papers (Contrino et al., 2014; Gobin and Martinez, 1985; He et al., 1997; Li et al., 2013; Wang et al., 2020). The flow and thermal boundary conditions are described using the distribution functions at the boundaries. At the boundary nodes, the outward distribution functions from the cavity are known from the streaming process and the inward distribution functions to the cavity are unknown for the implementation of both flow and thermal boundary conditions.

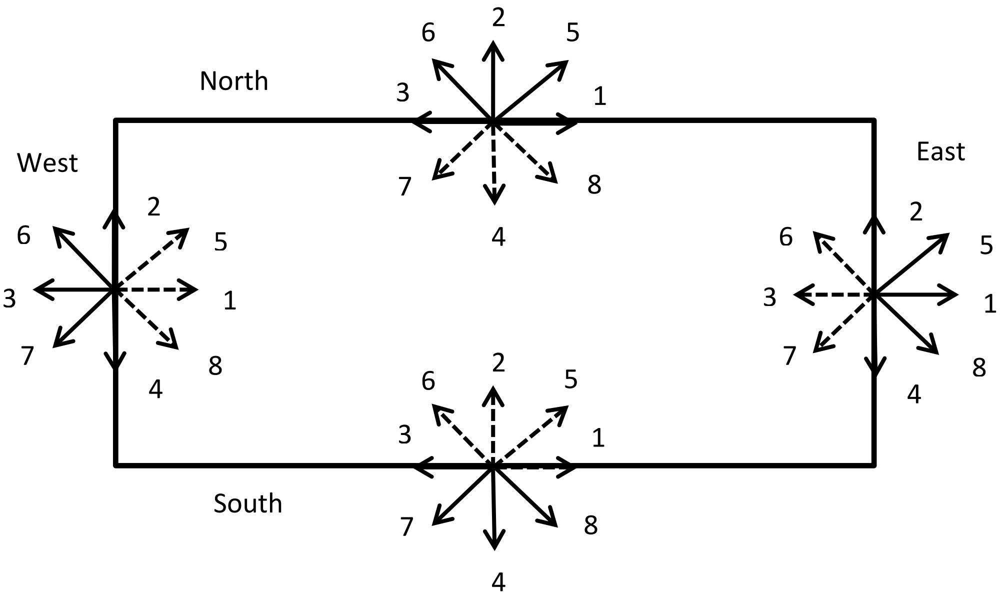

Figure 3.3: Schematic of direction of streaming velocities at boundary [Solid arrows indicate known distribution functions from streaming, and the dotted arrows represent the unknown distribution functions].

Figure 3.3 shows schematically the distribution functions at the boundary nodes. The solid arrows in the figure indicate the known distribution functions deriving from streaming, and the dotted arrows represent the unknown distribution functions.

***Flow Boundary Condition*:** In LBM method, bounce back method is applied for stationary boundary or moving wall boundary conditions. To calculate the velocity at the boundary bounce back method is used in two ways; for no-slip boundary condition the velocity at the adjacent wall to the wall boundary is similar while for moving boundary wall the velocity is calculated from wall distribution functions. For no-slip boundary condition at the west wall implies that the incoming particle towards the solid boundary bounces back into the fluid domain. At the west boundary in Fig. 3.3, the following conditions are imposed,

$$\left.\begin{array}{l} f_1(0,y) = f_3^*(0,y) \\ f_5(0,y) = f_7^*(0,y) \\ f_8(0,y) = f_6^*(0,y) \end{array}\right] \tag{3.16}$$

Similarly, when the north boundary is moving with a velocity then the expression of the north boundary condition is

$$\left.\begin{aligned}&f_4(x,m)=f_2^*(x,m)\\&f_8(x,m)=f_6^*(x,m)+\rho_{m,N}u_{m,0}/6\\&f_7(x,m)=f_5^*(x,m)-\rho_{m,N}u_{m,0}/6\\&\rho_{m,N}=f_0(x,m)+f_1(x,m)+f_3(x,m)+2\left[f_2(x,m)+f_6(x,m)+f_5(x,m)\right]\end{aligned}\right] \tag{3.17}$$

where, $f_i^*$ represents the distribution function after collision and streaming. $\rho_{m,N}$ is the density at the north boundary, $u=u_{m,0}$ is the $x$-component velocity, '$0$', and '$m$' indicate the first node of $x$ axis and last node of the $y$ axis respectively.

***Thermal Boundary Condition:*** The thermal boundary conditions are generally categorised as Dirichlet boundary condition (Chen and Müller, 2020; Suzuki et al., 2018), Neumann boundary condition (Suzuki et al., 2018; Tao et al., 2020) and Robin boundary condition (Krüger et al., 2017). In case of Dirichlet type boundary conditions (BC~~)~~, temperature is specified at the boundaries. To tackle such situations, using lattice Boltzmann methods, several methods can be adopted such as bounce back (BB) method, interpolation method and anti-bounce back (ABB) scheme (Huang et al., 2013b; Samanta et al., 2020; Liangqi Zhang et al., 2018).

The Neumann BC specifies a normal flux at the boundary (adiabatic condition or a known heat flux) (Huo and Rao, 2015), for which two different procedures can be used: either by directly imposing the flux on the boundary or through transformation of Neumann condition to Dirichlet BC at the wall (Dai et al., 2018). The values of the unknown distribution functions can be algebraically evaluated depending on the heat flux (Samanta et al., 2020). Based on Fig. 3.3 the adiabatic boundary condition at the top wall can be expressed as

$$\sum_{k=0}^{n} g_k(j)=\sum_{k=0}^{n} g_k(j-1) \tag{3.18}$$

where, $j$ denotes the last lattice node at $y$ axis. Similarly, the temperature specified boundary condition at the left wall can be formulated as

$$\sum_{k=0}^{n} g_k^{eq}(i)=\sum_{k=0}^{n} g_k(i) \tag{3.19}$$

where, $i$ denotes the first lattice node at $x$ axis.

## 3.2 Lattice Boltzmann Modelling For Corner Melting and Solidification

In this work, thermal Lattice Boltzmann method (TLBM) with double distribution functions is used to model the flow and the thermal field of corner melting and solidification of pure substances. The density distribution function of velocity $(f)$ and enthalpy $(g)$ are used to solve velocity and temperature field respectively.

The LB equation with Bhatnagar-Gross-Krook (BGK) collision form, the flow field can be solved using the velocity distribution function (*f*) according to (Hasan and Saha, 2021b; Huang et al., 2013b). Calculation of macroscopic velocity from the distribution functions can be calculated solving Eq. (3.1) to Eq. (3.4).

In a similar manner, for the energy equation, energy distribution function in terms of total enthalpy is written as Eq. (3.9) and corresponding equilibrium distribution function of enthalpy $g_k^{eq}$ is given as

$$g_k^{eq} = \begin{cases} H - c_p T_m + w_k c_p T_m \left(1 - \dfrac{u_m^2}{2c_s^2}\right) & k = 0 \\ w_k c_p T_m \left[1 + \dfrac{\boldsymbol{e}_k.\mathbf{u}_m}{c_s^2} + \dfrac{\boldsymbol{e}_k.\mathbf{u}_m}{2c_s^4} - \dfrac{\mathbf{u}_m^2}{2c_s^2}\right] & k \neq 0 \end{cases} \tag{3.20}$$

Through Chapman-Enskog analysis macroscopic equations can be recovered and the total enthalpy can be expressed as Eq. (3.12).

For the rest part of the thesis the value of temperature is calculated from enthalpy for melting and solidification of pure substance in the following manner:

$$\mathrm{T} = \begin{cases} \dfrac{H}{c_p} & \mathrm{T} < T_m \\ T_m + \dfrac{H - H_m}{H_l - H_m}\left(T_l - T_s\right) & T_m \leq \mathrm{T} \leq T_l \\ T_l + \left(H - H_l\right)/c_p & \mathrm{T} > T_l \end{cases} \tag{3.21}$$

where $T_l$ and $T_s$ are the liquidus and solidus temperatures of the material respectively, in the present work for pure metal $T_l = T_s = T_m$. Liquidus enthalpy and solidus enthalpy are expressed as $H_l$ and $H_s$ respectively.

By Chapman-Enskog analysis, the physical parameters in term of the kinematic viscosity $(\nu)$ and thermal diffusivity $(\alpha)$ are related with the mesoscopic parameters as given by

$$\nu = c_s^2 \left(\tau_f - 0.5\right)\Delta t \tag{3.22}$$

$$\alpha = c_s^2 \left(\tau_g - 0.5\right)\Delta t \tag{3.23}$$

Therefore, the Prandtl number can be expressed using Eq. (3.22) and (3.23) as

$$Pr = \frac{\tau_f - 0.5}{\tau_g - 0.5}. \tag{3.24}$$

## 3.3 Modified Lattice Boltzmann Model For Low Prandtl Number Liquid Metals

It is reported in the literature (Coreixas et al., 2020; Sterling and Chen, 1996; Yang et al., 2014) that, the numerical stability of LBM is strongly dependent on the dimensionless relaxation time which is correlated with the fluid viscosity or the diffusion coefficient in the available LBGK models for Navier-Stokes equations or convection-diffusion equations. The lattice Boltzmann Bhatnagar-Gross-Krook (LBGK) model would be unstable if the value of relaxation parameter $(\tau_f)$ was either too high or too low (near to 0.5), which would limit its applications to the study of low *Pr* or high *Ra* flow problem. The dimensionless relaxation time for fluid flows depends on the local viscosity, which is a function of the shear stress and strain rate. Therefore, as the shear stress rate approaches zero, the LBGK model may experience numerical instability.

Lattice kinetic scheme (LKS) was proposed by (Inamuro, 2002) for incompressible fluid flow with heat transfer. In his plan, a relaxation parameter for the stress tensor is provided to make the dimensionless relaxation time equal to one, which increases the stability of the LBGK model by including a term linked to the stress tensor in the equilibrium distribution function. (Yang et al., 2014) proposed modified LBGK models by including correction terms in the evolution equations, for the incompressible Navier-Stokes equation and the convection-diffusion equation. Through this alteration, the LBGK model's dimensionless relaxation time value can be maintained within acceptable bounds, enhancing the model's stability at low viscosity (Wang et al., 2018). The improved model was used in nano- fluid heat transfer to handle the instability caused by high Schmidt number (Soleimani et al., 2021) or instability studies at low Prandtl number fluid in differential heated cavity (Bawazeer et al., 2019).

In this work, a correction term in the evolution equation is added for momentum and energy transfer equations following (Yang et al., 2014) and the modified LB scheme has been used to study the thermal convection behavior in the melt zone for very low Prandtl number liquid metals. In order to tackle numerical instability for melting in low *Pr* fluids, this work modifies relaxation parameters terms in LBM for Navier-Stokes and convection-diffusion i.e. energy equation. The following sections describe the modified LB model capable of handling phase transition at low *Pr*.

### 3.3.1 The Modified LBGK Model For Incompressible Navier Stokes Equation

The modification of LBGK model is brought by introducing a new relaxation parameter $\tau'_m$.

The modified relaxation parameter may be expressed as

$$\tau'_f = \tau_f + A' \tag{3.25}$$

where, $A'$ is a tunable parameter.

The evaluation equation for modified density distribution function is written as

$$f_k\left(x + \boldsymbol{e}_k \Delta t, t + \Delta t\right) = f_k\left(x,t\right) - \omega'_f\left(f_k\left(x,t\right) - f_k^{eq}\left(x,t\right)\right) + \Delta t S_k \tag{3.26}$$

where $\boldsymbol{e}_k$ is the discrete velocity in direction $k$ and $S_k$ is the source term. $\omega'_f$ is the reciprocal of new relaxation parameter which is defined as

$$\omega'_f = \frac{1}{\tau'_f} \tag{3.27}$$

where $A'$ is a tuning parameter.

The equilibrium density distribution function $f_k^{eq}$ is given similar as Eq. (3.2).

The correction term has been added with force term in the evolution equation Eq. (3.26). The source term can be written as

$$S_k(x,t) = w_k \frac{A'\left[\nabla \mathbf{u}_m + (\nabla \mathbf{u}_m)^T\right] : \left(\boldsymbol{e}_k \boldsymbol{e}_k - c_s^2 \mathbf{I}\right)}{2\tau'_f c_s^2} + w_k\left(1 - 0.5\omega'_f\right) F_k(x,t) \tag{3.28}$$

The first term in Eq. (3.28) is the correction term and second term is force term. $\frac{\left[\nabla \mathbf{u}_m + (\nabla \mathbf{u}_m)^T\right]}{2} = S_r$ is the strain rate tensor in the correction term.

The force term in Eq. (3.28) can be written similar as Eq. (3.7). The strain rate tensor $S_r$ can be computed locally as

$$S_r = \frac{1}{2c_s^2\Delta t(A' - \tau_f')} \times \sum_k \left( f_k - f_k^{eq} \right) \boldsymbol{e}_k \boldsymbol{e}_k \tag{3.29}$$

Substituting Eq. (3.29) in Eq. (3.28) the source term is written as

$$S_k(x,t) = w_k \frac{1}{2c_s^2\Delta t(A' - \tau_f')} \times \frac{A' : \left( \boldsymbol{e}_k \boldsymbol{e}_k - c_s^2 \mathbf{I} \right)}{\tau_f' c_s^2} \sum_k \left( f_k - f_k^{eq} \right) \boldsymbol{e}_k \boldsymbol{e}_k + w_k \left( 1 - 0.5\omega_f' \right) F_k(x,t) \tag{3.30}$$

Assuming $\left( \boldsymbol{e}_k \boldsymbol{e}_k - c_s^2 \mathbf{I} \right) = Q_k$ , the correction term in Eq. (3.30) can be expressed as

$$S_k(x,t) = -4.5 Q_k \frac{2 w_k \omega_f'^2 A'}{1 - \omega_f' A'} \sum_{i=0}^{k} \left( f_k - f_k^{eq} \right) \boldsymbol{e}_k \boldsymbol{e}_k + w_k \left( 1 - 0.5\omega_f' \right) F_k(x,t) \tag{3.31}$$

Combining Eq. (3.7) and Eq. (3.31) the final form of the source term is illustrated as

$$S_k(x,t) = w_k \left( 1 - 0.5\omega_f' \right) \left( \frac{\boldsymbol{e}_k - \mathbf{u}_m}{c_s^2} + \frac{\boldsymbol{e}_k . \mathbf{u}_m}{c_s^4} \boldsymbol{e}_k \right) (\rho_m \mathbf{S}_m) - 4.5 Q_k \frac{2 w_k \omega_f'^2 A'}{1 - \omega_f' A'} \sum_{i=0}^{k} \left( f_k - f_k^{eq} \right) \boldsymbol{e}_k \boldsymbol{e}_k \tag{3.32}$$

It is obvious that by adjusting the parameter $A'$, the dimensionless relaxation time for a fixed viscosity can be changed within a suitable range. Density is calculated following Eq. (3.3) and velocity can be formulated as

$$\rho_m u_m = \sum_0^n \boldsymbol{e}_k f_k + \frac{\Delta t}{2} \rho_m \mathbf{S}_m \tag{3.33}$$

### 3.3.2 The Modified LBGK Model For Advection-Diffusion Equation

The energy equation in terms of temperature is treated as a convection-diffusion equation. Modified relaxation time for energy is $\tau_g'$ .

$$\tau_g' = \tau_g + B' \tag{3.34}$$

For LBM, energy equation in terms of temperature can be formulated as

$$g_k \left( x + \boldsymbol{e}_k \Delta t, t + \Delta t \right) = g_k \left( x, t \right) - \omega_g' \left( g_k \left( x, t \right) - g_k^{eq} \left( x, t \right) \right) + \Delta t S_k' \tag{3.35}$$

where $\omega_e' = {}^{1}\!/_{\tau_g'}$ is inverse of energy field relaxation time and $S_k'$ is energy source term.

$$S_k' = w_k \frac{e_k . B' \nabla (c_p T)}{\tau_g'} + F'(\mathrm{x}, \mathrm{t}) \tag{3.36}$$

The first term in Eq. (3.36) is energy correction term and second term corresponds to force term.

$$F'(x,t) = \Delta t q_e \tag{3.37}$$

The gradient term $\nabla(c_p T)$ in Eq. (3.36) can be expressed by

$$\nabla(c_p T) = \frac{1}{c_s^2 \Delta t (B' - \tau_g')} \sum_k \left( g_k - g_k^{eq} \right) \boldsymbol{e}_k \tag{3.38}$$

Substituting Eq. (3.38) in Eq. (3.36) the final form of the source term is given as

$$S_k' = F'(\mathrm{x,t}) - 3\frac{w_k \omega_g'^2 B'}{1-\omega_g' B'} \sum_{i=0}^{8} \left( g_k - g_k^{eq} \right) \boldsymbol{e}_k \tag{3.39}$$

The second term in Eq. (3.39) is the energy correction term in which $B'$ is the tunable parameter, as already mentioned.

By Chapman-Enskog analysis, the physical parameters in term of the kinematic viscosity $(\nu)$ and thermal diffusivity $(\alpha)$ are related with the mesoscopic parameters as given by

$$\nu = c_s^2 \left( \tau_f - 0.5 + A' \right) \Delta t \tag{3.40}$$

$$\alpha = c_s^2 \left( \tau_g - 0.5 + B' \right) \Delta t \tag{3.41}$$

Therefore, the Prandtl number can be expressed as

$$Pr = \frac{\tau_f - 0.5 + A'}{\tau_g - 0.5 + B'} \tag{3.42}$$

where, $A'$ and $B'$ are two tunable constants whose values are determined by numerical experiments as already discussed. In this work, while $A'$ was set at 0.02 the value of $B'$ in dependent on relaxation parameters on a case to case basis. The value of $B'$ is dependent on both $Pr$ and $A'$. $A'$ is fixed for a particular $Pr$, corresponding $B'$ was calculated. The value of $B'$ should be in a range of 0.1 to 0.2 for better numerical stability.

## 3.4 Hybrid LBM For Binary Alloy Solidification

Lattice Boltzmann method (LBM) coupled with finite difference method (FDM) is used to study solidification phenomena of a binary alloy. The flow field modelled is simulated using LBM while the thermal and species continuity equations are solved using FDM. The flow field modelling of LBM is discussed earlier in section 3.1.1. The macroscopic density and velocity are calculated using Eq. (3.3) and Eq. (3.4) respectively. The finite difference modelling part is discussed in chapter 6.

# CHAPTER 4

# MELTING OF LOW PRANDTL NUMBER LIQUID METAL

The present chapter describes simulation of melting phenomena of low Prandtl number liquid metals. The effect of natural convection in the melt zone has been studied in a wide range of low Prandtl number. The investigation is carried out for two global parameters which are Prandtl number and Rayleigh number. A detailed analysis of the melting dynamics has been studied using time series data for observing flow instability.

## 4.1 Melting of Low Prandtl Number Liquid Metal

For a variety of applications, including cooling systems (cooling of high-density power electronic devices, nuclear reactors), heat exchangers, metallurgical processes and solidification-melting of metals (such as development of crystals from melts, metal treatment, casting and welding), it is crucial to comprehend the melting dynamics of low Prandtl number liquid metals under the influence of natural convection. Prandtl numbers of fluids describe the relative strength of momentum diffusivity (kinematic viscosity) to thermal diffusivity. For liquid metals, thermal diffusivity is relatively high and kinematic viscosity is low leading to low values of $Pr$. A low Prandtl number value indicates that heat diffusion is occurring in liquid metals significantly faster than momentum diffusion. The value of Prandtl number has significant impact on the flow field including boundary layer formation and heat transfer.

### 4.1.1 Objective of the Work

Investigations of melting phenomena of low Prandtl number ($Pr$) materials in a side heated cavity is performed in this work using lattice Boltzmann Modeling. In order to overcome numerical instabilities for simulation of low $Pr$ fluids, modification of lattice Boltzmann Bhatnagar-Gross-Krook (LBGK) models for incompressible Navier-Stokes equation and the energy equation are proposed in this study. Evolution of flow field and the melting front with thermal behavior has been presented in a wide range of Prandtl number $Pr \in [0.001,0.1]$ and Rayleigh number $Ra \in [10^4 ,10^6]$.

### 4.1.2 Problem Statement

Melting in a square enclosure with a low *Pr* number material is subjected to differential heat along the vertical boundaries. The top and bottom boundaries are thermally insulated. All enclosure boundaries are presumptively impermeable and are subject to a no-slip condition. The two-dimensional square cavity filled with a solid substance is initially uniformly present throughout the cavity (length L=width W) at its melting point ($T_m$). In contrast to the right wall, which is heated to a melting point temperature, the left side wall is heated to a temperature ($T_h$) over the melting temperature. The schematic of the present problem has been shown in Fig. 4.1. Thermal gradients exist in the domain as a result of the differently heated side walls. Due to the interaction between heat and momentum diffusion, natural convection in the melt zone of low Prandtl number liquid metals—typically in the Prandtl number range of 0.001 to 0.1, displays distinctive properties. Low Prandtl number liquid metals' specific thermos-physical characteristics, such as thermal conductivity, viscosity, and specific heat capacity, as well as external factors like temperature and pressure, have an impact on the melting behaviour. In this study, the phase transition from solid to liquid is investigated using liquid metals such as Mercury (*Hg*), Sodium (*Na*), Lead (*Pb*), Potassium (*K*), Gallium (*Ga*), and Lithium (*Li*) in the range of *Pr* 0.001-0.1. Stefan number (*Ste*) is set as 0.01 which is typical for such low *Pr* melting problems (Dai et al., 2018; Gobin and Benard, 1992; Hasan and Saha, 2021b; Huang et al., 2013b; Zongqin and Bejan, 1989).

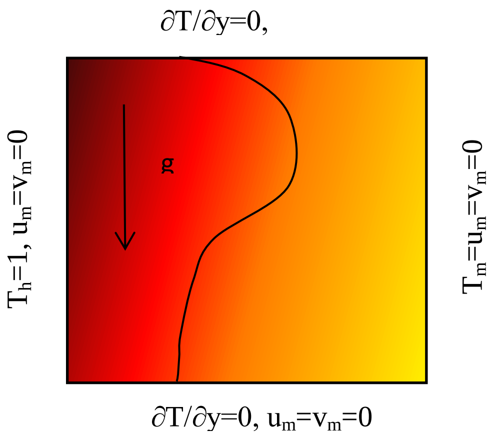

Figure 4.1: Schematic of physical domain with boundary conditions.

### 4.1.3 Mathematical Model Formulation

Understanding and forecasting natural convection in low Prandtl number liquid metals requires research into the governing equations, like the Navier-Stokes equations and the energy equation, as well as taking into account the metal's unique properties, like thermal conductivity, viscosity, and density variations. The flow patterns, melting rate, and temperature distributions within the melt zone can all be examined and described using lattice Boltzmann simulations. The macroscopic continuum mass, momentum, and energy conservation equations for thermo-fluidic transport in the presence of solid-liquid phase change can be characterized as follows under the assumption of a Newtonian, laminar, and incompressible flow.

Continuity Equation:

$$\frac{\partial \rho_m}{\partial t} + \nabla.\left(\rho_m \mathbf{u}_m\right) = 0 \tag{4.1}$$

Momentum equation:

$$\frac{\partial \rho_m}{\partial t} + \nabla.\left(\rho_m \mathbf{u}_m \mathbf{u}_m\right) = -\nabla p + \nabla.\left(\mu \nabla \mathbf{u}_m\right) + \rho_m \mathbf{S}_m \tag{4.2}$$

Energy equation in terms of temperature is rewritten same as used in section 2.2.2

$$\frac{\partial(\rho_m c_p T)}{\partial t} + \nabla(\rho_m c_p T \mathbf{u}_m) = \nabla(k_T \nabla T) - \frac{\partial\left(\rho_m \lambda f_l\right)}{\partial t} \tag{4.3}$$.

where $\rho_m, \mathbf{u}_m, p, \mu$ are the density, velocity, pressure, viscosity and respectively. $\mathbf{S}_m$ is the momentum source term in the corresponding equations. The source term in Eq. (4.2) can be expressed as long as the momentum equation uses the Boussinesq approximation given as

$$\mathbf{S}_m = \mathbf{g}\beta_T\left(T - T_{ref}\right) \tag{4.4}$$

where $\mathbf{g}$ is acceleration due to gravity, $\beta_T$ is coefficient of thermal expansion. The energy equation source term

Energy equation in terms of total enthalpy is expressed in section 2.2.2 following Eq. (2.1) through (2.8) to prevent non-linearity in the heat source term. The energy equation is rewritten as

$$\frac{\partial\left(\boldsymbol{H}\right)}{\partial t} + \nabla.\left(c_p T \mathbf{u}_m\right) = \nabla.[\alpha \nabla(c_p T)] \tag{4.5}$$

The initial condition is fixed assuming the cavity is filled with the fluid at the melting temperature.

Initial condition:

$$\text{at } t = 0,\ u_m = v_m = 0,\ T = T_m \ \text{ for } \ 0 \le x \le L \ \text{ and } \ 0 \le y \le W \tag{4.6}$$

The boundary conditions are given at $t > 0$.

$$\left.\begin{array}{lllll} u_m = v_m = 0, & \mathrm{T} = T_h & \text{for} & x = 0 & \text{and} \quad 0 \le y \le W \\ u_m = v_m = 0, & \dfrac{\partial T}{\partial y} = 0 & \text{for} & y = 0 & \text{and} \quad 0 \le x \le L \\ u_m = v_m = 0, & \mathrm{T} = T_m & \text{for} & x = L & \text{and} \quad 0 \le y \le W \\ u_m = v_m = 0, & \dfrac{\partial T}{\partial y} = 0 & \text{for} & y = W & \text{and} \quad 0 \le x \le L \end{array}\right] \tag{4.7}$$

The dimensionless numbers used in the present work are

$$\mathrm{T}^* = \frac{\mathrm{T} - T_h}{T_h - T_m},\ \mathbf{x}^* = \frac{\mathbf{x}}{W},\ \mathbf{y}^* = \frac{\mathbf{y}}{W},\ \Pr = \frac{\nu}{\alpha},$$

$$Ra = \frac{\mathbf{g}\beta \Delta T W^3}{\nu\alpha},\ Ste = \frac{c_p \Delta T}{\lambda},\ Bo = Ra.\Pr \text{ and } Fo = \frac{\alpha t}{W^2} \tag{4.8}$$

where $\mathrm{T}^*$ is dimensionless temperature, $\mathbf{x}^*$ and $\mathbf{y}^*$ are the dimensionless co-ordinates at $x$ and $y$ direction respectively. $\nu$ is kinematic viscosity, $\alpha$ is thermal diffusivity and $t$ is time. $\Pr$, $Ra$, $Ste$, $Bo$ and $Fo$ correspond to Prandtl number, Rayleigh number, Stephan number Boussinesq number and Fourier number. The asterisk mark (*) is dropped for the rest of the thesis which specify the non-dimensional form of the variable.

The average Nusselt number ($Nu_{avg}$) at the left heated wall can be calculated as

$$Nu_{avg} = -\int_0^W \left( \frac{\partial \mathrm{T}}{\partial x} \right)_{x=0} dy \tag{4.9}$$

Similarly, average Nu at the interface has been calculated at the interface.

$$Nu_{avg} = -\int_0^s \left( \frac{\partial \mathrm{T}}{\partial x} \right)_{\mathrm{int}} ds \tag{4.10}$$

where, s is interface.

### 4.1.4 Results and Discussion

Melting of low Prandtl number liquid materials in a side heated square cavity is investigated using lattice Boltzmann scheme in D2Q9 stencil. A modified lattice Boltzmann model as discussed in preceding section is used to overcome the difficulties of numerical stability reported for low *Pr* materials. In the proposed model, a tuning parameter $A'$ is added to the relaxation parameter ($\tau'_f$) which is set to 0.02 as discussed in section 3.3. Another tuning parameter $B'$ is also needed for energy equation which is calculated from the value of *Pr* as depicted in Eq. (3.44). A code for this has been developed in Fortran 90 and computations were performed in CDAC's PARAM SHAVAK system with a 16 core Intel Xeon processor. The lattice grid spacing and time step are considered as $\Delta x = \Delta t = 1$.

The effect of natural convection in the melt zone depends on both *Ra* and *Pr*. The present investigation is performed in a wide range of $Ra \in [10^4,10^6]$ with a liquid material range of $Pr \in [0.001, 0.1]$. While natural convection is governed by *Ra*, it is pointed out (Bejan, 2013) that for low *Pr* materials the combined effect of *Ra* and *Pr* decides the transport processes. Accordingly, certain results are depicted in terms of Boussinesq number (*Bo*) which is the product of *Ra* and *Pr*. As the melting behavior of such range of *Pr* is the concern of the present work, the flow and thermal behavior in the melt zone has been examined. The dynamics of moving front and advancement of convection prone irregular interface describes the physics of melt zone. The average heat flux is calculated on the heated wall as well as on the interface.

#### *Grid Independency test and validation of code*

For $Pr$=0.01, a grid independence investigation on calculation of average *Nu* is carried out varying $Ra=10^4$, $Ra=10^5$ and $Ra=10^6$ in a left heated melting square cavity with grid sizes of 80x80, 100x100, and 120x120. Table 4.1 represents the comparison of the Nusselt number for three different grid sizes at corresponding Rayleigh number of $10^4$,$10^5$ and $10^6$ respectively. As illustrated in Table 4.1, there is very little variation in *Nu* among the specified grids. For the case of 100x100 grids, it is observed that the deviation in *Nu* is less than 0.5% from that in 80x80 meshes for all *Ra*. Further refinement of nodes to 120x120, does not produce any applicable differences. Accordingly, 100x100 grids are chosen for further calculations.

Table 4.1: Calculated average *Nu* at left heated wall at all *Ra*

| **Grids** | ***Ra*=10$^4$** | **Deviation (%)** | ***Ra*=10$^5$** | **Deviation (%)** | ***Ra*=10$^6$** | **Deviation (%)** |
|---|---|---|---|---|---|---|
| **80x80** | 3.197 | | 0.361 | | 4.229 | |
| **100x100** | 3.194 | 0.3 | 3.357 | 0.37 | 4.225 | 0.43 |
| **120x120** | 3.195 | 0.05 | 3.358 | 0.09 | 4.226 | 0.12 |

The present FORTRAN code is further validated with experimental data of (Viskanta, 1988) in which the location of melting front is predicted which is shown in Fig. 4.2. The simulation is carried out at *Pr* = 0.021 and *Ra*=2.2x10$^5$ with aspect ratio 0.5. The outcomes demonstrate the present LB model shows a reasonable agreement with experimental data with a maximum deviation 5%.

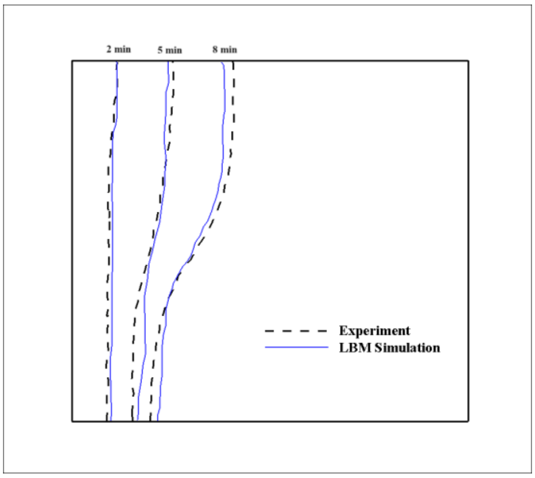

Figure 4.2: Validation of Melting front with (Viskanta, 1988) work.

## *Flow and thermal structure at the melt zone*

The location of the melting front is illustrated in Fig. 4.3 which exhibits different pattern of melting fronts depending on *Pr* and *Ra*. The melting front starts off with nearly vertical surface before it begins to tilt to right with vertical axis. The straight melting surface is an outcome of conduction dominated melting. As the effect of convection sets in the surface become contoured.

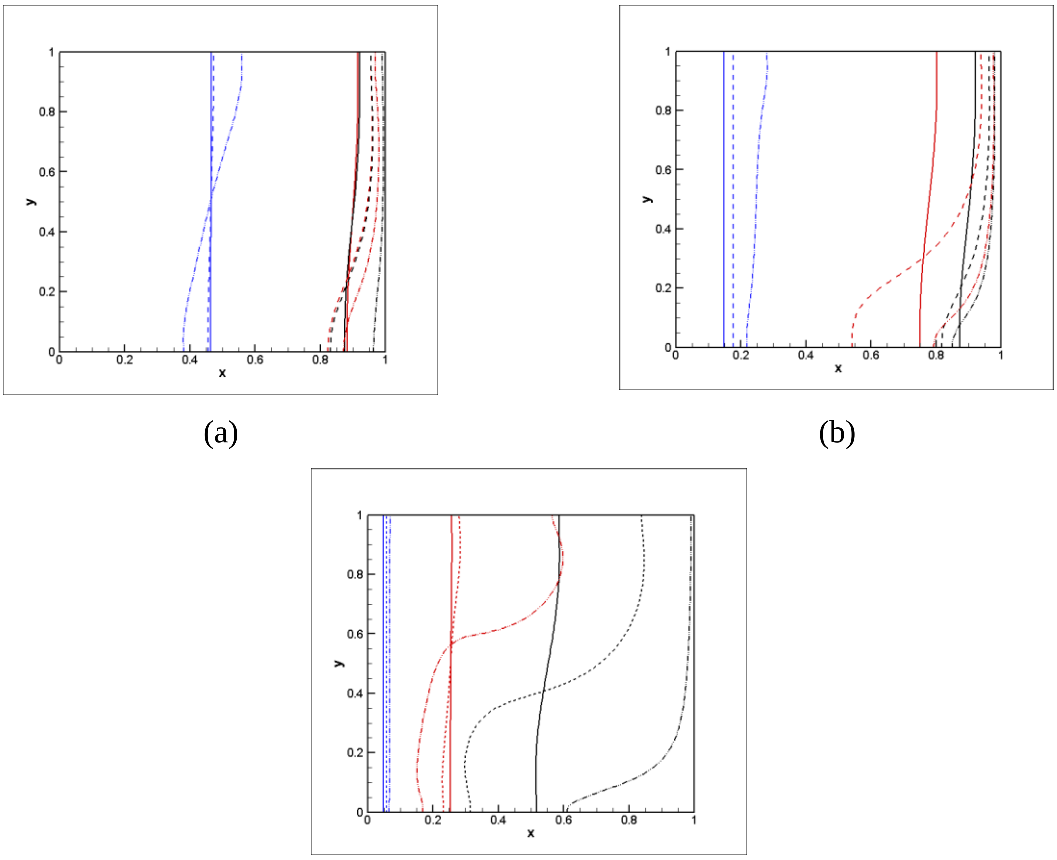

(a) (b)

(c)

Figure 4.3: Interface location in which colours indicate different time (Blue: *Ste***Fo*=0.002, Red: *Ste***Fo*=0.059 and Black: *Ste***Fo*=0.181) and line pattern specifies different *Ra* number (Solid line: *Ra*=$10^4$, Dashed line: *Ra*=$10^5$ and Dash-dot line express *Ra*=$10^6$) at different *Pr* a) *Pr*=0.001, b) *Pr*=0.01 and c) *Pr*=0.1.

Additionally, as *Ra* rises, the melting front advances in a horizontal direction, suggesting that the convection in the cavity is indeed becoming stronger at the same dimensionless moment. It is seen from Fig. 4.3(a) to (c) that the initial rate of melting is more and with progress of time it decreases. It is observed that at the time corresponding to *Ste***Fo*=0.002, melting zone at *Pr*=0.001 is largest in size followed by that of *Pr*=0.01 and 0.1. In other words, depth of the melting zone at initial level reduces with increasing *Pr* as the thermal diffusivity is reduces with increasing *Pr*. Generation of interface between solid-liquid phases initially is in the form of a straight line and with progress of time the front distortion occurs due to the presence of convection currents.

Fig. 4.4 through 4.6 describe the flow and thermal patterns in the melt zone for different *Ra* and *Pr*. As melting starts, a primary roll occupies the entire melt zone which grows with advancing time. With increase in *Ra*, the buoyancy force predominates the entire melt zone leading to stronger primary vortex. Low value of *Pr* implies weaker viscous fluid and hence it is observed that bigger cell may cascade down into smaller cells which are seen at *Ra*=$10^6$ where multi cells are generated at *Ste**Fo*=0.059 for *Pr*=0.001. Multi cells are appeared only at the end of melting at *Ste**Fo*=0.181 for *P*r=0.01 while only primary cell is present for *Pr*=0.1.

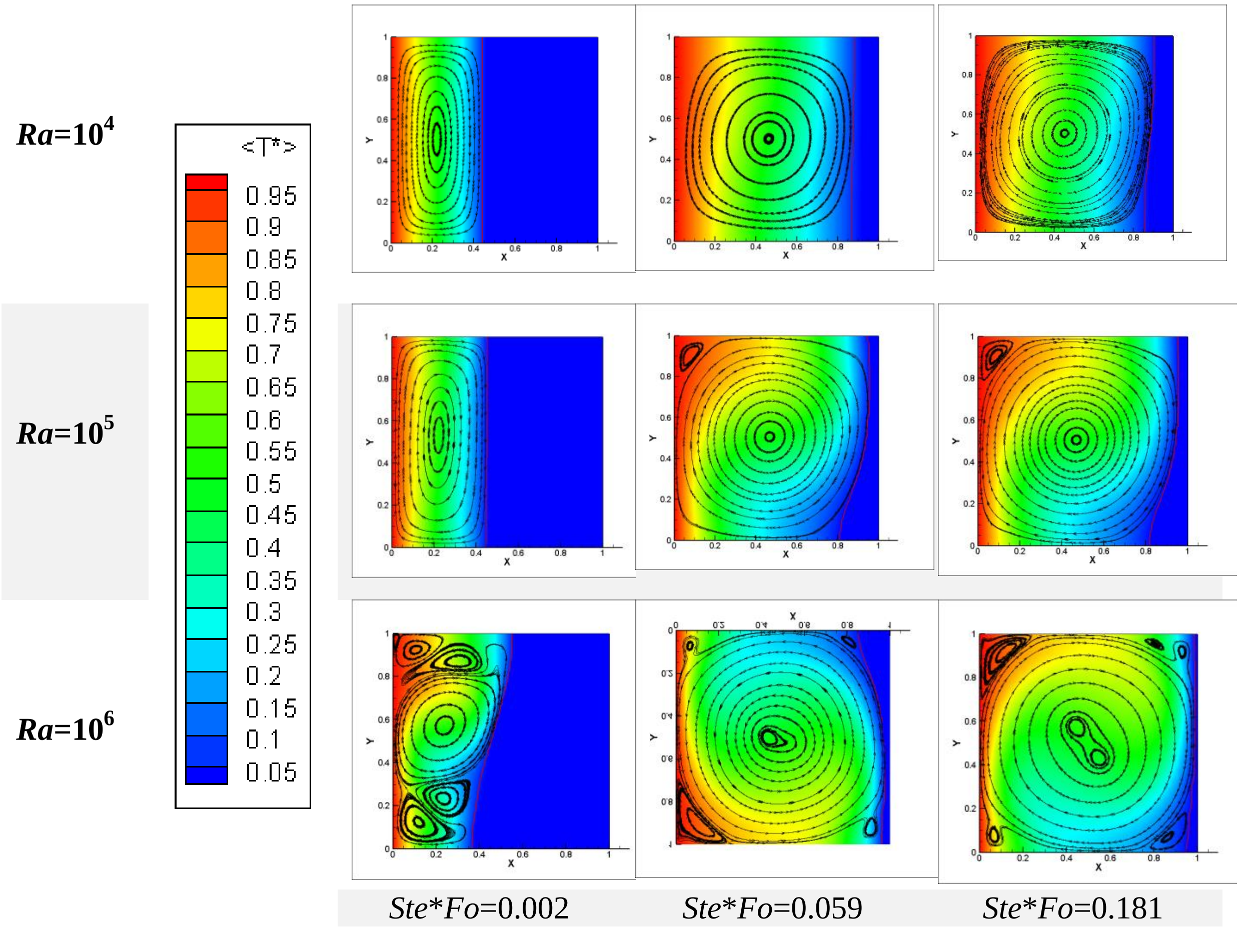

Figure 4.4: Evolution of Isotherms and Streamlines at *Pr*=0.001.

Fig 4.4 represents the thermo-fluidic dynamics in the melt zone for *Pr*=0.001 with varying *Ra*. Several interesting phenomena have come out through this study: formation of complete concentric cells takes place when interface is flat or, the curvature of interface is positionally aligned with the curvature of largest cell. Otherwise, apart from the larger cell, multi-cells are formed to satisfy the continuity of the flow field. With the increase in *Ra*, at *Ra*=$10^6$ several Rayleigh-Benard cells appeared in the melt zone while a single primary cell is present for both *Ra*=$10^4$ and *Ra*=$10^5$. It is seen that at high *Ra* with progress of time as melt zone becomes larger the formation of two lobes appear at the canter of primary cell which tends to separate from each other.

Fig. 4.5 shows the flow characteristics and thermal behavior at *Pr*=0.01 at different *Ra*. Comparing with Fig. 4.4 it is seen that, due to larger value of *Pr* formation of melt zone reduces owing to lower thermal diffusivity. Appearance of smaller cells is not seen in most of the cases irrespective of *Ra* and time, compared to previous case.

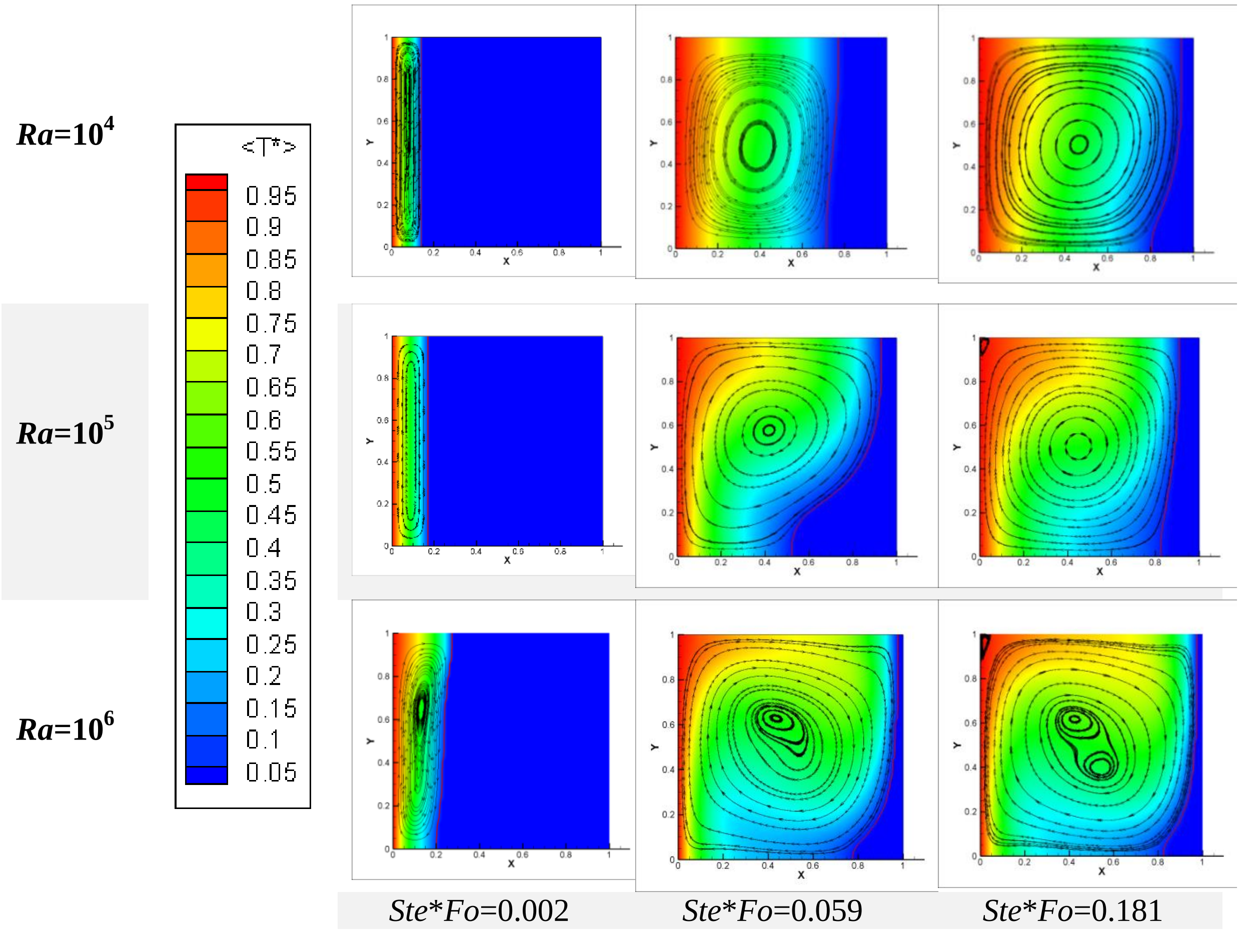

Figure 4.5: Evolution of isotherms and streamlines at *Pr*=0.01.

Due to the interaction of heating from left wall and downward gravity force, the axis of the rolls is slightly inclined towards right. At high *Ra* (*Ra*=$10^6$) as time increases, towards the end of melting, two counter rotating vortices appears in the core of the melt zone. Further numerical experimentation is presented in Fig. 4.6 for *Pr*=0.1. At this comparatively higher *Pr*, initial melting zone is rather slender at all *Ra*. With increasing time melting in the top part of the cavity is more prominent and the flow field looks like a plume bending over the upper region. Absence of smaller cells and formation of lobe in the melt zone makes an important difference with respect to the cases of low *Pr* i.e. below 0.1.

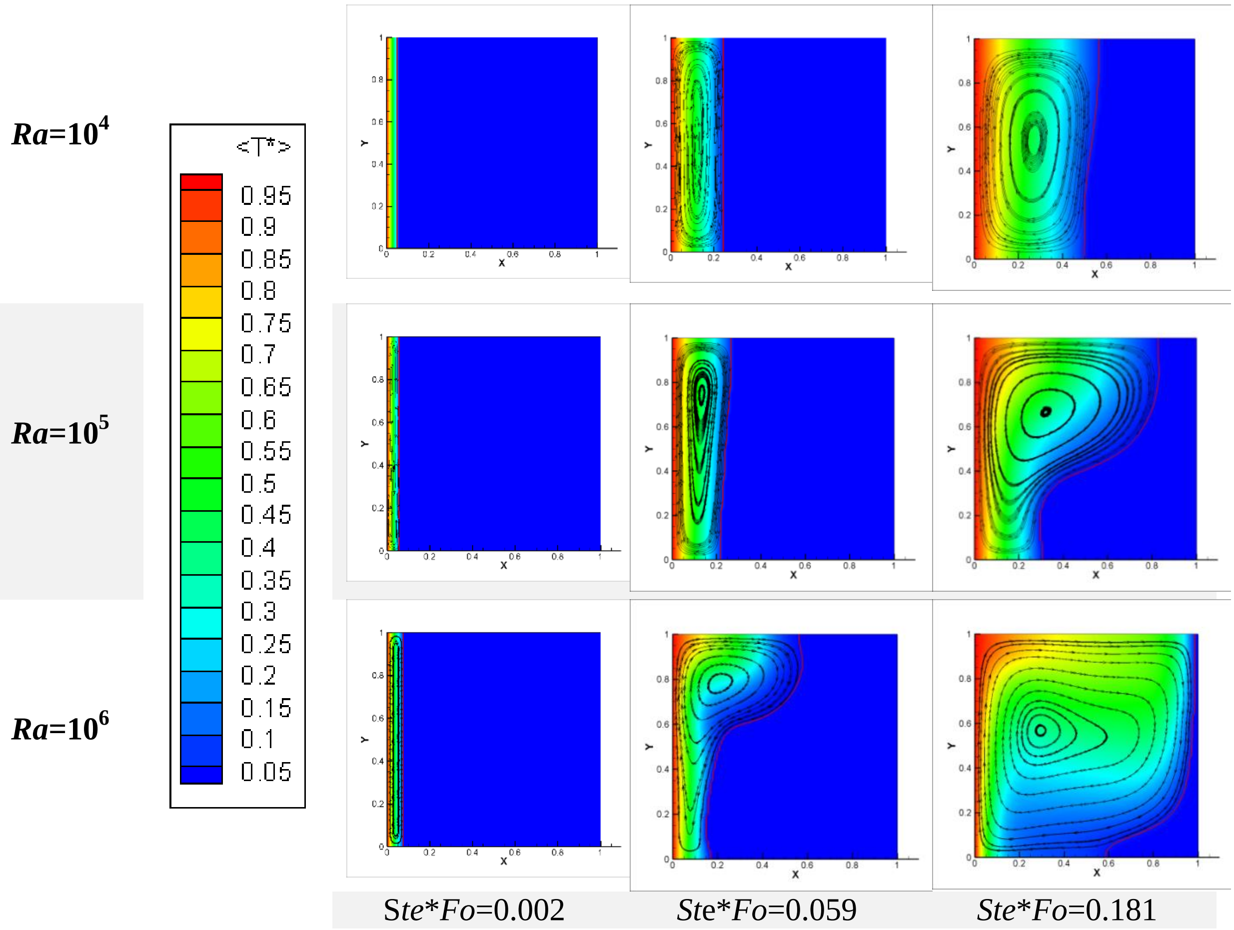

Figure 4.6: Evolution of isotherms and streamlines at *Pr*=0.1.

### *Average Nusselt number at heated wall and interface*

While average *Nu* at the wall is typically presented in literature for such studies, it is also worthwhile to look at the average *Nu* distribution at the interface (Gobin and Benard, 1992). Figure 4.7 displays the computed average *Nu* at the heated wall and the solid-liquid interface. The dotted lines denote the solid-liquid interface, whereas the solid line shows the average *Nu* at the heated wall. As can be observed in Fig. 4.7, the average *Nu* for heated walls is consistently greater than at the interface, indicating a stronger heat flux close to the heated wall than at the contact between two phases. For *Pr*=0.001, average Nu continuously reduces with time for the heated wall as well as the interface, regardless of change in *Ra*, as shown in Fig. 4.7a. For *Pr*=0.01, the average heat flux again monotonically reduces with time for *Ra*=$10^5$. However, at *Ra*=$10^6$, the average *Nu* initially falls then increases with time (Fig.

4.7b). The average *Nu* for heated walls and interfaces has a similar tendency for *Pr*=0.01. For all values of *Ra*, the average *Nu* initially declines then increases at *Pr*=0.1 (Fig. 4.7c). Although average *Nu* first has a larger value and then drops to a lower value before rising once more, quantitatively the initial *Nu* is always higher than the final value.

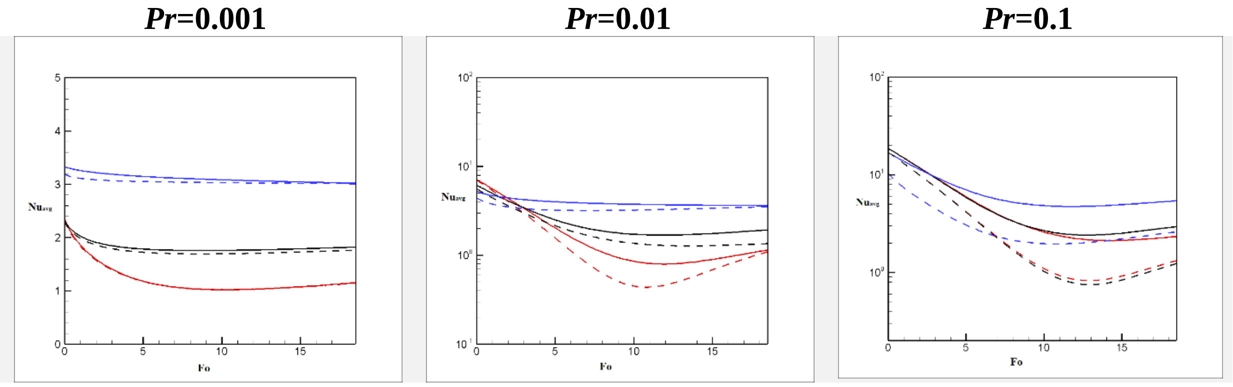
**Pr=0.001** **Pr=0.01** **Pr=0.1**

(a) (b) (c)

Figure 4.7: Average Nusselt number at different Prandtl number. Different colours indicate, variation of *Ra*: (Blue: *Ra*=$10^4$, black: *Ra*=$10^5$ and Red: *Ra*=$10^6$) and solid line and dotted lines correspond to Average *Nu* at heated wall and interface respectively.

## *Effect of Prandtl number and Rayleigh number*

The distribution of the liquid fraction has been described for defined *Pr* and *Ra* variations in Fig. 4.8. As can be observed here, a given amount of melted material can be achieved in less time as *Ra* increases. With an increase in *Pr*, the initial melting rate is reduced; for example, at very low *Pr*=0.001 (Fig. 4.8a), the melting rate is higher than *Pr*=0.1 (Fig. 4.8c). The driving force for melting rate is initially quite strong and gradually reduces over time for both *Pr*=0.001-0.01 materials, whereas it gradually increases for *Pr*=0.1 materials. Time for achieving 80% melting are 0.61, 3.06 and 26.33 for materials with *Pr*= 0.001, 0.01 and 0.1 respectively at *Ra*=$10^6$. As increasing the value of *Pr* indicates reduced thermal diffusivity an important consequence is the melt flow structure at a particular time at low *Pr* is realized at later time for higher *Pr*. For example, the flow pattern for *Pr*=0.01 at *Ste*Fo*=0.059 is similar to that for *Pr*=0.1 at *Ste*Fo*=0.185 which is shown in Fig. 4.9. The left wall of the square cavity serves as the initial contact for heating, and as time goes on, heat seeps in from the left heated wall. The initial contact length for heat transfer is equal to the cavity length. As melting begins the melt zone widens and the solid-liquid interface shifts in the direction of heat addition. As was previously mentioned, conduction is what causes the initial melting, and as time goes on, convection starts dominating. Distortion of the interface happens as a consequence of dominance of convection in the melt zone.

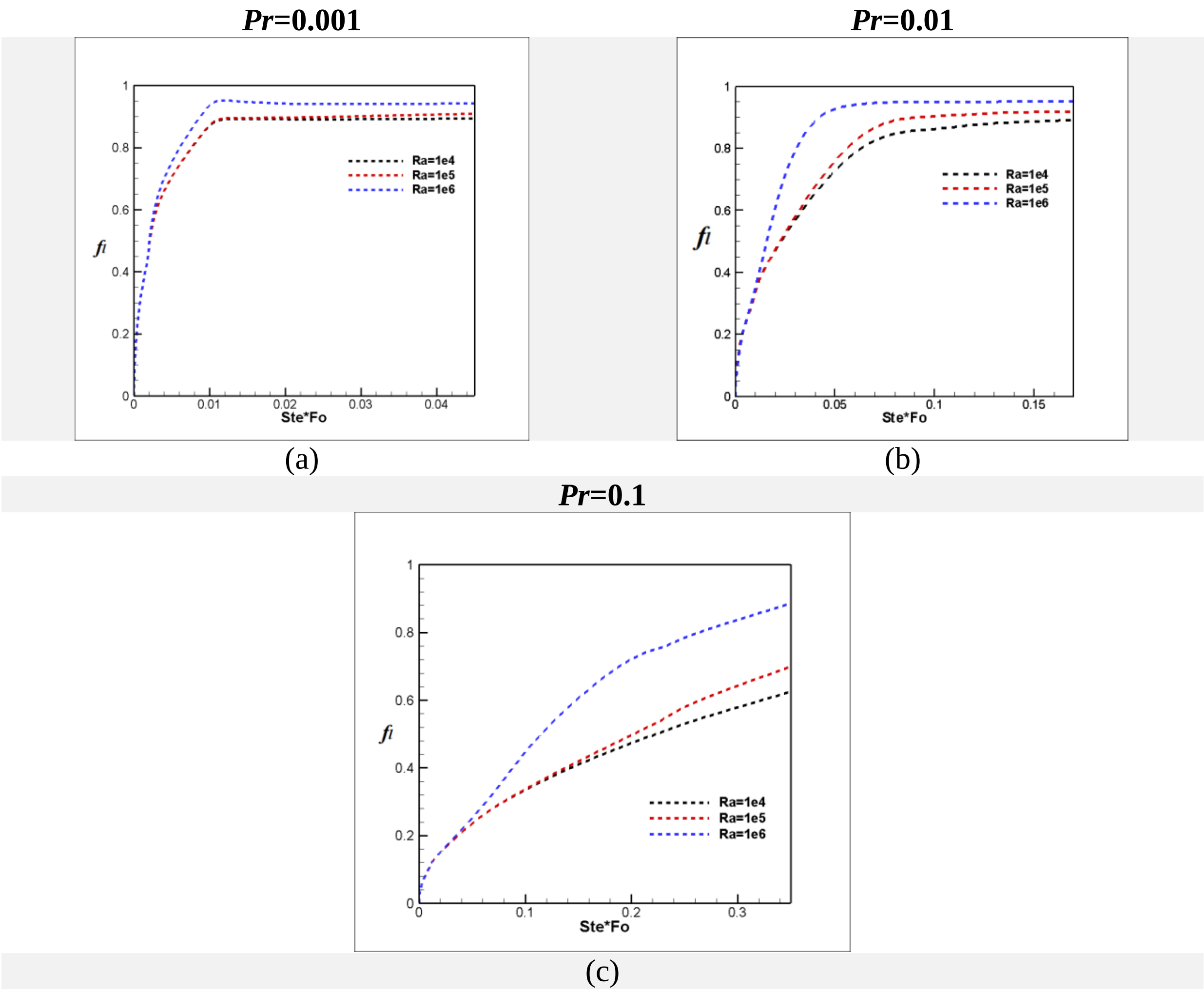

(a) (b)

(c)

Figure 4.8: Melt fraction at different *Pr*.

Maximum interface length increases with increase in *Ra* at all *Pr*. The reason can be attributed to the effect of convection leading to departure from conduction dominated model. This interface length first follows the size of the cavity, expands over time, and then changes back to the cavity dimension after full melting. The relationship between interface length with *Ra* and *Pr* is seen in Figure 4.10. The plots show that the interface length grows initially before decreasing. With advancing time, the interface length increases to its maximum value, demonstrating an inversely proportional relationship with *Fo*. Figures 4.10 (a) through 4.10 (c) show that when *Pr* increases, the maximum interface length also increases. It has been already observed that at low *Pr*, interfaces are almost flat due to high thermal diffusivity and reduced effect of convection. Additionally, it can be seen that regardless of *Pr*, the interface length is maximum for high *Ra*=$10^6$ compared to *Ra*=$10^4$ and *Ra*=$10^5$.

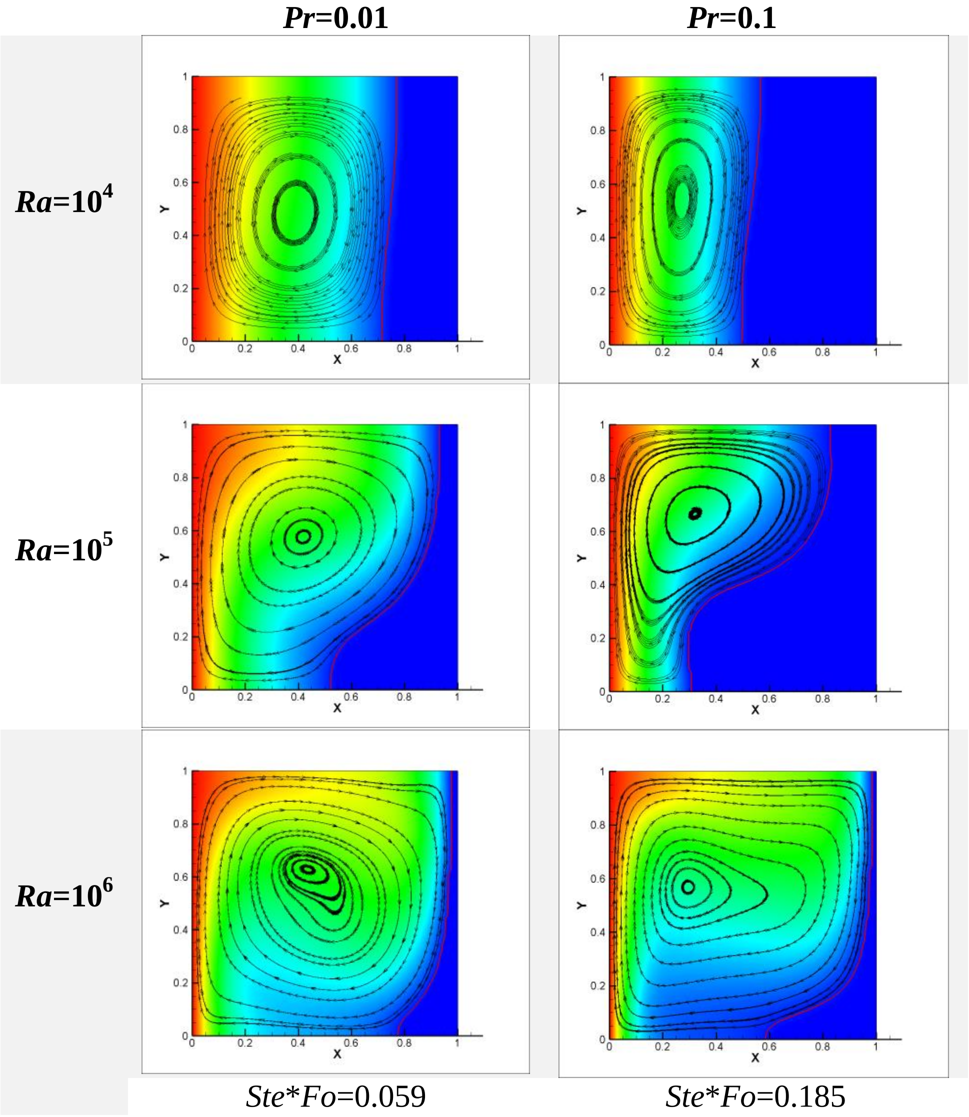

***Pr*=0.01** ***Pr*=0.1**

***Ra*=$10^4$**

***Ra*=$10^5$**

***Ra*=$10^6$**

*Ste***Fo*=0.059 *Ste***Fo*=0.185

Figure 4.9: Consequence of melt flow structure for two different *Pr*.

### *Maximum interface length*

Figure 4.11(a) illustrates how maximum interface length varies with time for different *Pr*. For *Pr*=0.001, it can be seen that the maximum interface length is almost independent of time as the melting occurs due to conduction. In comparison to *Pr*=0.01, the maximum interface length changes more quickly for *Pr*=0.1. In Fig. 4.11b, the variation in maximum interface length is reported against varying *Bo*, which is the product of *Ra* and *Pr*.

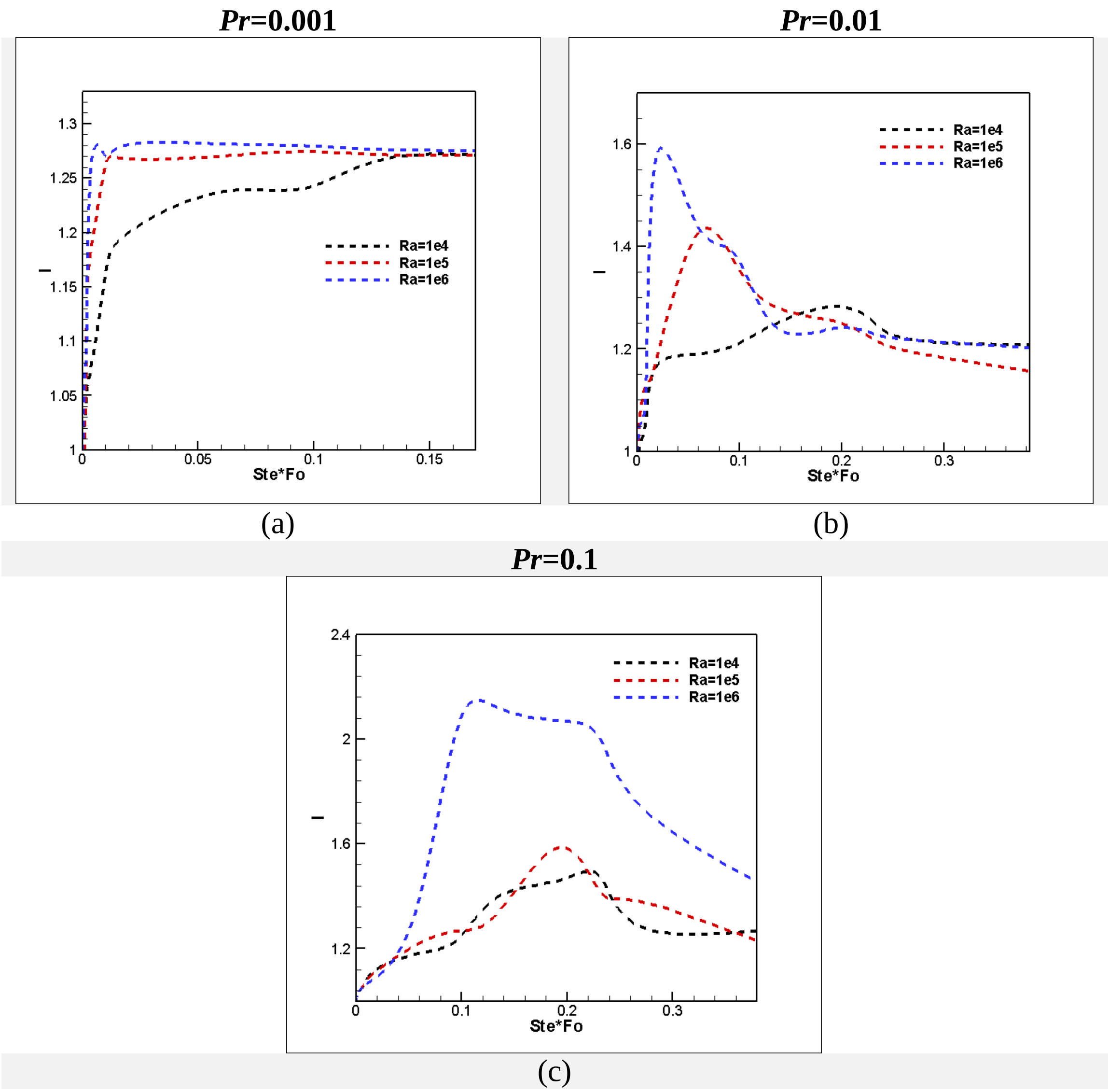

(a) (b)

(c)

Figure 4.10: Interface length at different *Pr*.

It can be observed from Fig. 4.11(b), the maximum interface length changes relatively little up to *Bo*=100, with a value of 1.21; however, when *Bo* increases from $10^2$ to $10^4$, the maximum interface length ranges from 1.21 to 1.6; and beyond *Bo*=$10^4$, the maximum interface length increases to 2.2. The dependence of interface size with *Bo* is an interesting result obtained in this study. This may find higher relevance in phase change problems involving morphological evolution in alloys.

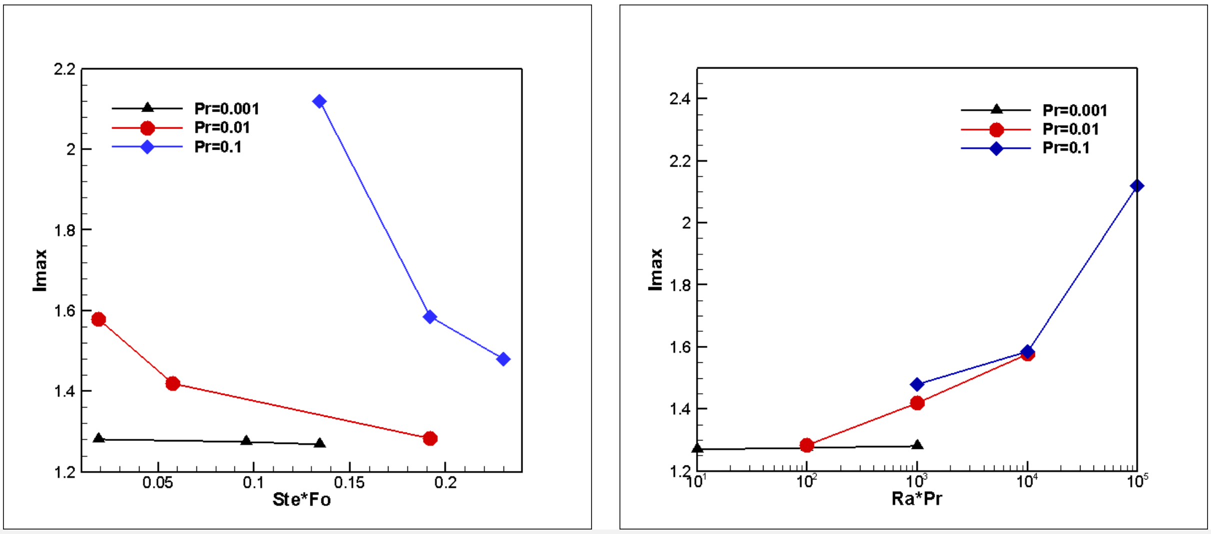

(a) (b)

Figure 4.11: Variation of maximum interface length with a) *Ste*Fo* and b) *Bo*.

## 4.2 Flow Instability in the Melt Zone

The first part of the ongoing study mainly concentrated on global parameters like the interface heat flux, melting rate and length of interface. Literature shows that several numerical works on melting and solidification have been done by many researchers to investigate the global parameters involved in solid-liquid phase change problem (Dai et al., 2018; Hasan and Saha, 2021a; Huang et al., 2013b). Evolution of melting boundary in solid-liquid phase change problem involves non-planer geometry due to the presence of Rayleigh-Benard convective cells in melted region. The presence of non-uniform heat fluxes causes the local distortion at the interface. The transition of flow behavior from steady to oscillatory in the melt zone is particularly an interesting phenomena to study. The interface dynamics and the thermo-fluidic behavior in a planer cavity are performed using modified lattice Boltzmann simulation. The parameters are taken as Prandtl number in the range of 0.005-0.05 and Rayleigh number between $10^5$-$10^6$.

### 4.2.1 Objective of the Work

Depending upon the parameters such as *Ra* and *Pr* the flow in a melting cavity transits from laminar to turbulent regime. While in the present range of *Ra* and *Pr* full phased transition is not established, it shall be interesting to study the non-linear dynamical evolution of the flow field. The melt zone grows with time and convective instability arises by interplay of *Ra* and *Pr* for low Prandtl number liquid metals. Change of melted area is directly related with the effective Rayleigh number which is dependent on liquid melt fraction. Different size and shape of the Rayleigh Benard (RB) convection rolls may occupy the melted zone which changes its size and shape with the growing melted area. This may be affecting the topography of the melting boundary. Inspired by the study of Rayleigh-Benard convection in a bottom heated melt boundary (Favier et al., 2019) the present investigation focus on the effect of natural convection on vertical melt boundary of low Prandtl number liquid metals. With the heat injecting through heated solid left boundary wall, the melting boundary moves. The presence of different flow circulation in the melt zone promotes to investigate the flow transition behavior from steady to oscillatory. The structure of oscillatory flow in the entire melt zone is investigated and a mapping is performed on oscillation frequency using Fast Fourier Transform (FFT) analysis.

### 4.2.2 Problem Formulation

Flow instability is investigated in a differentially heated square cavity in which heat flux is injected from the left wall. The schematic of the problem has been shown in Fig. 4.1. The melt boundary is moving and the melt zone grows with time. The oscillation behaviour of flow in melt zone is observed for melting low Prandtl number liquid metals. The nature of velocity components in the melt zone is analysed by monitoring several points at different positions. Figure 4.12 shows a schematic of melt zone in which black points indicate the position near bottom (A, B) and red points (C, D) are used for position at the top of the melt region. Position of A and D is near the heated wall while point B and C indicate the position at the vicinity of interface.

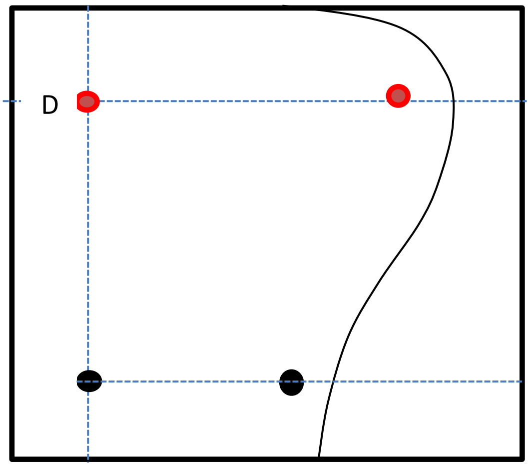

Figure 4.12: Schematic of different points in melt zone A, B, C and D in which red circle indicate the fixed points in the melt zone and black circles indicate the variable points in the melt zone which is changing with time.

The study of flow instability behaviour is studied at the points A, B, C and D which are changing with time. The time series data for *u* and *v* velocity components are analysed to study non-linear dynamics of the flow field.

### 4.2.3 Results and Discussion

Modified lattice Boltzmann method is used to simulate the flow instability for low *Pr* liquid metals. The in house FORTRAN lattice Boltzmann code is developed and applied to generate the phase change phenomena. Fast Fourier Transform (FFT) is used to quantify the *u* and *v* velocity components. MATLAB code is developed to perform FFT.

### *Validation of the Code*

A FORTRAN code is developed to study the oscillation behaviour of low Prandtl number fluid in a differentially heated cavity without melting. Figure 4.13 represents the validation plot of average Nusselt number at $Pr$=0.01.

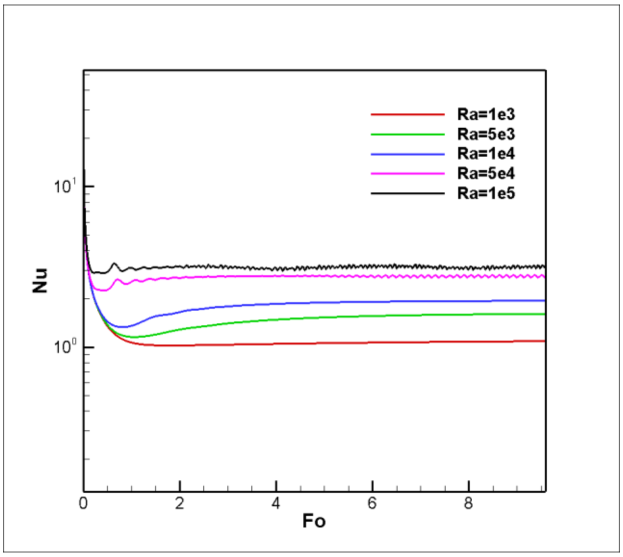

Fig. 4.13: Average $Nu$ at left heated wall at $Pr$=0.01.

It is seen from Fig. 4.13 that up to $Ra=10^4$ the flow shows a steady behaviour while from $Ra=5*10^4$ oscillation starts.

Table 4.2: Average $Nu$ at a range of Prandtl number and Rayleigh number validated with (Kosec and Šarler, 2013)* and (Bawazeer et al., 2019)** data.

| **Ra/Pr** | **0.001** | **0.005** | **0.01** |
|---|---|---|---|
| **$10^3$** | 1.060139 | 1.087405 | 1.150472 |
| **$5x10^3$** | 1.078906 | 1.102676 | 1.537773 |
| **$10^4$** | 1.082504 | 1.143072 | 1.908096<br>(1.95)*<br>(1.904786)** |
| **$5x10^4$** | 1.174996 | 1.562755 | 2.761905<br>(2.80)*<br>(2.780367)** |
| **$10^5$** | 1.335314 | 1.883092 | 3.165434<br>(3.25)*<br>(3.177619)** |

A corresponding validation has been done with the work of (Bawazeer et al., 2019; Z. Li et al., 2016) which is presented in Table 4.2. It is shown from Table 4.2 that the LBM code shows a good agreement with the published data. A thick bar demarcates the steady regime with the unsteady zone, a finding consistent with prior work (Bawazeer et al., 2019).

### *Effect of Rayleigh Number*

The moving melting front for low Prandtl number liquid metals moves with time. The transient evolution of melting boundary has been shown in Fig. 4.14 through 4.19 for the Prandtl number 0.005, 0.02 and 0.05 respectively. Figure 4.14 and 4.15 represent the thermal and flow characteristics in the melt zone for *Pr*=0.005. A primary circulation is observed in the melt zone at *Ra*=$10^5$ at all *Fo* =1.71, 2.42 and 5.97 (Fig. 4.14).

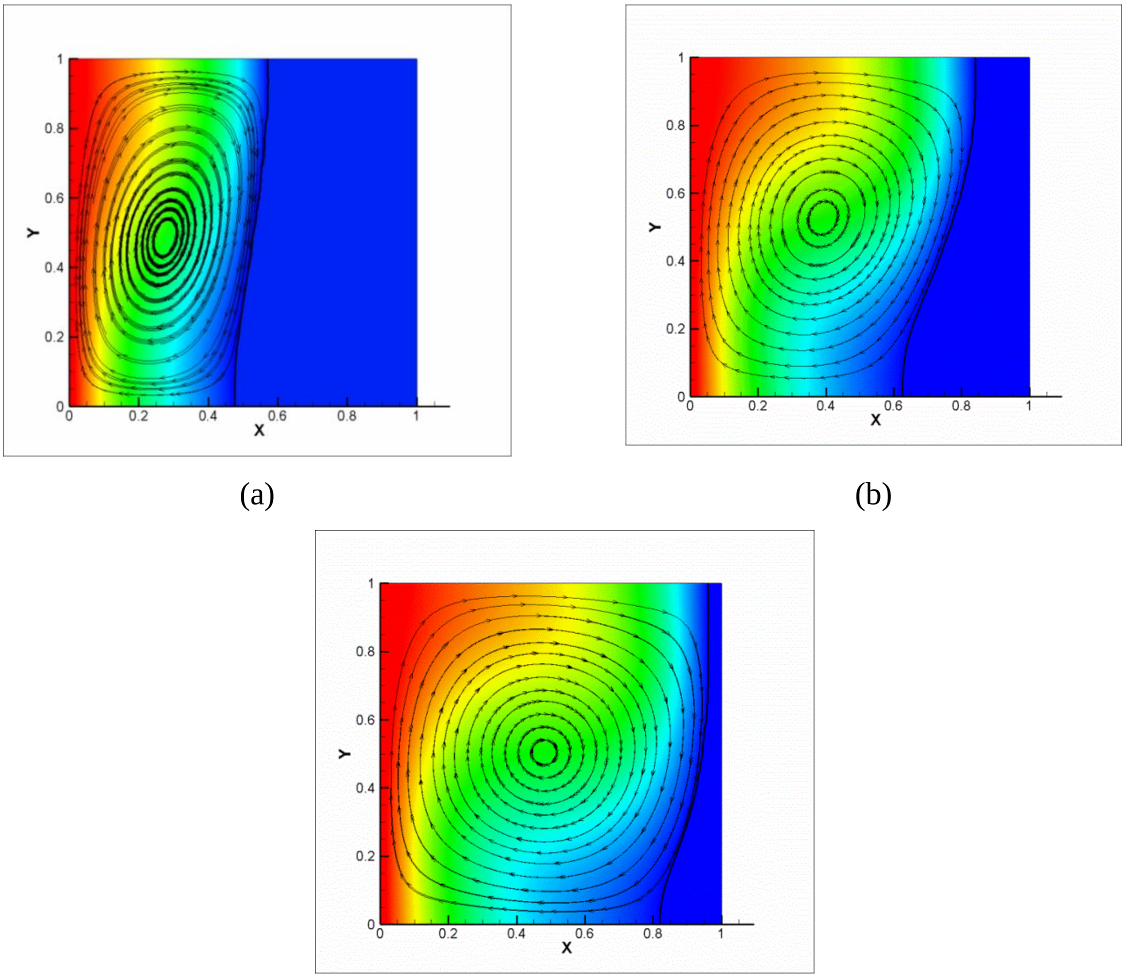

(a)

(b)

(c)

Figure 4.14: Transient evaluation of melting boundary at *Pr*=0.005 and *Ra*=$10^5$ a) *Fo*=1.71, b) *Fo*=2.42 and c) *Fo*=5.97.

Figure 4.15 represents the isotherms and fluid flow in the melt zone at *Ra*=$10^6$ for *Pr*=0.005. The nature of flow circulation is quite different from the earlier investigation. It is seen From Fig. 4.15(b) that a secondary circulation is generated in the center of the melted region at *Fo* 1.97. The primary circulation covers the entire melt zone while in the centre of the melt zone the primary flow circulation splits off into two secondary circulations with clockwise and anticlockwise direction.

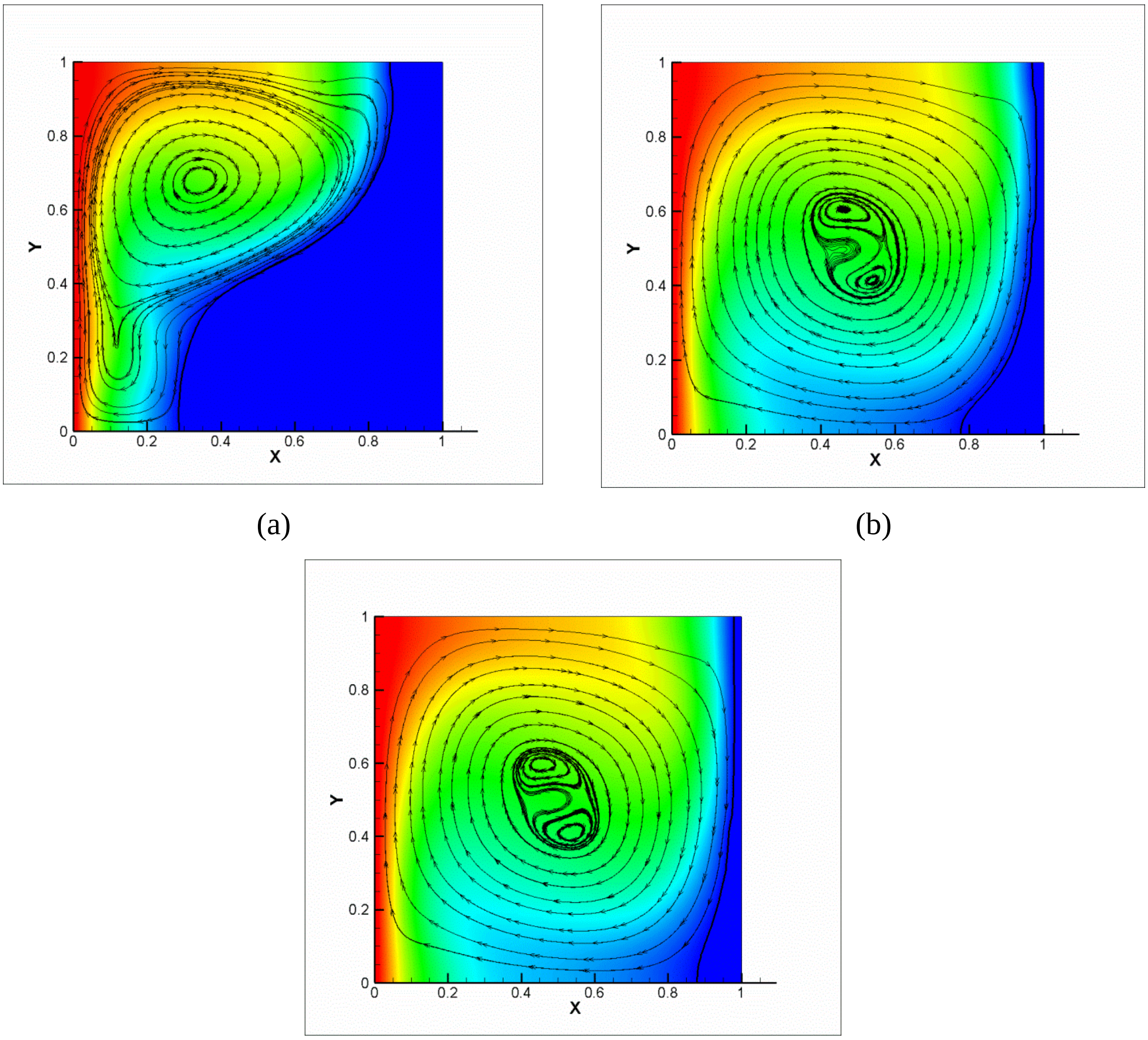

(a) (b)

(c)

Figure 4.15: Transient evaluation of melting boundary at *Pr*=0.005 and *Ra*=$10^6$ a) *Fo*=1.55, b) *Fo*=1.97 and c) *Fo*=9.71.

Figures 4.16 represents the isotherms and streamlines at *Ra*=$10^5$ while Fig. 4.17 illustrates the nature of melt zone at *Ra*=$10^6$ for *Pr*=0.02. A single cell is observed in the melt zone for *Ra*=$10^5$ at different *Fo* 2.42, 5.97 and 19.87 (Fig. 4.16).

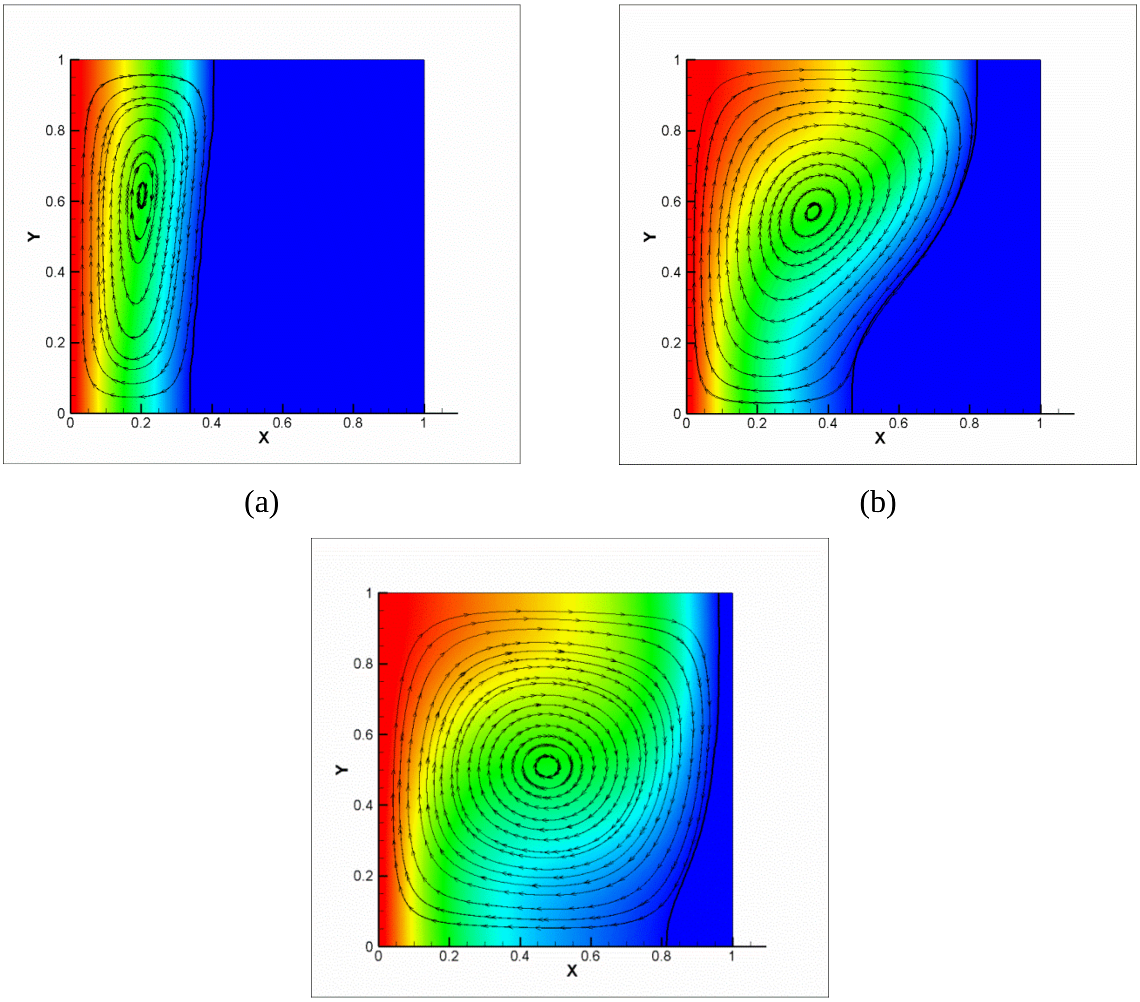

(a)

(b)

(c)

Figure 4.16: Transient evaluation of melting boundary at *Pr*=0.02 and *Ra*=$10^5$ a) *Fo*=2.42, b) *Fo*=5.97 and c) *Fo*=19.87.

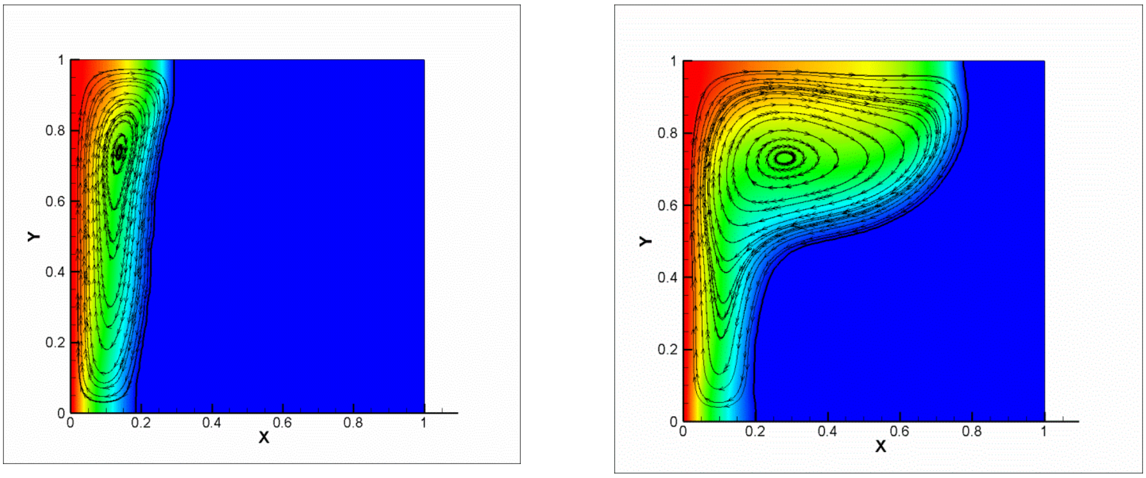

(a)

(b)

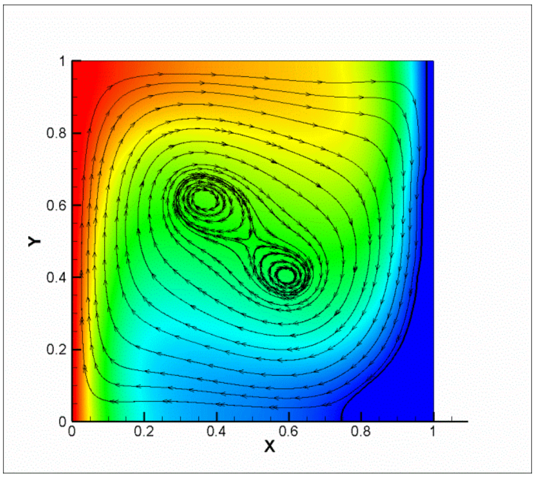

(c)

Figure 4.17: Transient evaluation of melting boundary at *Pr*=0.02 and *Ra*=$10^6$ a) *Fo*=3.81, b) *Fo*=4.97 and c) *Fo*=13.17.

Two separate secondary cells are generated from the primary cell at *Fo* =13.17 for *Ra*=$10^6$.

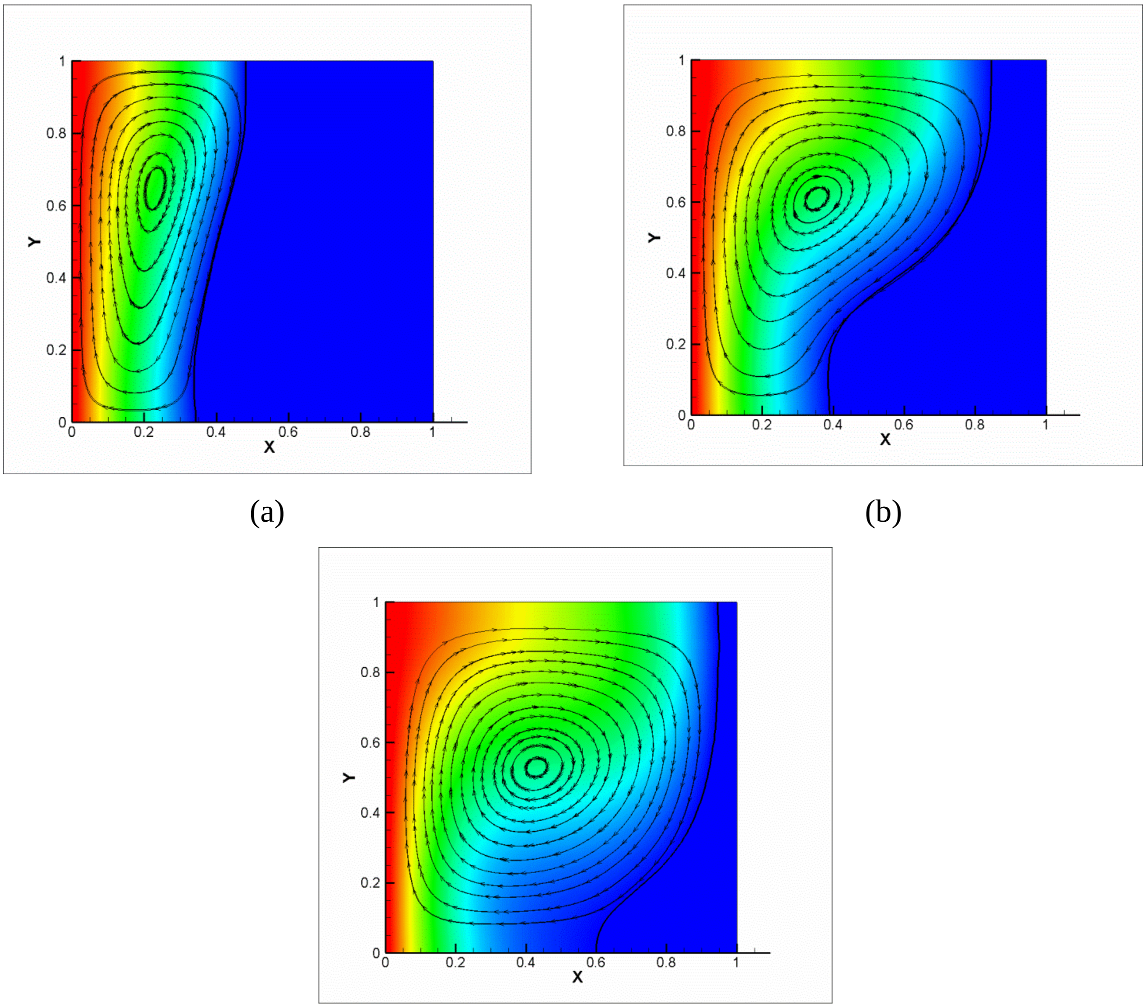

(a)

(b)

(c)

Figure 4.18: Transient evaluation of melting boundary at *Pr*=0.05 and *Ra*=$10^5$ a) *Fo*=13.18, b) *Fo*=19.07 and c) *Fo*=27.26.

(Bawazeer et al., 2019) also noticed such paired flow circulation with slightly inclined axes with vertical.

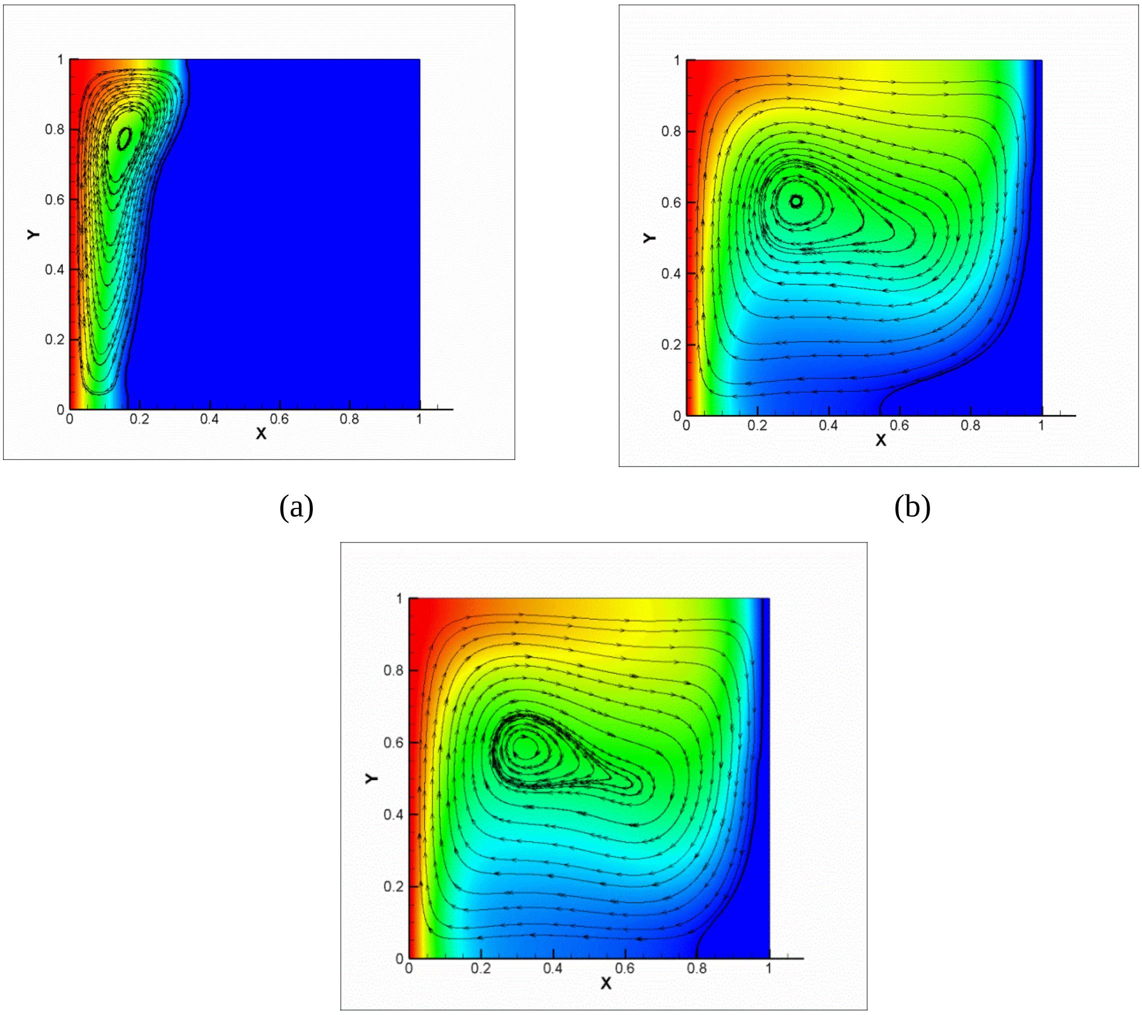

(a)

(b)

(c)

Figure 4.19: Transient evaluation of melting boundary at *Pr*=0.05 and *Ra*=$10^6$ a) *Fo*=7.59, b) *Fo*=14.73 and c) *Fo*=19.71.

In case of *Pr*=0.05, there is no generation of lobes in the melt zone which is represented in Fig. 4.18 and Fig. 4.19.

### *Convective Flow Instability in the Melt Zone*

The melting boundary dynamics is related with the convection current in the melt zone. The natural convection effect may show distinct behaviour at the top part and the bottom portion of the cavity. The present study analyses the nature of flow field at the top zone and bottom zone of the melted area. The convective instability in the melt is analysed at high *Ra* at a wide range of low $Pr \in [0.005, 0.05]$.

Heat flux from the left heated wall leads to melting of material with moving boundary. Flow instability appears in the melt zone due to the transition of fluid flow from conduction to convection regime. When convection starts, the oscillations may appear in the flow field. The time series plots of *u* and *v* velocity components are performed to study the inherent characteristics of the flow field. The onset of oscillatory flow instability has been investigated in the melt zone and time series of velocity fields has been observed at the vicinity of the heated wall and interface.

The results show time series plots of *u* and *v* velocity components at the position of A, B, C and D. The study is repeated for a *Pr* range of 0.005 to 0.05 in which the melt area changes with the moving melting boundary. FFT analysis of both *u* and *v* component velocity has been performed. The oscillatory flow behavior is found out over a long time duration which is analyzed using FFT analysis and the dominant non-dimensional frequencies are calculated. An appropriate slice of sampling from time series data has been chosen for FFT.

The time series plots of *u* and *v* velocity components are shown in which the oscillatory flows are presented corresponding to the position A, B, C and D for each *Pr* for varying *Ra*. Velocity oscillation of *u* and *v* components has been analyzed for *Pr*=0.005 which is illustrated in Figs. 4.20, through 4.25. Figures 4.20 through 4.22 summarize the oscillatory flow behavior with transient melting boundary at *Ra*=$10^5$. Similarly, Fig. 4.23 through 4.25 shows u and *v* components flow characteristics at *Ra*=$10^6$.

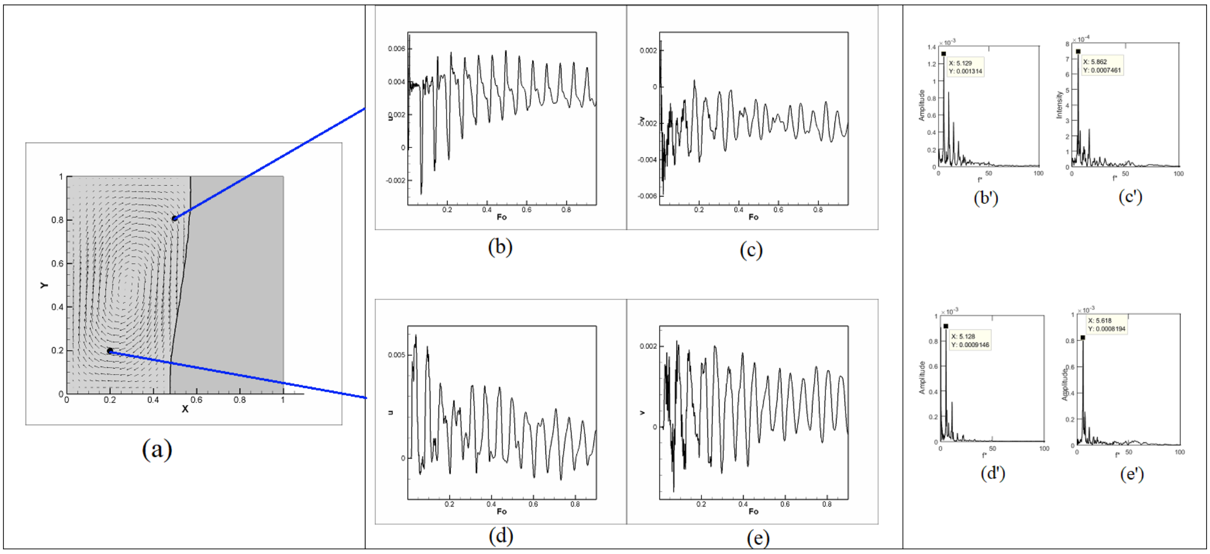

Figure 4.20: Time series plots of *u* and *v* velocity components with FFT analysis at *Pr*=0.005 and *Ra*=$10^5$ for position A (0.2, 0.2) and C (0.45, 0.8).

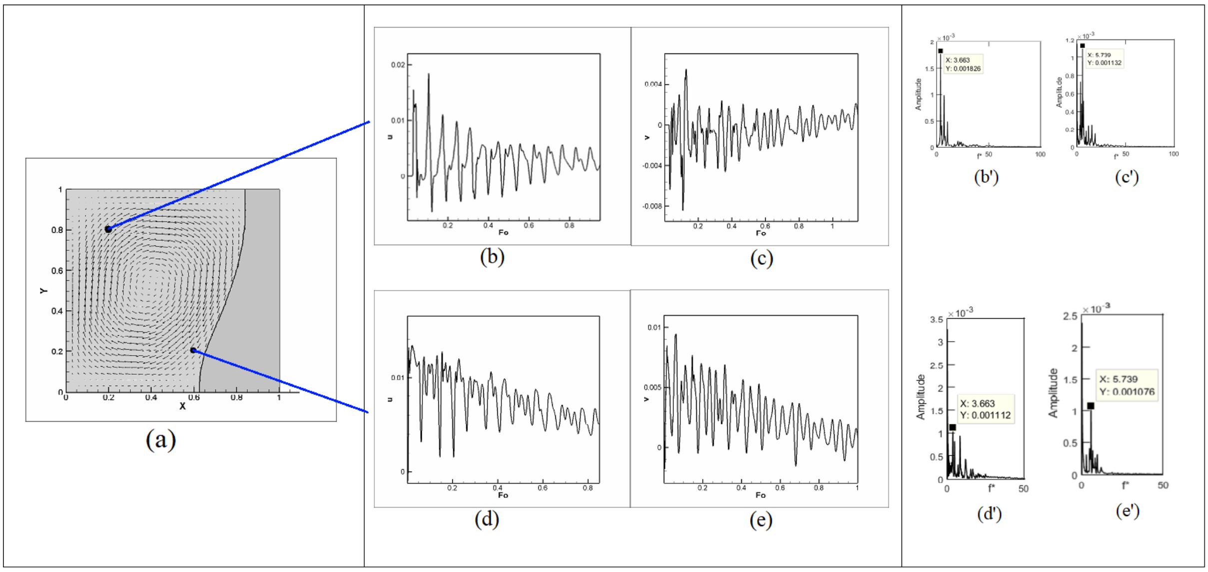

Figure 4.21: Time series plots of *u* and *v* velocity components with FFT analysis at *Pr*=0.005 and *Ra*=$10^5$ for position B (0.6, 0.2) and D (0.8, 0.8).

The melting boundary position changes with *Fo* and the flow behavior is presented in the effective melting area. Figure 4.20(a) represents the melting boundary at *Fo* =1.71 and oscillation nature is observed at the two fixed position in the melt zone. It is seen from Fig 4.21(b) that the pattern of flow oscillation is fractal by nature. The corresponding FFT plots are given in Fig. 4.21 (b') through (e'). The dimensionless peak frequencies for *Ra*=$10^5$ and *Pr*=0.005 are 5.129 and 5.862 respectively.

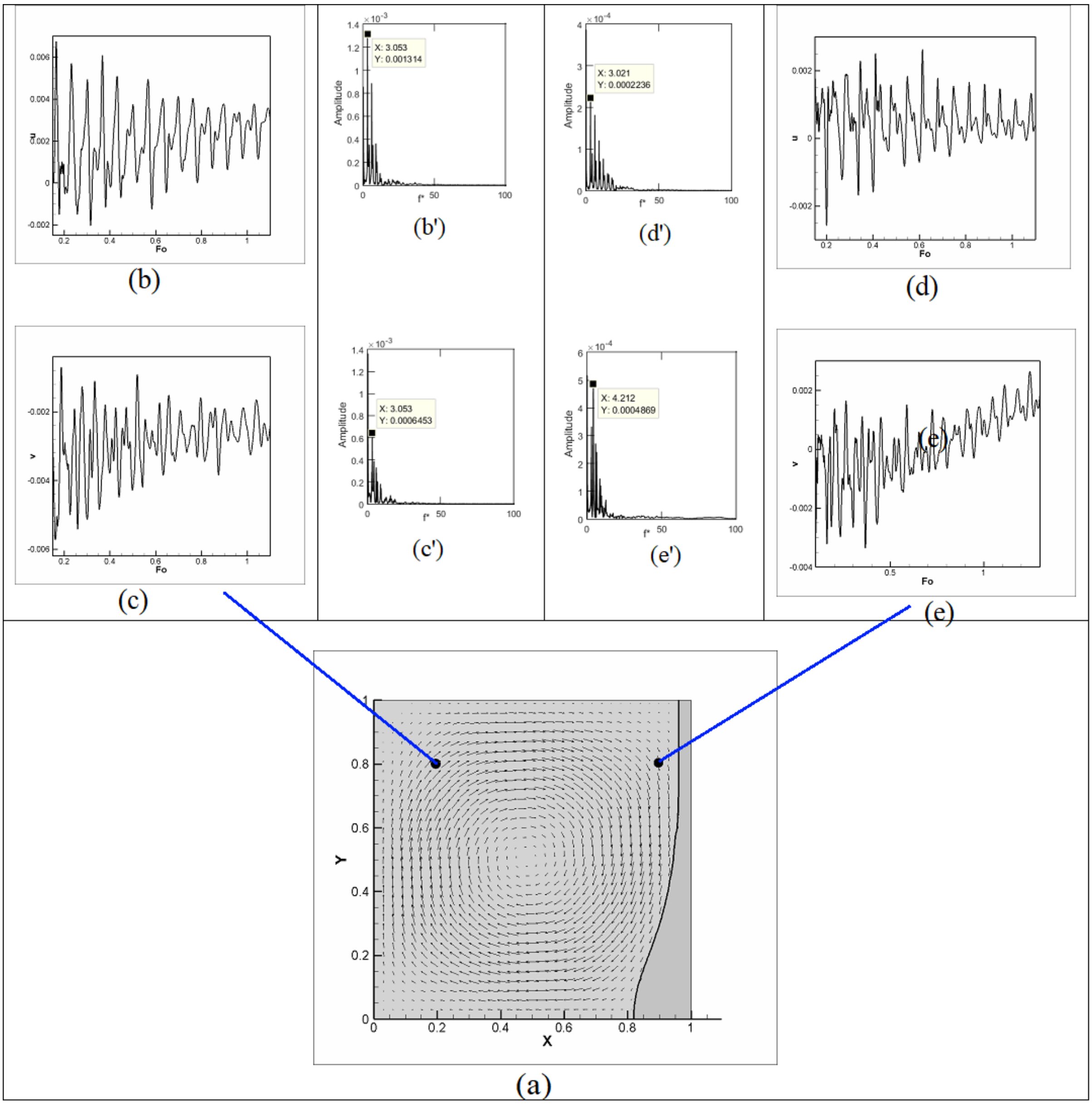

Figure 4.22: Time series plots of *u* and *v* velocity components with FFT analysis at *Pr*=0.005 and *Ra*=$10^5$ for position C (0.9, 0.8) and D (0.2, 0.8).

The time series plots of *u* and *v* velocity components are given in Fig. 4.23 through Fig. 4.25 for $Pr$=0.005 at $Ra$=$10^6$.

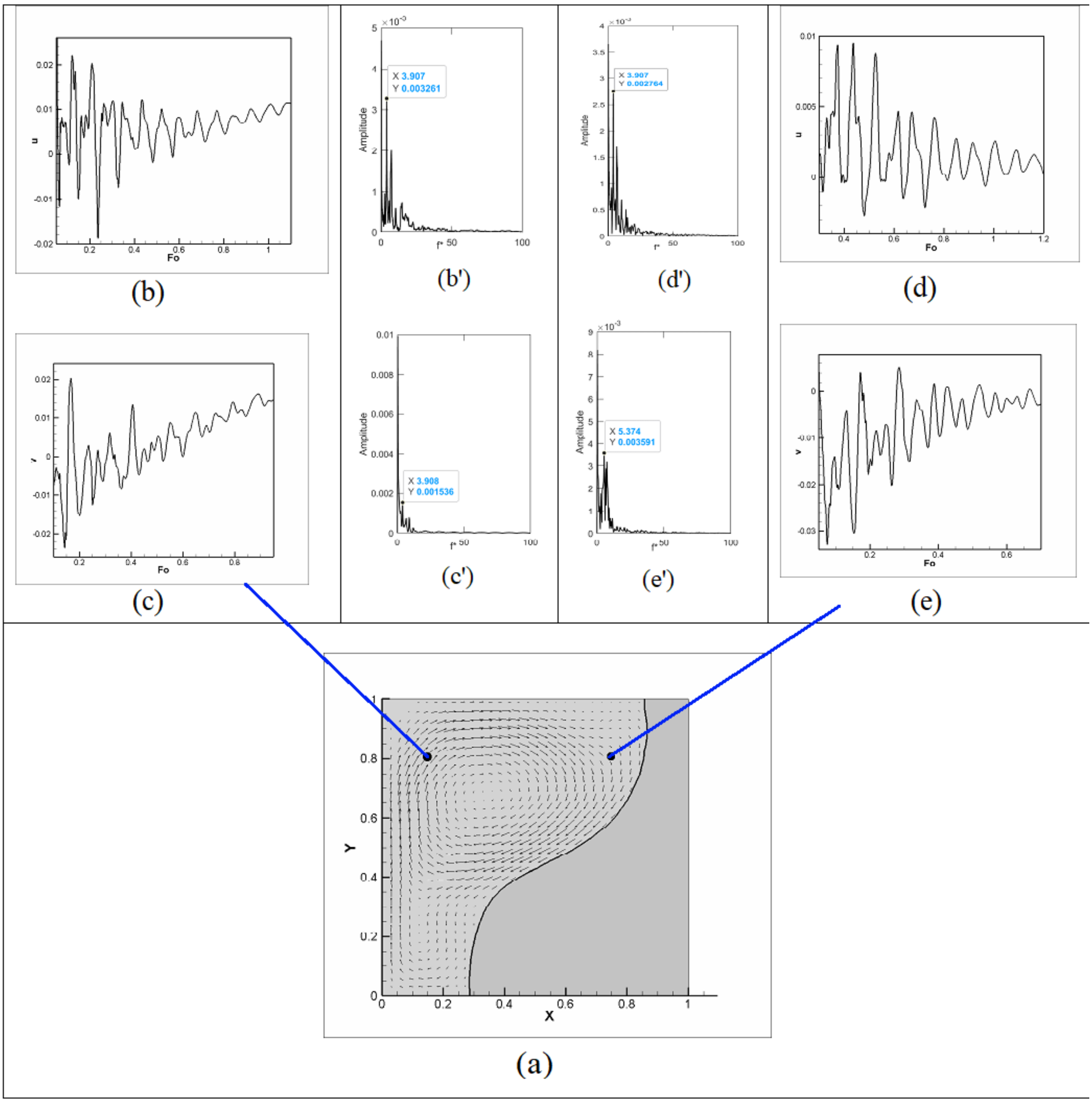

Figure 4.23: Time series plots of *u* and *v* velocity components with FFT analysis at $Pr$=0.005 and $Ra$=$10^6$ for position C (0.75, 0.8) and D (0.15, 0.8).

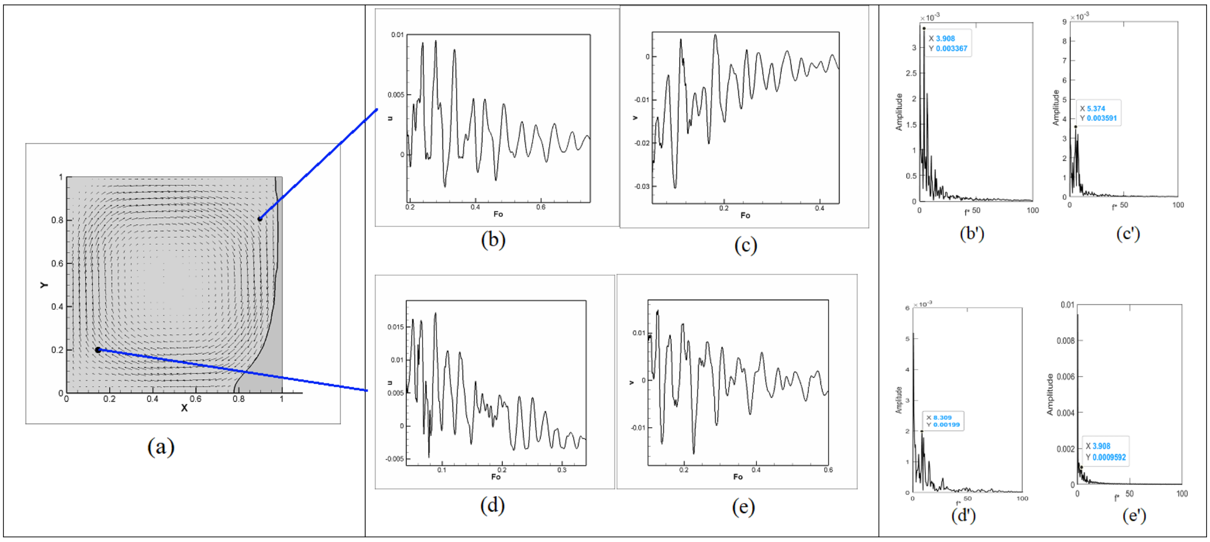

Figure 4.24: Time series plots of *u* and *v* velocity components with FFT analysis at *Pr*=0.005 and *Ra*=$10^6$ for position A (0.15, 0.2) and C (0.9, 0.8).

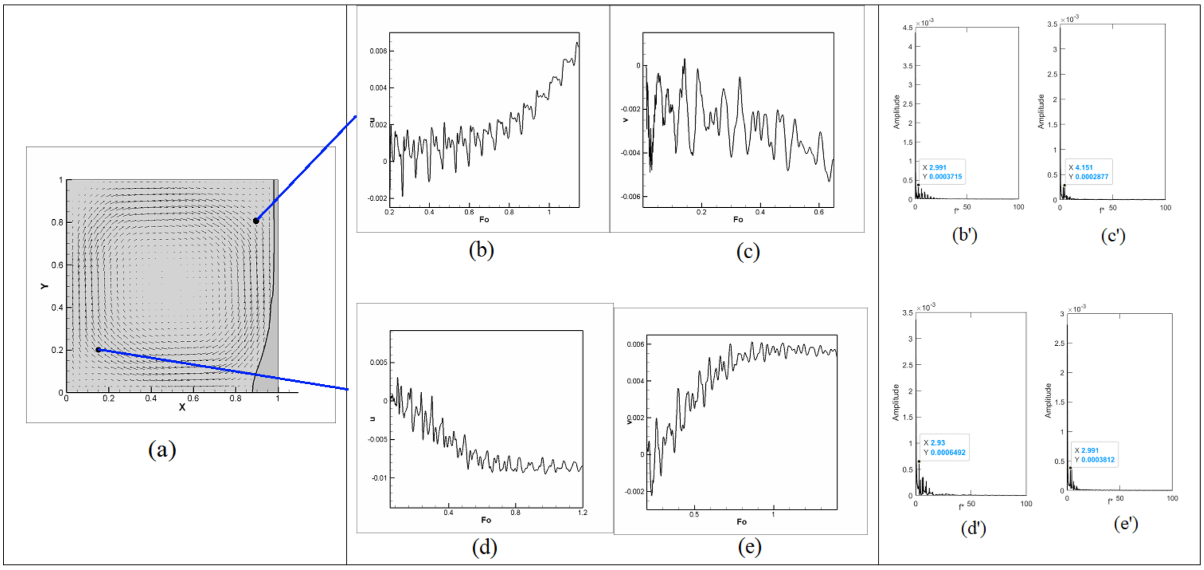

Figure 4.25: Time series plots of *u* and *v* velocity components with FFT analysis at *Pr*=0.005 and *Ra*=$10^6$ for position A (0.15, 0.8) and C (0.9, 0.8).

The FFT values for all plots from Figs. 4.20 through 4.25 are summarized in Table 4.3. It is observed from Table 4.3 that a higher peak frequency is observed for *u* and *v* component velocities at *Fo*=1.71 for *Ra*=$10^5$. As the melt area grows the primary frequency values decreases at fixed *Ra* for both *u* and *v* velocity component. At *Ra*=$10^6$ the *u* and *v* component frequency decreases with increment of melt zone.

Table 4.3: Peak frequencies at melted zone at *Pr* 0.005.

| | | ***Fo*=1.71** | | ***Fo*=2.42** | | ***Fo*=5.97** | |
|---|---|---|---|---|---|---|---|
| | | ***u*** | ***v*** | ***u*** | ***v*** | ***u*** | ***v*** |
| | **$Ra=10^5$** | 5.129 | 5.862 | 3.663 | 5.739 | 3.053 | 3.053 |
| | | 5.128 | 5.618 | 3.663 | 5.739 | 3.021 | 4.212 |
| ***Pr*=0.005** | | | | | | | |
| | | ***Fo*=1.55** | | ***Fo*=1.97** | | ***Fo*=9.71** | |
| | **$Ra=10^6$** | 3.907 | 3.908 | 3.908 | 5.374 | 2.991 | 4.151 |
| | | 3.907 | 5.374 | 3.309 | 3.908 | 2.93 | 2.991 |

At *Pr*=0.005 the flow field is isotropic and near isotropic for $Ra=10^5$ and $Ra=10^6$ at *Fo* ~ 2. With advancing time the flow field is homogeneous for $Ra=10^5$ at *Fo*=2.42 and at large *Fo*=5.97 the flow field is no longer homogeneous. At $Ra=10^6$ the flow non-homogenous as early as Fo~2.

The flow oscillation plots are given in Fig. 4.26 through Fig. 4.27 for *Pr*=0.02 at $Ra=10^5$.

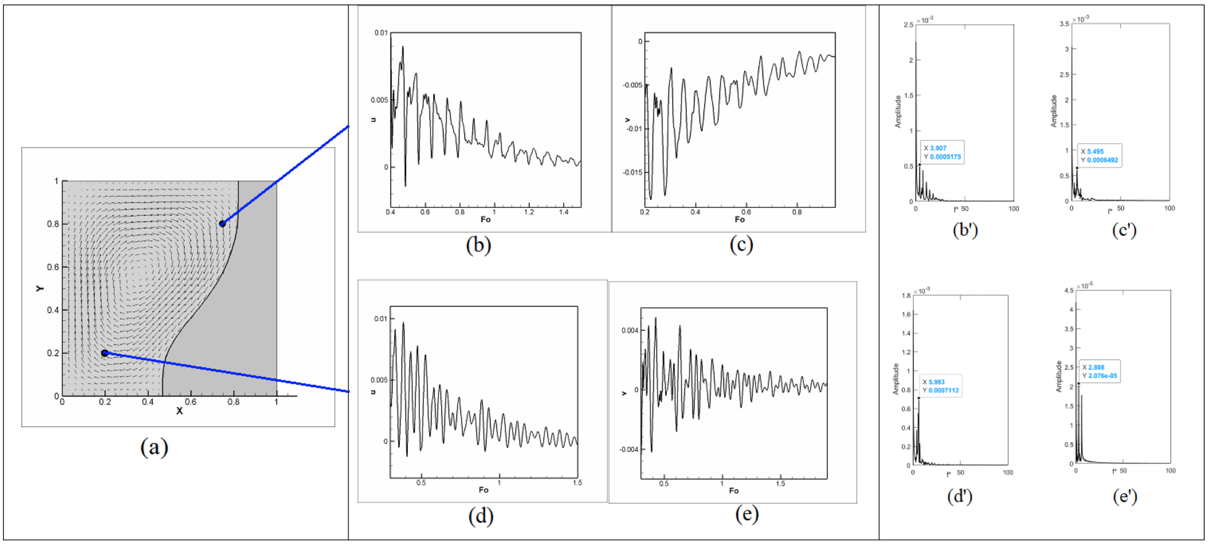

Figure 4.26: Time series plots of *u* and *v* velocity components with FFT analysis at *Pr*=0.02 and $Ra=10^5$ for position A (0.2, 0.2) and C (0.75, 0.8).

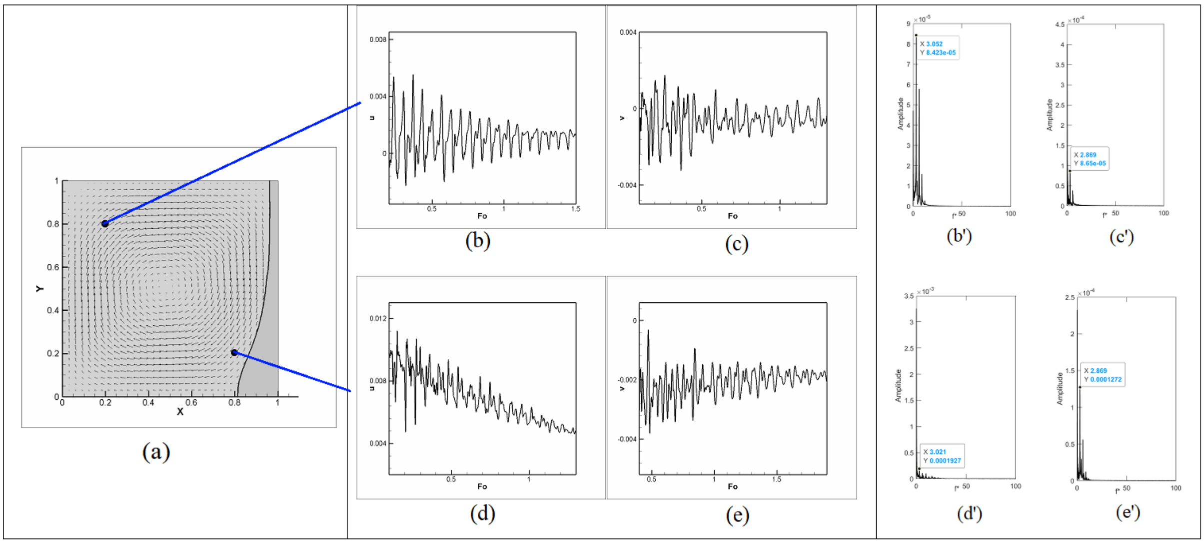

Figure 4.27: Time series plots of *u* and *v* velocity components with FFT analysis at *Pr*=0.02 and *Ra*=$10^5$ for position B (0.8, 0.2) and D (0.2, 0.8).

The time series plots of *u* and *v* components of velocity are given in Fig. 4.28 through Fig. 4.29 for *Pr*=0.02 at *Ra*=$10^6$.

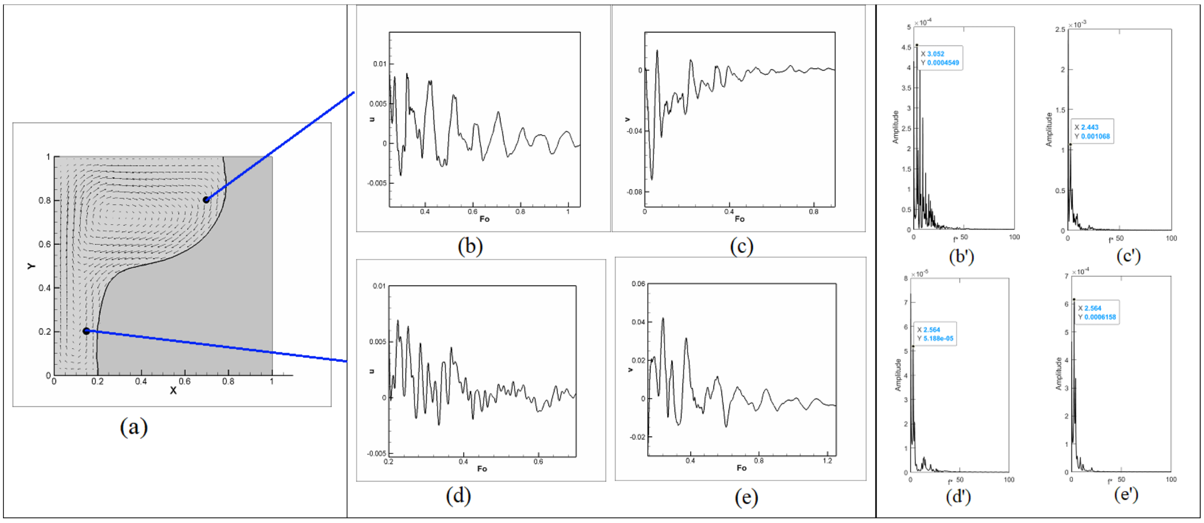

Figure 4.28: Time series plots of *u* and *v* velocity components with FFT analysis at *Pr*=0.02 and *Ra*=$10^6$ for position B (0.15, 0.2) and C (0.7, 0.8).

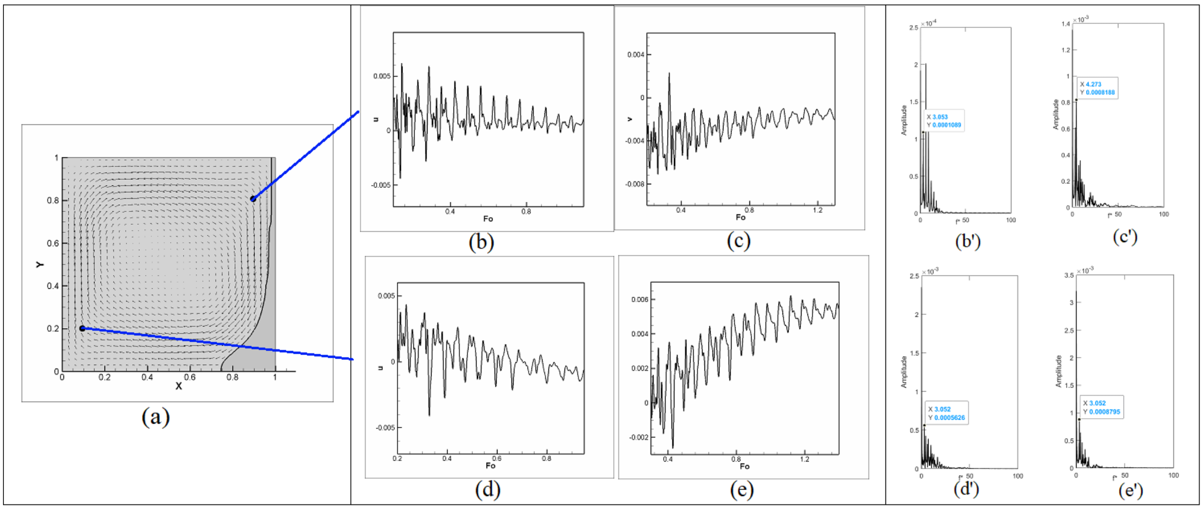

Figure 4.29: Time series plots of *u* and *v* velocity components with FFT analysis at *Pr*=0.02 and *Ra*=$10^6$ for position A (0.1, 0.2) and C (0.9, 0.8).

Table 4.4 represents the FFT values of *u* and *v* component velocities for *Pr*=0.02. It is seen from Table 4.4 that the *u* and *v* component frequency decreases with transient evaluation of time for both *Ra*=$10^5$ and *Ra*=$10^6$.

Table 4.4: Peak frequencies at melted zone at *Pr* 0.02.

| | | ***Fo*=5.97** | | ***Fo*=19.87** | |
|---|---|---|---|---|---|
| | | ***u*** | ***v*** | ***u*** | ***v*** |
| | | 3.907 | 5.495 | 3.052 | 2.896 |
| | ***Ra*=$10^5$** | 5.983 | 2.808 | 3.021 | 2.869 |
| ***Pr*=0.02** | | | | | |
| | | ***Fo*=4.97** | | ***Fo*=13.17** | |
| | | 3.052 | 2.443 | 3.053 | 4.273 |
| | ***Ra*=$10^6$** | 2.564 | 2.564 | 3.052 | 3.052 |

It is sown from Table 4.4 that, at *Pr*=0.02, the flow field is non-homogeneous at *Fo*~5 and the flow field is homogeneous and nearly homogenous for *Ra*=$10^5$ and *Ra*=$10^6$ at large elapse time *Fo* > 12. Initially non-uniformity of velocity and temperature appear in a shorter melt zone. The melted region grows with time and the velocity and temperature redistributed locally. The tendency to homogeneity observe as the perturbation is negligible for a large domain.

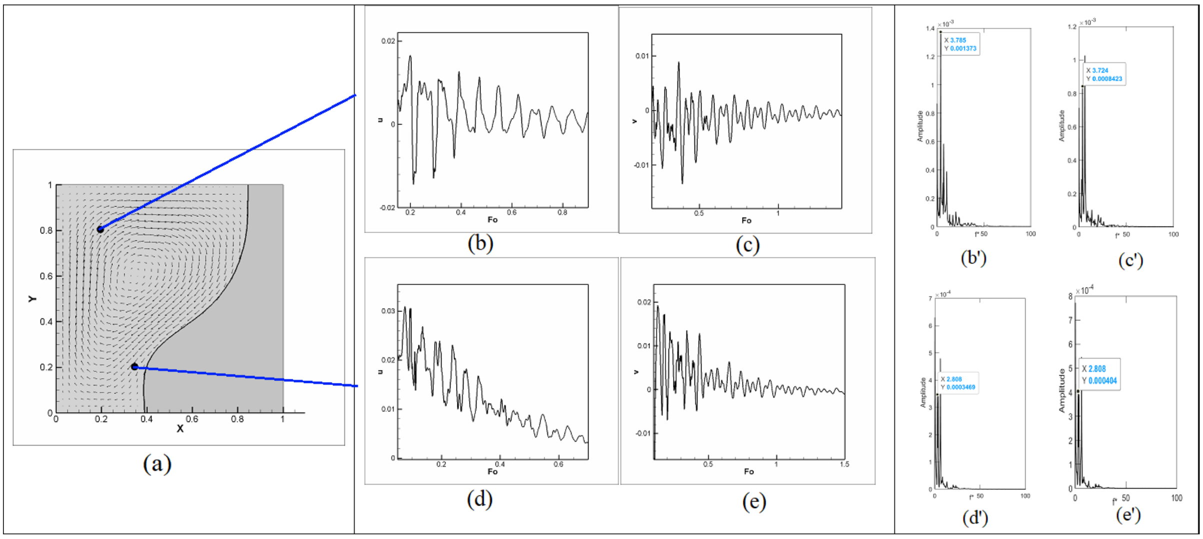

Figure 4.30: Time series plots of *u* and *v* velocity components with FFT analysis at *Pr*=0.05 and *Ra*=$10^5$ for position B (0.35, 0.2) and D (0.8, 0.8).

The flow oscillation plots are given in Fig. 4.30 through Fig. 4.31 for *Pr*=0.05 at *Ra*=$10^5$ while the flow oscillation plots are given in Fig. 4.32 through Fig. 4.33 for *Pr*=0.05 at *Ra*=$10^6$.

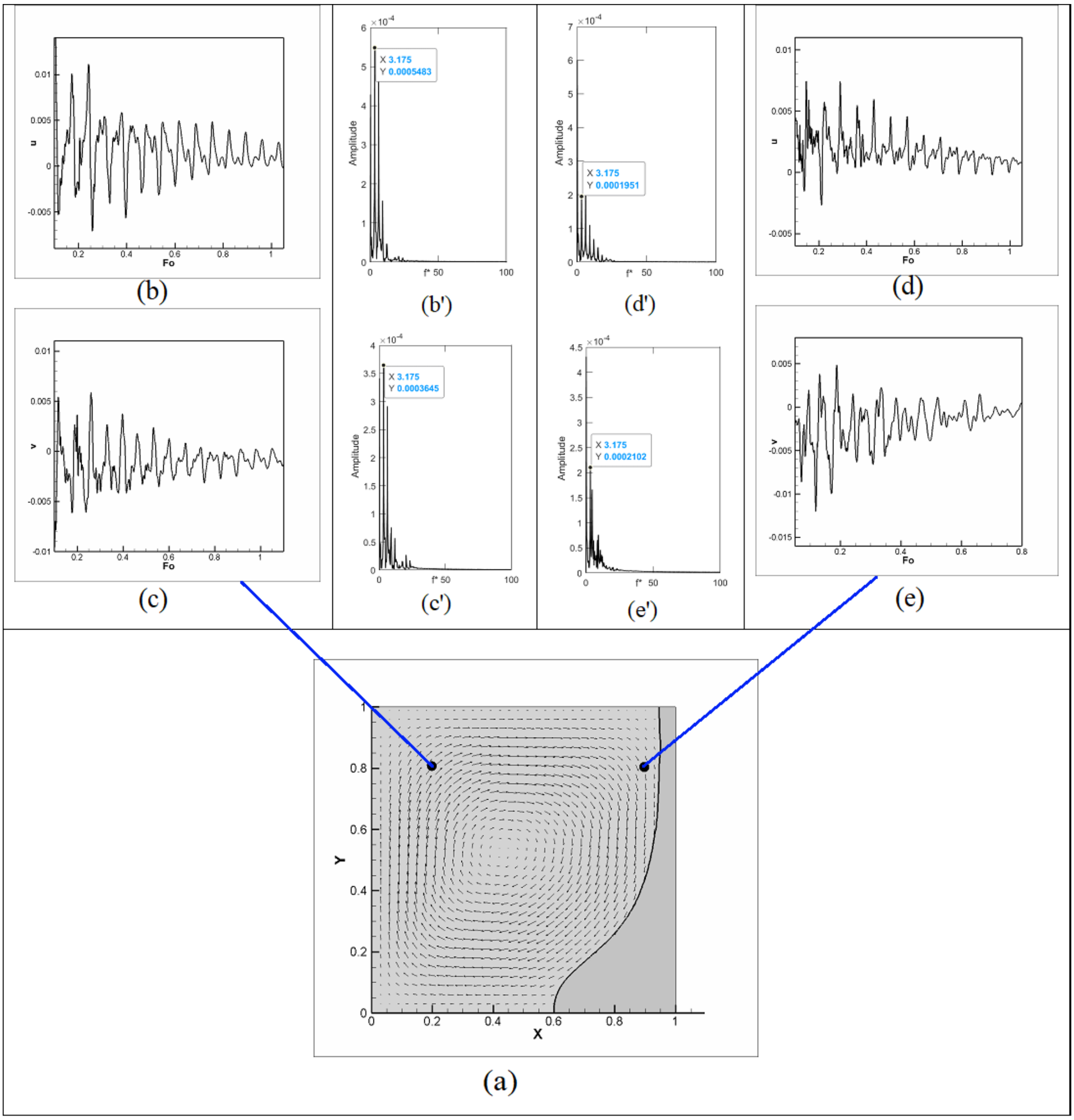

Figure 4.31: Time series plots of *u* and *v* velocity components with FFT analysis at *Pr*=0.05 and *Ra*=$10^5$ for position C (0.9, 0.8) and D (0.2, 0.8).

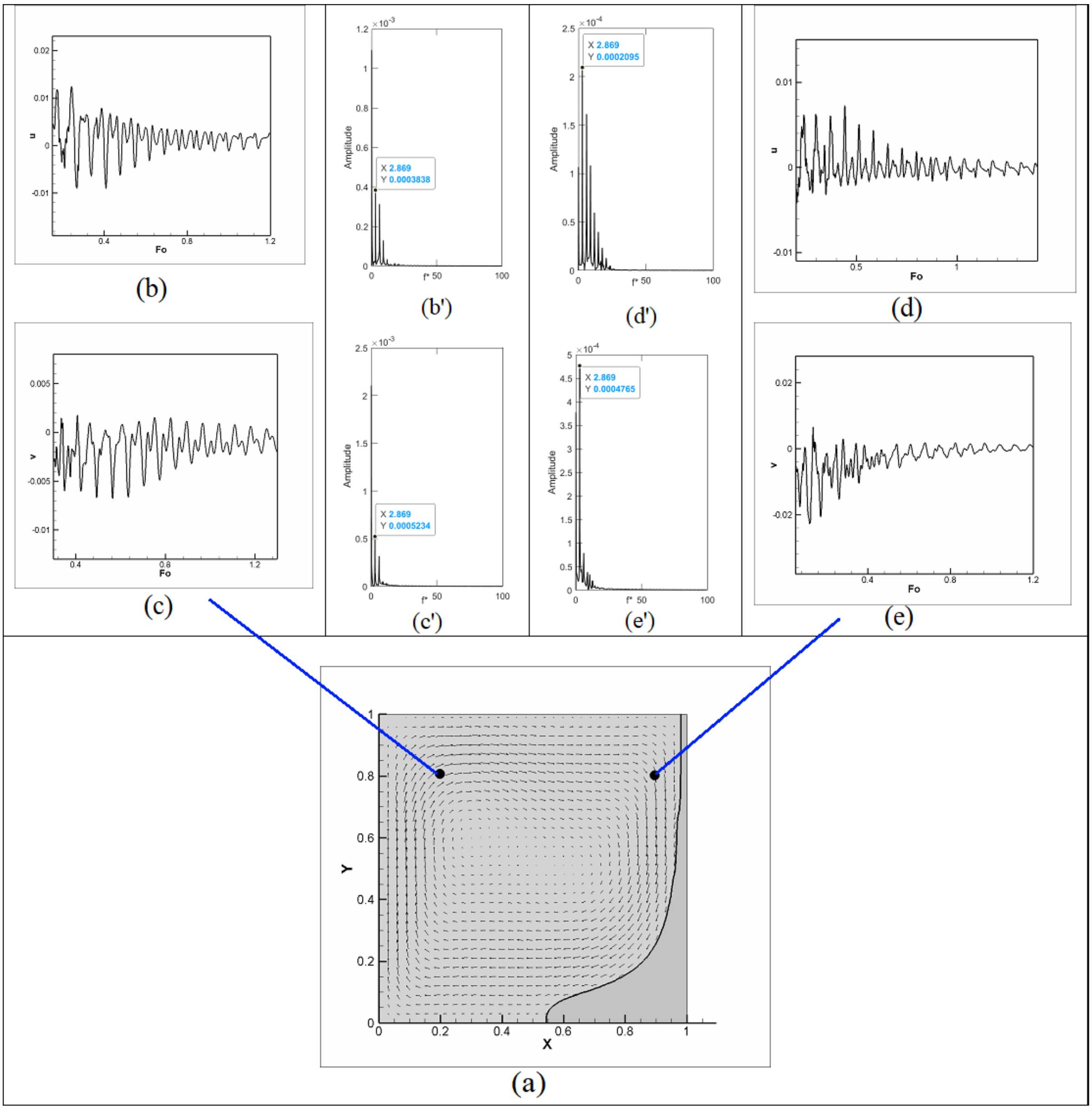

Figure 4.32: Time series plots of *u* and *v* velocity components with FFT analysis at *Pr*=0.05 and *Ra*=$10^6$ for position C (0.9, 0.8) and D (0.2, 0.8).

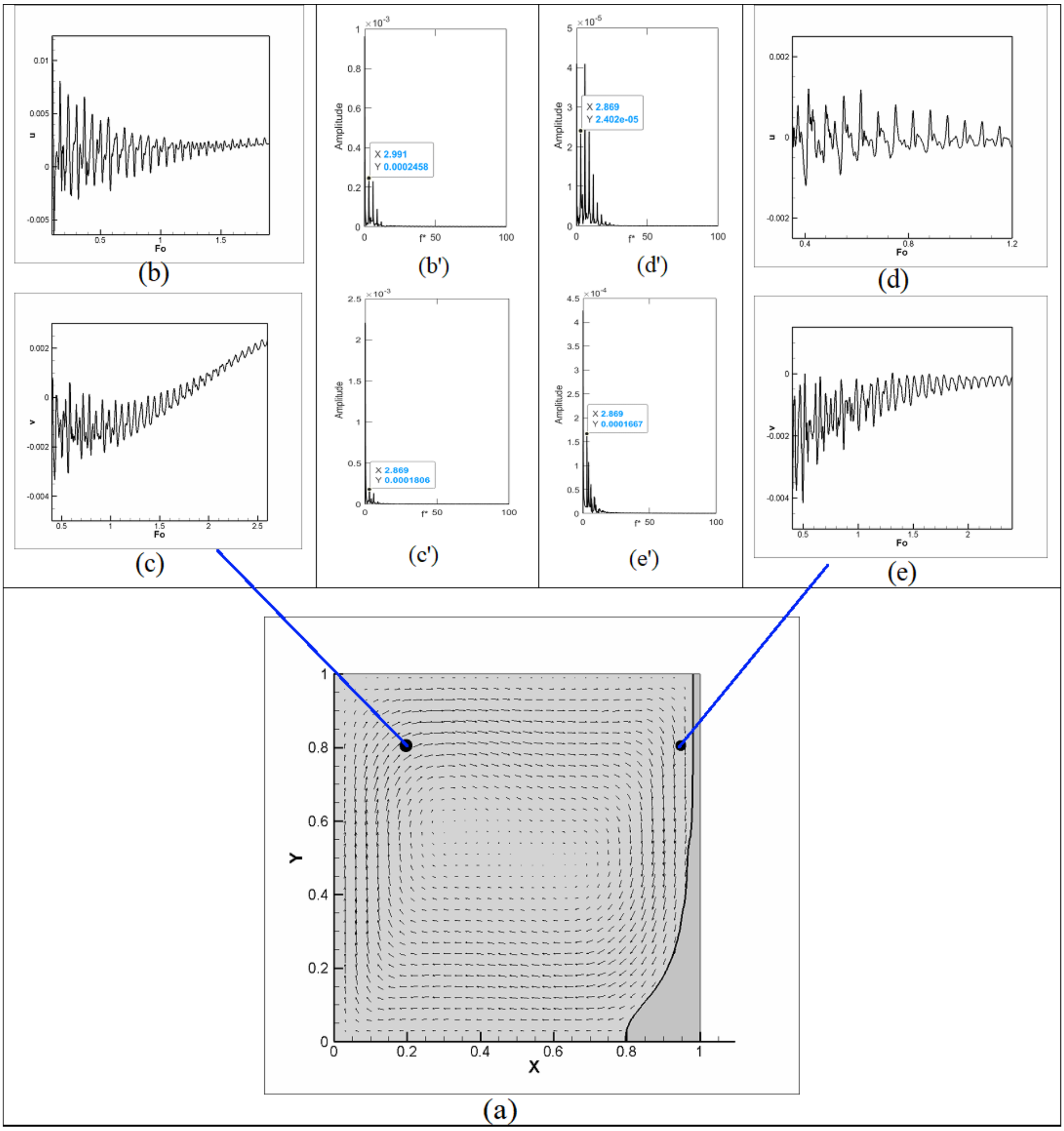

Figure 4.33: Time series plots of *u* and *v* velocity components with FFT analysis at *Pr*=0.05 and *Ra*=$10^6$ for position C (0.95, 0.8) and D (0.2, 0.8).

Similarly, Table 4.5 represents the FFT values of *u* and *v* component velocities for *Pr*=0.05. It is seen from Table 4.4 that the *u* and *v* component frequency decreases with transient evaluation of time for both *Ra*=$10^5$ and *Ra*=$10^6$. The *u* and *v* values are similar for *Ra* $10^5$ and *Ra* =$10^6$. For Pr=0.02, dominant frequency is about 3.2 at all time. However the frequency corresponding to *v* component changes in time. A peak frequency value *u*~*v* indicates an isotropic field.

Table 4.5: Peak frequencies at melted zone at *Pr* 0.05.

| | | ***Fo*=19.07** | | ***Fo*=27.16** | |
|---|---|---|---|---|---|
| | | ***u*** | ***v*** | ***u*** | ***v*** |
| | | 3.785 | 3.724 | 3.175 | 3.175 |
| | ***Ra*=$10^5$** | 2.808 | 2.808 | 3.175 | 3.175 |
| ***Pr*=0.02** | | | | | |
| | | ***Fo*=14.73** | | ***Fo*=19.71** | |
| | | 2.869 | 2.869 | 2.991 | 2.869 |
| | ***Ra*=$10^6$** | 2.869 | 2.869 | 2.869 | 2.869 |

It is observed from Table 4.5 that, unlike the cases of relatively low *Pr* (0.005 and 0.02) at *Pr*=0.05 the flow field is homogeneous till *Fo* about 20 and isotropic at *Fo*~25 at *Ra*=$10^5$. At *Ra* =$10^6$ the flow is isotropic at *Fo*>10. Thus it is observed that reducing *Pr* leads to higher level of flow instability.

## Kinetic Energy Density ($K_{ED}$)

The kinetic energy density of the fluid domain is defined by

$$K_{ED} = \frac{1}{V_m} \int_{V_m} \mathbf{u}^2 dV \tag{4.9}$$

where, $V_m$ is volume of melt zone. The kinetic energy density is calculated in the melted regime using Eq. 4.9. For the square cavity formulation, the length of the cavity is related with the cavity area as,

$$L = A^{0.5} \tag{4.10}$$

The melted area is thus related to liquid fraction as

$$A_{melt} = f_l A \tag{4.11}$$

While the melted zone may have irregular boundaries, the effective length of the melted area can be related with the liquid fraction as

$$\begin{aligned} L_{eff} &= \sqrt{A_{melt}} \\ &= \sqrt{f_l A} \\ &= f_l^{1/2} L \end{aligned} \tag{4.12}$$

From the definition of Rayleigh number,

$$Ra \propto L^3 \tag{4.13}$$

An effective Rayleigh number is introduced now which is related with the length of the cavity as

$$Ra_{eff} \propto f_l^{3/2} L^3 \tag{4.14}$$

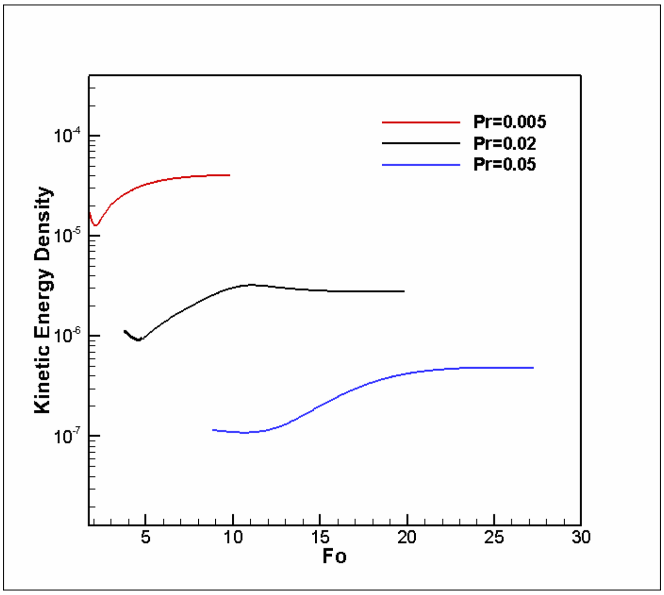

(a)

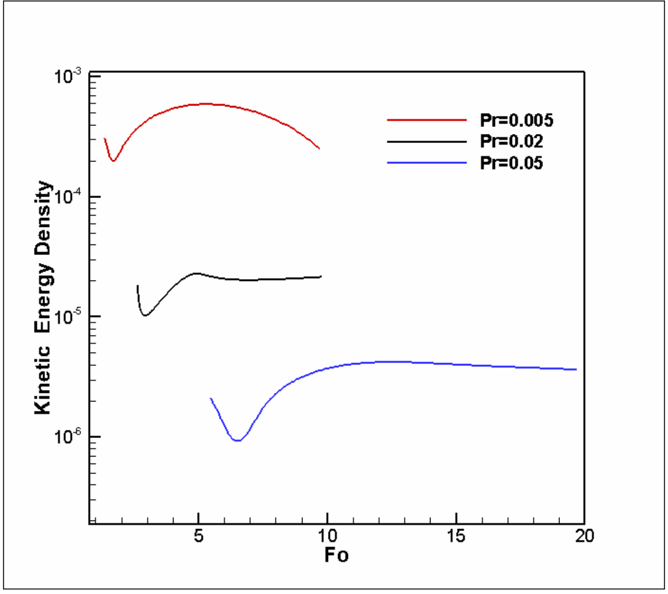

(b)

Figure 4.34: Kinetic energy density of low Prandtl number liquid metals a) $Ra=10^5$ and b) $Ra=10^6$.

The effective Rayleigh number is now expressed as a function of domain Rayleigh number ($Ra$) and liquid fraction as,

$$Ra_{eff} \propto f_l^{3/2} Ra \tag{4.15}$$

In Fig. 4.34, evolution of kinetic energy density along time is shown at different *Pr*. It is observed that the kinetic energy density ($K_{ED}$) increases with decreasing *Pr*. A low *Pr* indicates lower viscosity of fluid which leads to stronger fluid movement and hence higher kinetic energy density. At $Ra=10^5$ and $10^6$, $K_{ED}$ initially reduces and then goes on increasing for all *Pr*. It is seen from Fig. 4.34 (a) and (b) that kinetic energy density initially decreases then increases because initially local energy absorption occurs for phase transition of solid to liquid and as the melted zone grows the phase transition is well underway in the liquid state increase the kinetic energy density increases. It is to be noted that the kinetic energy density data is quite similar in a range of magnitude $10^{-4}$ -$10^{-8}$ with prior work (Favier et al., 2019). The effective Rayleigh number ($Ra_{eff}$) is tabulated in Table 4.6 for two situations. The first one is when the kinetic energy density is minimum in the domain. The second one related to when $K_{ED}$ attains the maximum value. In all cases the kinetic energy density remains constant after attaining the peak except for the case of $Ra=10^6$ and $Pr=0.005$. The attainment of peak $K_{ED}$ corresponds to $Ra_{eff}$~ 9x$10^4$ and $Ra_{eff}$ ~ 9x$10^5$ for *Ra* of $10^5$ and $10^6$ respectively.

Table 4.6: Effective Rayleigh number corresponding to minimum and maximum kinetic energy density at $Ra=10^5$ and $10^6$ for different *Pr*.

| **Prandtl Number (*Pr*)** | **Effective Raleigh Number ($Ra_{eff}$)** | | | |
|---|---|---|---|---|
| | **$Ra=10^5$** | | **$Ra=10^6$** | |
| | Minimum $K_{ED}$ | Maximum $K_{ED}$ | Minimum $K_{ED}$ | Maximum $K_{ED}$ |
| **0.005** | 40789.07 | 92956.62 | 472112.43 | 952930.96 |
| **0.02** | 23158.19 | 92051.17 | 122383.74 | 942195.08 |
| **0.05** | 27909.86 | 84925.74 | 94318.7 | 932676.645 |

Table 4.6 shows that the near stable kinetic energy density has been observed at an order of magnitude of $Ra_{eff}$~ $10^5$ for both $Ra=10^5$ and $10^6$.irrespective of *Pr*. However, the effective *Ra* for the minimum kinetic energy density varies with *Pr* and the variation with *Pr* for $Ra=10^5$ shows a large difference compared to the $Ra=10^6$.

### *Root-Mean-Square velocity* ($U_{RMS}$) *at Melt Zone*

An interesting observation has been found considering the root-mean-square velocity ($U_{RMS}$) in the growing melt zone. Calculation of $U_{RMS}$ is a statistical measurement which provides an insight about melt flow. $U_{RMS}$ is calculated as

$$U_{RMS} = \sqrt{\frac{1}{V_m} \int_{V_m} \left(u^2 + v^2\right) dV} \tag{4.16}$$

where $V_m$ denotes the volume of melt zone.

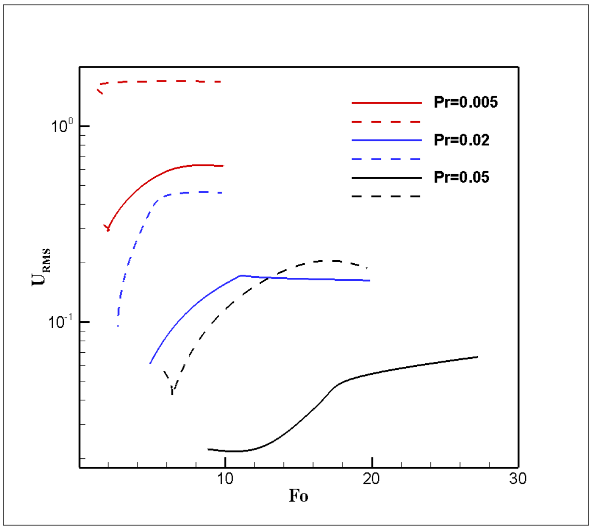

Figure 4.35: RMS velocity in the melt zone for different *Pr* liquid metal. Solid line represents root-mean-square velocity at *Ra*=$10^5$ while dashed line indicates at *Ra*=$10^6$.

Fig. 4.35 depicts distribution of $U_{RMS}$ over time in the melt zone for different *Pr*. Investigation of $U_{RMS}$ for different *Ra* has been performed in which solid and dashed lines are used for *Ra*=$10^5$ and *Ra*=$10^6$ respectively. It is seen from Fig. 4.35 that reducing the *Pr* value $U_{RMS}$ increases which ensure the flow instability at low *Pr*.

### *Rate of Entropy Generation*

The rate of entropy generation has been investigated for melt flow in which the total volumetric entropy generation ($s'_{Total}$) is summation of viscous and thermal dissipation. The total volumetric entropy generation is written as

$$S'_{Total} = S_f + S_{th} \tag{4.17}$$

where $S_f$ is entropy generation for fluid flow and $S_{th}$ is entropy generation for thermal dissipation. The entropy generation for fluid flow ($S_f$) can be expressed as (Herpe et al., 2009)

$$S_f = \frac{\mu}{T}\left[2\left\{\left(\frac{\partial u}{\partial x}\right)^2 + \left(\frac{\partial v}{\partial y}\right)^2\right\} + \left(\frac{\partial u}{\partial y} + \frac{\partial v}{\partial x}\right)^2\right] \tag{4.18}$$

Similarly, second term in Eq. 4.17 is the rate of entropy generation due to heat transfer is given as (Herpe et al., 2009)

$$S_{th} = \frac{K}{T^2}\left[\left(\frac{\partial T}{\partial x}\right)^2 + \left(\frac{\partial T}{\partial y}\right)^2\right] \tag{4.19}$$

The rate of local total entropy generation in the effective melt volume can be calculated integrating all the local distributions which can be stated as

$$S_{Total} = \int_{V_f} S'_{Total}\, dV \tag{4.20}$$

Figure 4.36 represents the total rate of entropy generation with evolution of time at different *Ra*. It is seen from form both figures that the total rate of entropy generation initially increases and then stabilizes.

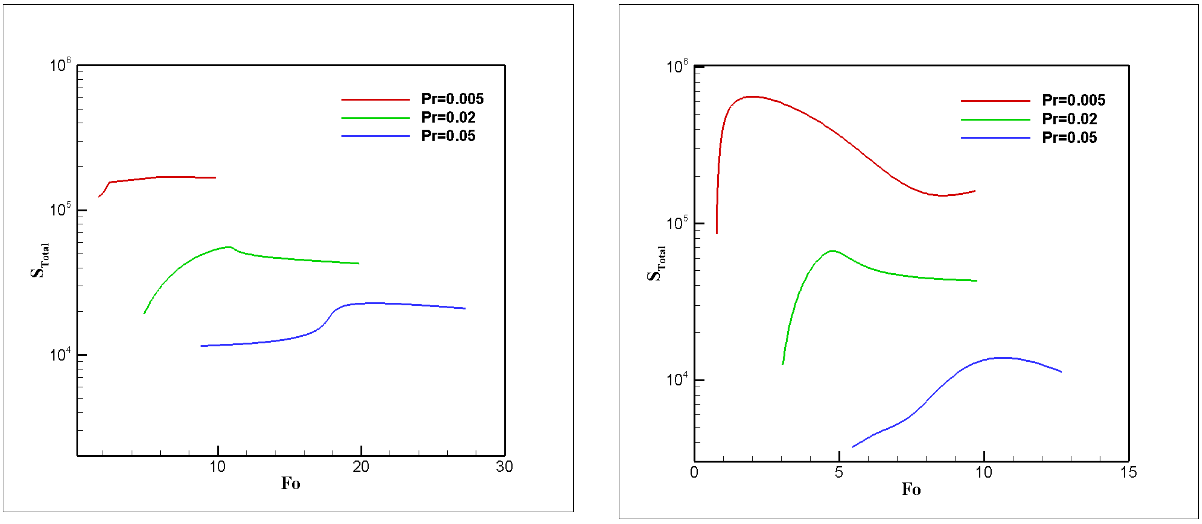

(a) (b)

Figure 4.36: Total entropy generation $S_{Total}$ in the growing melt zone a) *Ra*=$10^5$ and b) *Ra*=$10^6$.

The prior investigation confirms the slow rate of change of melt volume at the end of melting, which enables the stabilization of entropy generation even while the rate of entropy development varies. Figure 4.36 (a) through (b) depict with the decrease of *Pr* total entropy generation is higher which also support the flow instability phenomena for very low *Pr* liquid metals. It is also seen that, $S_{Total}$ is higher for high *Ra* ($Ra=10^6$) for $Pr=0.005$ while the change of total entropy generation is not much different for a range of *Pr* =0.02 to 0.05.

Investigation reveals that, heat transfer predominates in the overall total rate of entropy formation, with viscous dissipation contributing very little. The ratio of thermal entropy generation $(S_{th})$ and maximum thermal entropy generation $(S_{th,\max})$ has been plotted in Fig. 4.37. Highly efficient heat transfer with a minimum dissipation has been found in the melt zone and it varies with *Pr*. Thermal perturbation in the flow field ensures the irreversibility effect in the growing melt zone which is shown in Fig. 4.37 (a) through (b) for different *Ra*.

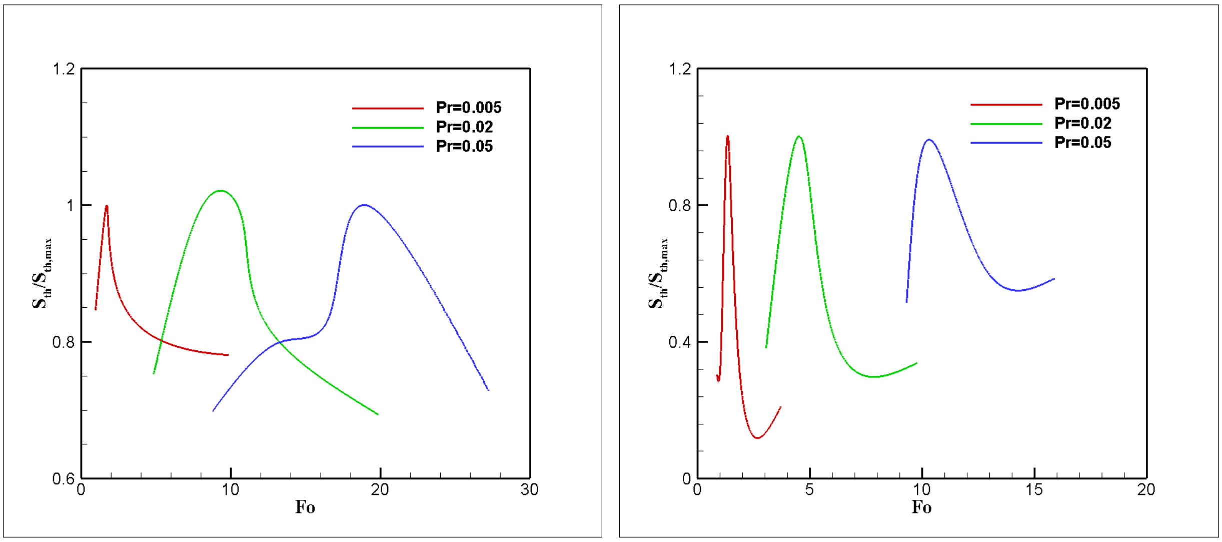

(a) (b)

Figure 4.37: Evolution of the ratio of thermal entropy generation and maximum thermal entropy generation $\left({S_{th}}/{S_{th,\max}}\right)$ in the melt zone over time a) $Ra=10^5$ and b) $Ra=10^6$.

## 4.3 Closure

The present work reports development of a lattice Boltzmann model to overcome the numerical instability associated in handling convection in ow *Pr* fluids. The stability of relaxation parameter is improved using a tunable parameter $A'$ in the modified relaxation parameter $\tau_f'$. Prandtl number is related with the relaxation parameters for flow and energy. The model is used successfully to study melting dynamics in a square cavity for $Pr \in [0.001, 0.1]$ and $Ra \in [10^4, 10^6]$. Important finding observed are summarized below:

As increasing the value of *Pr* indicates reduced thermal diffusivity an important consequence is the melt flow patterns at a particular instance at low *Pr* is realized at later time for higher Pr. For $Pr \in (0.001, 0.01)$ at high *Ra,* with progress of time as melt zone becomes larger the formation of two lobes appear at the canter of primary cell which tends to separate from each other. The interface length is found to reduce with increasing *Fo* and *Ra*.

The maximum interface length during the entire melting process is found to be nearly independent of *Fo* and *Ra* at low *Pr* of 0.001. However, at *Pr* of 0.01 and 0.1, the maximum interface length reduces with *Fo* and *Ra*. The mapping of maximum interface size with *Bo* is also performed in this work.

The velocity components show several oscillation patterns which is quantifies using FFT analysis. The flow instability in the melt zone shows a capacitive nature with the growth of melt zone. The *v* component oscillation frequency is more compared to *u* component oscillating frequency up to $Pr=0.02$ and both frequencies are nearly similar for $Pr=0.05$. The kinetic energy density in the melt zone initially decreases and then increases for $Ra=10^5$ and $10^6$ irrespective of *Pr*. The kinetic energy density increases with decreasing Prandtl number for Rayleigh number $10^5$ and $10^6$. The effective Rayleigh number for minimum kinetic energy density decreases with increasing of Prandtl number for $Ra=10^6$. The value of root-mean-square velocity ensures the flow instability for low *Pr* liquid metals ($Pr=0.005$) is higher compared to a range of $Pr=0.02$ to 0.05. Viscous dissipation makes up very little of the total rate of entropy generation while heat transfer dominates. The total rate of entropy generation confirms the irreversibility in the melt flow for low *Pr* liquid metals.

# CHAPTER 5

# CORNER MELTING AND SOLIDIFICATION

The present chapter comprises of the thermo-fluidic effect in corner melting followed by thermal effect in corner solidification process. Total enthalpy based lattice Boltzmann method is used to simulate corner melting and solidification problems. In the last part of the chapter the work is extended by the study of corner melting of very low Pr liquid metals using modified lattice Boltzmann method.

## 5.1Corner Melting in Closed Cavity

### 5.1.1 Objective of the Work

Numerical investigation of melting phenomena of low Prandtl number materials in a square cavity with two adjacent heated walls has been carried out using total enthalpy based lattice Boltzmann method (ELBM). The influence of natural convection in the melt zone has been observed for two different cases: i) heating from the left and the bottom walls and ii) heating from the top and the right walls. The effect of Rayleigh number in the range of $Ra=10^2$ -$10^7$ on the convective flow field is evaluated for a typical parametric values of Stefan number of 0.01 and Prandtl number of 0.025.

### 5.1.2 Problem Statement

In this work, a two dimensional square cavity filled with pure substance undergoing corner melting is investigated. The cavity (length L= width W) initially contains a solid material uniformly at its melting temperature ($T_m$). The heated side temperatures ($T_h$) are maintained higher than melting temperature ($T_m$). Two different situations of corner melting have been studied. Figure 5.1(a) and (b) represent corner melting from two opposite corners of two cases. Figure 5.1(a) and (b) displays the side walls temperature as boundary conditions in which heated sides are set at $T_h$=1 and melting temperature is set at $T_m$=0.

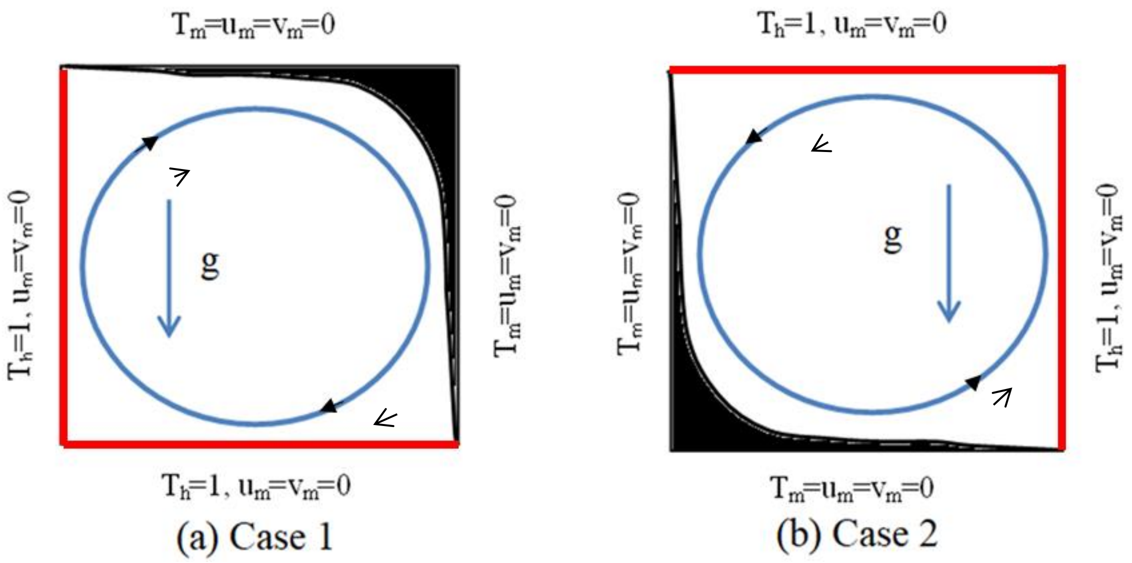

Figure 5.1: Square cavity with walls boundary conditions in which interface separates solid-liquid phases. Red color indicates hot wall boundaries. Velocity and temperature boundary conditions are shown at all wall boundaries. $u_m$ and $v_m$ are the $x$ and $y$ component velocities while $T_h$ and $T_m$ are hot and cold wall temperatures respectively. Blue arrow indicates the direction of gravitational force in the melt zone. Melt zone is covered with blue streamline in which black arrow indicates the flow direction. (a) corner melting heated from bottom ($\nabla\rho_m \times g \neq 0$ between side walls, $\nabla\rho_m \times g = 0$ between top-bottom walls in which $\nabla\rho_m$ is opposite to $g$) (b) corner melting heated from top ($\nabla\rho_m \times g \neq 0$ between side walls, $\nabla\rho_m \times g = 0$ between top-bottom walls in which $\nabla\rho_m$ is parallel to $g$).

Due to the differentially side heated wall temperatures; thermal gradients are same for both cases. The top-bottom walls temperature gradient and the direction of gravity are parallel but opposite to each other for case 1 while the temperature gradient and the direction of gravity are parallel with same direction. Thus case 1 and case 2 refer to ‘corner melting heated from bottom’ and ‘corner melting heated from top’ respectively. Arrow in Fig. 5.1 indicates the direction of gravitational acceleration in melted zone and all walls are at no-slip condition. It may be mentioned here that there exists no fundamental physical difference between top right and top-left heated cases as well as for bottom-left or bottom-right heated walls. In this study, the value of *Pr* is taken as 0.025. Several studies on melting in the range of *Pr* between 0.02-0.025 albeit not on corner solidification (Dai et al., 2018; Hasan and Saha, 2021b; Rui et al., 2020b). The value of *Pr* is applicable to material such as mercury, lead and lithium. The value of Stefan number *Ste* is fixed at 0.01 which has been widely used in prior works (Dai et al., 2018; Hasan and Saha, 2021b; Huang et al., 2013b; Q. Liu et al., 2022; Rui et al., 2020b).

The main concern of the present work is to investigate the effect of natural convection in the melt zone of a low Prandtl number (*Pr*) fluid and analyse the hot wall average heat flux which pronounces melting.

### 5.1.3 Mathematical Model Formulation

The simulation has been performed assuming the flow inside the cavity is incompressible in nature, thermo-physical properties of the material are constant, viscous dissipation is neglected and Boussinesq approximation has been considered in the melt zone. The governing equations of continuity equation, momentum equation and energy equation are already covered in section 4.1.3.

The initial condition is fixed assuming the cavity is filled with the solid at the melting temperature.

Initial condition:

$$\text{at } t=0,\quad \mathrm{u_m}=\mathrm{v_m}=0,\ \mathrm{T}=T_m \ \text{ for } 0\le x\le L \text{ and } 0\le y\le W \tag{5.1}$$

Boundary conditions are different for two cases of heating. The boundary conditions are applicable at $t>0$. It may be noted that while for the first case the bottom and left walls are at higher temperature, for the second case, high temperature is imposed on the right and the top walls.

<u>for case 1</u>

$$\left.\begin{aligned}
&\mathrm{u_m}=\mathrm{v_m}=0,\ \mathrm{T}=T_h \ \text{ for } x=0 \text{ and } 0\le y\le W\\
&\mathrm{u_m}=\mathrm{v_m}=0,\ \mathrm{T}=T_h \ \text{ for } y=0 \text{ and } 0\le x\le L\\
&\mathrm{u_m}=\mathrm{v_m}=0,\ \mathrm{T}=T_m \ \text{ for } x=L \text{ and } 0\le y\le W\\
&\mathrm{u_m}=\mathrm{v_m}=0,\ \mathrm{T}=T_m \ \text{ for } y=W \text{ and } 0\le x\le L
\end{aligned}\right\} \tag{5.2a}$$

<u>For case 2</u>

$$\left.\begin{aligned}
&\mathrm{u_m}=\mathrm{v_m}=0,\ \mathrm{T}=T_h \ \text{ for } x=L \text{ and } 0\le y\le W\\
&\mathrm{u_m}=\mathrm{v_m}=0,\ \mathrm{T}=T_h \ \text{ for } y=W \text{ and } 0\le x\le L\\
&\mathrm{u_m}=\mathrm{v_m}=0,\ \mathrm{T}=T_m \ \text{ for } x=0 \text{ and } 0\le y\le W\\
&\mathrm{u_m}=\mathrm{v_m}=0,\ \mathrm{T}=T_m \ \text{ for } y=0 \text{ and } 0\le x\le L
\end{aligned}\right\} \tag{5.2b}$$

The dimensionless numbers are used in the present work are

$$\mathrm{T}^* = \frac{T - T_m}{T_h - T_m}, \quad \mathbf{x}^* = \frac{\mathbf{x}}{W}, \quad \mathbf{y}^* = \frac{\mathbf{y}}{W}, \quad Pr = \frac{\nu}{\alpha}$$

$$Ra = \frac{\mathbf{g}\beta \Delta T W^3}{\nu\alpha}, \; Ste = \frac{c_p \Delta T}{\lambda} \text{ and } Fo = \frac{\alpha t}{W^2} \tag{5.3}$$

where $\mathrm{T}^*$ is dimensionless temperature, $\mathbf{x}^*$ and $\mathbf{y}^*$ are the dimensionless coordinates at $x$ and $y$ direction respectively. $\nu$ is kinematic viscosity, $\alpha$ is thermal diffusivity and $t$ is time. $\mathrm{Pr}$, $Ra$, $Ste$ and $Fo$ correspond to Prandtl number, Rayleigh number, Stephan number and Fourier number. The asterisk mark (*) is dropped for the rest part and unsubscripted variables are assumed to be dimensionless.

The average Nusselt number ($Nu_{avg}$) at the left heated wall can be calculated as

$$Nu_{avg} = -\int_0^W \left( \frac{\partial \mathrm{T}}{\partial x} \right)_{x=0} dy \tag{5.4}$$

Similarly, average Nusselt number for horizontal walls can be calculated from the vertical temperature gradients.

### 5.1.4 Results and Discussion

Study of two dimensional corners melting in square cavity has been investigated in the present work using D2Q9 LB stencil. Low Prandtl number material has been considered in cavity melting process in which the nuance of natural convection is studied. Under the thermal effect of heated corner walls, melting starts and subsequently the melt zone grows. Initially the energy transfer is dominated by conduction and as the melt zone grows effect of natural convection is discernible.

Interesting flow phenomena are observed in growing melt region in which temperature gradient in gravitational field induces circulation of fluid. Several flow patterns are generated in the melt zone within a distinct two-phase interface. The shape and location of interface movement change with time due to the presence of buoyancy effect in melt zone. The shape of the interface changes from a convex shape to concave shape toward the melting direction due to fixed temperature boundary conditions. The effect of natural convection in the melt zone for two cases has been studied for different *Ra* which has profound impact on melting. Both corner melting with bottom heated wall (case 1) and corner melting with top heated wall (case 2) show buoyancy effect in the presence of dual temperature gradient in the gravitational field. The isotherms in the cavity have been presented and the influence of velocity in melt zone is represented by streamlines.

#### *Grid Independence and Validation of the Code*

The present simulation has been performed by developing a FORTRAN based lattice Boltzmann code to study solid-liquid phase change problems. Grid independency study has been carried out using 75x75, 101x101, 151x151 and 201x201 lattice nodes. For this, average *Nu* at the heated walls is calculated using different grids resolution. Table 5.1 represents the average *Nu* with different grids at a specific time.

Table 5.1: Average Nusselt number on heating walls using different grids resolution

| | **Average Nusselt number** | |
|---|---|---|
| **Grids Resolution** | Bottom Heated wall | Side heated wall |
| **75x75** | 4.850 | 4.726 |
| **101x101** | 4.729 | 4.538 |
| **151x151** | 4.623 | 4.435 |
| **201x201** | 4.623 | 4.435 |

It is seen from Table 5.1 that the average *Nu* in bottom and side heated walls are nearly same for 151x151 and 201x201 grids. To optimize the computational cost vis-a-vis the accuracy, 151x151 grids are finally chosen for the present simulation. Using 151x151 grids the code is validated with a published research work by Lin and Chen (Lin and Chen, 1997), in which corner solidification in a semi-infinite corner was investigated assuming conduction heat transfer (Fig. 5.2a). Figure 5.2a shows a near-perfect match of the present results with the published study. The present FORTRAN code is further validated using 151 x151 grid resolution with benchmark data of (Mencinger, 2004) in which left heated melting in a square enclosure was carried out at *Pr* = 0.02 and *Ra*=2.5x10$^4$. In a left-heated square cavity melting, average *Nu* varies over time as seen in Fig. 5.2b.

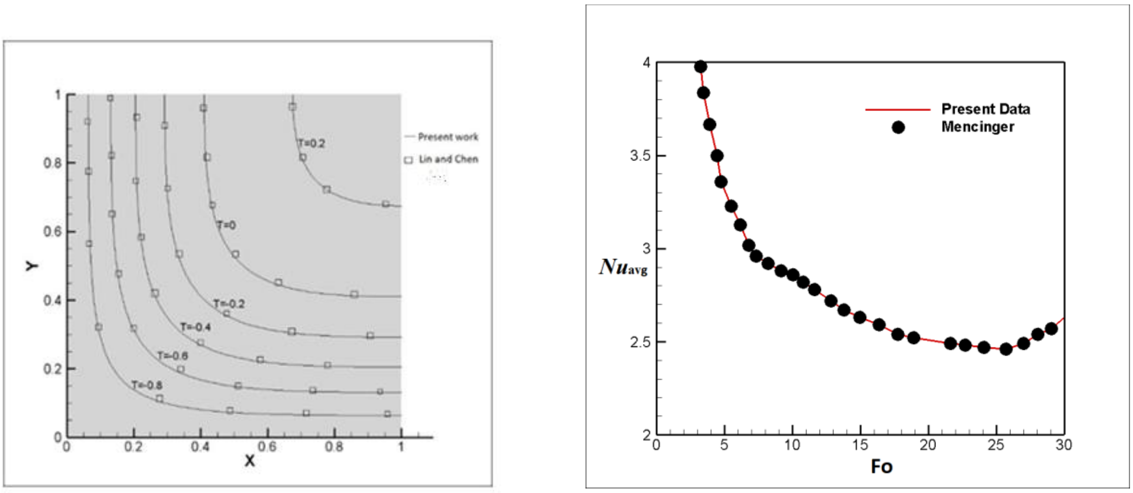

**(a)** (b)

Figure 5.2 : Code validation with the results of a) interface position (Lin and Chen, 1997) and b) average *Nu* vs *Fo* with (Mencinger, 2004) work.

Additional validation has been performed for natural convection dominated square cavity problem (Basak et al., 2006; Du et al., 2021). Table 5.2 shows the calculated average *Nu* for different *Ra* which agree favourably with data from literature.

Table 5.2: Average Nusselt number on heating wall of the square cavity

| | ***Ra*=10$^3$** | ***Ra*=10$^4$** | ***Ra*=10$^5$** |
|---|---|---|---|
| **(Basak et al., 2006)** | 4.1563 | 6.2476 | 9.391 |
| **(Du et al., 2021)** | 4.1655 | 6.2676 | 9.3518 |
| **Present** | 4.1584 | 6.2362 | 9.3571 |

### *LBM Parameters*

In this work, the computational domain is divided in lattice space with $\Delta x = 1$ and simulation is advanced in time with $\Delta t = 1$. The simulation has been performed assuming relaxation parameter for flow field as $\tau_m$=0.5187. The numerical accuracy of the problem depends on the relaxation parameter value as the sensitivity of the relaxation parameter is related with other LB parameters as well as the dimensionless parameters which are set at *Ra*=$10^4$ and $10^5$, *Ste*=0.01 and *Pr*=0.025. The incompressibility limit in the melt zone has been assumed using the relationship: $\sqrt{g\beta(T - T_{ref})W} \leq 0.1$ for the present simulation. The relaxation parameters are so chosen that the numerical stability of the problem is well maintained. Relaxation parameter for flow and energy can be calculated using dimensionless number *Ra* and *Pr* respectively.

### *Corner Melting: Heated From Bottom and Left Side Wall*

When the cavity is heated from left-bottom walls of the square cavity, melting occurs which can be termed as corner melting from bottom (case 1). A comparison has been made for different *Ra* when corner melting occurs with heated bottom surface. The isotherms and streamlines in the melt zone have been presented in Figures 5.3-5.6 for two levels of *Ra*.

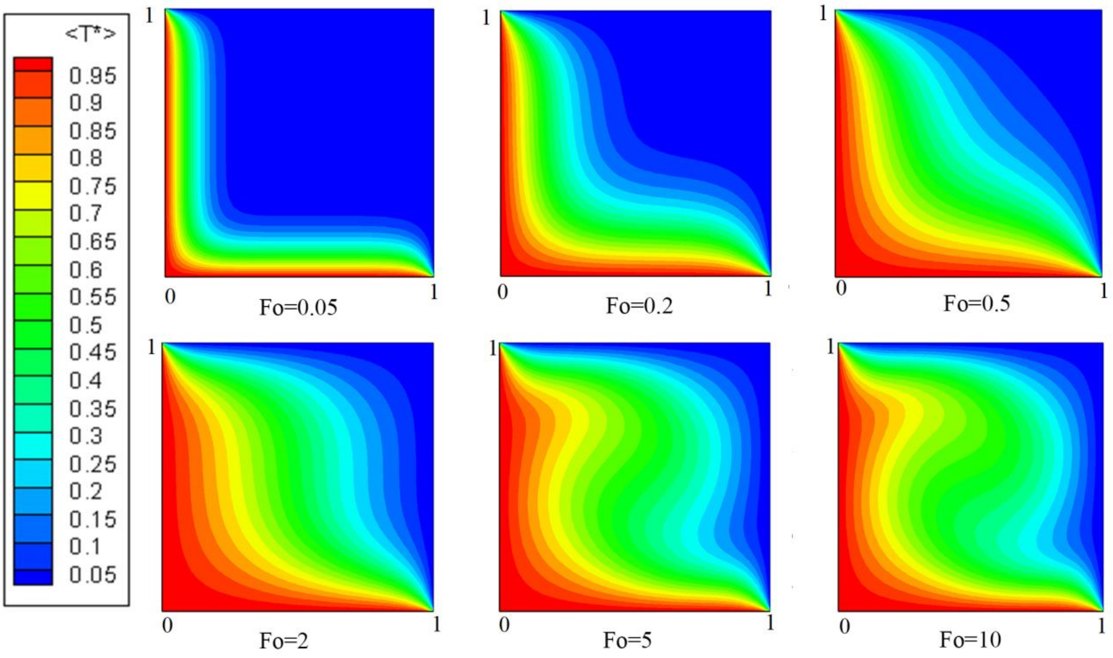

Figure 5.3: Evolution of isotherms with time at *Ra*=$10^6$ for case 1.

In Figure 5.3, it is observed that as the melting proceeds, isotherms are dominated by convection effect. At a non-dimensional time, *Fo* =0.05, the isotherms are diagonal-symmetric which indicates the melting process is still dominated by conduction. With further advance in time, the role of convection becomes evident which breaks the symmetry hitherto present and the interface shape changes the shape under the influence of natural convection. At *Fo* beyond 2, the temperature profiles do not change much as the rate of thermal flux from boundary to interface gradually approaches a fixed value with time in the molten zone of the cavity.

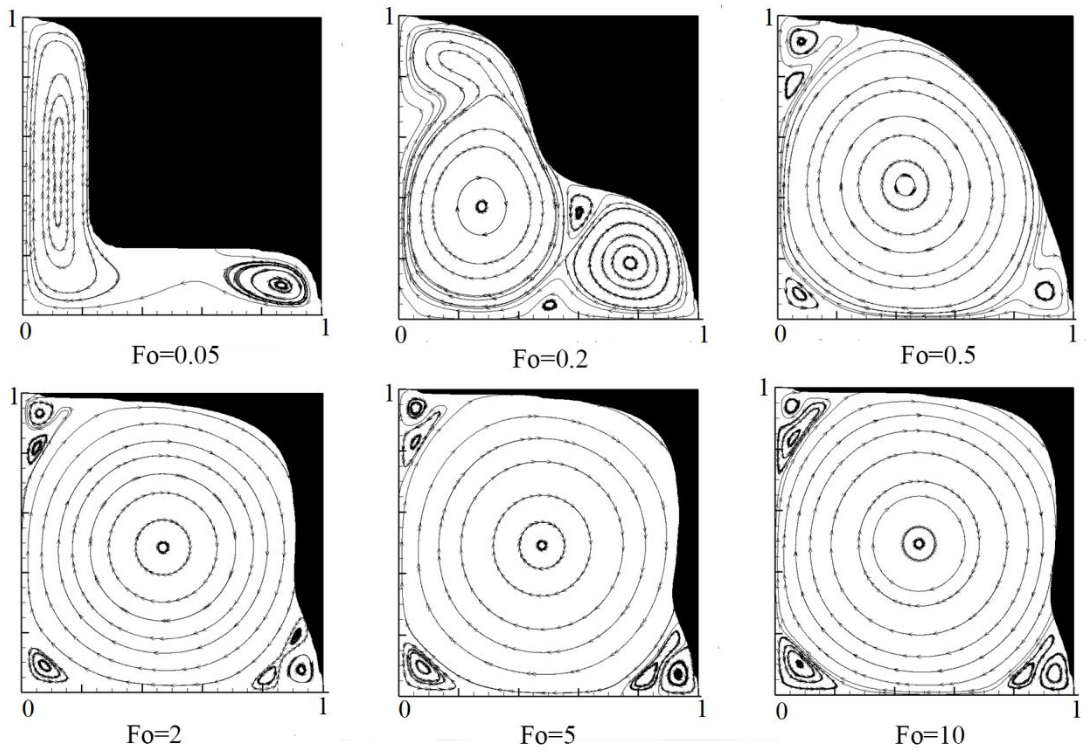

Figure 5.4: Transient evolution of streamlines at *Ra*=$10^6$ for case 1.

The flow field at *Ra*=$10^6$ is depicted in Figure 5.4 by presenting a family of streamlines at different dimensionless time. In the early stage of melting, clock-wise circulation of stream line in the vicinity of left wall is observed in a narrow molten region. As the time proceeds, the primary vortex in the melt zone grows with appearance of a dead zone at the left-bottom corner at *Fo*=0.5. The secondary and tertiary vortices appear due to very low velocity near the wall. With the progress of time, the center of the primary vortex shifts towards the center of the cavity. The secondary and tertiary vortices adjacent to the solid boundary walls grow in strength. Figure 5.5 and 5.6 show the temperature profiles and streamlines respectively at a higher value of $Ra=10^7$.

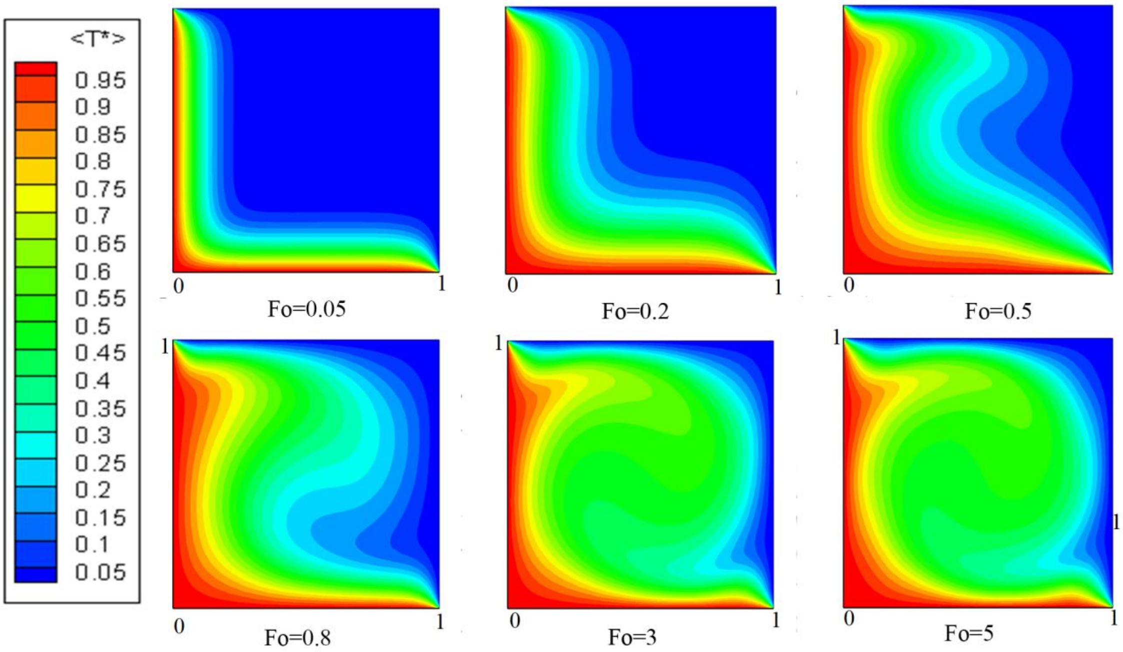

Figure 5.5: Temporal evolution of isotherms at $Ra=10^7$ for case 1.

At a higher *Ra*, the rate of melting naturally increases and the melt zone grows faster. Compared to the case of lower *Ra* (Figure 5.3) at *Fo*=0.5, it is clearly seen that the convection current in the melt zone is more which affects the flow pattern in the melt zone. Compared to the case at lower *Ra* (Figure 5.3), the isotherms in Figure 5.5 show distinct dominance of natural convection with presence of undulated temperature profiles, observed from *Fo*=0.5 onwards. Figure 5.6 shows the evolution of flow patterns in the melt zone at higher *Ra* of $10^7$. Unlike the case of lower *Ra*, here Bénard convection cells are found to be present along both the vertical and horizontal melt pools at *Fo* =0.05. The configuration at low *Fo*, as such resembles that of a Rayleigh- Bénard system with a thin liquid pool under an imposed temperature gradient. Such cells are also observed by Dhar et al. (Mrinmoy Dhar et al., 2015) at a similar level of *Ra*. It is interesting to see that the number of cells is more on the vertical wall as a complex interaction between gravity acting downwards and thermal gradient in horizontal direction. As melting zone grows, these cells merge leading to three primary convective rolls (*Fo*= 0.8). Eventually, one primary vortex fills the entire zone with presence of secondary vortices in the corners.

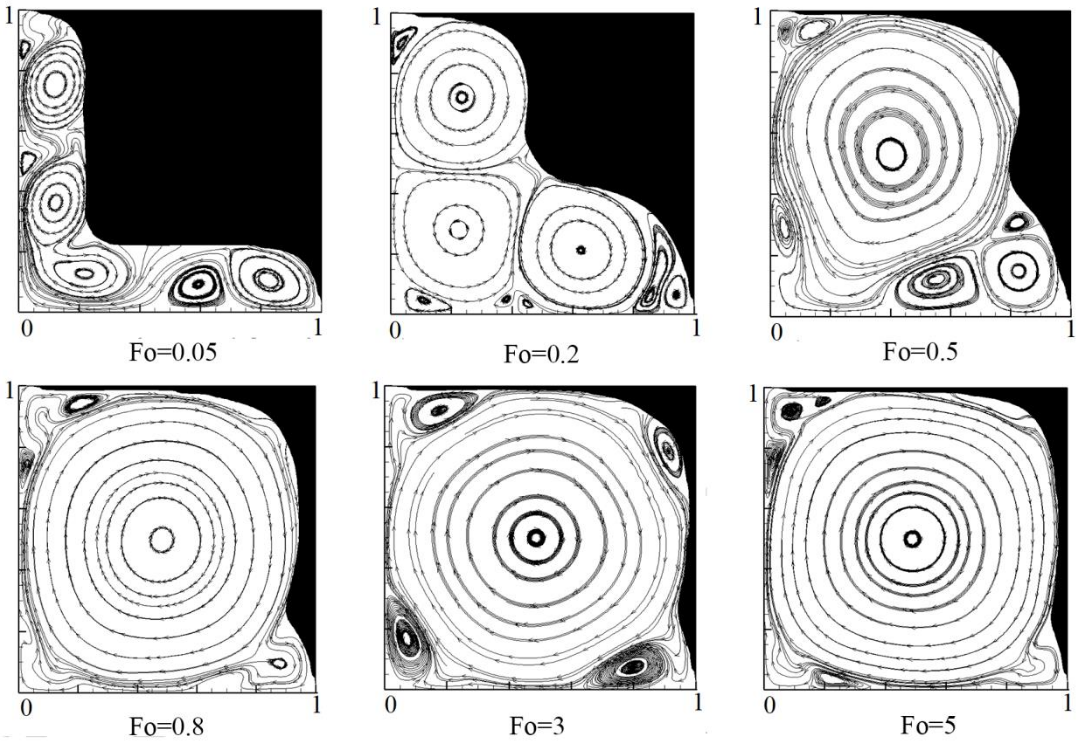

Fo=0.05 Fo=0.2 Fo=0.5

Fo=0.8 Fo=3 Fo=5

Figure 5.6: Transient evolution of streamlines at *Ra*=$10^7$ for case 1.

### Corner melting heated from top and side wall

In this section, we discuss melting process as the top and the right walls of cavity are heated. Corner melting from top has been studied at two different *Ra*.

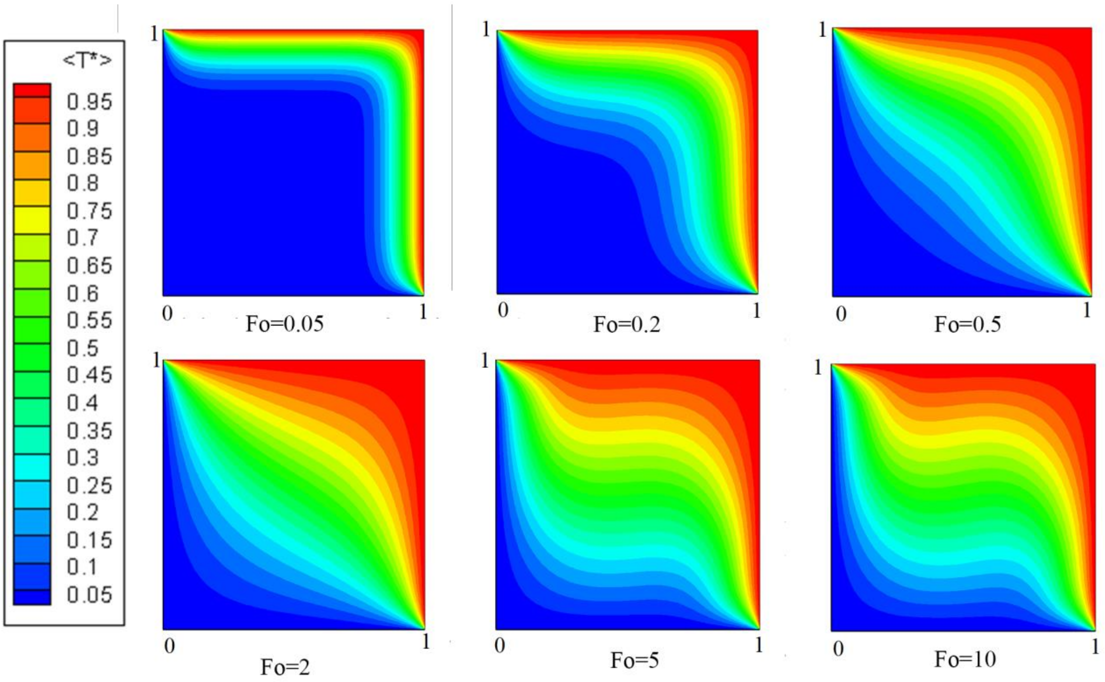

Fo=0.05 Fo=0.2 Fo=0.5

Fo=2 Fo=5 Fo=10

Figure 5.7: Evolution of isotherms with time at *Ra*=$10^6$ for Case 2.

Figures 5.7-5.8 shows the isotherms and flow field at *Ra*=$10^6$ while Figures 5.9-5.10 presents the temperature profiles and corresponding fluid patterns at *Ra*=$10^7$. Corner melting from top induces density gradient parallel to gravity field between the top-bottom walls. As the lighter liquid lies at the top of the cavity, the fluid layers adjacent is stratified. However. In the presence of hot side wall, warmer fluid moves upward along the right wall. Figure 5.7 shows the diagonal-symmetric isotherms till *Fo* =2.0, indiating the dominance of conduction.

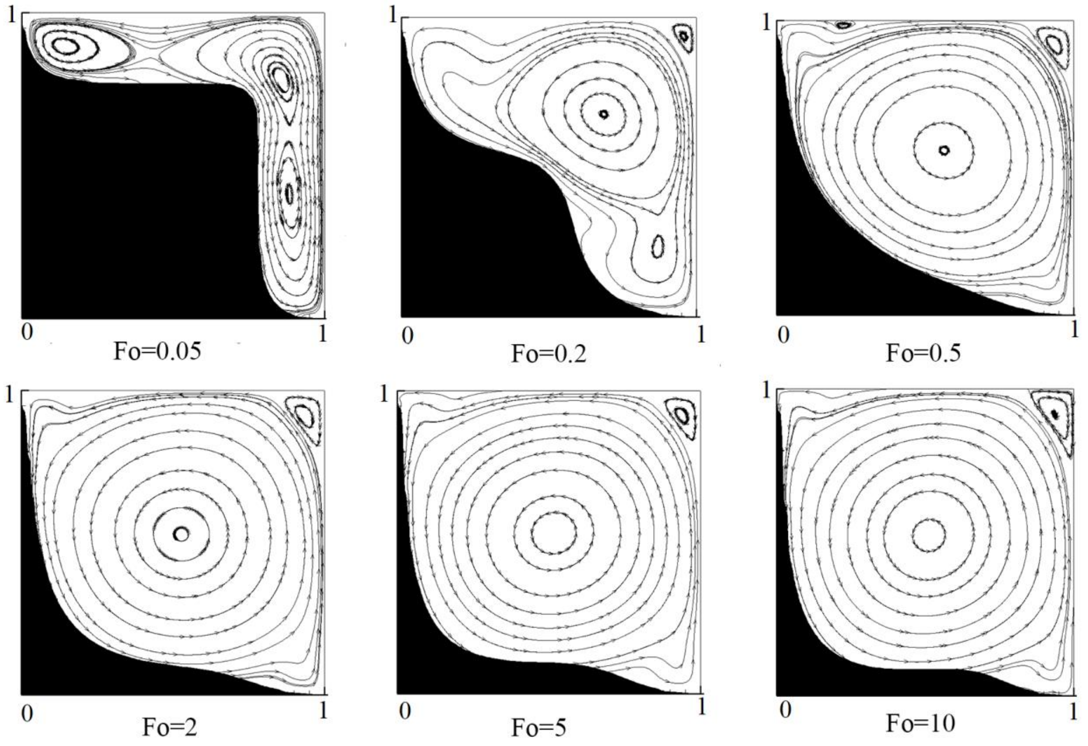

Figure 5.8: Transient evolution of streamlines at *Ra*=$10^6$ for case 2.

Thus, unlike the case of the bottom-side corner heating, in this case, effect of convection is realize at much later stage. The isotherms near the top wall are parallel, and become wavy in the presence of convection far from the top wall. A counter clockwise circulation is observed in Figure 5.8 which depicts the upward movement of  warmer fluid along the right wall. The fluid stream then flows parallel to the top wall and finally moves downward to complete the loop. A secondary vortex is generated at the top-right corner of the cavity which grows with time. Figure 5.9 describes a family of isotherms at *Ra*=$10^7$. Due to higher *Ra*, now the conduction doimnance is observed till *Fo* = 0.2 (which was 0.5 at lower *Ra* of $10^6$). The effcet of natural convection is thus found to destabilize the stratified layer.

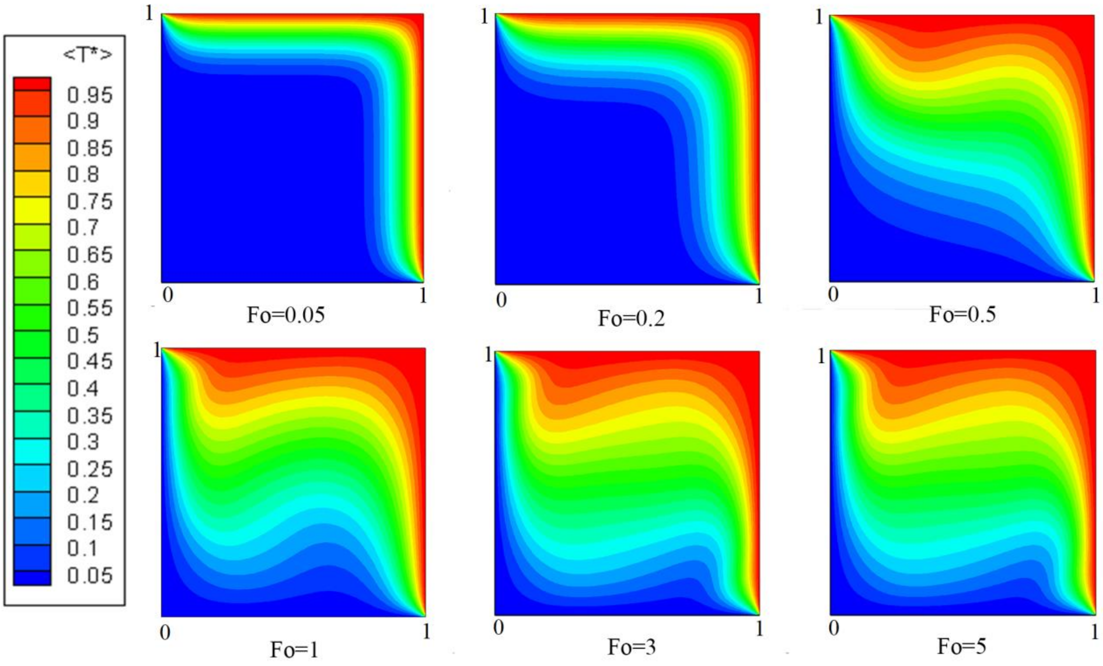

Figure 5.9: Temporal evolution of isotherms at $Ra=10^7$ for case 2.

Figure 5.10 shows the streamline patterns in the melt zone at different time instances.

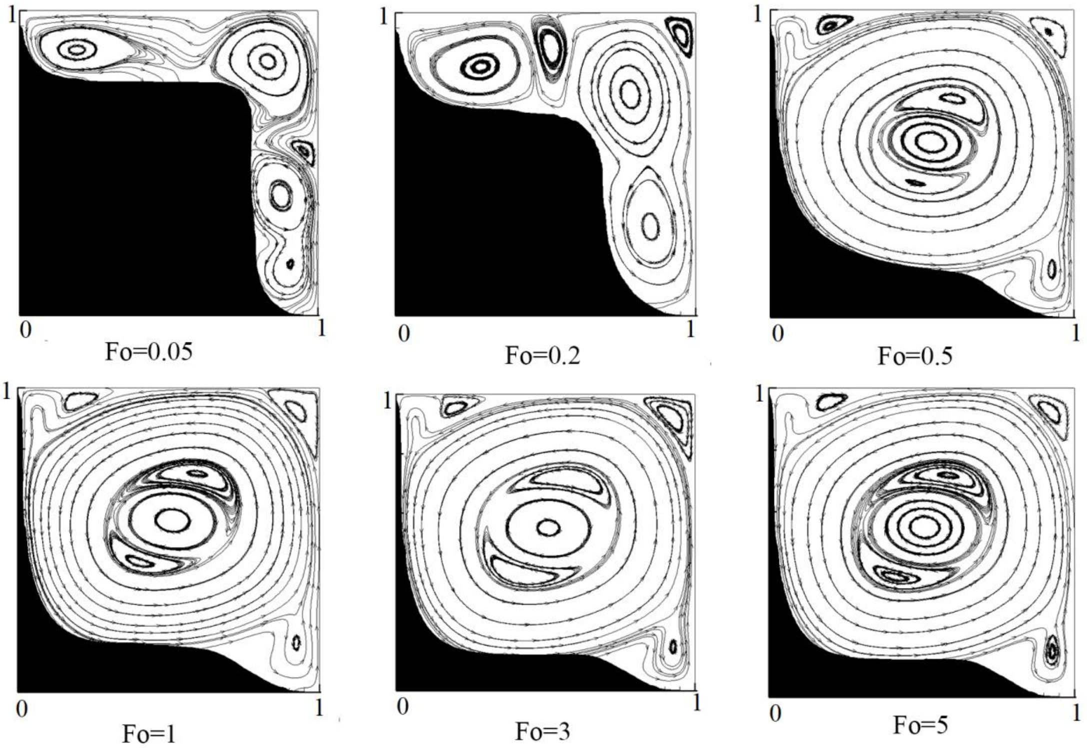

Figure 5.10: Transient evolution of streamlines at $Ra=10^7$ for case 2.

While comparing with the case of low *Ra* (Figure 5.8), it is seen that in Figure 5.10, the effect of natural convection is more pronounced. Several vortices are generated in the melt zone and at the centre of the cavity, a primary vortex is formed in a clockwise direction. Two counter-clockwise circulation has been developed around the centre of the primary circulation from *Fo* =0.5. A complex flow circulation is seen at the centre of the melt zone and the complex flow patterns so developed follow the vortex interactions and path of minimum resistance.

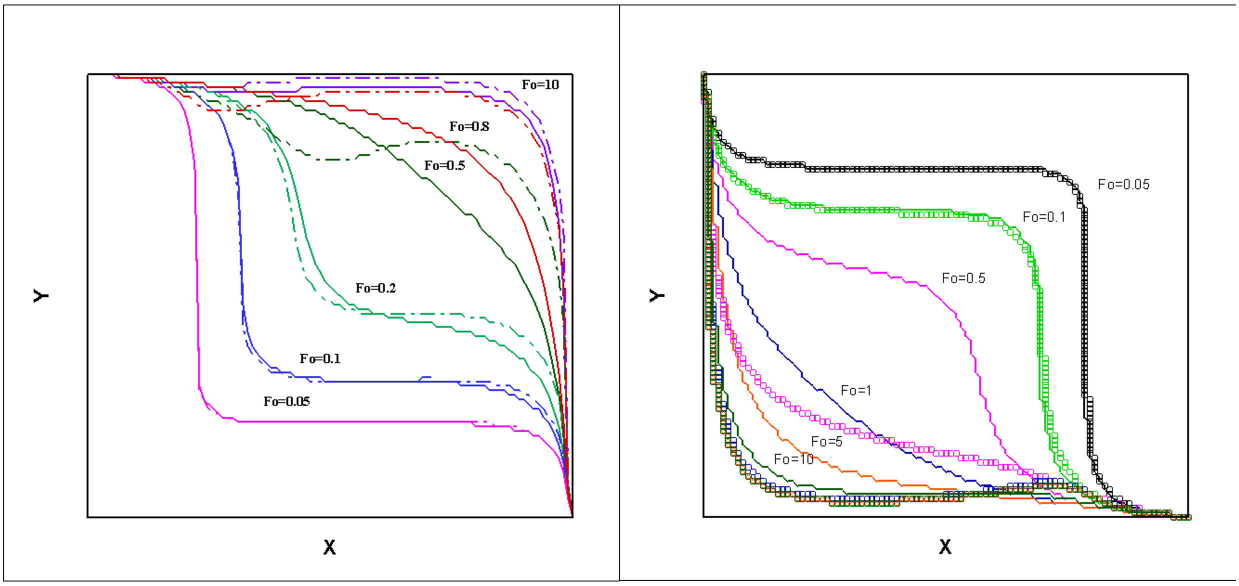

(a) (b)

Figure 5.11: Interface position at different time for two Rayleigh numbers. Solid lines indicate interface position at Rayleigh number $10^6$ while dotted lines denote at $Ra=10^7$ a) left-bottom corner melting b) top-right corner melting.

The location of interface with time has been plotted for both cases in Figure 5.11. The solid line and dotted lines indicate $Ra=10^6$ and $10^7$ respectively.

It is seen from Figure 5.11 (a) that initially the position of melting front for both *Ra* is nearly same for $Fo=0.05$ to 0.1. For case 1, at $Fo=0.2$ melting front for $Ra=10^7$ is different from $Ra=10^6$. A drastic change has been observed from $Fo=0.5$ to 0.8 in which the position of melting fronts are different for two *Ra*. At $Fo=10$, the melting front moves faster at $Ra=10^7$ compare to $Ra=10^6$. Figure 5.11(b) describes the interface location with time for case 2. For case 2 it is seen that, the movement of melting front is faster at $Ra=10^5$ rather than $Ra=10^6$. It is observed from the two cases that the shape of interface front has been changed from convex to concave shape as melting proceeds. The shape of cavity necessiates the transition from convex to concave so that the melting covers the entire domain. This transition of interface shape is found to occur at about *Fo*=0.5. It is worth noting that the diagonal between two hot walls divides the domain in two halves with an area of 0.5L$^2$. The melt interface changes shape about when material in one half of the cavity is melted. So a value of *Fo* =0.5 basically indicates the dimensionless time related to this area and thermal diffusivity.

### *Average Nusselt number*

Figure 5.12 is a representation of average Nusselt number at the heated walls for both the cases at *Ra*=10$^6$, *Ra*=5x10$^6$ and *Ra*=10$^7$ respectively. It is observed from these figures that heat transfer from bottom wall is higher than side wall for case 1 and heat penetration from side wall is more compared to the top wall for case 2. The average *Nu* for case 2 shows an increasing trend up to *Fo*=1 compared to case 1 at *Ra*=10$^6$ and beyond *Fo*=1 average *Nu* for case 1 increases.

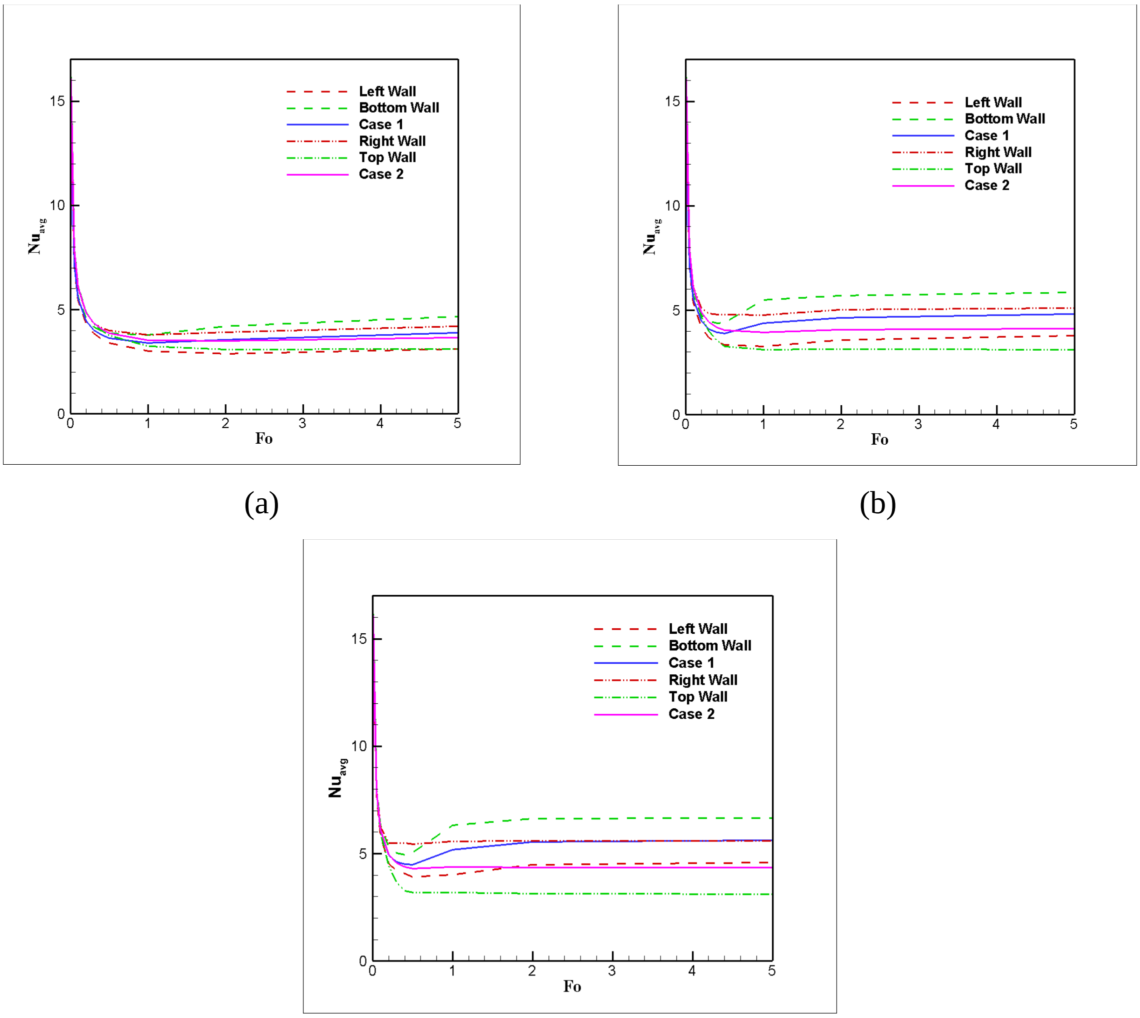

(a)

(b)

(c)

Figure 5.12: Average Nusselt number for a) *Ra*=10$^6$, b) *Ra*=5x10$^6$ and c) *Ra*=10$^7$

It is seen from here that the general trend of average *Nu* is that it reduces with *Fo* and then stabilizes as the starting of melting, average *Nu* is more due to conduction melting and as time increases melting occurs in the presence of convection heat transfer. With the increase of time, as melt zone grows and resistance of convection heat transfer increases. The temperature driving force reduces over time and average *Nu* stabilizes. However, when *Ra* is $5x10^6$ or more, there is a gain in $Nu_{\text{avg}}$ at around *Fo*= 0.62. The reason can be attributed to appearance of convective rolls at higher *Ra* leading to high heat transfer. As *Fo* increases beyond the above values, the average *Nu* for case 1 is higher over case 2 for both $Ra$=$5x10^6$ and $Ra$=$10^7$. Average *Nu* values reported at *Ra* of $2.5x10^6$ are 3.75 and 2.65 for side heated and bottom heated cavity by Dai el al. (Dai et al., 2018). In the present work the average *Nu* values for right-top and left-bottom corner melting are in the range of 3.65-3.88 for $Ra = 10^6$ and 4.36-5.62 for $Ra$=$10^7$ at *Fo*=5. The quantitative measurement of the average *Nu* has been presented in Table 5.3.

Table 5.3: Average Nusselt number for both left-bottom corner melting (case 1) and top-right corner melting (case 2)

| | **$Ra$=$10^6$** | | **$Ra$=$5x10^6$** | | **$Ra$=$10^7$** | |
|---|---|---|---|---|---|---|
| ***Fo*** | Case 1 | Case 2 | Case 1 | Case 2 | Case 1 | Case 2 |
| **0.05** | 7.17 | 7.91 | 7.26 | 7.92 | 7.92 | 7.93 |
| **0.5** | 3.62 | 3.87 | 3.88 | 4.03 | 4.60 | 4.56 |
| **1** | 3.39 | 3.51 | 4.37 | 3.93 | 5.17 | 4.37 |

### *Melt Fraction*

Figure 5.13 represents the average melt fraction with time for both left-bottom and right-top corner melting for three values of *Ra*. It is seen from Figure 5.13 (a) that the average melt fraction is more for case 1 upto Fo=0.5 due to the average heat flux from left and bottom walls suppling more energy compared to top-right walls. The difference of melt fraction for left-bottom corner melting (case 1) compared to the top-right corner melting (case 2) upto *Fo*=0.5 is 10.5% while beyond *Fo*=0.5 case 2 shows a higher melt fraction by 2.5% over that of case 1. With increasing time beyond *Fo*=0.5, average melt fraction is more for the case of right-top side corner melting. Figure 5.13 (b) and (c) depict the average melt fraction at $Ra$=$5x10^6$ and $Ra$=$10^7$ respectively. The average melt fraction due to top-right corner melting is increasing upto *Fo*=0.2 and beyond which the increase of melt fraction is slower while the melt fraction due to left-bottom melting is growing upto *Fo*=0.5. The difference of melt fraction for case 1 over case 2 beyond *Fo*=1.2 is just 0.2%. The overall change of melt fraction is nearly similar for both the cases in the long run (*Fo*>1) though the heat transfer rate is varied differently as shown in the transient average *Nu* curves (Figure 5.12). It is observed that 90% of melting is complete within $Fo \simeq 1$. This assumption is consistent with the work by (Rui et al., 2020a).

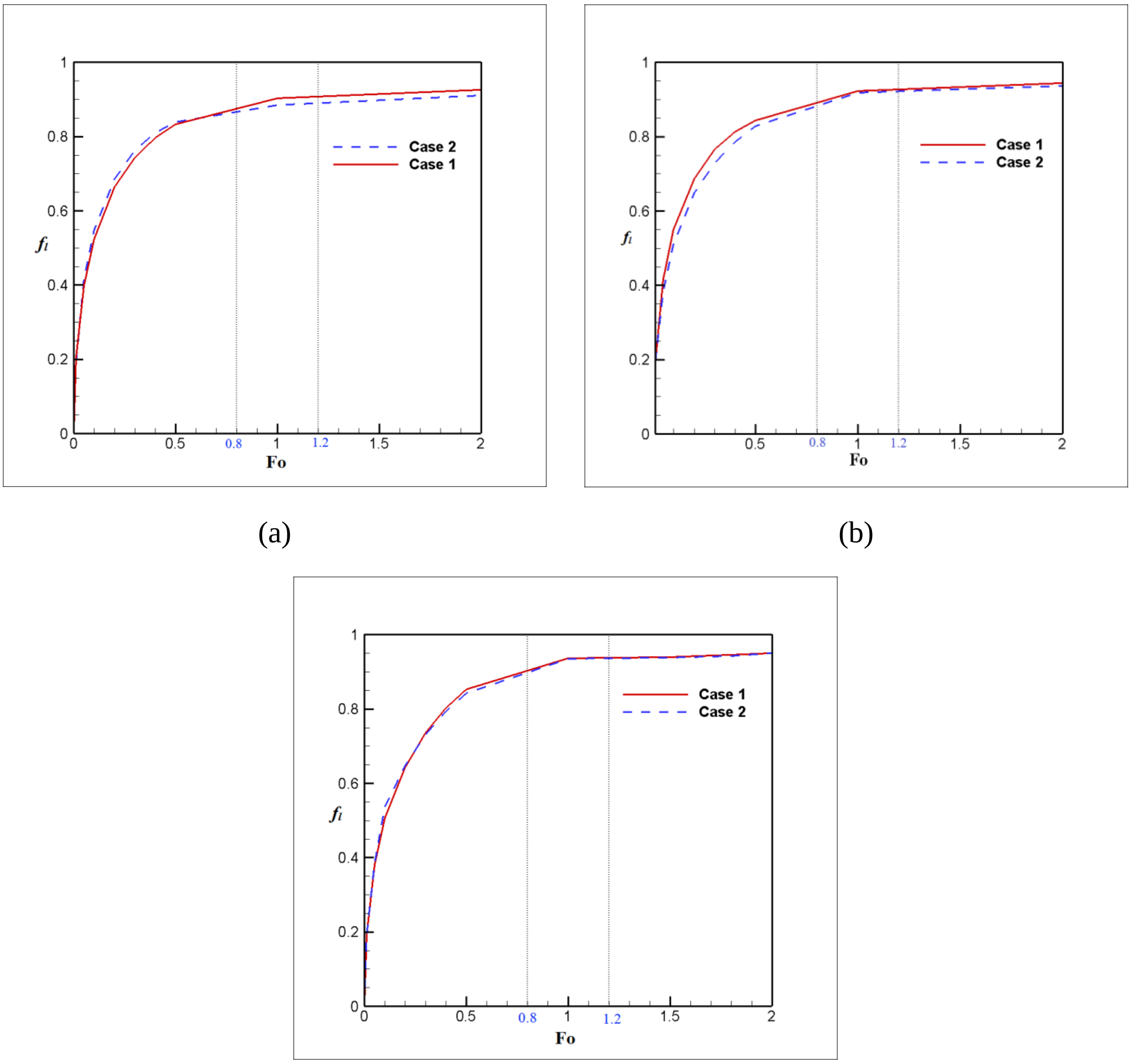

(a)

(b)

(c)

Figure 5.13: Melt fraction (a) *Ra*=$10^6$ (b) *Ra*=5x$10^6$ and c) *Ra*=$10^7$

### *Average heat flux*

The non-dimensional heat flux in such situations is given by the product of *Nu* and *Ra* (Krishnamurti, 1970). Average heat flux is shown at different walls against *Ra* in in Figure 5.14 when 90% melting is completed.

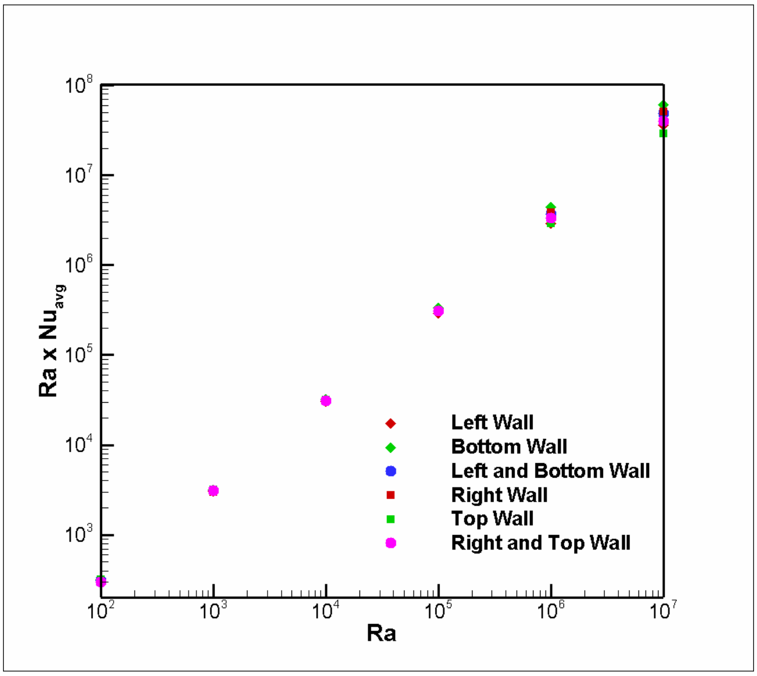

Figure 5.14: Average dimensionless heat flux ($Nu_{avg}$ x *Ra*) with *Ra*.

Figure shows average heat flux increases with *Ra* as expected. However, average heat flux at the bottom surface shows higher value compared to the heat flux obtained at the other walls. It is also found that heat flux at the top wall is minimum of all. The plots in log-log planes are having constant slopes and thus it is interesting to note that heat flux on all boundaries scale with $Ra^n$ where n is a constant. The value of n is 1.11 and 1.02 for bottom wall and the adjacent wall. The value changs to 0.98 and 1.08 for top wall and adjacent side wall.

## 5.2 Corner Solidification in Closed Cavity

Investigation of solidification phenomena of pure metal has been studied in a square cavity where the left and bottom walls are at lower temperature than that of the initial temperature of the melt. The situation leads to solidification from both the left and bottom walls which is termed as corner solidification. Lattice Boltzmann method (LBM) is used to perform the numerical simulation of the physical problem.

### 5.2.1 Objective of the Work

Looking at the literatures on solidification, it is found that relatively fewer investigations on solidification have been performed using LBM. Corner solidification is important in industrial application such as material processing, additive manufacturing, continuous casting etc. in which the better understanding of the basic metal behavior is important during solidification. Regarding the influence of natural convection in liquid metal, the location of solid-liquid interface has been traced using enthalpy method. The investigation is performed considering two different Rayleigh number (*Ra*) $10^4$ and $10^5$ to observe the natural convection effect on solidification.

### 5.2.2 Problem Statement and Mathematical Modeling

Pure substance at its melting temperature ($T_m$) is initially filled within a square cavity in which left side-wall and bottom wall are kept at a temperature lower than the melting temperature i.e. $T_c<T_m$. The upper and right boundaries of the cavity are adiabatic in nature. In this condition, a two dimensional solidification phenomenon has been investigated. The configuration of the model with boundary conditions is presented in Fig. 5.15. Heat is rejected from both left and bottom walls and the location of solidification front have been tracked with time. Assuming that, laminar and incompressible cavity fluid with constant thermal properties has been considered while the density change occurs with temperature. In the present solidification study, Boussinesq approximation has been used to describe the effect natural convection. The governing set of equations mass, momentum and energy with source terms can be formulated as section 4.1.3.

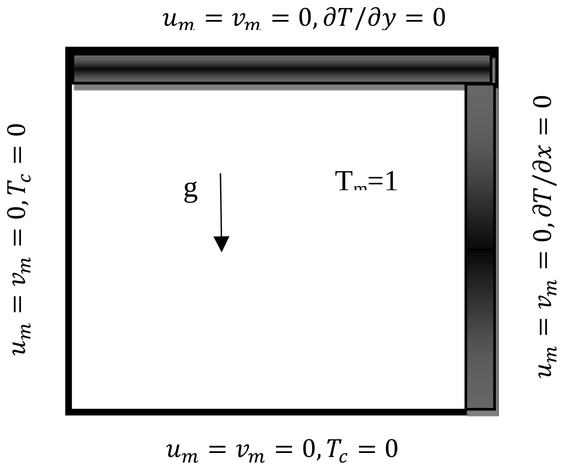

Fig. 5.15: Schematic of a cavity with aspect ratio of one in which heat removal occurs from left and bottom walls, while other two boundaries are kept insulated.

The initial as well as boundary conditions are given as,

$$\text{at } t=0, \quad \mathrm{u_m} = \mathrm{v_m} = 0,\ \mathrm{T} = T_m \ \text{ for } \ 0 \le x \le L \ \text{ and } \ 0 \le y \le W \tag{5.5}$$

Boundary conditions are given at $t > 0$ as

$$\left.\begin{array}{l}
\mathrm{u_m} = \mathrm{v_m} = 0,\ \mathrm{T} = T_c \ \text{ for } \ x = 0 \ \text{ and } \ 0 \le y \le W \\
\mathrm{u_m} = \mathrm{v_m} = 0,\ \mathrm{T} = T_c \ \text{ for } \ y = 0 \ \text{ and } \ 0 \le x \le L \\
\mathrm{u_m} = \mathrm{v_m} = 0,\ \dfrac{\partial T}{\partial x} = 0 \ \text{ for } \ x = L \ \text{ and } \ 0 \le y \le W \\
\mathrm{u_m} = \mathrm{v_m} = 0,\ \dfrac{\partial T}{\partial y} = 0 \ \text{ for } \ y = W \ \text{ and } \ 0 \le x \le L
\end{array}\right] \tag{5.6}$$

### 5.2.3 Results and Discussion

Solidification of pure substance has been investigated in a square cavity from left-bottom corner. Lattice Boltzmann method (LBM) with 101x101 lattice grids in D2Q9 model is used to investigate pure metal solidification in presence of convection. The time step (Δt) is taken 1 for the simulation. The study is performed at two different Rayleigh numbers (*Ra*) $10^4$ and $10^5$ keeping constant Prandtl number (*Pr*) as 0.02. The investigation has been performed to predict the location of the moving solidification front with variation of time. The investigation of corner solidification phenomena reveals that the energy is rejected from both left and bottom walls of the cavity. The effect of natural convection on the solidification front have been studied using two different *Ra* numbers.

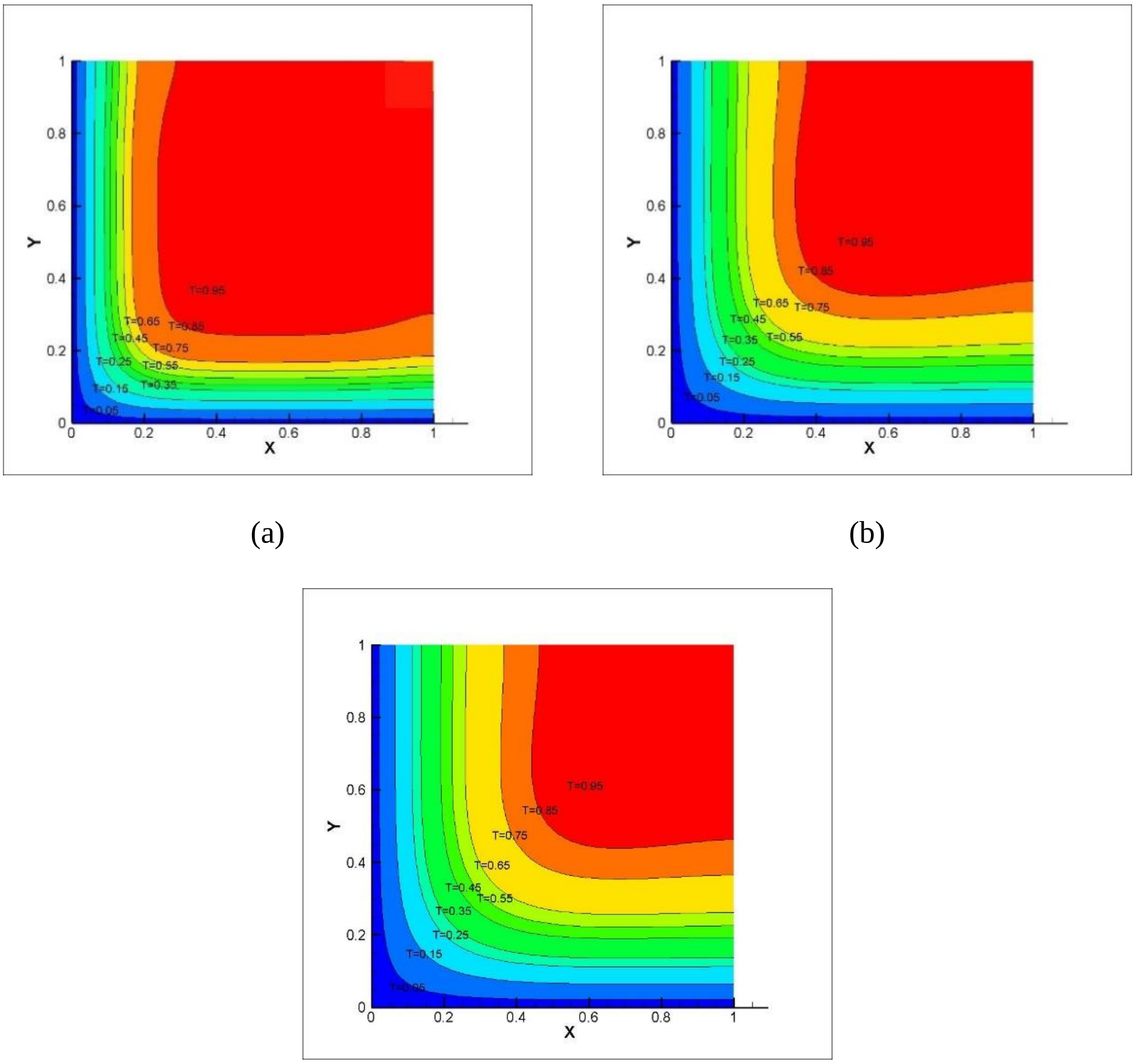

(a) (b)

(c)

Fig. 5.16: Isotherms at *Ra*=$10^4$ a) *Ste***Fo*=0.01, b) *Ste***Fo*=0.02, and c) *Ste***Fo*=0.03.

The effect of natural convection on the solidification front have been studied using two different *Ra* numbers. Figures 5.16(a), 5.16(b) and 5.16(c) illustrates the isotherms at *Ra*=$10^4$.

It is seen from Fig. 5.16(a) to 5.16(c) that the latent heat energy loss from both left and bottom walls are increases with time.

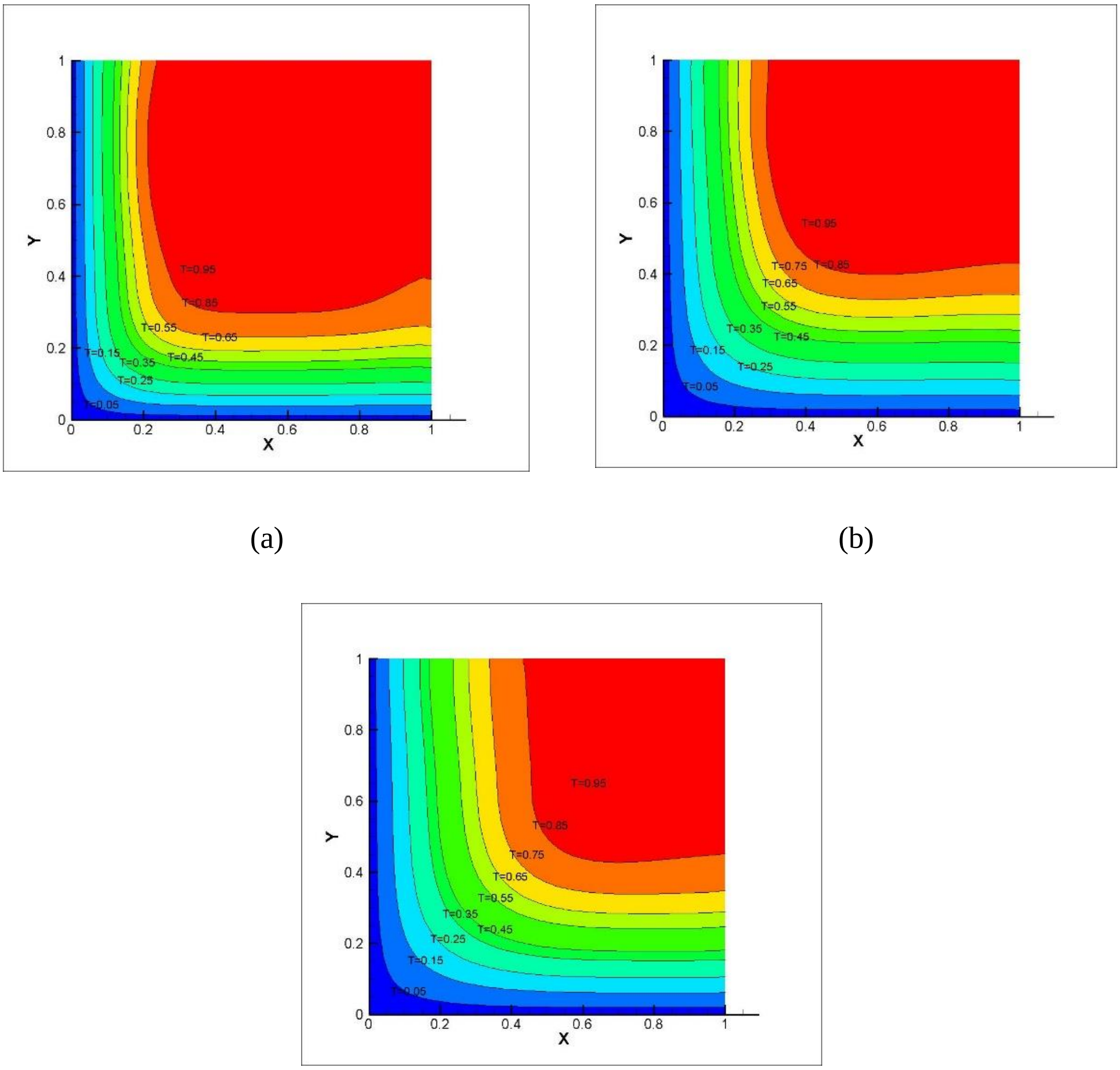

(a) (b)

(c)

Fig. 5.17: Isotherms at *Ra*=$10^5$ a) *Ste***Fo*=0.01, b) *Ste***Fo*=0.02, and c) *Ste***Fo*=0.03.

Similarly, Fig. 5.17(a) to 5.17(c) shows the temperature contours at a relatively high *Ra*=$10^5$. It is seen from the isotherm profiles that the initially the domain is conduction dominated and with increasing of time the convection domination starts.

With the increasing of *Ra* number and the presence of buoyancy, the interface becomes distorted and the latent heat loss from the two sides increases with time. Figure 5.18(a) and 5.18(b) represents the solidification front at two different *Ra* number.

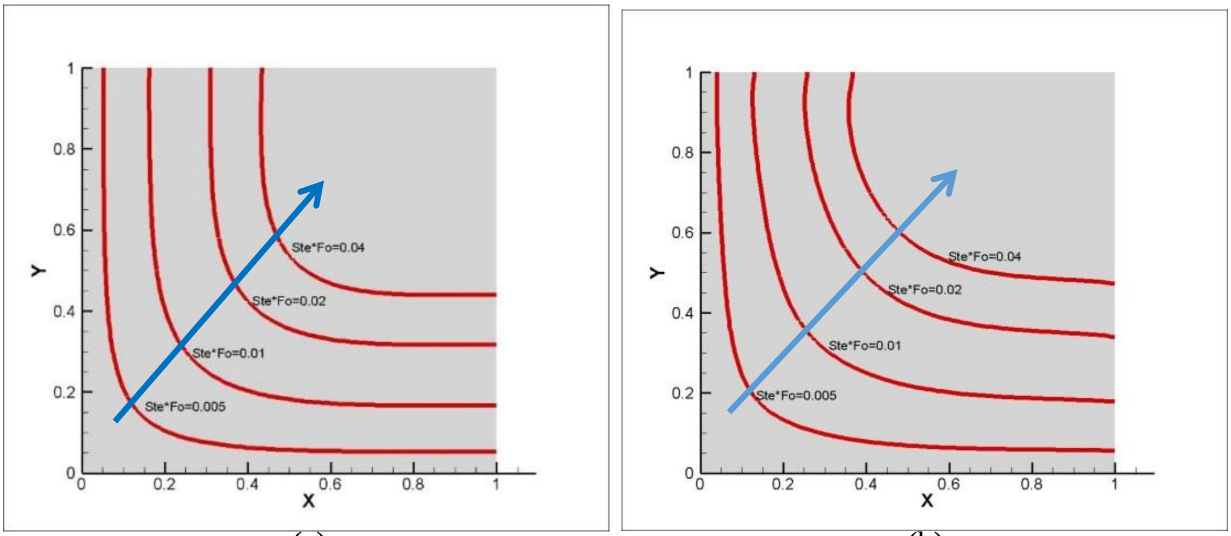

(a) (b)

Figure 5.18: The movement of solidification front at different $Ra$, a) $Ra=10^4$ b) b) $Ra=10^5$

It is seen from these two figures that, the position of solidification front is almost vertical near the cold walls and gradually inclined slope appears away from both cold walls as the heat transfer regimes shifts from conduction to convection. For same dimensionless time, the solidification front moves forward to the cavity indicating that strong influence of convection dominates at higher $Ra$ of $10^5$.

## 5.3 Corner Melting of Low Prandtl Number Liquid Metals

In this work, the lattice Boltzmann method (LBM) has been used to conduct a numerical analysis of the melting phenomena of low Prandtl number materials in a square enclosure with two adjacent heated walls. The energy equation and the incompressible Navier-Stokes equation's lattice Boltzmann Bhatnagar-Gross-Krook (LBGK) models are modified to address numerical instabilities for the simulation of low *Pr* fluids. Using a total enthalpy-based lattice Boltzmann approach, the flow field and the thermal behaviour in the melt zone are numerically modelled for corner melting problem. The investigation has been performed in a wide range of Prandtl number $Pr \in [0.001, 0.01]$ and high Rayleigh number $\mathrm{Ra} \in [10^5, 10^6]$. The evolution of the melting front with thermo-fluidic behaviour in the melt zone for low *Pr* materials is reported. For parametric values of Stepahn number $Ste=0.01$, the impact of Rayleigh number on the convective flow field with the variation of *Pr* is assessed.

### 5.3.1 Objective of the Work

The aim of the current research is to enhance the ability of lattice Boltzmann model to simulate melting in low Pr materials applied in the case of corner melting problems. Special modification has been employed to analyze very low *Pr* number liquid metals $Pr \in [0.001, 0.01]$.The main focus of the work includes the tracing of transient interface movement, calculation of average heat flux at the interface, determine the effect of natural convection in melt zone, distribution of isotherms in the cavity and average melt fraction with time of low Pr materials.

### 5.3.2 Problem Statement and Mathematical Modelling

The corner melting of a two-dimensional square enclosure filled with pure material is explored. A solid substance is initially uniformly present throughout the cavity (length L=width W) and is at its melting point ($T_m$). The temperatures on the heated sides ($T_h$) are kept above the melting point ($T_m$). Figure 5.19 represents the schematic of corner melting from two adjacent walls (left-bottom) with boundary conditions. The direction of gravitational acceleration in the melted zone is indicated by an arrow in Figure 5.19, and all of the walls are in a no-slip condition. Investigating the impact of natural convection in the melt zone varying Prandtl number (*Pr*) and examining the average heat flow at the interface are the main goals of the current investigation.

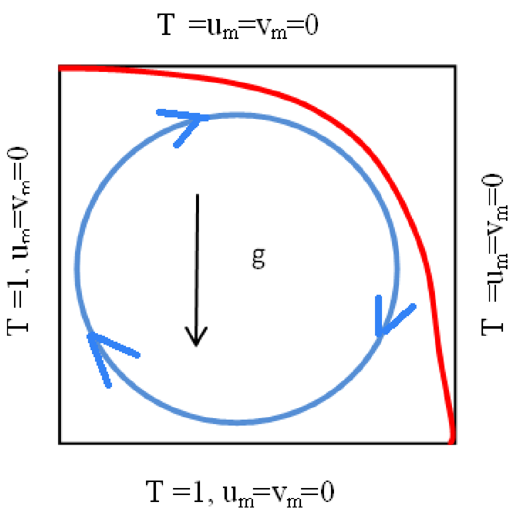

Figure 5.19: Schematic of square cavity corner melting.

The simulation was run under the assumptions that the flow inside the cavity is incompressible, that the material's thermos-physical characteristics remain constant, that viscous dissipation is neglected, and that the melt zone is modelled using the Boussinesq approximation. The governing equations are used to perform the numerical simulation mentioned in section 4.1.3. The initial and boundary conditions for the problem given as Initial condition:

$$\text{at } t=0,\quad \mathrm{u_m}=\mathrm{v_m}=0,\ \mathrm{T}=0 \ \text{ for } \ 0\le x\le 1 \text{ and } \ 0\le y\le 1 \tag{5.7}$$

Boundary conditions are given at $t>0$ given as

$$\left.\begin{aligned} &\mathrm{u_m}=\mathrm{v_m}=0,\ \mathrm{T}=1 \ \text{ for } \ x=0 \text{ and } \ 0\le y\le 1\\ &\mathrm{u_m}=\mathrm{v_m}=0,\ \mathrm{T}=1 \ \text{ for } \ y=0 \text{ and } \ 0\le x\le 1\\ &\mathrm{u_m}=\mathrm{v_m}=0,\ \mathrm{T}=0 \ \text{ for } \ x=1 \text{ and } 0\le y\le 1\\ &\mathrm{u_m}=\mathrm{v_m}=0,\ \mathrm{T}=0 \ \text{ for } \ y=1 \text{ and } 0\le x\le 1 \end{aligned}\right] \tag{5.8}$$

### 5.3.3 Results and Discussion

Using the lattice Boltzmann technique in the D2Q9 stencil, melting of low Prandtl number liquid materials in a side heated square cavity is explored. A modified lattice Boltzmann model is used to overcome the difficulties of numerical stability reported for low *Pr* materials. In the proposed model, a tuning parameter $A'$ is added to the relaxation parameter ($\tau'_f$) which is set to 0.02. Another tuning parameter $B'$ is also needed for energy equation which is calculated from the value of *Pr* as depicted in Eq. (3.71). A code for this has been developed in Fortran 90 and computations were performed in CDAC's PARAM SHAVAK system with a 16 core Intel Xeon processor. The lattice grid spacing and time step are considered as $\Delta x = \Delta t = 1$.

### *Effect of Rayleigh Number*

A comparison has been made for different *Pr* with the variation of *Ra* when corner melting occurs with heated left-bottom surface. The isotherms in the cavity and the streamlines at the melt zone have been presented in Figs. 5.20-5.22 for different *Pr*.

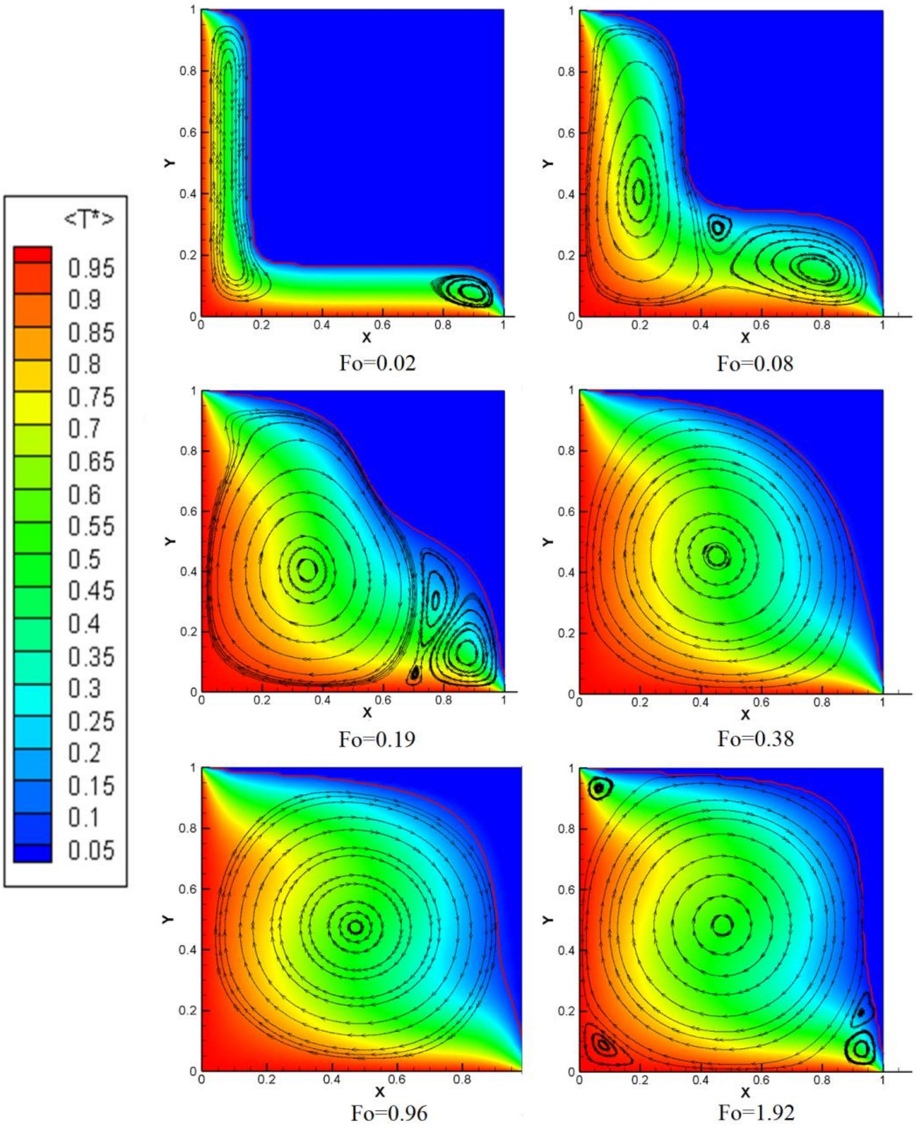

Fo=0.02 Fo=0.08

Fo=0.19 Fo=0.38

Fo=0.96 Fo=1.92

(a)

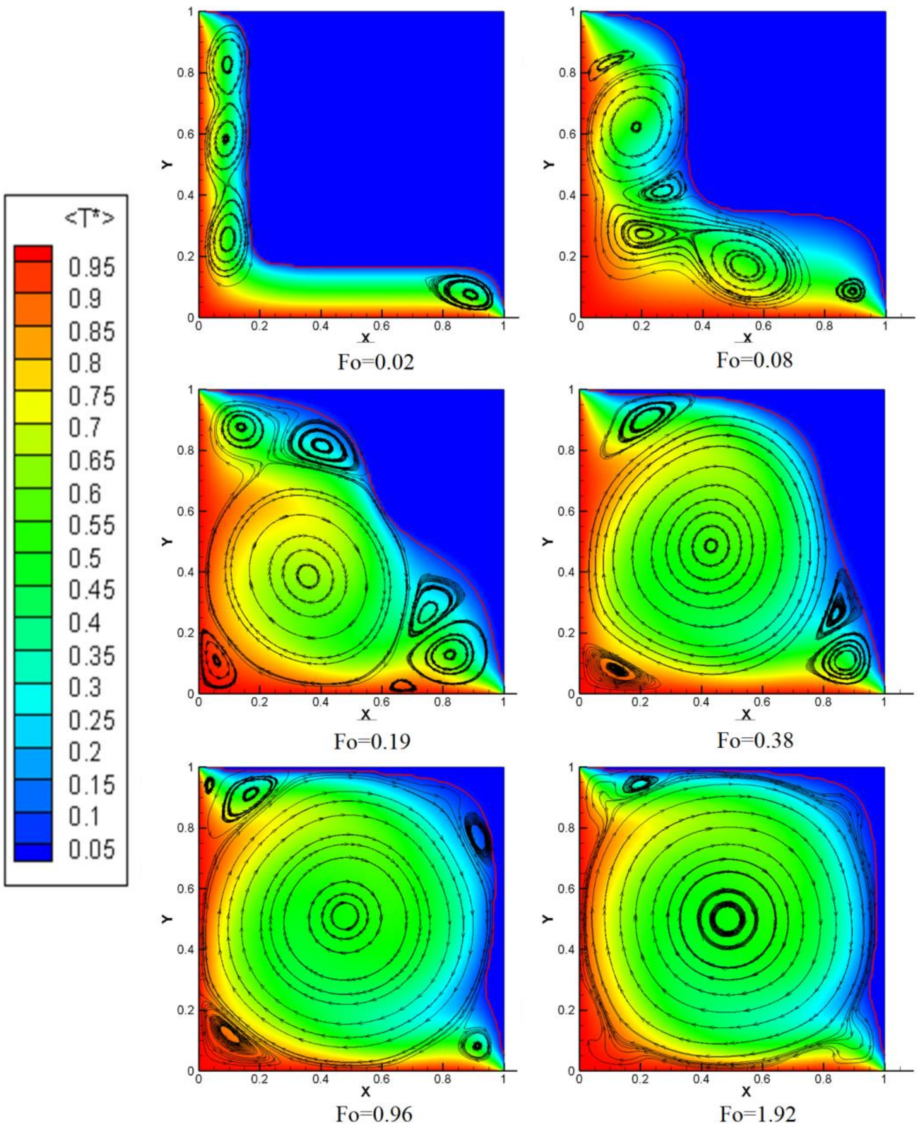

(b)

Figure 5.20: Evolution of isotherms with streamlines at *Pr*=0.001 a) *Ra*=$10^5$ and b) *Ra*=$10^6$.

Figure 5.20 represents the flow and thermal behaviour in melt zone for *Pr*=0.001. At *Fo* =0.02, the temperature isotherms are symmetrical in nature which signifies the conduction governs the melting process. After that with increase of time, the convection plays an important role in the cavity which dominates conduction melting and interface geometry changes its pattern due to flow circulation under natural convection. At *Fo* beyond 0.96, the temperature profiles do not change much as the rate of thermal flux from boundary to interface gradually approaches a fixed value with time in the molten zone of the cavity. It is seen from Fig. 5.20(a) and 5.20(b) that the shape of interface turns into convex to concave after *Fo*=0.19. The flow characteristics at *Ra*=$10^5$ is depicted in Fig. 5.20a in which a family of streamlines are presented with dimensionless time. In the early stage of melting, clock-wise circulation of stream line in the vicinity of left wall is observed in a narrow molten region. As the time increases the primary vortex in the melt zone grows as well as stagnation zone appears at the solid wall at *Fo*=0.08. The secondary and tertiary vortex appears due to very low velocity near the wall. Figure 5.20b shows the temperature profiles and streamlines at *Ra*=$10^6$. At a higher Ra the rate of melting increases and the melt zone grows faster and it is clearly seen that the convection current in the melt zone is more which affects the flow pattern in the melt zone.

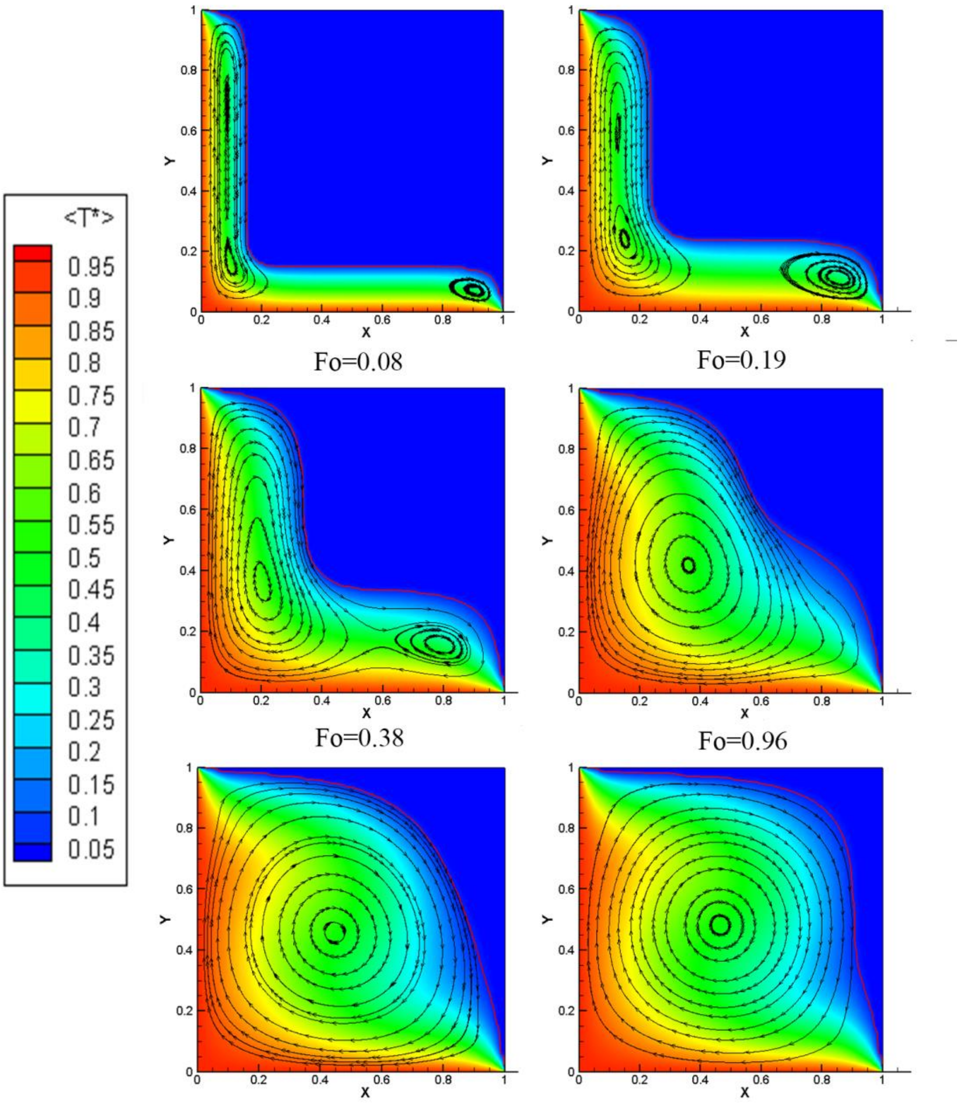

Fo=0.08 Fo=0.19

Fo=0.38 Fo=0.96

Fo=1.92 Fo=3.84

(a)

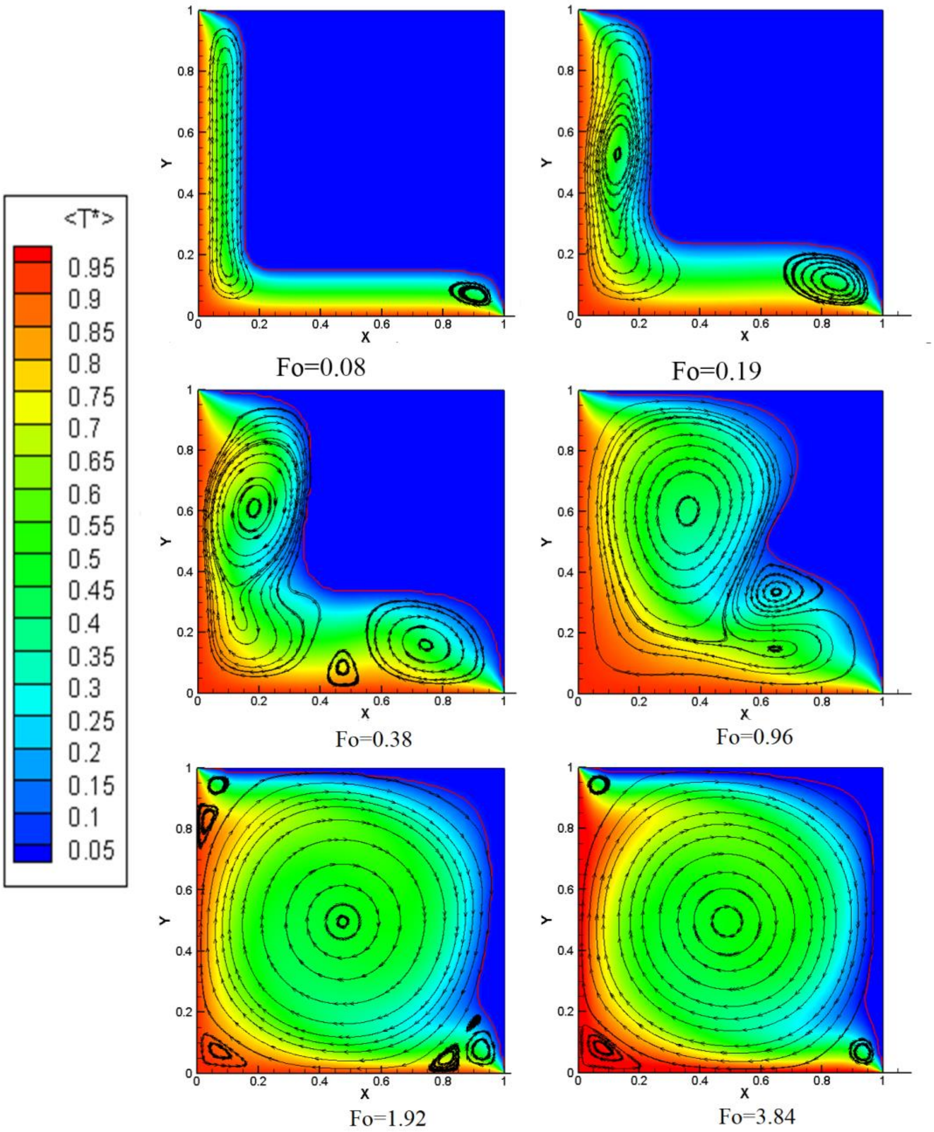

(b)

Figure 5.21: Evolution of isotherms with streamlines at *Pr*=0.005 a) *Ra*=$10^5$ and b) *Ra*=$10^6$.

Figure 5.21 represents the isotherms and streamlines plots in melt zone for *Pr*=0.005. As *Ra* increases more convective rolls appear in the melt zone for *Fo*=0.38. The interface front is distorted at high *Ra* as convection is more pronounced. The interface front turns into convex to concave at *Fo*=0.96.

Figure 5.22 represents a family of isotherms and streamlines at *Pr*=0.01. As can be seen from Fig. 5.22a, the primary cell initially fills the vertical melt zone because buoyancy is more apparent as a result of the hot fluid moving upward from the bottom as well as the left side walls. A secondary cell appears at the right bottom corner of the melt zone and it grows with time. At *Fo*=0.96 two cells are merged and rotate clockwise in the entire melt zone as a single cell. Figure 5.22b demonstrates comparative faster melting at high *Ra*=$10^6$. At *Fo*=0.04 multi Rayleigh –Benard cells apper in the melt zone and number of cells increases in the melt zone compared to the earlier observation. As *Ra* increases the flow field is getting more complex in nature. The inversion of the convex to concave melting front occurs at *Fo*=1.92.

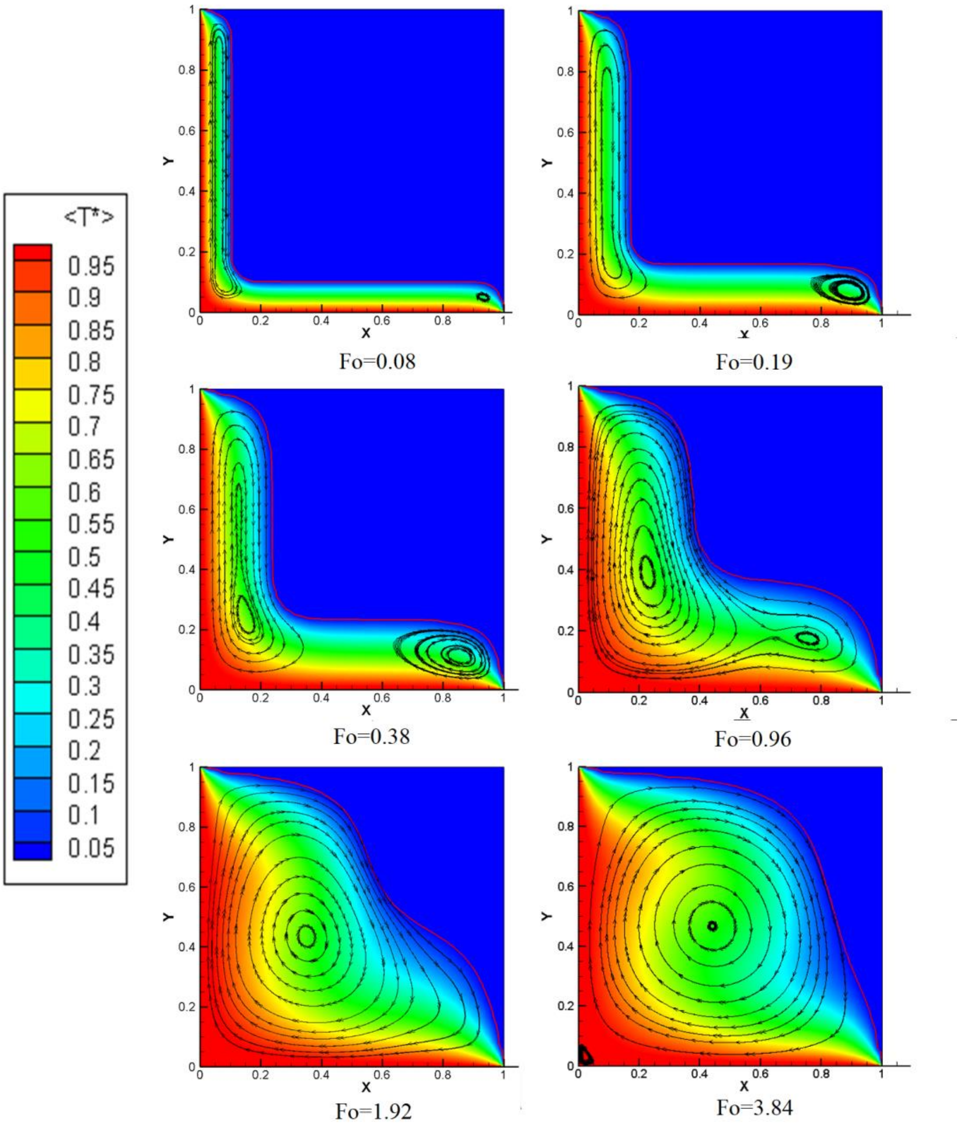

Fo=0.08

Fo=0.19

Fo=0.38

Fo=0.96

Fo=1.92

Fo=3.84

(a)

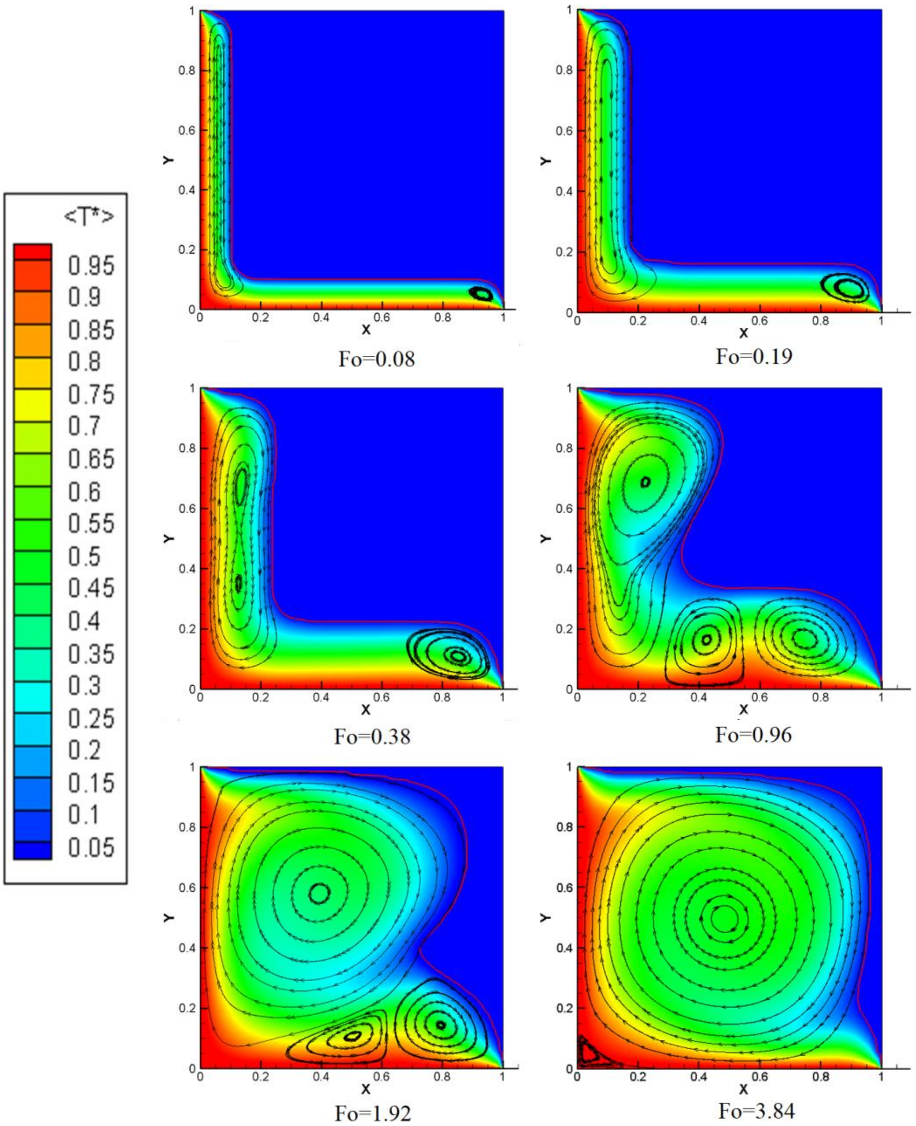

(b)

Figure 5.22: Evolution of isotherms with streamlines at *Pr*=0.01 a) *Ra*=$10^5$ and b) *Ra*=$10^6$.

Figure 5.23 depicts the average *Nu* at the interface for different *Pr*. The average heat flux at interface increases with increasing of *Pr*. Figure 5.23a shows the variation of average Nu over time and it is more as *Ra* increases beyond *Fo*=0.02. The average heat flux increases beyond *Fo*=2 for *Pr*=0.005 and *Ra*=$10^6$ which is represent in Fig. 5.23b. The average *Nu* for both *Ra* shows a similar nature for *Pr*=0.01 as depicted in Fig. 5.23c.

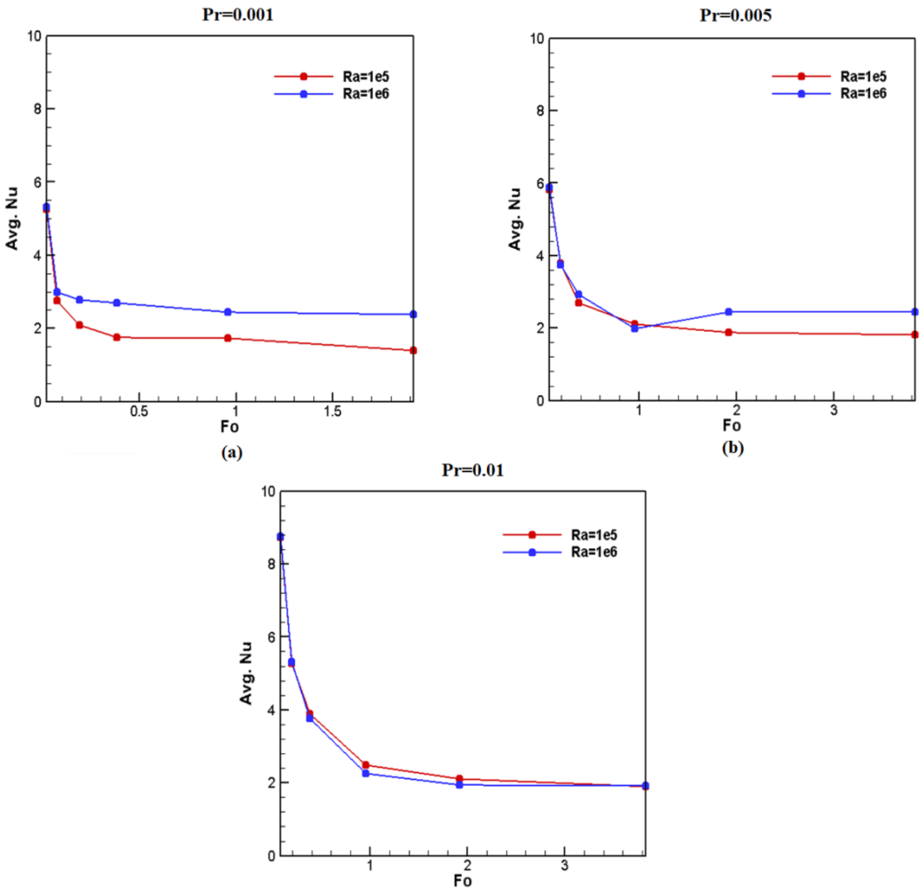

(a) (b)

(c)

Figure 5.23: Average Nusselt number at interface

## 5.4 Closure

In this work, corner melting and solidification of low Prandtl number material in a square cavity has been simulated using total enthalpy based lattice Boltzmann method. Comparison has been made between corner melting heated from bottom and corner melting heated from top boundaries. For the bottom-side heated case, initially Benard type convective cells appear in the side wall as well as in the bottom wall at *Ra* $=10^7$. With evolution of time melt region grows and occupying the cavity, finally there is one primary roll covering the entire domain. In case of the top-side corner melting, Benard cells are seen on the side walls which are limited in numbers i.e. maximum of two only. Here again one primary cell fills up the cavity as melting zone grows occupying the cavity. The study reveals that for both the cases initially convex melt front is formed which turns into concave shape after about *Fo*=0.5. For both the cases, the melting rate is high till *Fo*=0.8 which reduces afterwards. The heat flux in the bottom-side heated cavity is higher than the top-side heated cavity. The present study encourages in depth investigation within three dimensional cavity as the scope for future work.

Similarly, corner solidification has been studied under the influence of convection using enthalpy based LBM. The effect of natural convection on the solidification front varying time has been presented using two different *Ra* numbers. It is observed from the study that, initially the solidification occurs due to conduction and then convection comes into the attention as time increases. With the increasing *Ra* number, the solidification front moves faster under the effect of convection.

Corner melting in a square cavity has been observed with a range of $Pr \in [0.001, 0.01]$ and $Ra \in [10^5,10^6]$ using modified lattice Boltzmann method. While the melting processes the flow is dominated by natural convection, complex convective rolls are observed in the flow field at higher *Ra*. The study reveals that in corner melting initially convex melt front is formed which turns into concave shape after about *Fo*=0.19, 0.96 and 1.92 for *Pr*=0.001, 0.005 and 0.01 respectively. The heat flux at interface increases with increasing *Pr*.

## CHAPTER 6

# MACROSEGREGATION OF BINARY ALLOY

During solidification of binary alloy three distinct zones are encountered which are solid zone, liquid zone and mushy region in which solid-liquid co-exist. Solidification of alloy comprises of complex flow dynamics in the liquid zone, distribution of solute and solid fraction in mushy region. For a binary isomorphous alloy, as an example, *Ni*-*Cu* system, a component can dissolve at a certain proportion in the other component for both liquid and solid phases. Their equilibrium phase diagram representing the relation between temperature and percentage of the component is shown in Fig. 6.1(a) and morphological changes with decrease in temperature are pictorially shown in Fig. 6.1(b) as during solidification the system passes from liquid to solid phase through to phase mushy region. The nomenclature of lever rule is expressed in Fig. 6.1 (c).The mushy region is enveloped between two lines known as liquidus and solidus lines. The distribution of solid fraction $(f_s)$ varies from zero to one in the mushy zone where the solid fraction in liquid zone and solid zone is designated as zero and one respectively.Along these two lines composition varies with temperature. Above liquidus line alloy is in molten state and below solidus line alloy is in solid state. Composition atany point in the two-phase zone is found out from the tie line which is formed by intersection of a horizontal line with the liquidus and the solidus line as shown in Fig. 6.1 (c).

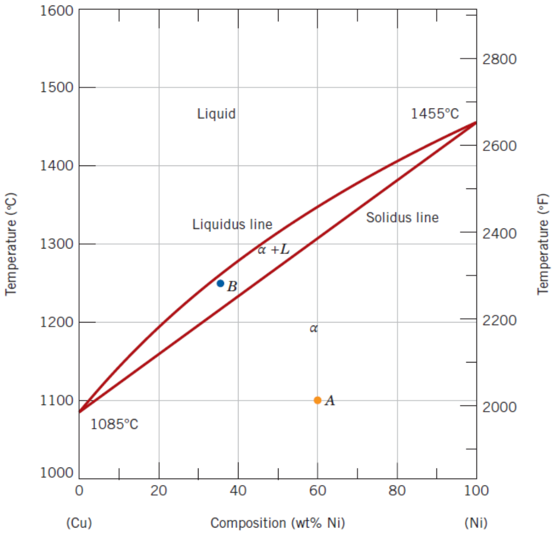

(a)

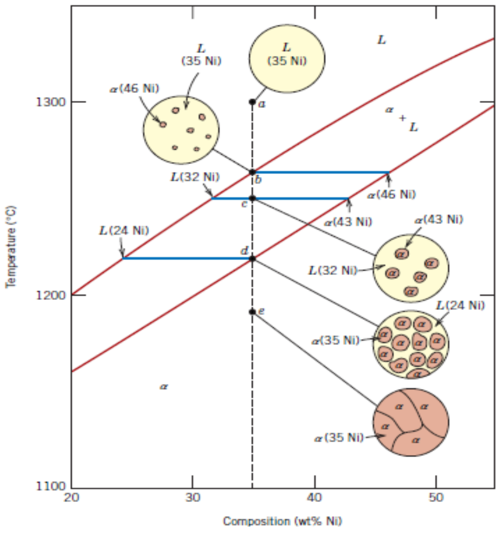

(b)

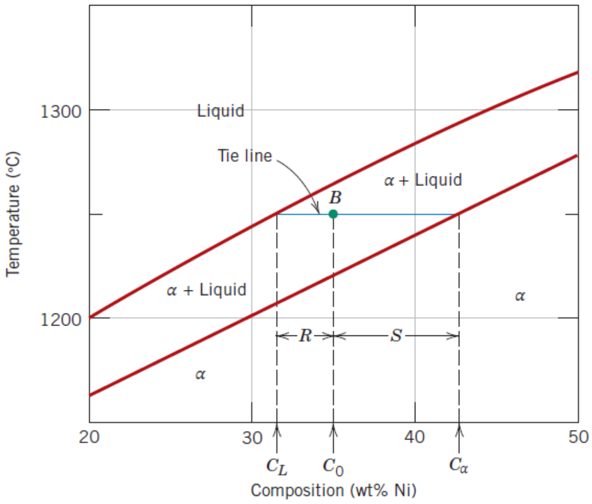

(c)

Figure 6.1 a) Phase diagram of binary alloy *Ni-Cu* system, b) Schematic of microstructure development during equilibrium cooling of *Ni-Cu* binary alloy and c) Nomenclature for use in lever rule reproduced from (Callister and Rethwisch, 2007).

From the ratio of the two segments of the tie line divided at a nodal point B as given in Fig. 6.1 (c) in the mushy region composition can be calculated using lever rule. Liquid fraction is given by as

$$W_L = \frac{S}{R+S} \tag{6.1}$$

and, solid fraction is given by,

$$W_\alpha = \frac{R}{R+S} \tag{6.2}$$

where R and S are the distances of solidus line and liquidus line from the point of interest.

## 6.1 Objective of the Work

Macro segregation during solidification of alloy is a complex process. Extent of macro segregation in the mushy region is a matter of concern because it causes casting defect. As the mushy region is highly non-homogeneous and changes its morphology with time, complex models and different numerical methods have been employed to study its dynamics. As solidification of molten alloy starts due to heat loss from domain boundary, boundary temperature has got very important effect on quality of casting process. The objective of the present study is to investigate effect of heat loss boundary temperature on macro-segregation of mushy region of alloy solidification.

## 6.2 Problem Identification

Investigation on macro segregation problems relating to thermo-physical dynamics of mushy region during solidification of binary alloy has been a point of attraction to many researchers (Flemings, 2000; Lesoult, 2005; Voller et al., 1989) which involve mathematical modelling and numerical simulation using different algorithms. There are a few works are available to study the mushy zone dynamics and macro-segregation in the mushy zone using hybrid LBM (Ohno and Sato, 2018b)  In the present work, 2D simulation of *Ni-Cu* (50-50%) alloy has been taken up to understand the effect of boundary conditions on the morphology of mushy region dynamics. As solidification process has numerous applications in metallurgy, geology and other disciplines where environment may not be always predictable and complex boundary conditions which vary with time and space, it is an important area to investigate mushy region dynamics and segregation within it for study of the concerned physical processes. The schematic of the problem is presented in Fig. 6.2

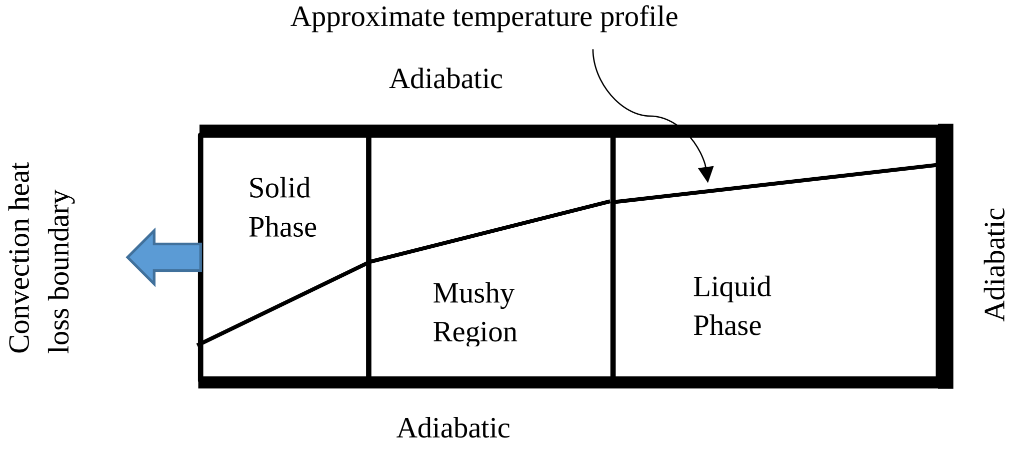

Figure 6.2: Schematic of solidification in alloys.

Figure 6.2 shows schematically a domain for study of solidification of an alloy where a mushy zone is formed in between the solid and liquid zones. The composition of the alloy during solidification shall be changing in these zones mainly governed by the phase diagram and the cooling dynamics.

The relative thickness of solid layer and mushy layer depends on the boundary conditions through which energy is lost, and thermo-physical properties of the melt phase. Due to density difference in the liquid in the mushy layer generates convection current. Density difference may take place due to combined thermal gradient and concentration gradient and results in thermo-solutal convection. The interfacial compositions, $C_l(T)$, for the liquid and

$C_s(T)$ for the solid at any instant of time are connected via local tie-line in the phase diagram's liquidus and solidus line. Using lever rule relative composition and weight fraction in the two-phase zone can be calculated. A representative phase diagram of *Ni-Cu* alloy and compositional change along the two phase zone are reproduced from (Callister and Rethwisch, 2007)

## 6.3 Mathematical Model

The problem under consideration involves a square cavity filled with *Ni-Cu* alloy which is undergoing cooling and solidification. The following set of equations governs the transport processes.

Continuity equation in liquid and mushy zone

$$\frac{\partial u_m}{\partial x}+\frac{\partial v_m}{\partial y}=0 \tag{6.3}$$

Non-conservative form of $x$ and $y$-momentum equations are

$$\frac{\partial u_m}{\partial t}+u_m\frac{\partial u_m}{\partial x}+v\frac{\partial u_m}{\partial y}=-\frac{1}{\rho_m}\frac{\partial p}{\partial x}+\nu\left[\frac{\partial^2 u_m}{\partial x^2}+\frac{\partial^2 u_m}{\partial y^2}\right]+\frac{\mu u_m}{F_x}+g_x \tag{6.4}$$

$$\frac{\partial v_m}{\partial t}+u_m\frac{\partial v_m}{\partial x}+v_m\frac{\partial v_m}{\partial y}=-\frac{1}{\rho_m}\frac{\partial P}{\partial y}+\nu\left[\frac{\partial^2 v_m}{\partial x^2}+\frac{\partial^2 v_m}{\partial y^2}\right]+\frac{\mu v_m}{F_y}+g_y \tag{6.5}$$

where, $F_x$ and $F_y$ are resistance terms in mushy region.

The gravitational term in the Eq. (6.4) is

$$g_x=0 \tag{6.6}$$

The gravitational term in Eq. (6.5) associated with combination of thermal and solutal buoyancy effect (Lesoult, 2005) which is written as

$$g_y=\beta_T\left(T-T_0\right)+\beta_C\left(C-C_0\right) \tag{6.7}$$

Energy equation in terms of temperature is written as

$$\frac{\partial T}{\partial t}+u_m\frac{\partial T}{\partial x}+v_m\frac{\partial T}{\partial y}=+\alpha\left[\frac{\partial^2 T}{\partial x^2}+\frac{\partial^2 T}{\partial y^2}\right]-\frac{\lambda}{c_P}\frac{\partial f_s}{\partial t} \tag{6.8}$$

where, solid fraction $(f_s)$ is written as

$$f_s=\frac{T_L-T}{T_L-T_S} \tag{6.9}$$

Species continuity equation for secondary phase

$$\frac{\partial C_k}{\partial t} + u\frac{\partial C_k}{\partial x} + v\frac{\partial C_k}{\partial y} = +D_k\left[\frac{\partial^2 C_k}{\partial x^2} + \frac{\partial^2 C_k}{\partial y^2}\right] \tag{6.10}$$

where, $C_k$ is the secondary phase (*Ni*) in mushy region and $D_k$ is mass diffusivity of component *Ni*.

The initial and boundary conditions are given as

***Initial condition***

$$\left.\begin{array}{ll} \text{at } t=0, & \\ u_m=v_m=0 & \text{for } 0 \le x \le L; 0 \le y \le H; \\ T=T_i & \text{for } 0 \le x \le L; 0 \le y \le H; \\ C_k=C_i & \text{for } 0 \le x \le L; 0 \le y \le H; \end{array}\right] \tag{6.11}$$

***Temperature Boundary conditions***

$$\left.\begin{array}{ll} t > 0 & \\ \text{at } x=0, x=L, & u_m=v_m=0 \\ \text{at } y=0, y=H, & u_m=v_m=0 \\ \text{at } x=0, & T=T(0,y) \\ \text{at } x=L, & \dfrac{dT}{dx}=0 \\ \text{at } y=0, y=H, & \dfrac{dT}{dy}=0 \\ \textit{Concentration boundary conditions} & \\ \text{at } x=0, & C=C(1,y) \\ \text{at } x=L, & C=C(1,y) \\ \text{at } y=0, y=H, & C=C(1,x) \end{array}\right] \tag{6.12}$$

## 6.4 Numerical Scheme and Solution Methodology

The present simulation has been performed using hybrid lattice Boltzmann method (LBM) in which finite difference method (FDM) is coupled with (LBM). The flow field is simulated using LBM which is discussed in chapter 3. The thermal field and the species continuity equation are solved using FDM. The details of FDM implementation are now discussed.

## *Grid Generation*

The solution domain is considered as 2-D square on which 100x100 grid is generated which is shown in Fig. (6.3).

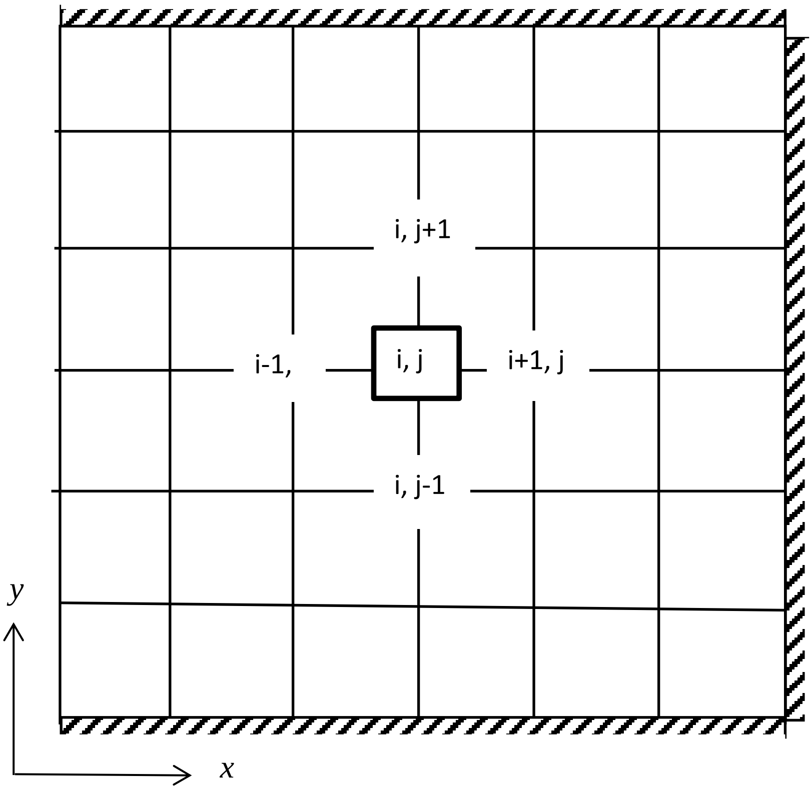

Figure 6.3: Schematic of grid generation on a square solution domain

A general node (i,j) and its associated nodes forming a template is marked on Fig.6.3. where the top, bottom and right boundaries are insulated. The left boundary is subjected to a temperature below melting point for heat removal. Different spatial temperature distributions are applied at left boundary to study its effect on rate of growth of solid region and mushy zone, and predicting corresponding macro segregation in terms of weight fraction. The central difference scheme is applied to solve energy equation and species continuity equation. *x* and *y* component momentum equations have been solved applying LBM method which has been already described in chapter 3.to get the velocity field. Combining FDM with LBM formulations leads to a hybrid LBM for obtaining solutions of the governing equations. Implementation of boundary condition in Hybrid LBM has been performed on the boundary nodes. The bounce back boundary condition has been used for solid and moving boundary in LB method while temperature and concentration boundary conditions are imposed on the boundary nodes using conventional FDM.

## *Finite Difference Numerical Formulation*

Semi-implicit finite difference scheme at a general node (i,j) is given below where velocity terms are considered future level (n+1 level).

***Energy equation***

$$\begin{aligned}&\frac{T_{i,j}^{n+1}-T_{i,j}^{n}}{\Delta t}+u_{i,j}^{n+1}\frac{T_{i+1,j}^{n}-T_{i-1,j}^{n}}{2\Delta x}+v_{i,j}^{n+1}\frac{T_{i,j+1}^{n}-T_{i,j-1}^{n}}{2\Delta y}\\&=\alpha_{i,j}^{n}\left[\frac{T_{i-1,j}^{n}-2T_{i,j}^{n}+T_{i-1,j}^{n}}{\Delta x}+\frac{T_{i,j-1}^{n}-2T_{i,j}^{n}+T_{i,j+1}^{n}}{\Delta y^{2}}\right]-\frac{H_f}{C_P}\frac{f_{si,j}^{\,n+1}-f_{si,j}^{\,n}}{\Delta t}\end{aligned} \qquad (6.13)$$

which may be rearranged as,

$$\begin{aligned}T_{i,j}^{n+1}&=-u_{i,j}^{n+1}\Delta t\frac{\left(T_{i+1,j}^{n}-T_{i-1,j}^{n}\right)}{2\Delta x}-v_{i,j}^{n+1}\Delta t\frac{\left(T_{i,j+1}^{n}-T_{i,j-1}^{n}\right)}{2\Delta y}\\&+\alpha_{i,j}^{n}\Delta t\left[\frac{T_{i-1,j}^{n}-2T_{i,j}^{n}+T_{i-1,j}^{n}}{\Delta x}+\frac{T_{i,j-1}^{n}-2T_{i,j}^{n}+T_{i,j+1}^{n}}{\Delta y^{2}}\right]-\frac{\Delta t H_f}{C_P}\frac{f_{si,j}^{\,n+1}-f_{si,j}^{\,n}}{\Delta t}+T_{i,j}^{n}\end{aligned} \qquad (6.14)$$

Similarly, the final form of species continuity equation may be written as

$$\begin{aligned}C_{ki,j}^{\,n+1}&=-u_{i,j}^{n+1}\Delta t\frac{\left(C_{ki+1,j}^{\,n}-C_{ki-1,j}^{\,n}\right)}{2\Delta x}-v_{i,j}^{n+1}\Delta t\frac{\left(C_{ki,j+1}^{\,n}-C_{ki,j-1}^{\,n}\right)}{2\Delta y}\\&+\frac{D_k}{\rho}\Delta t\left[\frac{C_{ki-1,j}^{\,n}-2C_{ki,j}^{\,n}+C_{ki-1,j}^{\,n}}{\Delta x^{2}}+\frac{C_{ki,j-1}^{\,n}-2C_{ki,j}^{\,n}+C_{ki,j+1}^{\,n}}{\Delta y^{2}}\right]+C_{ki,j}^{\,n}\end{aligned} \qquad (6.15)$$

The density at a node is linked to the temperature as (Tesfaye and Taskinen, 2010)

$$\rho_{i,j}^{n+1}=9040-0.00021T_{i,j}^{n+1} \qquad (6.16)$$

## *Solution Algorithm*

In this hybrid solution method, computational algorithm comprises of following steps.

1) The time step $\Delta t$ is so calculated that the CFL value is kept lower than $10^{-3}$ to ensure stable solution. To achieve this automatic $\Delta t$ control algorithm is used at each time step, which actually yields a range of $\Delta t$ from 0.01 to 0.001s.
2) To start the calculations, energy equation is solved to get temperature field.
3) Based on the temperature field, density distribution is calculated at nodal points using Eq. (6.16).
4) Depending on density distribution and using LBM method velocity field is calculated.
5) Once velocity field is obtained energy equation, and species continuity equation are solved to obtain new temperature field, concentration field, and density distribution.
6) Solid fraction is calculated using Eq.(6.9)

7) From temperature distribution solid zone, mushy zone, and liquid zone are identified.

8) Within the mushy zone segregation profile is calculated using lever rule.

9) Steps 2 to 8 are repeated till the prescribed length of time is complied.

## 6.5 Results and discussion

Solidification of *Ni*-*Cu* (50%-50%) alloy in a square cavity has been studied for different boundary conditions. A hybrid LB model is developed and the dynamics of mushy region is investigated in *Ni*-*Cu* binary alloy.

The present hybrid LB code is validated for a pure fluid system in which the *u* velocity was calculated along the y direction. Figure 6.4 shows the present hybrid LB code validation with well-known analytical solution of Poiseuille flow and numerical model developed by (Ohno and Sato, 2018b). The results show a good agreement with the analytical and numerical solution for Poiseuille flow.

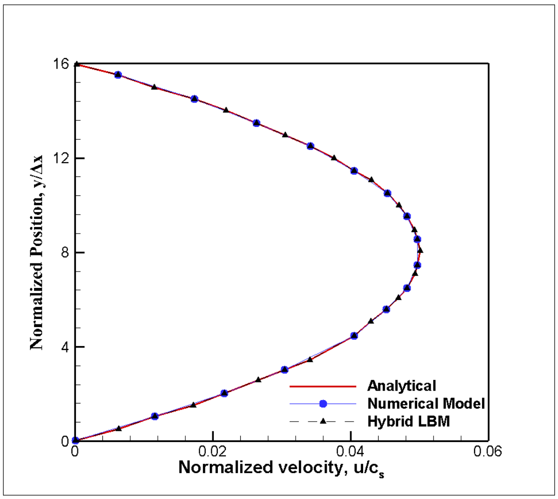

Figure 6.4: Validation of hybrid LBM with analytical Poiseuille flow and numerical model by (Ohno and Sato, 2018a)

Left boundary is subjected to heat loss and other boundaries are insulated. For numerical calculations, thermo-physical properties of *Ni*-*Cu* alloy are given in the following table in terms of order of magnitude which is presented in Table 6.1.

Table 6.1: Physical and thermo-physical data for *Ni*- *Cu* alloy solidification (Porter et al., 2009)

| | |
|---|---|
| **Initial Temperature ($T_i$)** | **1460 $^{0}$C** |
| **Liquidus Temperature ($T_l$)** | 1310 $^{0}$C |
| **Solidus Temperature ($T_s$)** | 1265 $^{0}$C |
| **Melting Point of Pure *Cu*** | 1085 $^{0}$C |
| **Melting Point of Pure *Ni*** | 1455 $^{0}$C |
| **Density ($\rho_m$)** | 9040-0.00021*T ($^{0}$C) |
| **Average Viscosity (µ)** | 4.0 Pa. Sec |
| **Thermal Conductivity (*k*)** | 90.7 W/(m·K). |
| **Specific Heat ($c_p$)** | 0.1 KJ/kg K. |
| **Thermal Diffusivity (α)** | $10^{-5}$ $m^2$/sec |
| **Kinematic Viscosity (ν)** | $10^{-6}$ $m^2$/sec |
| **Mass Diffusivity (*D*)** | $10^{-8}$ $m^2$/sec |
| **Volume expansion coefficient ($\beta_T$,$\beta_c$)** | $10^{-5}$ 1/K, $m^3$/kg |
| **$T_{ref}$** | 1460 $^{0}$C |

In present investigation LBM and semi-implicit finite difference numerical scheme has been employed. Analysis has been carried out in square cavity and up to $5x10^5$ time steps in each case.

It is found that boundary conditions have got prominent effect on the solidification process and phasic profiles are consistent mostly with the boundary conditions. In the present work the effect of different boundary conditions on the mushy region has been studied. The segregation ratio (SR) is defined by the ratio of local volume averaged molar composition of *Ni* and the averaged composition of the *Ni*-*Cu* alloy. The effect of three different boundary conditions on the segregation ratio at the mushy region also studied. The segregation ratio is calculated for all three different types of boundary conditions. The temperature distribution at the left boundary wall can be presented in three ways. The different boundary conditions are shown in Fig. 6.5 (a) through (c).

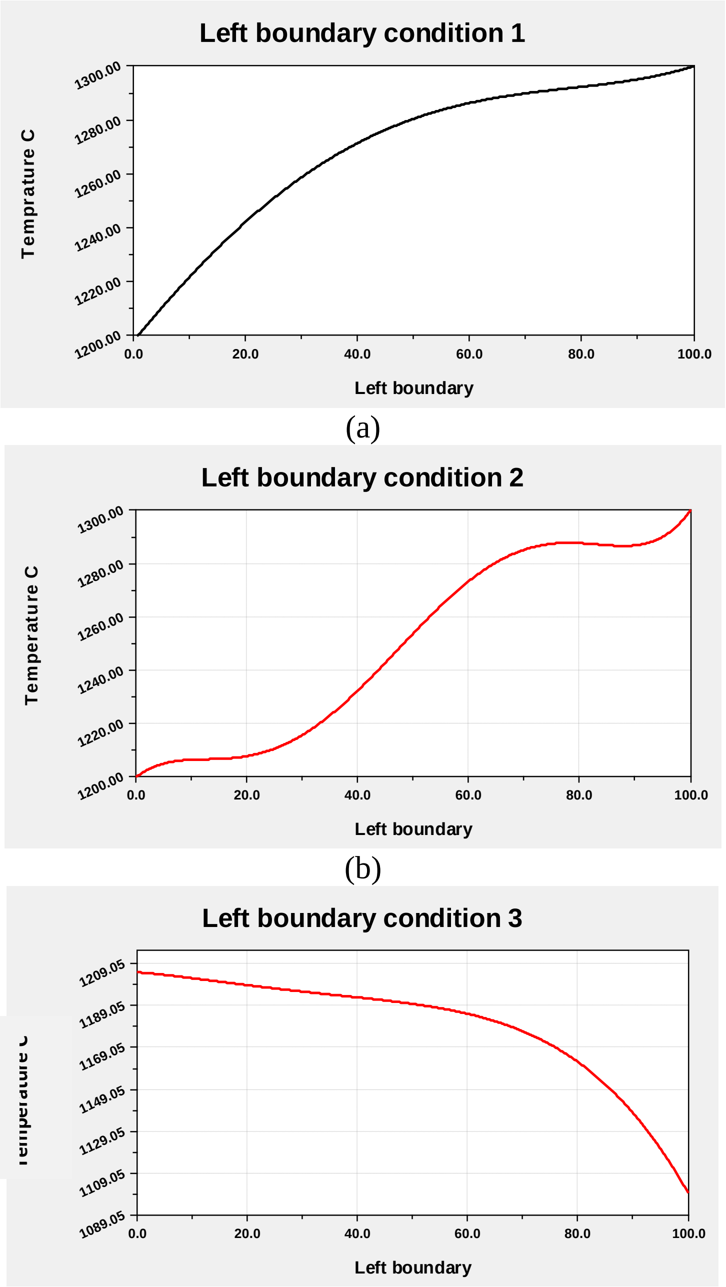

(a)

(b)

(c)

Figure 6.5: Thermal boundary on left wall for a) boundary condition 1, b) boundary condition 2 and c) boundary condition 3.

Figure 6.6 (a) to (c) show the domain of mushy region by plotting isotherms using boundary condition-1. Due to non-uniform boundary condition temperature driving force are different along *y*-axis. Hence rate of heat loss varies accordingly. The shape of mushy region becomes irregular depending on the local rate of heat removal.

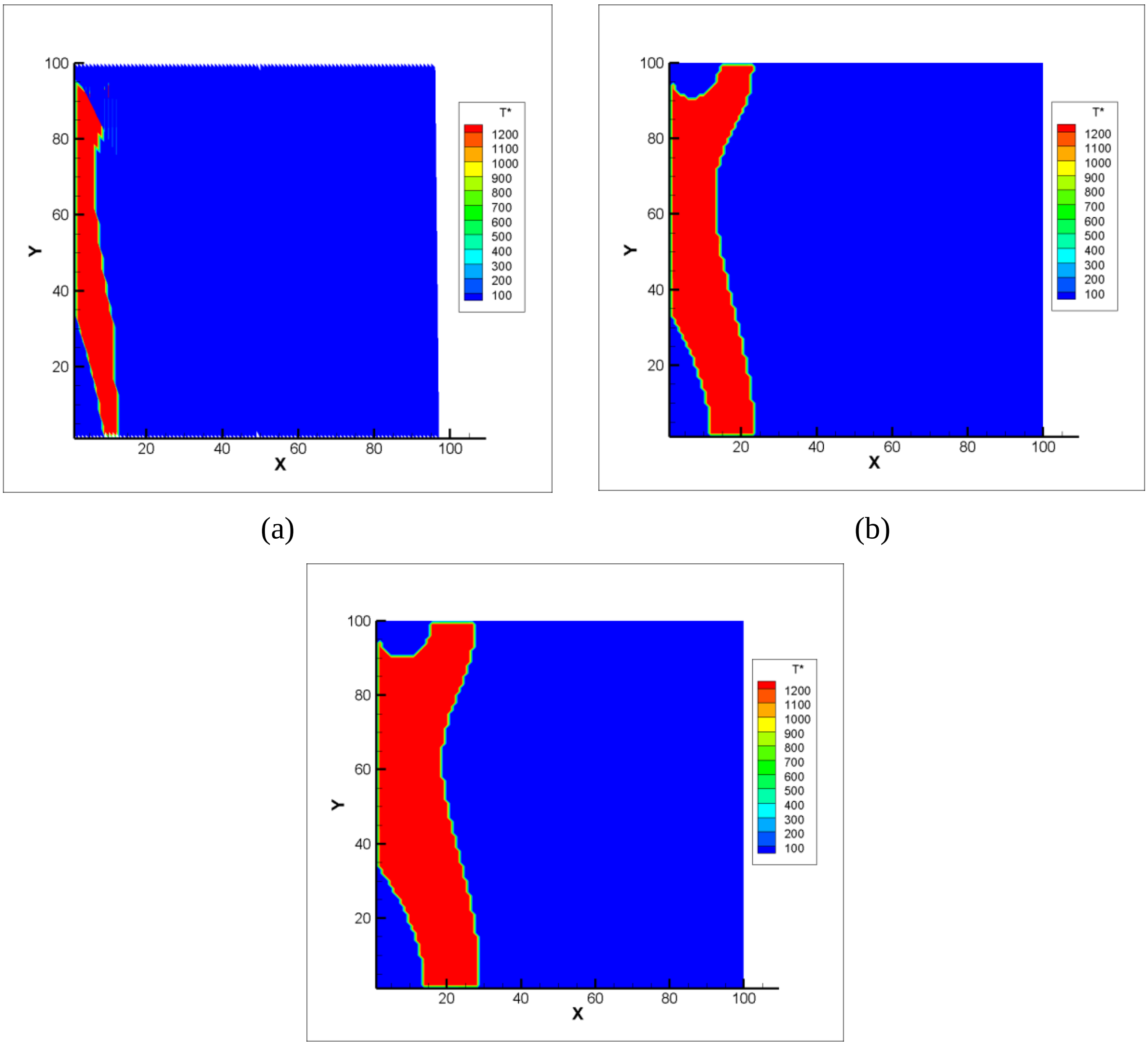

(a)

(b)

(c)

Figure 6.6: Thermal dynamics of mushy region for boundary condition 1 after time steps a) $10^5$ b) $3x10^5$ and c) $5x10^5$.

The temperature distribution in mushy region is presented in Fig. 6.6 (a) to (c) for boundary condition 1. It is found that not much temperature variation is observed in that zone.

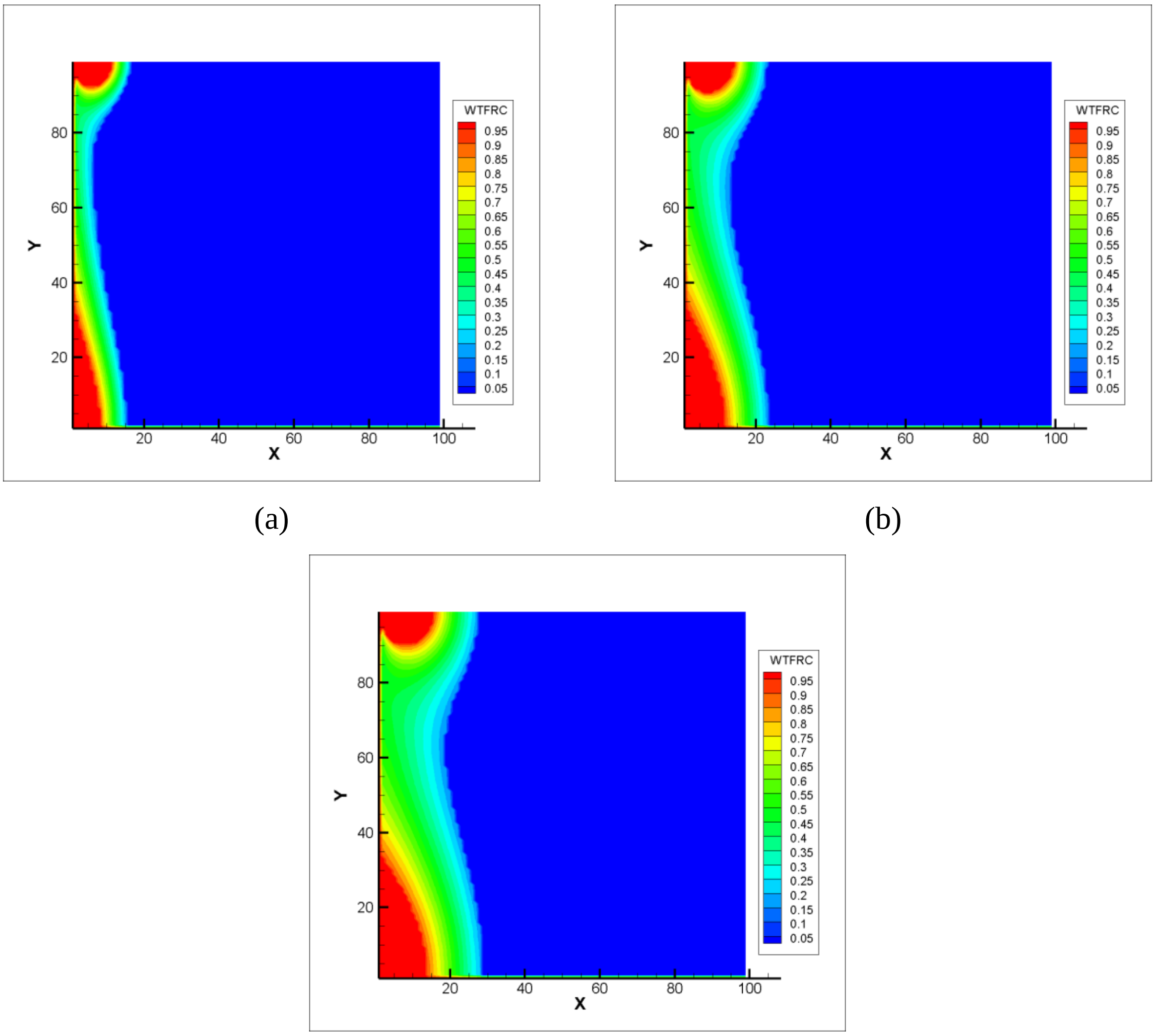

(a) (b)

(c)

Figure 6.7: Solid weight fraction distribution at mushy region using boundary condition 1 after time steps a) $10^5$ b) $3x10^5$ and c) $5x10^5$.

Figure 6.7 (a) to (c) represent the weight fraction distribution in mushy region at different time levels. As time step was taken as 0.0001 to meet the required CFL limit, in such a short time scale solidification processes is conduction dominated and that is reflected in weight fraction distribution in mushy region.

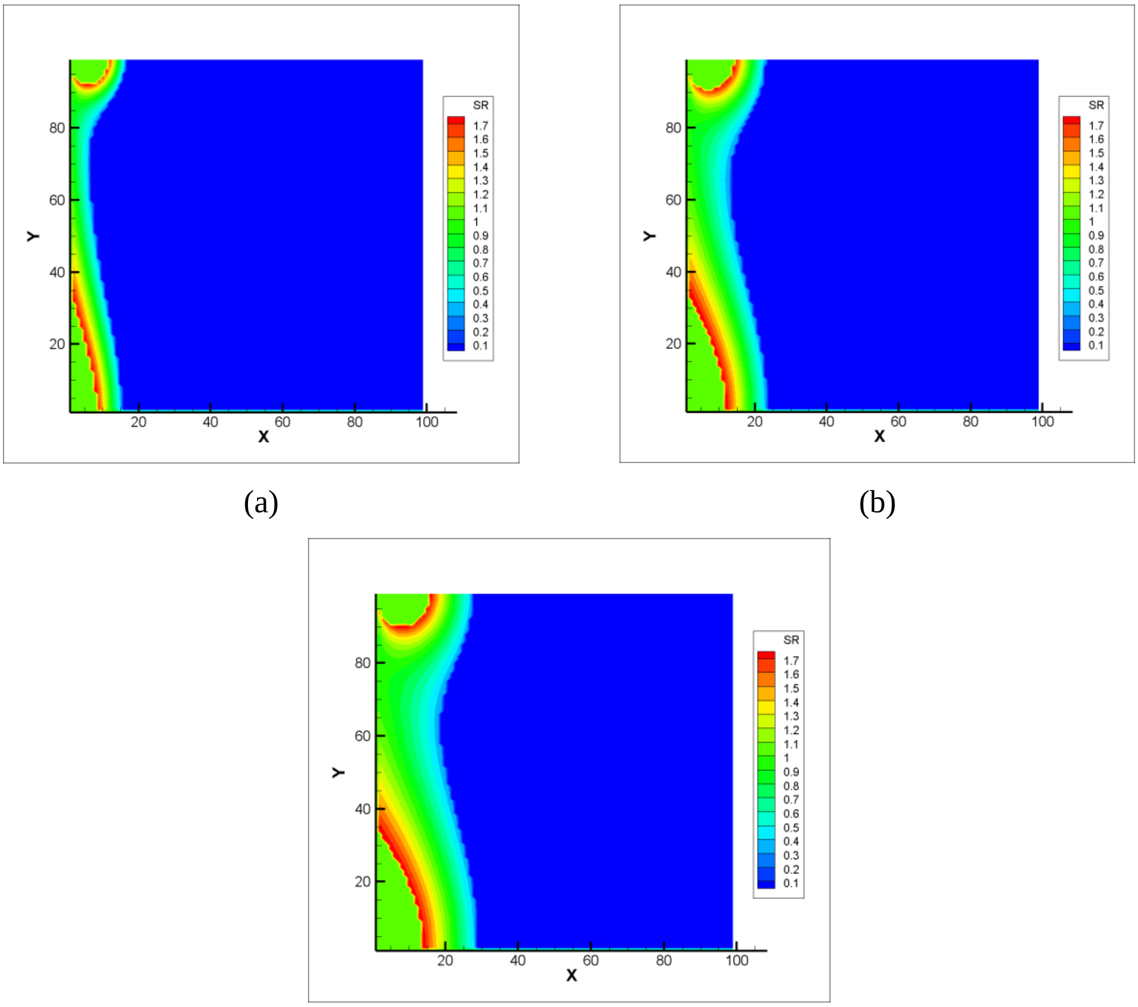

(a) (b)

(c)

Figure 6.8: Segregation ratio in mushy region for boundary condition 1 after time steps a) $10^5$ b) $3x10^5$ and c) $5x10^5$.

Mixing in the concentration field is therefore quite feeble. The segregation for boundary condition 1 is shown in Fig. 6.8.

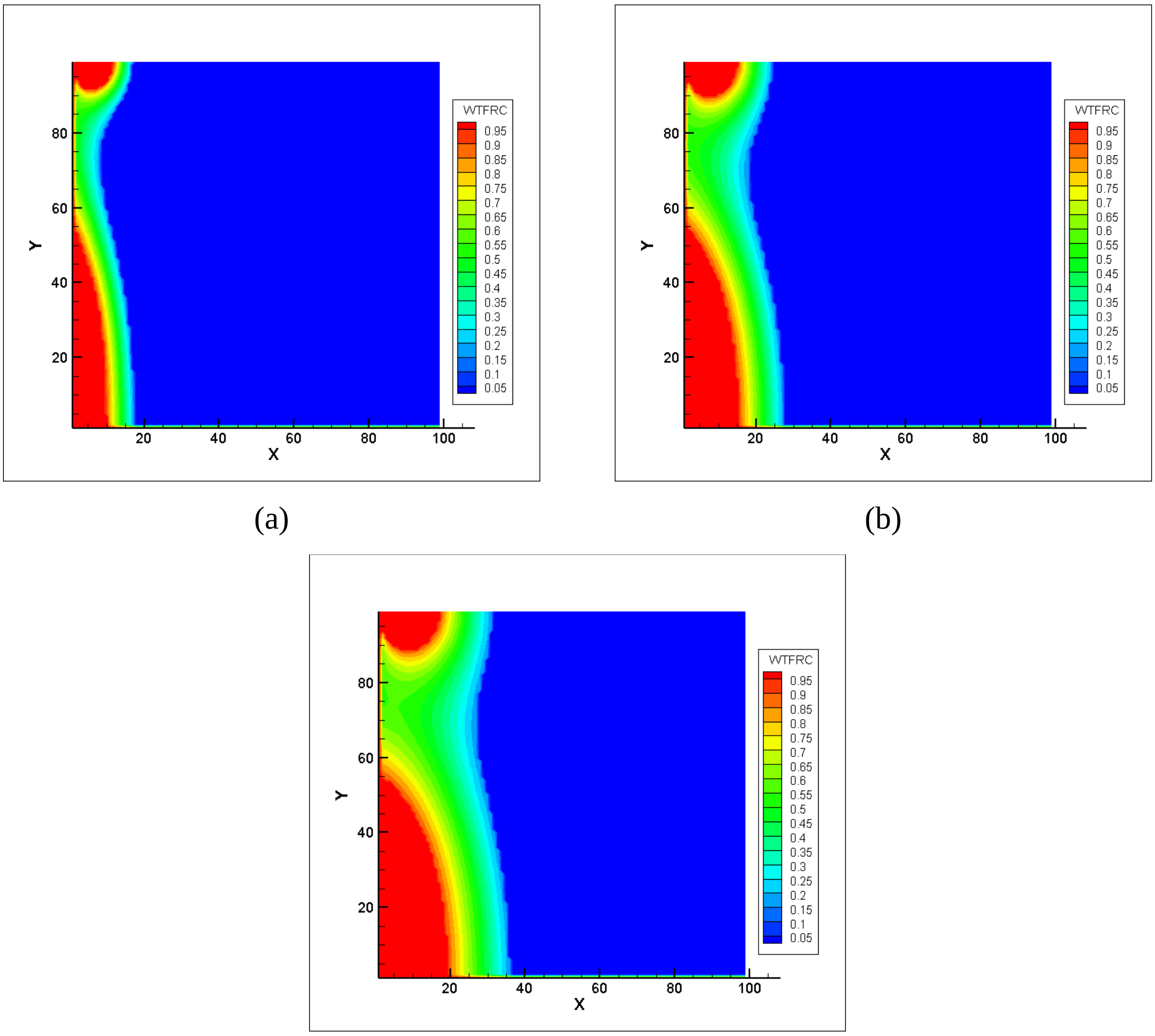

(a) (b)

(c)

Figure 6.9: Solid weight fraction distribution in mushy region for boundary condition 2 after time steps a) $10^5$ b) $3x10^5$ and c) $5x10^5$.

Figure 6.8 shows growth of mushy region with time and corresponding segregation ratio of solute ($Ni$ ).

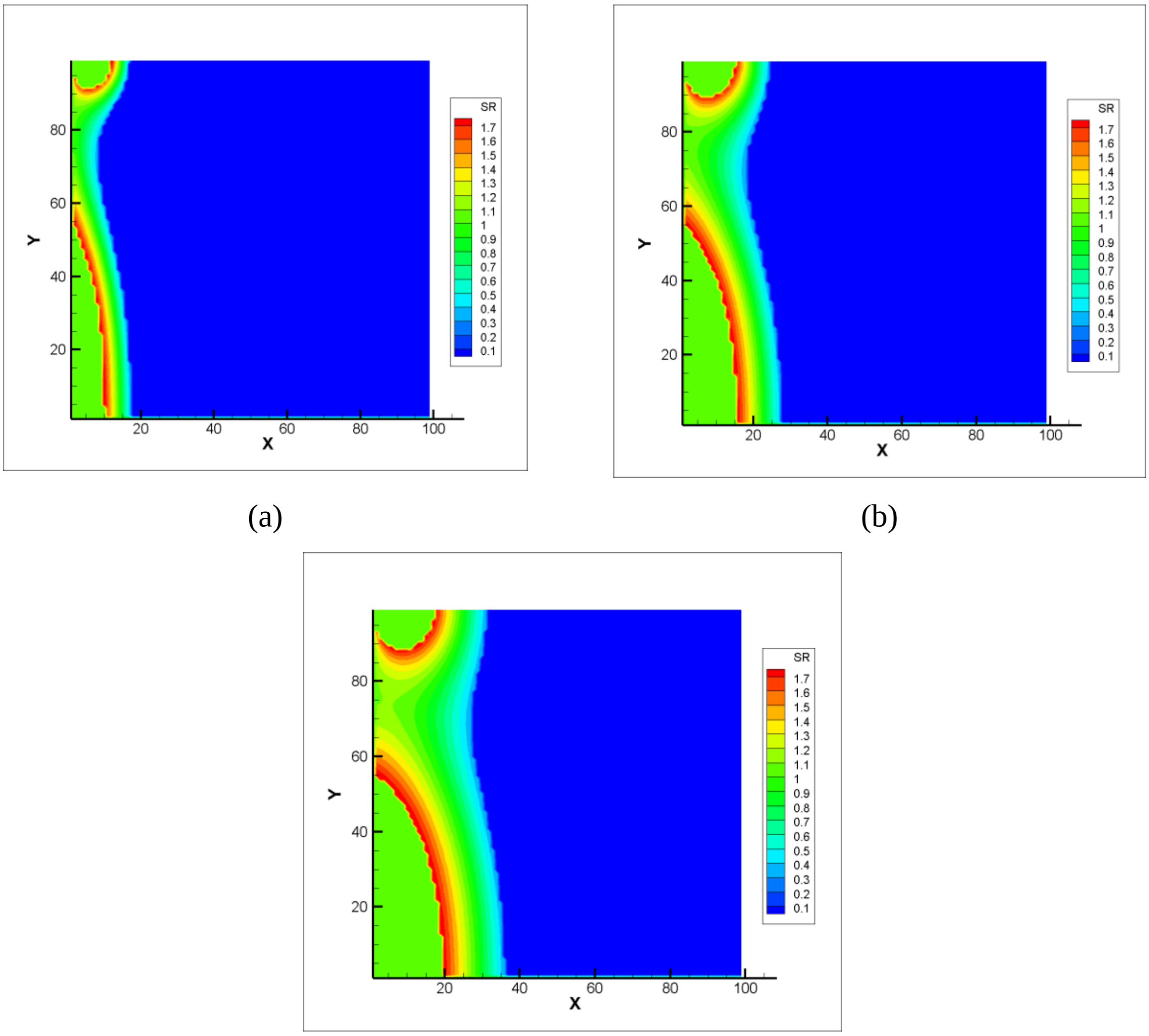

(a) (b)

(c)

Figure 6.10: Segregation ratio in mushy region for boundary condition 2 after time steps a) $10^5$ b) $3\text{x}10^5$ and c) $5\text{x}10^5$.

It is clear from the figures that concentration of solute near the solid interface may be more than 1.0 as per definition of segregation ratio given in (Ohno and Sato, 2018b) local volume averaged molar composition of solute divided by the average composition of the alloy.

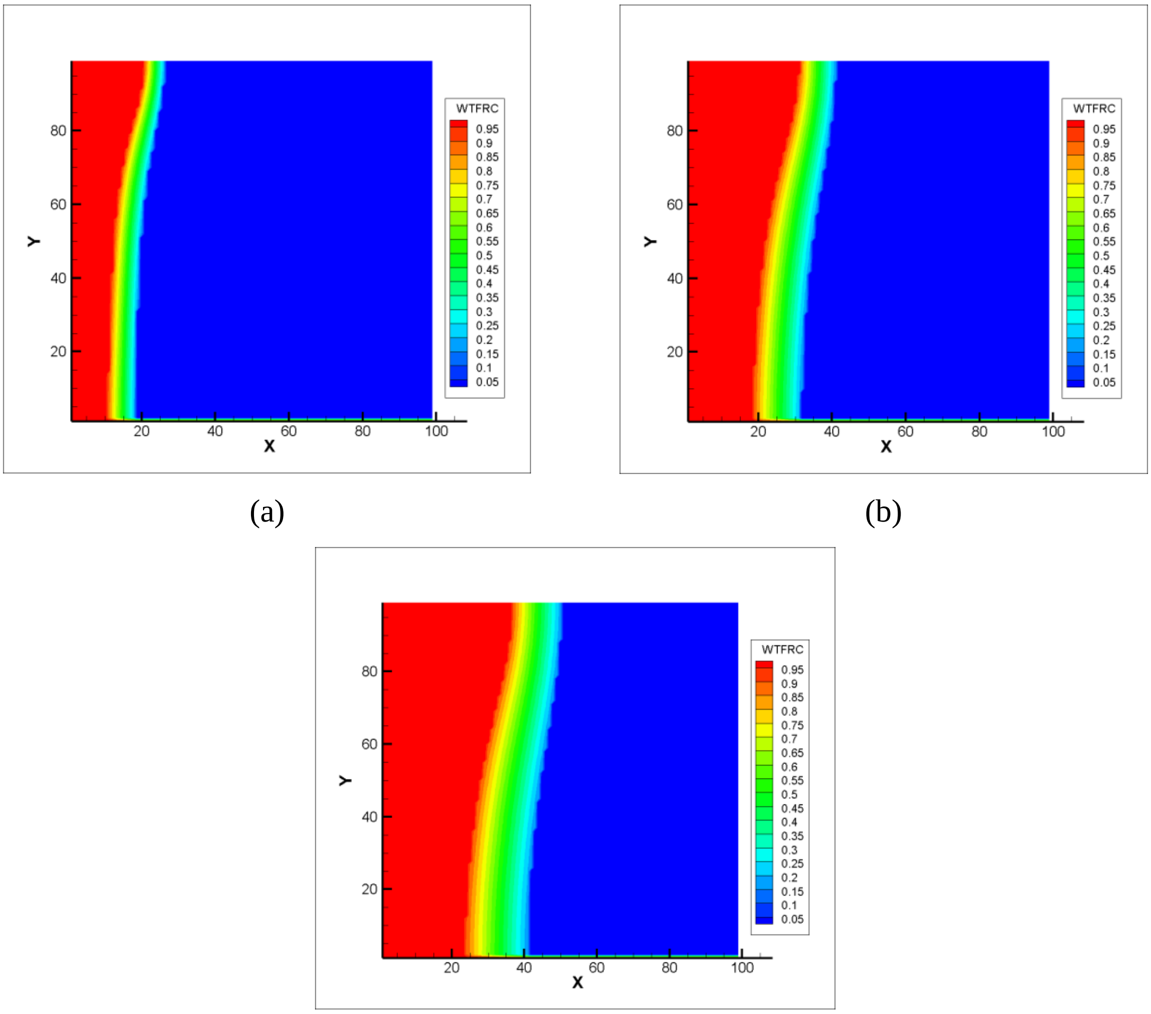

(a) (b)

(c)

Figure 6.11: Solid weight fraction distribution in mushy region for boundary condition 3 after time steps a) $10^5$ b) $3x10^5$ and c) $5x10^5$.

The change of solid weight fraction in the mushy region for boundary condition 2 has been presented in Fig. 6.9. For boundary condition 2 which is wavier in nature, leads to wavy macro-segregation profiles.

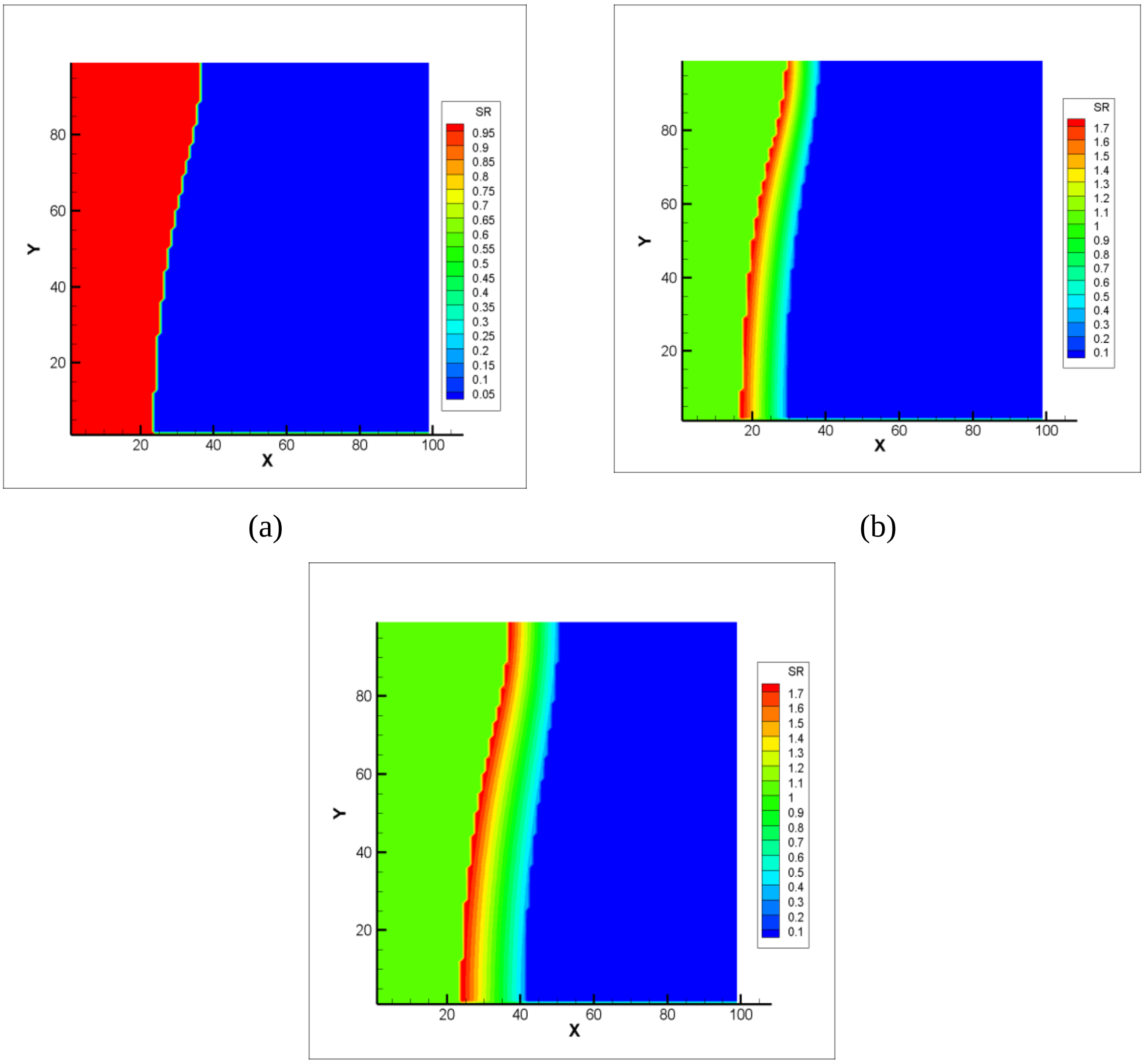

(a) (b)

(c)

Figure 6.12: Segregation ratio in mushy region for boundary condition 3 after time steps a) $10^5$ b) $3x10^5$ and c) $5x10^5$.

The dynamic evolution of mushy region at different time step is shown in Fig. 6.9(a) through (c). It is seen from Fig. 6.9 that the mushy region grows and the distribution of solid fraction in the mushy region changes with time. Though heat loss is only from one side, irregular nature of boundary condition causes non uniform heat flux at the boundary, which not only generates irregular phase boundary , but also criss-cross transfer of momentum, heat and mass transfer become apparent in the vicinity of the boundary. This generates rather a complex local mixing which is not seen with regular boundary conditions.

The segregation ratio for boundary condition 2 is presented in Fig. 6.10.

The nature of temperature distribution for boundary condition 3 is quite different from the earlier two cases. It is seen from Fig. 6.5 (c) that at the bottom of the left wall possesses higher temperature and the temperature decreases at the left wall from bottom to top direction.

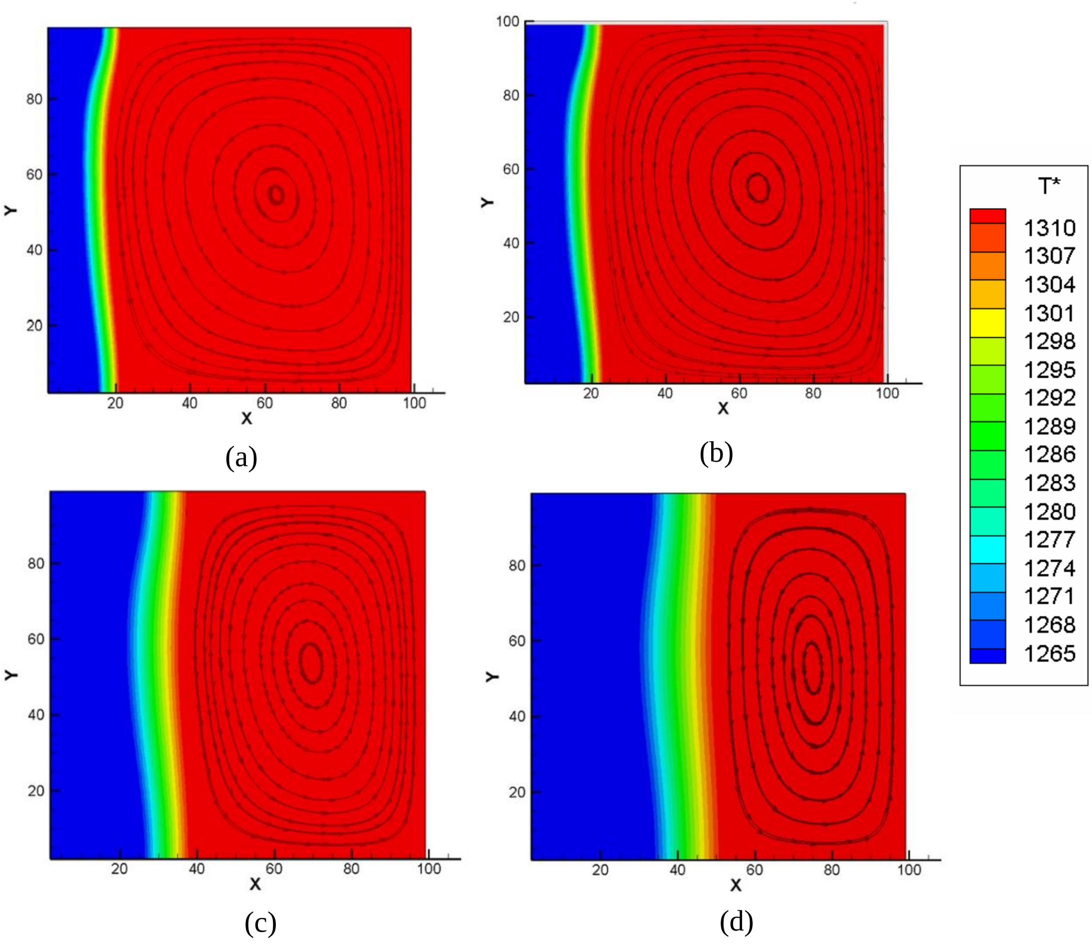

(a) (b)

(c) (d)

Figure 6.13: Temperature distribution in mushy region with velocity field in liquid zone for boundary condition 3 after time steps a)5x$10^4$, b) $10^5$ c) 3x$10^5$ and d) 5x$10^5$.

The solid weight fraction distribution at the mushy region has been presented in Fig. 6.11 for boundary condition 3. The growth dynamics of the mushy region with time increment is predicted in Fig 6.11. The segregation ratio for boundary condition 3 is shown in Fig. 6.12 (a) to (c). The upper value of the segregation ratio is 1.2 and it decreases to the direction of solidus line. The temperature distribution in the mushy zone and the fluid flow distribution in liquid zone are presented in Fig. 6.13. Results show that, the boundary condition has slight curvature and due to density difference causes mild circulatory flow in the molten region. The progress of the solid phase increases with time which is common in nature.

## 6.5 Conclusions

In these chapter results of solidification study of *Ni-Cu* (50%-50%) binary alloy in a square cavity is presented. Main objective of study is to observe the effect of different cooling boundary conditions on solidification rate, dynamics of mushy region, and shapes of different phasic boundaries. The investigation has been carried out for three different boundary conditions and following conclusions may be drawn.

- Heat loss to surrounding through left boundary causes start of the solidification.
- Front of the solidified domain moves inward approximately parallel to the heat loss boundary.
- The moving front approximately takes the shape of the temperature profile of the thermal boundary conditions.
- Thickness of the solidified domain and mushy region grows with time.
- During time scale of the dynamics study heat loss near convective boundary is conduction dominated.
- In the liquid zone velocity circulation is observed as shown for one case.
- Weight fraction distribution of *Ni* in the mushy region changes from high to low value from solid interface to liquid interface.
- Circulation in the mushy region is feeble hence heat, mass and momentum transfer in that region are mostly diffusion dominated.

## CHAPTER 7

# CONCLUSON AND FUTURE SCOPE OF WORK

The present thesis concerns solid –liquid phase change studies for metals and alloys. A brief summary of the work carried out and the future scope is now reported below.

### 7.1 Summary and Conclusions

The study reported in the work can be categorized as

- Development of lattice Boltzmann code to study melting and solidification of low Prandtl number liquid metals. A modification of existing lattice Boltzmann method (LBM) has been proposed for low *Pr* materials.
- Investigation of the convective flow instability in the melt regime for low Prandtl number liquid metals
- Investigation of the natural convection effect in corner melting and solidification problem in a wide range of Prandtl number
- Development a hybrid lattice Boltzmann model to simulate the mushy region for *Ni-Cu* binary alloy solidification.

The present work reports development of a lattice Boltzmann model to overcome the numerical instability associated in handling convection in low *Pr* fluids. The model is used successfully to study melting dynamics in a square cavity for $Pr \in [0.001, 0.1]$ and $Ra \in [10^4, 10^6]$. After the global findings of the melting of low Prandtl number liquid metal, the flow instability in the melt zone is analyzed by studying the flow transients. The peak frequencies that appear as the flow enters the transition regime are quantified using Fast Fourier Transform (FFT).

Corner melting and solidification of low Prandtl number material in a square cavity has been simulated using total enthalpy based lattice Boltzmann method. Comparison has been made between corner melting heated from bottom and corner melting heated from top boundaries. The study reveals that for both the cases initially convex melt front is formed which turns into concave shape with time. Then the corner melting study is extended for low Prandtl number liquid metals with a range of $Pr \in [0.001, 0.01]$. The study reveals that in corner melting initially convex melt front is formed which turns into concave shape at increasing time interval for *Pr*=0.001, 0.005 and 0.01 respectively.

A hybrid lattice Boltzmann model is developed to investigate the mushy zone dynamics and macro-segregation in *Ni-Cu* binary alloy solidification. The flow field is modelled using standard LBM and thermal and species continuity equations are solved using finite difference method (FDM). Effects of cooling boundary conditions on solidification rate, dynamics of mushy region, and shapes of different segregation profiles are studied in this work.

## 7.2 Future Scope of Work

The present work involves studies on melting and solidification in two dimensional domains. Extension to three-dimensional problems shall be challenging which shall require optimization of computational resources. It is expected that additional nuances of the flow and thermal field shall be observed. This shall also call for programming for accelerated convergence with scope of improvement in the numerical schemes.

It is to be noted that for handling the change of morphology and segregation in alloys, LBM is to be coupled with a suitable interface tracking model to simulate the growth of microstructure during solidification. While there has been a lot of developments in the area of LBM, quest for improvement in capability of these methods which can predict realistic microstructure with optimum computing resources are still on. Improved algorithms along with deployment of high performance computing are special requirements for moving to simulation of real life problems. Thus development of an effective full LBM method to study binary alloy solidification is again a futuristic problem.

Finally, the present work is limited to regular geometry with orthogonal sides. As natural processes and industrial jobs both can have irregular geometries, schemes for handling arbitrary curved boundaries using LBM is the need of the hour.

## REFERENCES

Anderson, D. M., McFadden, G. B., and Wheeler, A. A. (2000). A phase-field model of solidification with convection. *Physica D: Nonlinear Phenomena*, *135*(1–2), 175–194.

Arcidiacono, S., and Ciofalo, M. (2001). Low-Prandtl number natural convection in volumetrically heated rectangular enclosures III. Shallow cavity, AR = 0.25. *International Journal of Heat and Mass Transfer*, *44*(16), 3053–3065. https://doi.org/10.1016/S0017-9310(00)00347-1

Azad, M., Groulx, D., and Donaldson, A. (2021). Natural convection onset during melting of phase change materials: Part II – Effects of Fourier, Grashof, and Rayleigh numbers. *International Journal of Thermal Sciences*, *170*(March), 107062. https://doi.org/10.1016/j.ijthermalsci.2021.107062

Azad, M., Groulx, D., and Donaldson, A. (2022). Natural convection onset during melting of phase change materials: Part III – Global correlations for onset conditions. *International Journal of Thermal Sciences*, *172*(PB), 107368. https://doi.org/10.1016/j.ijthermalsci.2021.107368

Basak, T., Roy, S., and Balakrishnan, A. R. (2006). Effects of thermal boundary conditions on natural convection flows within a square cavity. *International Journal of Heat and Mass Transfer*, *49*(23), 4525–4535. https://doi.org/https://doi.org/10.1016/j.ijheatmasstransfer.2006.05.015

Bawazeer, S., Mohamad, A. A., and Oclon, P. (2019). Natural convection in a differentially heated enclosure filled with low Prandtl number fluids with modified lattice Boltzmann method. *International Journal of Heat and Mass Transfer*, *143,* 118562. https://doi.org/10.1016/j.ijheatmasstransfer.2019.118562

Bejan, A. (2013). *Convection heat transfer*. John wiley and sons.

Bhattacharya, M., and Basak, T. (2021). Critical role of Prandtl number on multiple steady states during natural convection in square enclosures: Analysis of heat transfer rates, flow and thermal maps. *International Journal of Heat and Mass Transfer, 170,* 120900. https://doi.org/10.1016/j.ijheatmasstransfer.2021.120900

Callister, W., and Rethwisch, D. (2007). *Material Science and Engineering – An Introduction*.

Chakraborty, S., Chakraborty, N., Kumar, P., and Dutta, P. (2003). Studies on turbulent momentum, heat and species transport during binary alloy solidification in a top-cooled rectangular cavity. *International Journal of Heat and Mass Transfer*, *46*(7), 1115–1137. https://doi.org/10.1016/S0017-9310(02)00402-7

Chatterjee, D., and Chakraborty, S. (2005). An enthalpy-based Lattice Boltzmann model for diffusion dominated solid–liquid phase transformation. *Physics Letters A*, *341*, 320–330. https://doi.org/10.1016/j.physleta.2005.04.080

Chatterjee, D., and Chakraborty, S. (2006). A hybrid lattice Boltzmann model for solid–liquid phase transition in presence of fluid flow. *Physics Letters A*, *351*(4–5), 359–367.

Chatterjee, D., and Chakraborty, S. (2008). An enthalpy-source based lattice Boltzmann model for conduction dominated phase change of pure substances. *International Journal of Thermal Sciences*, *47*(5), 552–559.

Chattopadhyay, H. (2011). Estimation of solidification time in investment casting process. *The International Journal of Advanced Manufacturing Technology*, *55*(1–4), 35–38.

Chen, B., Song, L., Gao, K., and Liu, F. (2018). Two zone model for mushy region of solid–liquid phase change based on Lattice Boltzmann method. *International Communications in Heat and Mass Transfer*, *98*, 1–12.

Chen, L., Yu, Y., and Hou, G. (2013). Sharp-interface immersed boundary lattice Boltzmann method with reduced spurious-pressure oscillations for moving boundaries. *Physical Review E*, *87*(5), 53306.

Chen, S., and Doolen, G. D. (1998). Lattice Boltzmann method for fluid flows. *Annual Review of Fluid Mechanics*, *30*(1), 329–364.

Chen, Y., and Müller, C. R. (2020). A Dirichlet boundary condition for the thermal lattice Boltzmann method. *International Journal of Multiphase Flow*, *123*, 103184.

Chen, Z, Shu, C., Yang, L. M., Zhao, X., and Liu, N. Y. (2021). Phase-field-simplified lattice Boltzmann method for modeling solid-liquid phase change. *Physical Review E*, *103*(2), 23308.

Chen, Zhiqiang, and Wang, M. (2020). An improved immersed moving boundary for hydrodynamic force calculation in lattice Boltzmann method. *International Journal for Numerical Methods in Engineering*, *121*(20), 4493–4508.

Chessa, J., Smolinski, P., and Belytschko, T. (2002). The extended finite element method (XFEM) for solidification problems. *International Journal for Numerical Methods in Engineering*, *53*(8), 1959–1977. https://doi.org/https://doi.org/10.1002/nme.386

Chiappini, D, Festuccia, A., and Bella, G. (2018). Coupled lattice Boltzmann finite volume method for conjugate heat transfer in porous media. *Numerical Heat Transfer, Part A: Applications*, *73*(5), 291–306. https://doi.org/10.1080/10407782.2018.1444868

Chiappini, Daniele. (2021). A coupled lattice Boltzmann-finite volume method for phase change material analysis. *International Journal of Thermal Sciences*, *164*(February), 106893. https://doi.org/10.1016/j.ijthermalsci.2021.106893

Chopard, B., and Droz, M. (1998). Cellular Automata Modeling of Physical Systems. In *Collection Alea-Saclay: Monographs and Texts in Statistical Physics*. Cambridge University Press. https://doi.org/DOI: 10.1017/CBO9780511549755

Contrino, D., Lallemand, P., Asinari, P., and Luo, L.-S. (2014). Lattice-Boltzmann simulations of the thermally driven 2D square cavity at high Rayleigh numbers. *Journal of Computational Physics*, *275*, 257–272.

Coreixas, C., Wissocq, G., Chopard, B., Latt, J., Lallemand, P., and Luo, L.-S. (2020). Theory of the lattice Boltzmann method: Dispersion, dissipation, isotropy, Galilean invariance, and stability. *Physical Review E*, *378*(6), 20190397.

Dai, R., Bian, Q., Wang, Q., and Zeng, M. (2018). Evolution of natural convection melting inside cavity heated from different sides using enthalpy based lattice Boltzmann method. *International Journal of Heat and Mass Transfer*, *121*, 715–725.

Danaila, I., Moglan, R., Hecht, F., and Le Masson, S. (2014). A Newton method with adaptive finite elements for solving phase-change problems with natural convection. *Journal of Computational Physics*, *274*, 826–840.

De Fabritiis, G., Mancini, A., Mansutti, D., and Succi, S. (1998). Mesoscopic models of liquid/solid phase transitions. *International Journal of Modern Physics C*, *9*(08), 1405–1415.

Delouei, A. A., Nazari, M., Kayhani, M. H., and Succi, S. (2015). Immersed boundary–thermal lattice Boltzmann methods for non-Newtonian flows over a heated cylinder: a comparative study. *Communications in Computational Physics*, *18*(2), 489–515.

Dhar, M, Barman, N., Mandal, S., and Chattopadhyay, H. (2014). Remelting and interface dynamics during solidification of a eutectic solution in a top-cooled rectangular cavity: A numerical study. *International Journal of Heat and Mass Transfer*, *77*, 730–737.

Dhar, Mrinmoy, Barman, N., Chattopadhyay, H., and Simlandi, S. (2015). Heatline Visualization During Solidification of a Eutectic Solution in a Rectangular Cavity. *Transactions of the Indian Institute of Metals*, *68*(6), 1187–1192. https://doi.org/10.1007/s12666-015-0674-x

Dhar, Mrinmoy, Barman, N., Mandal, S., and Chattopadhyay, H. (2014). Effect of Prandtl Number on Solidification Behavior of Eutectic Solutions. *Procedia Materials Science*, *5*, 704–711. https://doi.org/10.1016/j.mspro.2014.07.318

Dong, B., Zhou, X., Zhang, Y., Chen, C., and Li, W. (2018). Numerical simulation of thermal flow of power-law fluids using lattice Boltzmann method on non-orthogonal grids. *International Journal of Heat and Mass Transfer*, *126*, 293–305.

Du, W., Chen, S., and Wu, G. (2021). A new lattice Boltzmann method for melting processes of high Prandtl number phase change materials. *Journal of Energy Storage*, *41*(June), 103006. https://doi.org/10.1016/j.est.2021.103006

Dubois, F., and Lallemand, P. (2008). Towards higher order lattice Boltzmann schemes. *J. Stat. Mech.*, *2009*. https://doi.org/10.1088/1742-5468/2009/06/P06006

Eshraghi, M., and Felicelli, S. D. (2012). An implicit lattice Boltzmann model for heat conduction with phase change. *International Journal of Heat and Mass Transfer*, *55*(9–10), 2420–2428.

Fakhari, A., and Lee, T. (2015). Numerics of the Lattice Boltzmann Method on Nonuniform Grids: Standard LBM and Finite-difference LBM. *Computers and Fluids*, *107*, 205–213. https://doi.org/10.1016/j.compfluid.2014.11.013

Favier, B., Purseed, J., and Duchemin, L. (2019). Rayleigh-Bénard convection with a melting boundary. *Journal of Fluid Mechanics*, *858*, 437–473. https://doi.org/10.1017/jfm.2018.773

Feng, Z.-G., and Michaelides, E. E. (2004). The immersed boundary-lattice Boltzmann method for solving fluid–particles interaction problems. *Journal of Computational Physics*, *195*(2), 602–628.

Filippova, O., and Hänel, D. (2000). A novel lattice BGK approach for low Mach number combustion. *Journal of Computational Physics*, *158*(2), 139–160.

Flemings, M. (2000). Our Understanding of Macrosegregation. Past and Present. *Isij International - ISIJ INT*, *40*, 833–841. https://doi.org/10.2355/isijinternational.40.833

Ganaoui, M. El, and Semma, E. A. (2009). A lattice Boltzmann coupled to finite volumes method for solving phase change problems. *Thermal Science*, *13*(2), 205–216. https://doi.org/10.2298/TSCI0902205E

Gao, D., and Chen, Z. (2011). Lattice boltzmann simulation of natural convection dominated melting in a rectangular cavity filled with porous media. *International Journal of Thermal Sciences*, *50*(4), 493–501. https://doi.org/10.1016/j.ijthermalsci.2010.11.010

Gao, D., Tian, F.-B., Chen, Z., and Zhang, D. (2017). An improved lattice Boltzmann method for solid-liquid phase change in porous media under local thermal non-equilibrium conditions. *International Journal of Heat and Mass Transfer*, *110*, 58–62.

Gao, Y., Yu, Y., Yang, L., Qin, S., and Hou, G. (2021). Development of a coupled simplified lattice Boltzmann method for thermal flows. *Computers and Fluids*, 105042.

Gau, C., and Viskanta, R. (1986). Melting and solidification of a pure metal on a vertical wall. *Journal of Heat Transfer*, *108*(1), 174–181. https://doi.org/10.1115/1.3246884

Ginzburg, I. (2005). Generic boundary conditions for lattice Boltzmann models and their application to advection and anisotropic dispersion equations. *Advances in Water Resources*, *28*(11), 1196–1216. https://doi.org/https://doi.org/10.1016/j.advwatres.2005.03.009

Ginzburg, I. (2008). Study of Simple Hydrodynamic Solutions with the Two-Relaxation-Times Lattice Boltzmann Scheme. *Communications in Computational Physics*.

Ginzburg, I., and d'Humières, D. (2003). Multireflection boundary conditions for lattice Boltzmann models. *Physical Review E*, *68*(6), 66614. https://doi.org/10.1103/PhysRevE.68.066614

Gobin, D., and Benard, C. (1992). Melting of metals driven by natural convection in the melt: Influence of prandtl and rayleigh numbers. *Journal of Heat Transfer*, *114*(2), 521–524. https://doi.org/10.1115/1.2911308

Gobin, D., and Martinez, F. (1985). *MeltinginRectangularEnclosuresC.BenardD.GobinF.Martinez1985 free paper.pdf*. *107*(November 1985).

Gu, Q., Zhu, L., Zhang, Y., and Liu, H. (2019). Pore-scale study of counter-current imbibition in strongly water-wet fractured porous media using lattice Boltzmann method. *Physics of Fluids*, *31*(8), 86602.

Guo, X., Zhong, C., Zhuo, C., and Cao, J. (2014). Multiple-relaxation-time lattice Boltzmann method for study of two-lid-driven cavity flow solution multiplicity. *Theoretical and Computational Fluid Dynamics*, *28*(2), 215–231.

Guo, Z., and Shu, C. (2013). *Lattice Boltzmann method and its application in engineering* (Vol. 3). World Scientific.

Hasan, M. S., and Saha, S. K. (2021a). Evolution of solid-liquid interface in bottom heated cavity for low Prandtl number using lattice Boltzmann method. *Physics of Fluids*, *33*(5). https://doi.org/10.1063/5.0044462

Hasan, M. S., and Saha, S. K. (2021b). Evolution of solid–liquid interface in bottom heated cavity for low Prandtl number using lattice Boltzmann method. *Physics of Fluids, 33*(5), 57102.

He, X., and Luo, L.-S. (1997). Lattice Boltzmann Model for the Incompressible Navier–Stokes Equation. *Journal of Statistical Physics, 88,* 927–944. https://doi.org/10.1023/B:JOSS.0000015179.12689.e4

He, X., Zou, Q., Luo, L.-S., and Dembo, M. (1997). Analytic solutions of simple flows and analysis of nonslip boundary conditions for the lattice Boltzmann BGK model. *Journal of Statistical Physics*, *87*(1), 115–136. https://doi.org/10.1007/BF02181482

He, Y.-L., Liu, Q., Li, Q., and Tao, W.-Q. (2019). Lattice Boltzmann methods for single-phase and solid-liquid phase-change heat transfer in porous media: A review. *International Journal of Heat and Mass Transfer, 129,* 160–197.

Herpe, J., Bougeard, D., Russeil, S., and Stanciu, M. (2009). Numerical investigation of local entropy production rate of a finned oval tube with vortex generators. *International Journal of Thermal Sciences,* *48*(5), 922–935. https://doi.org/10.1016/j.ijthermalsci.2008.07.006

Hu, Y., Li, D., Niu, X., and Shu, S. (2019a). A diffuse interface lattice Boltzmann model for thermocapillary flows with large density ratio and thermophysical parameters contrasts. *International Journal of Heat and Mass Transfer*, *138*, 809–824.

Hu, Y., Li, D., Niu, X., and Shu, S. (2019b). An immersed boundary-lattice Boltzmann method for electro-thermo-convection in complex geometries. *International Journal of Thermal Sciences*, *140*, 280–297.

Hu, Y., Li, D., Shu, S., and Niu, X. (2017). Lattice Boltzmann simulation for three-dimensional natural convection with solid-liquid phase change. *International Journal of Heat and Mass Transfer*, *113*, 1168–1178.

Huang, R., and Wu, H. (2014). An immersed boundary-thermal lattice Boltzmann method for solid–liquid phase change. *Journal of Computational Physics*, *277*, 305–319.

Huang, R., and Wu, H. (2015). Phase interface effects in the total enthalpy-based lattice Boltzmann model for solid–liquid phase change. *Journal of Computational Physics*, *294*, 346–362.

Huang, R., and Wu, H. (2016). Total enthalpy-based lattice Boltzmann method with adaptive mesh refinement for solid-liquid phase change. *Journal of Computational Physics*, *315*, 65–83.

Huang, R., Wu, H., and Cheng, P. (2013a). A new lattice Boltzmann model for solid-liquid phase change. *International Journal of Heat and Mass Transfer*, *59*(1), 295–301. https://doi.org/10.1016/j.ijheatmasstransfer.2012.12.027

Huang, R., Wu, H., and Cheng, P. (2013b). A new lattice Boltzmann model for solid–liquid phase change. *International Journal of Heat and Mass Transfer*, *59*, 295–301.

Huber, C., Parmigiani, A., Chopard, B., Manga, M., and Bachmann, O. (2008). Lattice Boltzmann model for melting with natural convection. *International Journal of Heat and Fluid Flow*, *29*(5), 1469–1480.

Huo, Y., and Rao, Z. (2015). Lattice Boltzmann simulation for solid–liquid phase change phenomenon of phase change material under constant heat flux. *International Journal of Heat and Mass Transfer*, *86*, 197–206.

Huo, Y., and Rao, Z. (2017). The quasi-enthalpy based lattice Boltzmann model for solid-liquid phase change. *Applied Thermal Engineering*, *115*, 1237–1244.

Huo, Y., and Rao, Z. (2018). Investigation of solid-liquid phase change in the spherical capsule using axisymmetric lattice Boltzmann model. *International Journal of Heat and Mass Transfer*, *119*, 1–9.

Hussein, A. K., Ashorynejad, H. R., Sivasankaran, S., Kolsi, L., Shikholeslami, M., and Adegun, I. K. (2016). Modeling of MHD natural convection in a square enclosure having an adiabatic square shaped body using Lattice Boltzmann Method. *Alexandria Engineering Journal*, *55*(1), 203–214.

Inamuro, T. (2002). A lattice kinetic scheme for incompressible viscous flows with heat transfer. *Philosophical Transactions of the Royal Society A: Mathematical, Physical and Engineering Sciences*, *360*(1792), 477–484. https://doi.org/10.1098/rsta.2001.0942

Jelinek, B., Eshraghi, M., Felicelli, S., and Peters, J. F. (2014). Large-scale parallel lattice Boltzmann–cellular automaton model of two-dimensional dendritic growth. *Computer Physics Communications*, *185*(3), 939–947.

Jiaung, W.-S., Ho, J.-R., and Kuo, C.-P. (2001). Lattice Boltzmann method for the heat conduction problem with phase change. *Numerical Heat Transfer: Part B: Fundamentals*, *39*(2), 167–187.

Jiji, L. M., Rathjen, K. A., and Drzewiecki, T. (1970). Two-dimensional solidification in a corner. *International Journal of Heat and Mass Transfer*, *13*(1), 215–218. https://doi.org/10.1016/0017-9310(70)90037-2

Jones, B. J., Sun, D., Krishnan, S., and Garimella, S. V. (2006). Experimental and numerical study of melting in a cylinder. *International Journal of Heat and Mass Transfer*, *49*(15–16), 2724–2738. https://doi.org/10.1016/j.ijheatmasstransfer.2006.01.006

Jourabian, M., Farhadi, M., Rabienataj Darzi, A. A., and Abouei, A. (2013). Lattice boltzmann simulation of melting phenomenon with natural convection from an eccentric annulus. *Thermal Science*, *17*(3), 877–890. https://doi.org/10.2298/TSCI110510012J

Kang, S. K., and Hassan, Y. A. (2011). A direct-forcing immersed boundary method for the thermal lattice Boltzmann method. *Computers and Fluids*, *49*(1), 36–45.

Karlin, I. V, Sichau, D., and Chikatamarla, S. S. (2013). Consistent two-population lattice Boltzmann model for thermal flows. *Physical Review E*, *88*(6), 63310.

Klass, F., Gabbana, A., and Bartel, A. (2021). A non-equilibrium bounce-back boundary condition for thermal multispeed LBM. *Journal of Computational Science*, *53*, 101364.

Knutson, C. E., and Noble, D. R. (2009). Embedding sharp interfaces within the lattice Boltzmann method for fluids with arbitrary density ratios. *The European Physical Journal Special Topics*, *171*(1), 21–29.

Kosec, G., and Šarler, B. (2013). Solution of a low Prandtl number natural convection benchmark by a local meshless method. *International Journal of Numerical Methods for Heat and Fluid Flow*, *23*(1), 189–204. https://doi.org/10.1108/09615531311289187

Krishnamurti, R. (1970). On the transition to turbulent convection. Part 1. The transition from two- to three-dimensional flow. *Journal of Fluid Mechanics*, *42*(2), 295–307. https://doi.org/10.1017/S0022112070001271

Krüger, T., Kusumaatmaja, H., Kuzmin, A., Shardt, O., Silva, G., and Viggen, E. M. (2017). The lattice Boltzmann method. *Springer International Publishing*, *10*(978–3), 4–15.

Lacroix, M., and Voller, V. R. (1990). FINITE DIFFERENCE SOLUTIONS OF SOLIDIFICATION PHASE CHANGE PROBLEMS: TRANSFORMED VERSUS FIXED GRIDS. *Numerical Heat Transfer, Part B: Fundamentals*, *17*(1), 25–41. https://doi.org/10.1080/10407799008961731

Lallemand, P., and Luo, L.-S. (2000). Theory of the lattice Boltzmann method: Dispersion, dissipation, isotropy, Galilean invariance, and stability. *Physical Review E*, *61*(6), 6546.

Lallemand, P., and Luo, L.-S. (2003). Hybrid finite-difference thermal lattice Boltzmann equation. *International Journal of Modern Physics B*, *17*(01n02), 41–47.

Lamarti, H., Mahdaoui, M., Bennacer, R., and Chahboun, A. (2019). Numerical simulation of mixed convection heat transfer of fluid in a cavity driven by an oscillating lid using lattice Boltzmann method. *International Journal of Heat and Mass Transfer*, *137*, 615–629.

Lee, S. L., and Tzong, R. y. (1991). An enthalpy formulation for phase change problems with a large thermal diffusivity jump across the interface. *International Journal of Heat and Mass Transfer*, *34*(6), 1491–1502. https://doi.org/10.1016/0017-9310(91)90291-L

Lesoult, G. (2005). Macrosegregation in steel strands and ingots: Characterisation, formation and consequences. *Materials Science and Engineering: A*, *413*, 19–29. https://doi.org/10.1016/j.msea.2005.08.203

Li, D., Ren, Q., Tong, Z.-X., and He, Y.-L. (2017). Lattice Boltzmann models for axisymmetric solid–liquid phase change. *International Journal of Heat and Mass Transfer, 112,* 795–804.

Li, D., Tong, Z.-X., Ren, Q., He, Y.-L., and Tao, W.-Q. (2017). Three–dimensional lattice Boltzmann models for solid–liquid phase change. *International Journal of Heat and Mass Transfer, 115,* 1334–1347.

Li, L., Mei, R., and Klausner, J. F. (2013). Boundary conditions for thermal lattice Boltzmann equation method. *Journal of Computational Physics, 237,* 366–395. https://doi.org/https://doi.org/10.1016/j.jcp.2012.11.027

Li, L., Mei, R., and Klausner, J. F. (2017). Lattice Boltzmann models for the convection-diffusion equation: D2Q5 vs D2Q9. *International Journal of Heat and Mass Transfer, 108,* 41–62. https://doi.org/https://doi.org/10.1016/j.ijheatmasstransfer.2016.11.092

Li, Q., He, Y. L., Wang, Y., and Tao, W. Q. (2007). Coupled double-distribution-function lattice Boltzmann method for the compressible Navier-Stokes equations. *Physical Review E, 76*(5), 56705.

Li, Q., Yang, H., and Huang, R. (2021). Lattice Boltzmann simulation of solid-liquid phase change with nonlinear density variation. *Physics of Fluids, 33*(12). https://doi.org/10.1063/5.0070407

Li, Q., Zhou, P., and Yan, H. J. (2017). Improved thermal lattice Boltzmann model for simulation of liquid-vapor phase change. *Physical Review E, 96*(6), 63303.

Li, W., Wang, W.-Q., Yan, Y., and Yu, Z.-F. (2020). A strong-coupled method combined finite element method and lattice Boltzmann method via an implicit immersed boundary scheme for fluid structure interaction. *Ocean Engineering, 214,* 107779. https://doi.org/10.1016/j.oceaneng.2020.107779

Li, X., Ma, T., Liu, J., Zhang, H., and Wang, Q. (2018). Pore-scale investigation of gravity effects on phase change heat transfer characteristics using lattice Boltzmann method. *Applied Energy, 222,* 92–103.

Li, Z., Yang, M., and Zhang, Y. (2014). A hybrid lattice Boltzmann and finite-volume method for melting with convection. *Numerical Heat Transfer, Part B: Fundamentals, 66*(4), 307–325.

Li, Z., Yang, M., and Zhang, Y. (2016). Double MRT thermal lattice Boltzmann method for simulating natural convection of low Prandtl number fluids. *International Journal of Numerical Methods for Heat and Fluid Flow*, *26*(6), 1889–1909. https://doi.org/10.1108/HFF-04-2015-0135

Liao, Q., and Jen, T.-C. (2011). Application of Lattice Boltzmann method in fluid flow and heat transfer. *Computational Fluid Dynamics Technologies and Applications*, 29–68.

Lin, J. Y., and Chen, H. T. (1997). Hybrid numerical scheme for nonlinear two-dimensional phase-change problems with the irregular geometry. *Heat and Mass Transfer/Waerme-Und Stoffuebertragung*, *33*(1–2), 51–58. https://doi.org/10.1007/s002310050160

Liu, J., Huang, C., Chai, Z., and Shi, B. (2022). A diffuse-interface lattice Boltzmann method for fluid–particle interaction problems. *Computers and Fluids*, *233,* 105240.

Liu, Q., He, Y.-L., and Li, Q. (2017). Enthalpy-based multiple-relaxation-time lattice Boltzmann method for solid-liquid phase-change heat transfer in metal foams. *Physical Review E*, *96*(2), 23303.

Liu, Q., Wang, X., Feng, X. B., and Liu, F. (2022). An enthalpy-based cascaded lattice Boltzmann method for solid-liquid phase-change heat transfer. *Applied Thermal Engineering*, *209*(February), 118283. https://doi.org/10.1016/j.applthermaleng.2022.118283

Liu, Y., So, R. M. C., and Cui, Z. X. (2006). Bluff body flow simulation using lattice Boltzmann equation with multiple relaxation time. *Computers and Fluids*, *35*(8–9), 951–956.

López, J., Gómez, P., Hernández, J., and Faura, F. (2013). A two-grid adaptive volume of fluid approach for dendritic solidification. *Computers and Fluids*, *86*, 326–342.

Lu, J. H., Lei, H. Y., and Dai, C. S. (2019). An optimal two-relaxation-time lattice Boltzmann equation for solid-liquid phase change: the elimination of unphysical numerical diffusion. *International Journal of Thermal Sciences*, *135*, 17–29.

Luo, K., Wu, J., Yi, H.-L., and Tan, H.-P. (2016). Lattice Boltzmann modelling of electro-thermo-convection in a planar layer of dielectric liquid subjected to unipolar injection and thermal gradient. *International Journal of Heat and Mass Transfer*, *103,* 832–846.

Luo, K., Yao, F. J., Yi, H. L., and Tan, H. P. (2015). Lattice Boltzmann simulation of convection melting in complex heat storage systems filled with phase change materials. *Applied Thermal Engineering*, *86*, 238–250. https://doi.org/10.1016/j.applthermaleng.2015.04.059

Luo, L.-S. (1993). *Lattice-gas automata and lattice Boltzmann equations for two-dimensional hydrodynamics*.

Lyon, R. N., and Poppendiek, H. (1951). Liquid-metal heat transfer. *Liquid-Metals Handbook*, 184.

Mallya, N., and Haussener, S. (2021). Buoyancy-driven melting and solidification heat transfer analysis in encapsulated phase change materials. *International Journal of Heat and Mass Transfer*, *164*, 120525. https://doi.org/10.1016/j.ijheatmasstransfer.2020.120525

Medvedev, D., and Kassner, K. (2005). Lattice Boltzmann scheme for crystal growth in external flows. *Physical Review E*, *72*(5), 56703.

Mencinger, J. (2004). Numerical simulation of melting in two-dimensional cavity using adaptive grid. *Journal of Computational Physics*, *198*(1), 243–264.

Mezrhab, A., Bouzidi, M., and Lallemand, P. (2004). Hybrid lattice-Boltzmann finite-difference simulation of convective flows. *Computers and Fluids*, *33*(4), 623–641.

Miller, W., Succi, S., and Mansutti, D. (2001). Lattice Boltzmann model for anisotropic liquid-solid phase transition. *Physical Review Letters*, *86*(16), 3578.

Mohamad, A. A., and Viskanta, R. (1991). Low-Prandtl-Number Fluids I N a Differentially Heated Cavity. *International Journal for Numerical Methods in Fluids*, *13*(July 1990), 61–81.

Mohamad, A. A., and Viskanta, R. (1993). Modeling of turbulent buoyant flow and heat transfer in liquid metals. *International Journal of Heat and Mass Transfer*, *36*(11), 2815–2826. https://doi.org/10.1016/0017-9310(93)90101-B

Nabavizadeh, S. A., Barua, H., Eshraghi, M., and Felicelli, S. D. (2021). A Multiple-Grid Lattice Boltzmann Method for Natural Convection under Low and High Prandtl Numbers. *Fluids*, *6*(4), 148.

Nabavizadeh, S. A., Lenart, R., Eshraghi, M., Felicelli, S. D., Tewari, S. N., and Grugel, R.

N. (2020). Dendritic solidification of Succinonitrile-0.24 wt% water alloy: A comparison with microgravity experiments for validating dendrite tip velocity. *Acta Astronautica*, *175*, 163–173.

Năstase, G., Perez, P. A., Șerban, A., Dobrovicescu, A., Ștefănescu, M.-F., and Rubinsky, B. (2016). Advantages of isochoric freezing for food preservation: A preliminary analysis. *International Communications in Heat and Mass Transfer*, *78*, 95–100.

Nee, A. (2021). Hybrid Lattice Boltzmann Simulation of Three-Dimensional Natural Convection. *Journal of Computational and Theoretical Transport*, *50*(4), 280–296.

Noble, D. R., and Torczynski, J. R. (1998). A lattice-Boltzmann method for partially saturated computational cells. *International Journal of Modern Physics C*, *9*(08), 1189–1201.

Nourgaliev, R. R., Dinh, T.-N., Theofanous, T. G., and Joseph, D. (2003). The lattice Boltzmann equation method: theoretical interpretation, numerics and implications. *International Journal of Multiphase Flow*, *29*(1), 117–169.

Noyola-García, B. S., and Rodriguez-Romo, S. (2021). Simulations of Ga melting based on multiple-relaxation time lattice Boltzmann method performed with CUDA in Python. *Mathematics and Computers in Simulation*, *181*, 170–191.

Ohno, M., and Sato, H. (2018a). Macrosegregation simulation model based on Lattice-Boltzmann method with high computational efficiency. *International Journal of Heat and Mass Transfer*, *127*, 561–570.

Ohno, M., and Sato, H. (2018b). Macrosegregation simulation model based on Lattice-Boltzmann method with high computational efficiency. *International Journal of Heat and Mass Transfer*, *127*, 561–570. https://doi.org/10.1016/j.ijheatmasstransfer.2018.07.076

Pepona, M., and Favier, J. (2016). A coupled Immersed Boundary–Lattice Boltzmann method for incompressible flows through moving porous media. *Journal of Computational Physics*, *321*, 1170–1184.

Perumal, D. A., and Dass, A. K. (2015). A Review on the development of lattice Boltzmann computation of macro fluid flows and heat transfer. *Alexandria Engineering Journal*, *54*(4), 955–971.

Pielichowska, K., and Pielichowski, K. (2014). Phase change materials for thermal energy storage. *Progress in Materials Science*, *65*, 67–123.

Porter, D. A., Easterling, K. E., and Sherif, M. Y. (2009). Phase transformations in metals and alloys, third edition. In *Phase Transformations in Metals and Alloys, Third Edition*.

Prescott, P. J., and Incropera, F. P. (1996). Convection Heat and Mass Transfer in Alloy Solidification. In D. B. T.-A. in H. T. Poulikakos (Ed.), *Transport Phenomena in Materials Processing* (Vol. 28, pp. 231–338). Elsevier. https://doi.org/https://doi.org/10.1016/S0065-2717(08)70142-4

Rao, Z., Wang, S., and Peng, F. (2013). Molecular dynamics simulations of nano-encapsulated and nanoparticle-enhanced thermal energy storage phase change materials. *International Journal of Heat and Mass Transfer*, *66*. https://doi.org/10.1016/j.ijheatmasstransfer.2013.07.065

Rathjen, K. A., and Jui, L. M. (1971). Heat conduction with melting or freezing in a corner. *Journal of Heat Transfer*, *93*(1), 101–109. https://doi.org/10.1115/1.3449740

Ren, Q., He, Y.-L., Su, K.-Z., and Chan, C. L. (2017). Investigation of the effect of metal foam characteristics on the PCM melting performance in a latent heat thermal energy storage unit by pore-scale lattice Boltzmann modeling. *Numerical Heat Transfer, Part A: Applications*, *72*(10), 745–764.

Ren, Q., Meng, F., and Guo, P. (2018). A comparative study of PCM melting process in a heat pipe-assisted LHTES unit enhanced with nanoparticles and metal foams by immersed boundary-lattice Boltzmann method at pore-scale. *International Journal of Heat and Mass Transfer*, *121*, 1214–1228.

Rui, Z., Li, J., Ma, J., Cai, H., Nie, B., and Peng, H. (2020a). Comparative study on natural convection melting in square cavity using lattice Boltzmann method. *Results in Physics*, *18*, 103274. https://doi.org/10.1016/j.rinp.2020.103274

Rui, Z., Li, J., Ma, J., Cai, H., Nie, B., and Peng, H. (2020b). Comparative study on natural convection melting in square cavity using lattice Boltzmann method. *Results in Physics*, *18*, 103274.

Sahraoui, N. M., Houat, S., and El-Ganaoui, M. (2020). Numerical investigation of low Prandtl number effect on mixed convection in a horizontal channel by the lattice

Boltzmann method. *Heat Transfer, 49*(8), 4528–4542.

Sakane, S., Takaki, T., Ohno, M., Shibuta, Y., and Aoki, T. (2020). Two-dimensional large-scale phase-field lattice Boltzmann simulation of polycrystalline equiaxed solidification with motion of a massive number of dendrites. *Computational Materials Science, 178*, 109639.

Samanta, R., Chattopadhyay, H., and Guha, C. (2020). Transport phenomena in a differentially heated lid-driven cavity: A study using multi-relaxation-time thermal lattice Boltzmann modeling. *Physics of Fluids, 32*(9), 93610.

Samanta, R., Chattopadhyay, H., and Guha, C. (2022). A review on the application of lattice Boltzmann method for melting and solidification problems. *Computational Materials Science*, *206*(October 2021), 111288. https://doi.org/10.1016/j.commatsci.2022.111288

Samanta, R., Chattopadhyay, H., and Guha, C. (2023). Study of Corner Solidification of Pure Metal using Lattice Boltzmann Method. *Lecture Notes in Mechanical Engineering*, 79–84. https://doi.org/10.1007/978-981-19-6270-7_15

Sammouda, H., Belghith, A., and Surry, C. (1999). Finite element simulation of transient natural convection of low-Prandtl-number fluids in heated cavity. *International Journal of Numerical Methods for Heat and Fluid Flow*, *9*(5), 612–624. https://doi.org/10.1108/09615539910276124

Satjaritanun, P., Cetinbas, F. C., Hirano, S., Zenyuk, I. V, Ahluwalia, R. K., and Shimpalee, S. (2021). Hybrid Lattice Boltzmann Agglomeration Method for Modeling Transport Phenomena in Polymer Electrolyte Membrane Fuel Cells. *Journal of The Electrochemical Society*, *168*(4), 44508.

Selzer, M., Jainta, M., and Nestler, B. (2009). A Lattice-Boltzmann model to simulate the growth of dendritic and eutectic microstructures under the influence of fluid flow. *Physica Status Solidi (B), 246*(6), 1197–1205.

Semma, E., El Ganaoui, M., Bennacer, R., and Mohamad, A. A. (2008). Investigation of flows in solidification by using the lattice Boltzmann method. *International Journal of Thermal Sciences*, *47*(3), 201–208.

Sharma, K. V., Straka, R., and Tavares, F. W. (2017). New cascaded thermal lattice Boltzmann method for simulations of advection-diffusion and convective heat transfer.

*International Journal of Thermal Sciences*, *118*, 259–277.

Sheriff, N., and Davies, N. W. (1979). Liquid metal natural convection from plane surfaces: A review including recent sodium measurements. *International Journal of Heat and Fluid Flow*, *1*(4), 149–154. https://doi.org/10.1016/0142-727X(79)90002-X

Shi, B., and Guo, Z. (2009). Lattice Boltzmann model for nonlinear convection-diffusion equations. *Physical Review E*, *79*(1), 16701.

Shibuta, Y., Sakane, S., Miyoshi, E., Okita, S., Takaki, T., and Ohno, M. (2017). Heterogeneity in homogeneous nucleation from billion-atom molecular dynamics simulation of solidification of pure metal. *Nature Communications*, *8*(1), 1–9.

Soleimani, R., Zargartalebi, M., Azaiez, J., and Gates, I. D. (2021). Hydrodynamic analysis of nanofluid's convective heat transfer in channels with extended surfaces. *Physics of Fluids*, *33*(1), 12011.

Song, W., Zhang, Y., Li, B., and Fan, X. (2016). A lattice Boltzmann model for heat and mass transfer phenomena with phase transformations in unsaturated soil during freezing process. *International Journal of Heat and Mass Transfer*, *94*, 29–38.

Specklin, M., Dubois, P., Albadawi, A., and Delauré, Y. M. C. (2019). A full immersed boundary solution coupled to a lattice–Boltzmann solver for multiple fluid–structure interactions in turbulent rotating flows. *Journal of Fluids and Structures*, *90*, 205–229.

Sterling, J. D., and Chen, S. (1996). Stability analysis of lattice Boltzmann methods. *Journal of Computational Physics*, *123*(1), 196–206.

Succi, S. (2001). *The lattice Boltzmann equation: for fluid dynamics and beyond*. Oxford university press.

Sun, D., Zhu, M., Pan, S., and Raabe, D. (2009). Lattice Boltzmann modeling of dendritic growth in a forced melt convection. *Acta Materialia*, *57*(6), 1755–1767.

Suzuki, K., Kawasaki, T., Asaoka, T., and Yoshino, M. (2020). Numerical simulations of solid–liquid and solid–solid interactions in ice slurry flows by the thermal immersed boundary–lattice Boltzmann method. *International Journal of Heat and Mass Transfer*, *157*, 119944.

Suzuki, K., Kawasaki, T., Furumachi, N., Tai, Y., and Yoshino, M. (2018). A thermal immersed boundary–lattice Boltzmann method for moving-boundary flows with Dirichlet and Neumann conditions. *International Journal of Heat and Mass Transfer*, *121*, 1099–1117.

Tao, S., Xu, A., He, Q., Chen, B., and Qin, F. G. F. (2020). A curved lattice Boltzmann boundary scheme for thermal convective flows with Neumann boundary condition. *International Journal of Heat and Mass Transfer*, *150*, 119345.

Tesfaye, F., and Taskinen, P. (2010). *Densities of Molten and Solid Alloys of ( Fe , Cu , Ni , Co ) - S at Elevated Temperatures - Literature Review and Analysis Aalto University Publications in Materials Science and Engineering Aalto-yliopiston materiaalitekniikan julkaisuja Densities of Mol* (Issue January).

Tiwari, A., Samanta, R., and Chattopadhyay, H. (2023). Droplet solidification: Physics and modelling. *Applied Thermal Engineering*, *228*(December 2022), 120515. https://doi.org/10.1016/j.applthermaleng.2023.120515

Viskanta, R. (1988). Heat transfer during melting and solidification of metals. *Journal of Heat Transfer*, *110*(4), 1205–1220. https://doi.org/10.1115/1.3250621

Voller, V. R., Brent, A. D., and Prakash, C. (1989). The modelling of heat, mass and solute transport in solidification systems. *International Journal of Heat and Mass Transfer*, *32*(9), 1719–1731. https://doi.org/10.1016/0017-9310(89)90054-9

Voller, V. R., Brent, A. D., and Prakash, C. (1990). Modelling the mushy region in a binary alloy. *Applied Mathematical Modelling*, *14*(6), 320–326. https://doi.org/10.1016/0307-904X(90)90084-I

Wang, C.-S., Shen, P.-Y., and Liou, T.-M. (2020). A consistent thermal lattice Boltzmann method for heat transfer in arbitrary combinations of solid, fluid, and porous media. *Computer Methods in Applied Mechanics and Engineering*, *368*, 113200.

Wang, D., and Cheng, P. (2021). Nanoparticles deposition patterns in evaporating nanofluid droplets on smooth heated hydrophilic substrates: A 2D immersed boundary-lattice Boltzmann simulation. *International Journal of Heat and Mass Transfer, 168*, 120868.

Wang, J., Wang, D., Lallemand, P., and Luo, L.-S. (2013). Lattice Boltzmann simulations of thermal convective flows in two dimensions. *Computers and Mathematics with Applications*, *65*(2), 262–286.

Wang, L., Zhao, W., and Wang, X.-D. (2018). Lattice kinetic scheme for the Navier-Stokes equations coupled with convection-diffusion equations. *Physical Review E*, *98*(3), 33308.

Wang, S., Faghri, A., and Bergman, T. L. (2010). A comprehensive numerical model for melting with natural convection. *International Journal of Heat and Mass Transfer*, *53*(9–10), 1986–2000.

Wintruff, I., Günther, C., and Class, A. G. (2001). An interface-tracking control-volume finite-element method for melting and solidification problems-Part I: Formulation. *Numerical Heat Transfer: Part B: Fundamentals*, *39*(2), 101–125.

Wolf-Gladrow, D. A. (2004). *Lattice-gas cellular automata and lattice Boltzmann models: an introduction*. Springer.

Wolff, F., and Viskanta, R. (1987). Melting of a pure metal from a vertical wall. *Experimental Heat Transfer*, *1*(1), 17–30. https://doi.org/10.1080/08916158708946328

Wolff, F., and Viskanta, R. (1988). Solidification of a pure metal at a vertical wall in the presence of liquid superheat. *International Journal of Heat and Mass Transfer*, *31*(8), 1735–1744. https://doi.org/10.1016/0017-9310(88)90285-2

Wu, W., Zhang, S., and Wang, S. (2017). A novel lattice Boltzmann model for the solid–liquid phase change with the convection heat transfer in the porous media. *International Journal of Heat and Mass Transfer*, *104*, 675–687.

Xu, P., Xu, S., Liu, P., Gao, Y., and Liu, X. (2019). Investigation of heat source location on solid-liquid phase change using lattice Boltzmann method. *Energy Procedia*, *158*, 4389–4395.

Yang, X.-H., and Liu, J. (2018). Probing the Rayleigh–Benard convection phase change mechanism of low-melting-point metal via lattice Boltzmann method. *Numerical Heat Transfer, Part A: Applications*, *73*(1), 34–54.

Yang, X., Shi, B., and Chai, Z. (2014). Generalized modification in the lattice Bhatnagar-Gross-Krook model for incompressible Navier-Stokes equations and convection-diffusion equations. *Physical Review E - Statistical, Nonlinear, and Soft Matter Physics*, *90*(1), 1–18. https://doi.org/10.1103/PhysRevE.90.013309

Yang, Z. L., Dinh, T.-N., Nourgaliev, R. R., and Sehgal, B. R. (2000). Evaluation of the

Darcy's law performance for two-fluid flow hydrodynamics in a particle debris bed using a lattice-Boltzmann model. *Heat and Mass Transfer*, *36*(4), 295–304.

Zhang, A., Du, J., Guo, Z., Wang, Q., and Xiong, S. (2018). A phase-field lattice-Boltzmann study on dendritic growth of Al-Cu alloy under convection. *Metallurgical and Materials Transactions B*, *49*(6), 3603–3615.

Zhang, A., Du, J., Guo, Z., Wang, Q., and Xiong, S. (2019). Phase-field lattice-Boltzmann investigation of dendritic evolution under different flow modes. *Philosophical Magazine*, *99*(23), 2920–2940.

Zhang, Liangqi, Yang, S., Zeng, Z., and Chew, J. W. (2018). Lattice model effects on the accuracy of the boundary condition implementations for the convection–diffusion lattice Boltzmann method. *Computers and Fluids*, *176*, 153–169.

Zhang, Liwei, Waters, R. F., MacDonald, K. F., and Zheludev, N. I. (2021). Cellular automata dynamics of nonlinear optical processes in a phase-change material. *Applied Physics Reviews*, *8*(1), 11404.

Zhang, X., Wang, L., and Li, D. (2021). Lattice Boltzmann simulation of natural convection melting in a cubic cavity with an internal cylindrical heat source. *International Journal of Thermal Sciences*, *165*, 106917.

Zhao, Y., Wang, L., Chai, Z., and Shi, B. (2019). Comparative study of natural convection melting inside a cubic cavity using an improved two-relaxation-time lattice Boltzmann model. *International Journal of Heat and Mass Transfer*, *143*, 118449.

Zhu, M.-F., Dai, T., Lee, S.-Y., and Hong, C.-P. (2008). Modeling of solutal dendritic growth with melt convection. *Computers and Mathematics with Applications*, *55*(7), 1620–1628.

Zhu, W., Wang, M., and Chen, H. (2017). 2D and 3D lattice Boltzmann simulation for natural convection melting. *International Journal of Thermal Sciences*, *117*, 239–250.

Zongqin, Z., and Bejan, A. (1989). The problem of time-dependent natural convection melting with conduction in the solid. *International Journal of Heat and Mass Transfer*, *32*(12), 2447–2457. https://doi.org/10.1016/0017-9310(89)90204-4

Zorrilla, S. E., and Rubiolo, A. C. (2005). Mathematical modeling for immersion chilling and freezing of foods: part II: model solution. *Journal of Food Engineering*, *66*(3), 339–351.